

**A sensitive laser-induced
fluorescence system for the detection
of trace level sulfur dioxide in the
remote troposphere**

Loren Gabrielle Temple

Doctor of Philosophy

University of York

Chemistry

September, 2024

Abstract

Sulfur dioxide (SO₂) impacts climate by influencing the cloud condensation nuclei budget, particularly in the remote marine troposphere, thereby contributing to uncertainties in climate model estimates of effective radiative forcing. It is thus crucial to accurately and precisely quantify trace levels of SO₂ in these environments, however, typical commercial instruments lack the necessary sensitivity. This thesis describes the development and validation of the University of York's laser-induced fluorescence (LIF) instrument, the second in the world, for highly sensitive in situ measurements of SO₂ based on custom fibre-laser technology. Its performance is then demonstrated through airborne and ship-based measurements in the remote North Atlantic and Arctic respectively.

Aircraft SO₂ measurements were made by the York LIF instrument in the remote and ship-polluted marine troposphere, providing a wide range of target concentrations. These were compared to simultaneous SO₂ measurements from a commercial pulsed fluorescence (PF) analyser and iodide chemical ionisation mass spectrometer (I⁻CIMS). Given their limits of detection (LoD, 3 σ) of 0.07, 0.4 and 2 ppb at 10 seconds for the LIF, PF and I⁻CIMS respectively, the percentage of data below their LoDs across the three flights were 9, 91 and 98 % respectively. Therefore, a comparison of instruments could only be made in polluted environments where the LIF, PF and I⁻CIMS agreed well, once an interference affecting the sensitivity of the I⁻CIMS was accounted for.

The first ship-based LIF-SO₂ measurements were performed to obtain a unique dataset of SO₂ in the Arctic, and used to explore its potential sources. Peaks of enhanced SO₂ were accounted for by local shipping activity while background measurements were attributed to oxidation of dimethyl sulfide, emitted from the open ocean and sea ice edge.

Contents

Abstract	1
List of figures	5
List of tables	19
Acknowledgements	21
Author's declaration	24
1 Introduction	25
1.1 Why do we want to measure SO ₂ ?	25
1.1.1 Sources	26
1.1.2 Gas phase removal	26
1.1.3 Aqueous phase removal	29
1.1.4 Physical removal	31
1.1.5 Climate impacts	32
1.1.6 Remote marine chemistry	35
1.2 SO ₂ measurement techniques	40
1.2.1 Pulsed fluorescence (PF)	40
1.2.2 Differential optical absorption spectroscopy (DOAS)	42
1.2.3 Chemical ionisation mass spectrometry (CIMS)	44
1.2.4 Laser-induced fluorescence (LIF)	45
2 Experimental	47
2.1 Spectroscopy of LIF	48
2.2 The laser	57

2.2.1	Principle of operation	57
2.2.2	Linewidth versus power	66
2.2.3	Mitigation strategies and improvements	72
2.3	The LIF system	79
2.3.1	Harmonic generation	79
2.3.2	The sample cell	83
2.3.3	The reference cell	84
2.3.4	Instrument control, timings and data logging	86
2.3.5	Gas flow system	89
2.4	Analysis code	92
2.5	Characterisation	97
2.5.1	PT calibration	97
2.5.2	Sensitivity	98
2.5.3	Precision	102
2.5.4	Effect of pressure	105
2.5.5	Effect of temperature	106
2.5.6	Response time	107
2.5.7	Uncertainty analysis	109
2.6	Conclusions and future work	112
3	Intercomparison of SO₂ Techniques	116
3.1	Abstract	118
3.2	Introduction	119
3.3	SO ₂ Instrumentation	122
3.3.1	Laser-induced fluorescence	123
3.3.2	Pulsed fluorescence	129
3.3.3	Iodide chemical ionisation mass spectrometry	130
3.4	Results and Discussion	134
3.4.1	Polluted environments	135
3.4.2	Remote environments	141

3.5	Conclusions	144
3.6	Supplementary Information	146
4	Arctic SO₂ Measurements	153
4.1	The SEANA campaign	156
4.1.1	Project details	156
4.1.2	Instrumentation	158
4.2	LIF performance	160
4.2.1	Characterisation during campaign	160
4.2.2	Instrument issues	167
4.3	Observations of SO ₂ mixing ratios	178
4.3.1	Time series	178
4.3.2	Comparison to literature values	179
4.4	Potential sources of Arctic SO ₂	184
4.4.1	Anthropogenic	184
4.4.2	Biogenic	187
4.4.2.1	Disko Bay	194
4.4.2.2	Pack ice	195
4.4.2.3	Sea ice edge: a case study	196
4.4.2.4	Maniitsoq	202
4.5	Conclusions	206
	Bibliography	207

List of figures

1.1	Schematic diagram of the aerosol indirect effects. TOA refers to the top-of-the-atmosphere. [Reproduced from the IPCC Fourth Assessment Report (Denman et al., 2007)]	32
1.2	Change in effective radiative forcing (ERF) from 1750 to 2019 by contributing forcing agents. Solid bars represent best estimate, and very likely (5 - 95 %) ranges are given by error bars. [Reproduced from the IPCC Sixth Assessment Report (Forster et al., 2021)]	34

1.3	A schematic summary of the expanded atmospheric chemistry of DMS oxidation in CAM6-chem. Key relatively long-lived species (DMS, MSA, HPMTF, SO ₂ , and sulfate), with lifetimes of > 0.5 d, are highlighted in bold. The blue shadings denote species and reactions in the aqueous phase in interstitial aerosols and cloud droplets. DMS (highlighted in green) can undergo OH addition (rightward path) or H abstraction (upper paths). The H-abstraction pathway further diverts into the isomerisation branch (top path) and the MSA-producing branch. SO ₂ is the dominant product of most gas-phase pathways, while MSA is formed mainly via the aqueous-phase oxidation of DMS. Oxidation of SO ₂ to sulfate or sulfuric acid is handled by the CAM6-chem standard chemistry. The resultant particulate MSA and sulfate (highlighted in red) are key species with important radiative impacts. [Reproduced from Fung et al., 2022]	37
2.1	Jablonski diagram showing the various radiative and non-radiative emission pathways following excitation.	48
2.2	SO ₂ absorption cross-sections of SO ₂ for the gas phase from 106 to 403 nm at 293 ± 10 K. [Reproduced from Manatt et al., 1993]	51

2.3	<p>(a) Absorption of 0.3 Torr of SO₂ , path length 6.95 cm, in the region from 2000 to 2300 Å, resolution 3 Å. (b) Fluorescence intensity (undispersed) of 0.3 Torr of SO₂ as a function of incident wavelength, resolution 3 Å, scanning speed 10 Å/min, time constant 5 sec. An arrow shows the thermochemical threshold of dissociation, corresponding to 2192 Å. (c) Fluorescence intensity as a function of incident wavelength of a mixture of 0.3 Torr of SO₂ and 400 Torr of Ar. (d) Fluorescence intensity as a function of incident wavelength of 0.3 Torr of SO₂ in ambient air. The dashed lines indicate the wavelengths 216.9 nm (yellow) and slightly longer than 220 nm corresponding to greatest fluorescence intensity (green). [Reproduced from Okabe, 1971]</p>	54
2.4	<p>Schematic of the relevant SO₂ electronic structure and LIF process. Excitation from the ground state, \tilde{X}, to above the dissociation threshold in the \tilde{C} state at 216.9 nm (purple line) leads to predissociation in the majority of SO₂ molecules. A small fraction undergo internal vibrational relaxation (dashed blue arrow) followed by red-shifted fluorescence (red arrows). [Reproduced from Rollins et al., 2016]</p>	56
2.5	<p>Absorption and emission cross-sections of ytterbium(Yb³⁺)-doped germanosilicate glass, as used in the cores of ytterbium-doped fibers (data from spectroscopic measurements by Paschotta et al., 1997). [Reproduced from RP Photonics (<i>Ytterbium-doped Laser Gain Media</i> n.d.)]</p>	58
2.6	<p>Schematic of the fiber-amplified diode laser system at 1084.5 nm, followed by the production of the fifth harmonic at 216.9 nm using nonlinear crystals.</p>	62

2.7	Pulses from the 1 % tap within the regenerative loop triggered off the pulse produced by the SOA from the 10 % tap, as displayed by the oscilloscope.	63
2.8	The effect of laser pulse duration as displayed on the oscilloscope (left) on the degree of SO ₂ spectral detail seen in the resulting fluorescence spectrum. The spectra show three subsequent scans (blue, red, green) and are compared to a literature absorption spectrum (data from Stark et al., 1999). The LIF counts are normalised by laser power.	67
2.9	Optics alignment setup into the interferometer with the visible alignment beam path (blue) and our invisible laser beam path (yellow) marked.	70
2.10	Interferometer response of our 1084.5 nm laser after the regenerative amplification stage using a 10 GHz scanning Fabry-Pérot interferometer. Each vertical division corresponds to 50 ms.	71
2.11	Optical spectra of (a) a working laser system and (b) a damaged laser system, displayed on the OSA. To note, the resolution of the OSA is insufficient to provide an accurate representation of the laser linewidth and the peak intensities and relative ratios of intensities is arbitrary as it depends on how you angle the fibre into the OSA.	73
2.12	Photograph of the splicer display in end view mode of one of the fibers to be spliced, showing a clean, non-damaged cleave. Note the mark on the left edge of the fiber is due to the blade from the cleaving method and is present on all cleaved fibers.	76
2.13	Optical powers along the length of a Yb ³⁺ -doped fiber amplifier with different types of ion pumping schemes. [Reproduced from RP Photonics (<i>Tutorial “Fiber Amplifiers”</i> n.d.)].	77

2.14	Schematic of the nonlinear optics setup showing the polarisation of the fundamental ($\nu_1 = 1084.5$ nm) and various harmonics (second harmonic = $\nu_2 = 542.3$ nm, third harmonic = $\nu_3 = 361.5$ nm, fifth harmonic = $\nu_5 = 216.9$ nm).	80
2.15	Pulse energy and corresponding average power as a function of current supplied to the pump diode by Kliner et al. ¹³ for their amplifier output at 1064 nm and for the indicated harmonics. The points are the experimental results and the curves are smoothing splines. [Reproduced from Kliner et al.]	81
2.16	Example of the observed reference cell fluorescence counts during a scan of laser excitation wavelength, plotted in red on the right axis. The literature SO ₂ absorption cross section is plotted in black on the left axis.	85
2.17	Laser timings for a single laser shot, as controlled by the FPGA LabVIEW code at 200 MHz, where 1000 ticks is equal to 5 μ s.	86
2.18	Schematic of the gas flow and calibration system. All instrument components within the grey box are housed in the LIF box. The five mass flow controllers (Cal SO ₂ , Ref ZA, Inlet ZA, Cal ZA and ZA SB (suck back)) are labelled with their maximum flow rate.	89
2.19	Flow diagram showing the steps taken in the Python analysis code to convert the fluorescence sample cell counts within the 100 Hz counts file into an SO ₂ mixing ratio.	92
2.20	Relationship between the observed and true photon count values (orange), calculated via Equation 2.5, assuming 1 count per laser shot (200 kHz) and hence a maximum of 2000 counts for a 100 Hz data point. The blue line indicates a 1:1 ratio for the observed count values and the black dashed lines represent the upper limit of this correction, as described by Rollins et al., 2016.	93

2.21	Mean online linearised and normalised count values for a minute long calibration point.	95
2.22	Calibration of the PT against a UV power meter. The data is fitted to a curve of the form $y = a \cdot e^{(-b \cdot x)}$ where $a = -0.0647$, $b = 0.454$, and $c = 0.0644$, with a root mean square error of 0.0004.	98
2.23	Example laboratory SO ₂ calibration in zero air where the LIF signal is the difference between linearised and normalised online and offline sample cell counts. The orange line shows a York regression fit to the seven data points, indicating a slope of 38.7 ± 2.1 cps mW ⁻¹ ppt ⁻¹ , a y-intercept of 620 ± 1700 cps mW ⁻¹ (both 2 σ confidence), and a correlation coefficient of $R^2 = 1.00$	99
2.24	Histogram of each calibration point shown in Figure 2.23, coloured by the corresponding SO ₂ mixing ratio to 3 significant figures. The mean LIF signal value for each calibration point is marked by the coloured dashed line.	101
2.25	Instrument precision (Allan deviation) of a 1 h duration zero air measurement for different laser powers, as performed in the laboratory before the aircraft and ship-based campaigns (orange) and more recently with improved laser power (blue). Both traces are compared to the expected precision (Poisson limit).	103
2.26	Relative instrument sensitivity, determined experimentally and theoretically, over a cell pressure range of 100 to 500 mbar.	105
2.27	A comparison of exponential fitting methods to determine the 3 e-folding response time (τ) from a stable concentration to ambient air during a laboratory calibration. [Figure made by Sam Rogers.]	108
2.28	Uncertainty in SO ₂ mixing ratios for the range 0 to 100 ppt. .	111

3.1	Example laboratory SO ₂ calibration in zero air where the LIF signal is the difference between linearised and normalised on-line and off-line sample cell counts. The orange line shows a York regression fit to the seven data points, indicating a slope of 38.7 ± 2.1 cps mW ⁻¹ ppt ⁻¹ , a y-intercept of 620 ± 1700 cps mW ⁻¹ (both 2 σ confidence), and a correlation coefficient of $R^2 = 1.00$	125
3.2	Relative instrument sensitivity over a cell pressure range of 100 to 500 mbar.	126
3.3	Instrument precision (Allan deviation) of a 10 min stable ambient measurement of mean mixing ratio 75 pptv during flight C287 (orange) and a 3.5 h zero air measurement, performed recently in the laboratory with improved laser power and sensitivity (blue). Both traces are compared to the expected precision (Poisson limit). The precision (1 σ) at an averaging time of 10 s for each trace is marked by the red dots (23 pptv for the orange trace, 5.4 pptv for the blue).	128
3.4	High resolution peak fitting at m/z 191 during ambient sampling in ACRUISE-3 (A) and calibration using a commercial standard (B).	131
3.5	Time series of the high-resolution peak fitting at m/z 191 taken at 4 Hz.	132
3.6	Changes in the intensity of the peaks identified at m/z 191 as a result of A) offset in the mass calibration and B) changes in the peak width.	133
3.7	UoM I ⁻ CIMS humidity dependent sensitivity to SO ₂ determined from an offline calibration using a commercial standard of SO ₂ . The error bars represent one standard deviation. . . .	134

3.8	Time series of 10 s averaged, time matched data during flight C285, comparing the LIF, PF and I ⁻ CIMSSO ₂ measurements for an offline pre-campaign I ⁻ CIMS sensitivity (A) and in-flight I ⁻ CIMS sensitivity (B).	135
3.9	Correlation of the 10 s averaged, time matched data for all three ACRUISE-3 flights, excluding points which are below the instrument's LoD. (A) Correlation between the PF and LIF instruments. (B) Correlation between the I ⁻ CIMS and LIF instruments, for an offline pre-campaign I ⁻ CIMS sensitivity (purple) and in-flight I ⁻ CIMS sensitivity (green). The coloured dashed lines represent the linear fit and the solid black line represents the 1:1 ratio.	135
3.10	Response of I ⁻ CIMS SO ₂ signal as a function of SO ₂ concentration measured by LIF (A) UoM I ⁻ CIMS humidity dependent sensitivity to SO ₂ determined from an in-flight intercomparison calibration with LIF (B).	137
3.11	Time series comparing instrument response time, matched by the increasing SO ₂ mixing ratio due to measurement of a ship plume during flight C285. The LIF data is presented at 5 Hz, the PF at 1 Hz, the I ⁻ CIMS at 4 Hz and the CO ₂ data at 10 Hz.	138
3.12	Time series of 10 s averaged, time matched data during flight C286, comparing the LIF, PF and I ⁻ CIMS SO ₂ measurements.	141
3.13	Histogram of data presented in Figure 3.12, comparing the noise distributions of the LIF, PF and I ⁻ CIMS SO ₂ measurements for a mixing ratio of 176 ppt, as marked by the black solid line.	143
3.14	LIF sensitivity variation over time during flight C285 for calibrations in ambient air and zero air. Error bars are given to a 2 σ confidence interval.	146

3.15 LIF sensitivity variation over time during flight C286 for calibrations in ambient air and zero air. Error bars are given to a 2σ confidence interval.	147
3.16 LIF sensitivity variation over time during flight C287 for calibrations in ambient air and zero air. Error bars are given to a 2σ confidence interval.	148
3.17 Autocorrelation plot of the LIF data presented in Figure 3.12 and Figure 3.13 at 10 Hz.	148
3.18 Colour map of 10 s LIF SO ₂ mixing ratios along all three ACRUISE-3 flight tracks.	149
3.19 Profiles of mean (A) and median (B) 10 s LIF SO ₂ mixing ratios for each 100 m altitude bin, comparing the ACRUISE-3 and ACSIS-7 data. The error bars indicate 2 standard errors. . . .	150
3.20 Variation of LIF zero measurements (red dots) over time, plotted against the LIF-SO ₂ ambient time series averaged to 10 seconds (blue) and the altitude (grey) during flight C287. . .	151
4.1 Map showing the sailing route of the RRS Discovery with the stations that were stopped at marked by a star.	157
4.2 The container laboratories on deck of the RRS Discovery. The LIF-SO ₂ instrument was housed inside the red container. . .	160
4.3 The plumbing setup for the two different calibration methods, showing the sample line (blue arrow) and the calibration line (red arrow).	160

4.4	Instrument sensitivities over time for back-of-the-box calibrations performed in both ambient and zero air during the SEANA campaign are plotted as scatter points (blue), with error bars representing 2σ standard error of the York regression fit. These scatter points are overlaid onto the reference LIF signal data (10 Hz, blue). Significant decreases in the reference LIF signal due to poor laser linewidth are highlighted in orange, along with the corresponding sensitivities during these times, for which the data has been discarded. The length of each data block is indicated by pink shading, showing the sensitivities used to calculate the mean sensitivity for each block. The cell pressure (5 Hz, red) was mainly maintained at 600 mbar, with some unintended periods at 500 mbar due to an unchanged default value at instrument startup.	163
4.5	Reference LIF signal variation over time (10 Hz, blue) with yellow coloured periods, corresponding to the grey shaded regions, indicating data discarded due to laser linewidth issues. Large variations in the laser box temperature (green) are thought to causes these linewidth deviations, which can also be seen in the online seed laser voltage (cyan), representing tracking of the transition peak.	164
4.6	Instrument precision (Allan deviation) of a 9 h long ambient measurement on 11th June (mean mixing ratio of -10 ppt due to laser clipping). The trace is compared to the Poisson limit (dashed line) and the precision at an averaging time of 5 minutes is marked by the red dot.	166
4.7	Experimentally determined wavelength tuning of the seed laser diode via driving current supplied from the seed laser driver board and temperature. The laser wavelength was measured using a wavemeter (moglabs MWM wavemeter). .	173

4.8	Calibrations performed in ambient air at the back of the LIF box (blue, starting at 19:05) and the inlet (orange, starting at 19:33) on 17th June 2022 during the SEANA campaign, yielding sensitivities of 33.6 ± 4.7 cps mW ⁻¹ ppt ⁻¹ and 20.8 ± 3.0 cps mW ⁻¹ ppt ⁻¹ (both 2 σ confidence) respectively.	175
4.9	Calibrations performed in the laboratory post-campaign using the same length calibration line but introducing the calibration gas at the end of the 10 m long inlet (orange) versus at the back of the box (blue). The calibration at the inlet was repeated (red) to capture any drift in instrument sensitivity. [Data collected by Eve Grant.]	177
4.10	5-minute averaged SO ₂ time series for the campaign, shaded by the ship position. The time series is coloured by background SO ₂ measurements (green) and anthropogenic influenced measurements (orange). The 3 σ limit of detection of the LIF-SO ₂ during the campaign is marked by the red dashed line (15 ppt).	178
4.11	Histogram of the background SO ₂ measurements made on the SEANA campaign, annotated with statistical parameters, compared to literature concentration values or ranges of SO ₂ in the Arctic. For literature values that were reported in units other than ppt (mainly either nmol m ⁻³ or μ g m ⁻³), a conversion has been made into ppt using a standard temperature of 273 K and pressure of 1 atm.	181
4.12	1-minute averaged SO ₂ , NO _x , CO ₂ and CO time series at the sea ice station. All datasets have been filtered for relative wind speed and direction to remove instances when we are measuring our own ship stack.	184

- 4.13 Satellite density map of west Greenland showing the total number of shipping routes (for all ship types) per 4.89 km² per year during 2022. A snapshot of the positions of fishing vessels only is captured by the orange triangles on 31.07.24 at 11 am (similar time of year to when the measurements were taken in 2022) to demonstrate that this region of the Arctic is already being exploited for fishing purposes. The map is also marked (red circle with central white dot) with our ship position at the sea ice edge, during which time the measurements in Figure 4.12 were taken. 186
- 4.14 Mapped satellite sea ice and chlorophyll concentrations. Sea ice concentrations are obtained from the National Snow and Ice Data Center (<https://nsidc.org/data/g02135/versions/3>) and have a temporal resolution of 1 day (on 6th June 2022) and a spatial resolution of 25 km. Chlorophyll-a concentrations from the AQUA MODIS satellite can be found here (https://modis.gsfc.nasa.gov/data/dataproduct/chlor_a.php), and have a temporal resolution of 8 days (from 2nd June to 9th June 2022) and a spatial resolution of 4 km. 189

- 4.16 48-hour air mass back trajectories at 1-hour intervals, simulated by the HYSPLIT model which was run by collaborators at the University of Birmingham for Disko Bay, the pack ice, ice edge, and Maniitsoq. The back trajectories are coloured by hourly averaged SO₂ and DMS mixing ratios respectively (provided that at least 20 % of data is available within that hour) and overlaid onto satellite sea ice and chlorophyll concentrations. Sea ice concentrations are obtained from the National Snow and Ice Data Center (<https://nsidc.org/data/g02135/versions/3>) and have a temporal resolution of 1 day (on 6th June 2022) and a spatial resolution of 25 km. Chlorophyll-a concentrations from the AQUA MODIS satellite can be found here (https://modis.gsfc.nasa.gov/data/dataproduct/chlor_a.php), and have a temporal resolution of 8 days (from 2nd June to 9th June 2022) and a spatial resolution of 4 km. 194
- 4.17 Photograph of the sea ice edge, taken from the ship on 7th June. 196
- 4.18 Hourly averaged diel profiles of observed DMS and SO₂ mixing ratios, and modelled SO₂ and OH mixing ratios, obtained from a 0-D box model run by collaborators at the University of Cambridge (more details below). The coloured shading around the observed mixing ratios represents two standard errors since some hours contain more measurements than others. Note the hour of day is UTC, which is 2 hours ahead of local time. The grey shading between hours 2 and 5 corresponds to a modelled UVA and UVB irradiance from the Tropospheric Ultraviolet and Visible (TUV) Radiation Model of zero, which defines nighttime at the sea ice. 197

4.19	Correlation of SO ₂ and DMS mixing ratios at a 5 minute averaging time coloured by modelled UVA irradiance from the Tropospheric Ultraviolet and Visible (TUV) Radiation Model. The linear least squares best fit is plotted as the dashed black line. The slope of the best fit line is -0.83, and R ² = 0.21. . . .	199
4.20	1-minute averaged SO ₂ , DMS, CO and O ₃ time series at the sea ice station, with the sea ice edge data highlighted in blue. All datasets have been filtered for relative wind speed and direction (to remove ship stack measurements) as well as spike enhancements due to anthropogenic influences. Hourly modelled UVA irradiance from the TUV Radiation Model is also plotted.	201

List of tables

1.1	Literature measurements of SO ₂ in the remote marine troposphere made using either the PF, DOAS, CIMS or LIF technique.	41
3.1	Comparison of the LIF, PF and I ⁻ CIMS techniques in terms of limit of detection (LoD), response time, sampling rate, and mixing ratio uncertainty as performed during the ACRUISE-3 campaign. The I ⁻ CIMS parameters are given for the in-flight calibration method (see subsection 3.4.1 for discussion on different calibration methods for I ⁻ CIMS).	123
3.2	Summary of the calibrations performed in both ambient air and zero air during each flight, showing the mean sensitivity (\bar{x}), standard deviation of the sensitivities (σ) and the number of calibrations (N).	127

3.3	Comparison of integration and regression methods for calculating SO ₂ :CO ₂ emission ratios of four ship plumes during different flights. The SO ₂ data has been obtained from the fast I ⁻ CIMS, and its peak area has been scaled to match the accuracy of the LIF. Therefore, the uncertainties associated with the emission ratios calculated via the integration method are based on the LIF data. All emission ratio uncertainties have been given to a 2 σ confidence interval. The corresponding sulfur fuel content (SFC) has been calculated via Equation 3.2 using the mean of the emission ratios obtained from the two methods.	140
4.1	Summary of the back-of-the-box calibrations performed in both ambient and zero air during the SEANA campaign. The mean (\bar{x}), standard deviation (σ), number of calibrations (N) and mean uncertainty for the sensitivities within each data block are given.	165
4.2	Estimated atmospheric lifetimes of DMS due to the oxidants OH, NO ₃ and BrO, calculated from the IUPAC recommended reaction rates of DMS + oxidant and the approximated campaign mean oxidant concentrations. *The mixing ratio of BrO is taken from observations made by Jeong et al., 2022.	203

Acknowledgements

First and foremost, I would like to thank my supervisor, Pete Edwards. I am incredibly grateful for this fantastic opportunity alongside your unwavering support, guidance and patience over the past four years. You have always made time for me and your vast knowledge, enthusiasm and optimism has provided a constant source of inspiration. I would also like to thank my co-supervisor, James Lee, for your valuable insights and feedback as well as vital support during fieldwork campaigns and conferences.

I owe a lot of thanks to Stuart Young, who has likely aged from the countless questions I've thrown his way! Your instrumental expertise constantly inspires me, and you have taught me so much (with the help of your trusty whiteboard)! Thank you for always being there for me, even over the phone when I was in the Arctic. A huge thanks to Jake for all your support and coding help – you truly are a coding wizard.

To WACL, thank you for all the group socials and daily office chats and, of course, Zumba with Beth, Dominika and Sari! I especially want to thank Maggie, Lucy, and Sera who have been with me through this entire journey, celebrating our successes together and supporting each other during challenging times – I owe you guys a lot. Eve and Sam, thank you for helping me through this write up, it's been great having you in the LIF group!

I would like to thank DEFRA for providing me with valuable insights into life in the Civil Service. Special thanks to Neil Ward, my placement supervisor, for all the opportunities to engage with stakeholders. My placement allowed me to grow both personally and professionally whilst contributing to meaningful air quality work.

My PhD journey took me to incredible places, from the Arctic to the Azores, that I would never have had the opportunity to see ordinarily, which made all the hard work worth it! Special thanks to Jake and Dominika for

your support and company during the aircraft campaign, and to Anna for keeping my spirits high during the Arctic cruise (even when the laser broke!) – I couldn't have asked for a better person to share those unforgettable experiences with.

I would like to extend my heartfelt thanks to Liz and Jonny for their amazing hospitality during what was meant to be a 'few months' of my PhD but ended up being nine! I really enjoyed living with you both and you made me feel incredibly comfortable and welcome – it definitely felt like home away from home. To Ann and Dave, my York grandparents, thank you for always inviting me over for dinner and for all the chemistry chats with a fellow Dr!

To my amazing sisters, Ellen and Imogen, thank you for your endless encouragement and understanding. You've always known what's best for me, whether its taking me away for a weekend to recharge or just being at the other end of the phone. I'm so proud of all you've accomplished over the last four years while I've been buried in my work, and I promise to be a little less annoying now that my thesis is done!

To Tom, thank you for being there for me every step of the way – I couldn't have done it without you. Your constant understanding, support, and positive (and pro-active!) advice has helped me through the tough times. From teaching me to drive to sharing a house together, you have made the past four years significantly better and I look forward to all the adventures that lie ahead for us.

To my parents, I cannot thank you enough for being there at every stage of my life and career so far. Mum, you've inspired and nurtured my love of science from the very beginning, whether it was watching Brian Cox together on TV or discussing something interesting you read in the New Scientist magazine. Even though my work may be difficult to understand, you're always interested to hear about my day and always there for me no

matter what. Dad, your endless humour, care, and, of course, legendary Sunday Roasts have kept me going throughout this entire process. You always manage to make me laugh, no matter how stressed I am! I couldn't have asked for better parents to get me through this.

Lastly, I would like to thank anyone I may have missed. The past four years have certainly been a rollercoaster, but I couldn't have done it without the support and kindness of so many people.

Author's declaration

I declare that this thesis is a presentation of original work and I am the sole author. This work has not previously been presented for a degree or other qualification at this University or elsewhere. All sources are acknowledged as references.

Chapter 1

Introduction

1.1 Why do we want to measure SO₂?

Sulfur dioxide (SO₂) plays a pivotal role in the chemistry of the troposphere, influencing regional and global air quality and climate. SO₂ is the predominant anthropogenic sulfur-containing air pollutant, posing risks to human health, and a major contributor to acid rain (Likens et al., 1979), which can have detrimental effects on aquatic and terrestrial ecosystems. SO₂ is also a precursor to aerosols, which are of particular health concern since they can penetrate deep into the lungs, leading to respiratory issues, cardiovascular problems, and exacerbating conditions such as asthma and bronchitis. Since these harmful effects were realised following significant emissions during the Industrial Revolution, global SO₂ emissions have been declining since the 1970s (Smith et al., 2011) and are now below many countries' emission limits. However, even at these low concentrations, SO₂ still plays an important role in the production cloud condensation nuclei (CCN), especially in remote marine environments, which affect the Earth's radiation balance and climate (Williamson et al., 2019).

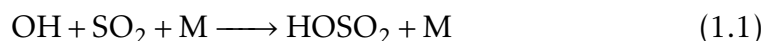
1.1.1 Sources

Sulfur dioxide (SO_2) is released into the atmosphere from both anthropogenic and natural sources. The major source of SO_2 to the troposphere is from anthropogenic emissions, which account for 70 % of global sulfur emissions (Penner et al., 2001). This is mainly due to primary SO_2 anthropogenic emissions from fossil fuel combustion in power plants, industrial facilities, and petroleum refineries, where coal, oil, and other sulfur-containing fuels are burned and metal smelting, particularly from the processing of sulfide ores in copper, zinc, and lead production. Additionally, the shipping sector is a significant contributor to primary anthropogenic emissions, estimated to be responsible for 13 % of global SO_2 emissions (Watson-Parris et al., 2022). The natural primary sources of SO_2 to the troposphere are volcanoes and biomass burning. Large volcanic eruptions can also eject SO_2 into the stratosphere where it exists on much longer timescales compared to in the troposphere. SO_2 can also be formed through secondary biogenic emissions from the oceans, which release dimethyl sulfide that undergoes oxidation in the troposphere to SO_2 (more on this in section subsection 1.1.6). Both anthropogenic and natural sources of SO_2 can have significant implications for air quality, acid rain formation, and human and ecosystem health.

1.1.2 Gas phase removal

The major sink of atmospheric SO_2 is oxidation to sulphuric acid (H_2SO_4) and ultimately sulfate (SO_4^{2-}) aerosols. SO_2 oxidation can occur either in the gas or aqueous phase, with average branching ratios of 24 % and 76 % respectively (Faloona, 2009). Firstly, the gas-phase oxidation of SO_2 in the atmosphere primarily takes place through its reaction with the hydroxyl radical (OH) (Blitz et al., 2003). This highly reactive radical is produced in the atmosphere from the photolysis of ozone to form $\text{O}(^1\text{D})$ followed by reaction with water vapour, or through other mechanisms such as the

photolysis of nitrous acid (HONO) and hydrogen peroxide (H₂O₂). Therefore, SO₂ oxidation by OH is largely restricted to the daytime when the production of OH radicals is most favoured. The predominant reaction is given below, which yields HOSO₂ adducts (Blitz et al., 2003):



where M is a molecule of O₂ or N₂ that removes the energy liberated in the reaction. These adducts react quickly with O₂ to form SO₃ (Atkinson et al., 2004), which is transformed into H₂SO₄ in the presence of water vapour (Seinfeld et al., 1998):



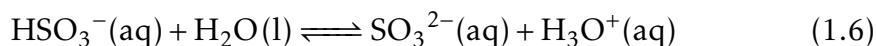
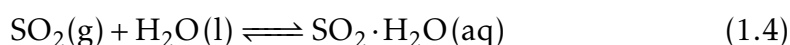
However, other oxidants can contribute to the gas-phase oxidation of SO₂ (O₃, Criegee intermediates, O (³P), HO₂). For example, Mauldin et al., 2012 proposed that another compound, likely a stabilised Criegee intermediate or its derivative, may have a considerable oxidative capacity for SO₂. Based on their observations from a boreal forest region, they estimated that this non-OH source may contribute up to 50 % of the total H₂SO₄ budget (Mauldin et al., 2012), demonstrating the importance of alternative oxidants for SO₂, especially during evening and night when OH concentrations are lower. Other important gas phase oxidants include the nitrate radical as a nighttime oxidant and halogen species, which may be particularly important in the remote marine boundary layer.

Since gaseous H₂SO₄ is hygroscopic and has extremely low volatility (Pye et al., 2020), it rapidly condenses either through heterogeneous nucleation onto pre-existing aerosols (Pham et al., 1995) found in more polluted environments, or via homogeneous nucleation to form new particles in cleaner

conditions where pre-existing aerosol loading is low (Kulmala et al., 1998). Homogeneous nucleation and growth of new aerosol particles from trace atmospheric vapours is thought to provide up to half of global CCN (Merikanto et al., 2009), for which H_2SO_4 is a significant source gas. However, since theory suggested that peak concentrations of H_2SO_4 in the boundary layer ($10^6 - 10^7 \text{ cm}^{-3}$, Kerminen et al., 2010) are too low for the binary nucleation of $\text{H}_2\text{SO}_4\text{-H}_2\text{O}$ to proceed (Kirkby et al., 2011), there was an increase in experimental research in this area which found that nucleation rates are enhanced by the presence of ternary vapours, such as ammonia, amines, as well as ion-induced nucleation. The most comprehensive laboratory experiments to directly measure homogeneous nucleation rates under atmospheric conditions have been made by the CLOUD (Cosmics Leaving Outdoor Droplets) chamber at CERN Proton Synchrotron. Firstly, Kirkby et al., 2011 found that atmospherically relevant ammonia mixing ratios of 100 pptv, or less, increase the nucleation rate of sulphuric acid particles more than 100–1,000-fold. However, concentrations of ammonia and sulphuric acid alone were insufficient to account for observed boundary-layer nucleation. More recently, Almeida et al., 2013 demonstrated that dimethylamine concentrations > 3 pptv can enhance particle formation rates by over 1,000-fold compared to ammonia, adequately explaining particle formation rates observed in the atmosphere. Even more recently, condensable vapours such as highly oxygenated organics and iodine oxoacids have also been found to play key roles in homogeneous nucleation (Sarnela et al., 2018; He et al., 2021; Kirkby et al., 2023). After nucleation, there is generally insufficient H_2SO_4 to grow the clusters to CCN sizes, so other supersaturated substances, especially low vapour pressure organics often take part in the subsequent aerosol growth (Boy et al., 2005; Wang et al., 2010).

1.1.3 Aqueous phase removal

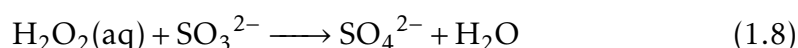
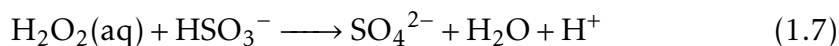
Aqueous phase oxidation of SO_2 plays a more important role than its gas phase counterpart in sulfate formation (Faloona, 2009), especially under high humidity conditions (McMurry et al., 1982) and during nighttime when gas phase pathways are reduced (Middleton et al., 1980). It proceeds with SO_2 dissolution in water from cloud, fog and aerosol particles. Acidity, defined by pH, is a crucial component of aqueous chemistry because it influences the solubility of various gases, their phase partitioning, and chemical reaction rates (Pye et al., 2020). Therefore, the solubility of SO_2 in water produces three dissolved S(IV) species depending on the pH of the solution: $\text{SO}_2 \cdot \text{H}_2\text{O}$, HSO_3^- , SO_3^{2-} , as shown below.



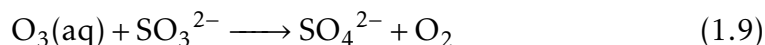
(Hoffmann, 1986; Seinfeld et al., 1998; Hobbs, 2000)

Although there are many pathways for the oxidation of dissolved SO_2 to sulfate, the two most significant are its reaction with dissolved H_2O_2 and O_3 . In fact, H_2O_2 has been found to play the dominant role in aerosol aqueous sulfate formation on a global scale (Gao et al., 2024) due to its high solubility. The rate of aqueous oxidation of dissolved SO_2 by H_2O_2 is largely pH-independent for pH's above 2 (Hobbs, 2000). This is because the effects arising from the pH dependence of the SO_2 solubility offset the reaction rate constant (Liu et al., 2020; Gao et al., 2024). Hence, H_2O_2 mainly reacts with HSO_3^- and SO_3^{2-} which are formed at $\text{pH} > 2$, and their overall reactions

are shown below (which occur via the sulfuric acid intermediate) (Hobbs, 2000).



In contrast, aqueous phase oxidation by O_3 is strongly pH dependent. Since O_3 reacts most rapidly with SO_3^{2-} , the O_3 oxidation pathway becomes particularly significant in regions of high alkalinity (Seinfeld et al., 1998; Hobbs, 2000; Gao et al., 2024) and follows the following reaction.



Alternative aqueous reactions are generally limited by either the lower solubility of other oxidants or their slower reaction rates with dissolved SO_2 . However, the hypohalous acids (HOBr, HOCl, HOI) are thought to play a significant role in aqueous-phase sulfate production in the marine boundary layer (Chen et al., 2016; Sherwen et al., 2016). Some reactions are also catalysed in the presence of metals, which can influence the yield of products.

Sulfate ions within aerosols can be base-stabilised by ammonia and other organic amines (as mentioned previously), contributing to the persistence of sulfate aerosols in the atmosphere. This determines the pH of the aerosol, which, in addition to the physical and chemical properties of the aerosol, governs its scavenging efficiency and ability to serve as CCN (Turnock et al., 2019). If aerosols reach diameters of approximately 60 nm via coagulation and condensation, they can act as CCN and can influence cloud brightness, albedo, lifetime, precipitation etc., which subsequently impacts the Earth's radiative balance.

1.1.4 Physical removal

SO₂ can also be removed from the atmosphere via dry and wet deposition (Seinfeld et al., 1998; Pham et al., 1995) that operate at different stages of its atmospheric lifetime. It is estimated that about half of the SO₂ emitted into the atmosphere is removed by dry deposition through its interaction with surfaces, such as vegetation, soil, buildings, or water bodies (Garland et al., 1978). Additionally, SO₂ can be converted to aerosols in the atmosphere, leading to its removal when the aerosols are deposited, either by dry or wet deposition. If aerosols composed of sulfuric acid and its salts (ammonium bisulfate, ammonium sulfate) are incorporated into precipitating clouds, then the deposition of these species can be faster than that of gaseous SO₂ (Kerr et al., 1985).

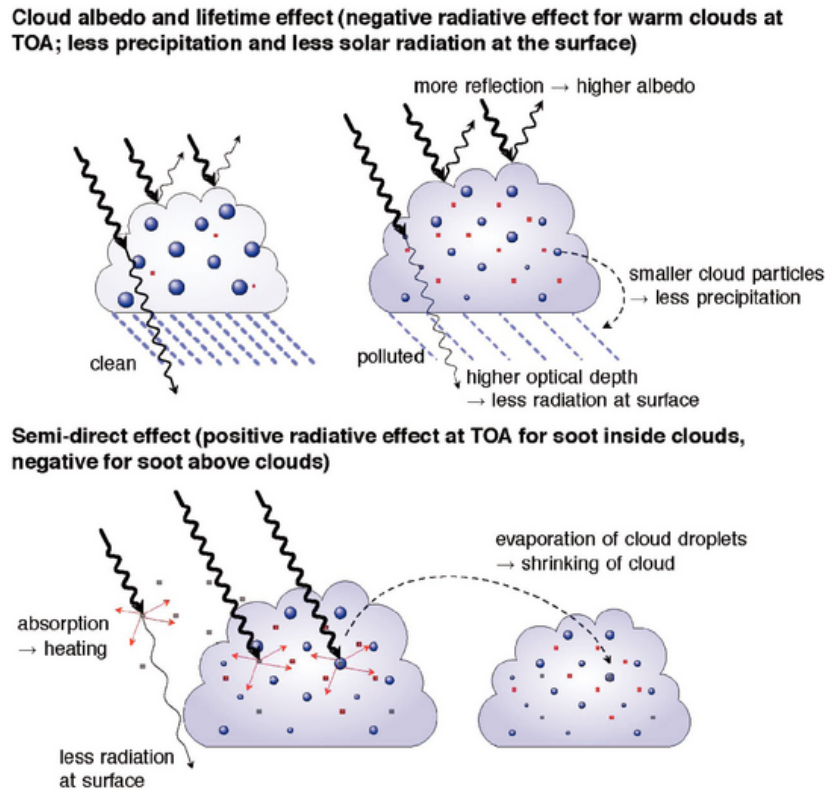


Figure 1.1: Schematic diagram of the aerosol indirect effects. TOA refers to the top-of-the-atmosphere. [Reproduced from the IPCC Fourth Assessment Report (Denman et al., 2007)]

1.1.5 Climate impacts

Sulfate aerosols affect the Earth’s radiation balance and hence climate through the direct scattering of sunlight (Charlson et al., 1992), and also indirectly via modification of cloud albedos, lifetimes, and precipitation cycles (Twomey, 1977; Jones et al., 2001; Penner et al., 2001). As shown in Figure 1.1, the cloud albedo effect describes the cloud droplet number concentration for a given cloud liquid water content, where an increase in aerosol particles results in the water being distributed among more particles, leading to a greater number of smaller cloud droplets. This makes clouds optically thicker and whiter (Twomey, 1977), increasing their reflectivity and creating a larger cooling effect than the aerosol particles would on their own. As a

result of this albedo effect, subsequent feedback effects in the climate system can arise. For example, smaller cloud droplets decrease precipitation formation, resulting in longer-lasting clouds that maintain high reflectivity (cloud lifetime effect). Additionally, the presence of absorbing aerosols e.g. black carbon can lead to localised atmospheric heating, which can reduce cloud formation or inhibit cloud ascent by stabilising the surrounding air (semi-direct effect), thus further influencing the cloud dynamics and radiative properties. The direct and indirect effects for sulfate aerosols have a cooling effect on the planet and contribute to the net negative effective radiative forcing (ERF) estimates for aerosols, given in Figure 1.2 (Forster et al., 2021). As outlined in the IPCC's Fifth Assessment Report (Myhre et al., 2013), ERF is a better metric for quantifying the climate response compared to radiative forcing since it accounts for rapid adjustments of the Earth's surface and troposphere, such as the impact of aerosols on atmospheric temperature profiles and cloud properties. This is because in contrast to greenhouse gases (CO_2 , CH_4 , N_2O and halocarbons) which last for decades to centuries, aerosols have a relatively short lifetime of days to weeks and thus exhibit a spatially inhomogeneous distribution. Therefore, aerosol effects change much more quickly than those of greenhouse gases, meaning they are a more powerful player in global climate extremes. For example, aerosols were a major driver of the late-twentieth-century Sahel drought, which led to a famine that claimed 100,000 lives (Persad et al., 2022). Therefore, it is important to include aerosol impacts in regional estimates of risk from climate change, as current near-term climate evaluations used by policymakers either overlook aerosols or merely average their effects globally, failing to address their critical influence on regional climate dynamics (Persad et al., 2022).

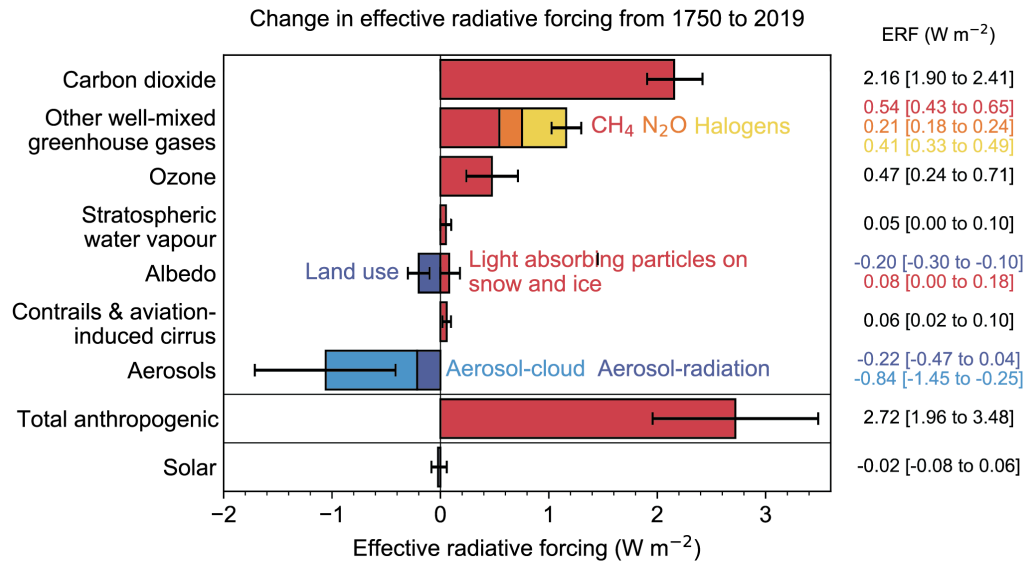


Figure 1.2: Change in effective radiative forcing (ERF) from 1750 to 2019 by contributing forcing agents. Solid bars represent best estimate, and very likely (5 - 95 %) ranges are given by error bars. [Reproduced from the IPCC Sixth Assessment Report (Forster et al., 2021)]

Long-lived greenhouse gases that do not undergo major reactive loss processes generally exhibit a homogeneous distribution throughout the troposphere, and hence their concentrations can be modelled using emission inventory data and also measured through point sampling for estimating global scale radiative forcing potentials. Therefore, since this is relatively accurately known, the error bars associated with ERF estimates for greenhouse gases are fairly small, for example spanning +1.90 to +2.41 W m⁻² for CO₂. In contrast, aerosol ERF has a significantly larger error bar, predominantly driven by the indirect effect, which ranges from -1.45 to -0.25 W m⁻² and accounts for 80 % of the total aerosol ERF. The aerosol indirect ERF represents the largest source of uncertainty in climate model simulations, and is masking global warming to an unknown extent. Carslaw et al., 2013 performed a sensitivity analysis on a global model and found that the uncertainty in aerosol indirect ERF is dominated by the uncertainty in

natural aerosols. This is because to estimate the magnitude of anthropogenic-induced warming, climate models constrain to a baseline, for which the pre-industrial atmosphere is used. The closest present-day analog to a pre-industrial atmosphere, with only natural aerosols, can be found in pristine environments, such as the remote marine troposphere. The importance of natural aerosols has also been highlighted by subsequent modelling studies (Gryspeerdt et al., 2023; Lee et al., 2016; Ghan et al., 2016; Fung et al., 2022). Therefore, improving the model representation of pre-industrial aerosols requires a better understanding of aerosols and their formation processes in remote marine environments.

1.1.6 Remote marine chemistry

Dimethyl sulfide (DMS) is the most significant precursor of oxidised sulfur gases in the marine atmosphere (Andreae et al., 1985; Andreae, 1990; Bates et al., 1992), which originates from the breakdown of dimethylsulphoniopropionate (DMSP) produced by marine organisms, particularly phytoplankton (Carslaw et al., 2010). It undergoes efficient oxidation to sulfuric acid (H_2SO_4) and methane sulfonic acid (MSA), which can facilitate the formation of new particles, making it a major contributor to aerosols and hence CCN. The idea that DMS can have a profound impact on the populations of CCN over the world's oceans has been long recognised and has become known as the CLAW hypothesis after the authors of Charlson et al., 1987. However, they hypothesised that DMS could provide a feedback mechanism to stabilise the Earth's climate in response to climate change. Although a feedback mechanism has not been identified, this hypothesis has spurred numerous studies to ascertain the effects of DMS on climate (Ayers et al., 2007). Despite this, the oxidation mechanism of DMS to sulfate aerosols still remains poorly understood. It was only recently that a previously unquantified DMS oxidation product: hydroperoxymethyl thioformate (HPMTF) was measured

in the lower troposphere and marine boundary layer by Veres et al., 2020, after being proposed as a possible formation process by Wu et al., 2015, and first measured in the laboratory by Berndt et al., 2019. Therefore, sulfate aerosol formation from DMS oxidation contributes to uncertainties not only in global model estimates of the impact of DMS emissions on CCN (Lucas et al., 2002; Chen et al., 2018; Faloon, 2009; Quinn et al., 2011; Carslaw et al., 2013), but also in the pre-industrial aerosol budget. Thus, accurately representing the DMS oxidation mechanism in models is crucial for reducing these global uncertainties, and for that, we need measurements.

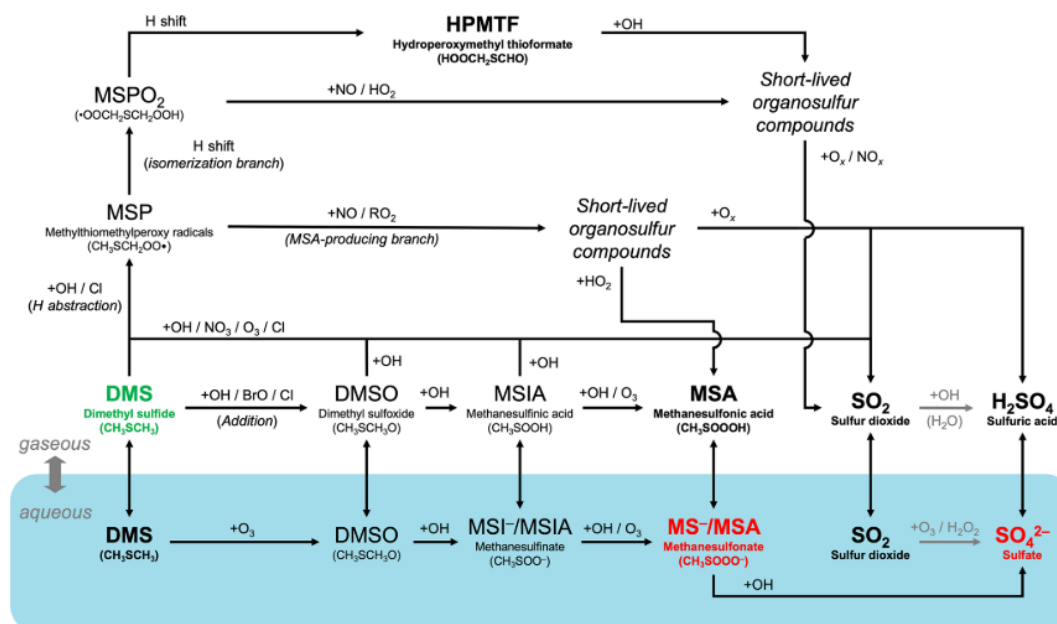


Figure 1.3: A schematic summary of the expanded atmospheric chemistry of DMS oxidation in CAM6-chem. Key relatively long-lived species (DMS, MSA, HPMTF, SO_2 , and sulfate), with lifetimes of > 0.5 d, are highlighted in bold. The blue shadings denote species and reactions in the aqueous phase in interstitial aerosols and cloud droplets. DMS (highlighted in green) can undergo OH addition (rightward path) or H abstraction (upper paths). The H-abstraction pathway further diverts into the isomerisation branch (top path) and the MSA-producing branch. SO_2 is the dominant product of most gas-phase pathways, while MSA is formed mainly via the aqueous-phase oxidation of DMS. Oxidation of SO_2 to sulfate or sulfuric acid is handled by the CAM6-chem standard chemistry. The resultant particulate MSA and sulfate (highlighted in red) are key species with important radiative impacts. [Reproduced from Fung et al., 2022]

Figure 1.3 by Fung et al., 2022 provides a summary of our current understanding of the DMS oxidation mechanism, as implemented in their Community Atmospheric Model version 6 with chemistry (CAM6-chem). DMS oxidation in the atmosphere is affected by temperature, NO_x , the distribution

of oxidants including OH, NO₃ and halogen compounds (Butkovskaya et al., 1995; Chen et al., 2018; Patroescu et al., 1998), and the availability of water for multiphase oxidation in aerosols and droplets (Hoffmann et al., 2016; Hoffmann et al., 2020). The major loss process of DMS is oxidation in the gas phase by OH (Faloona, 2009). Two OH oxidation pathways compete: OH addition to form DMSO and H atom abstraction to form MSP. The branching ratios of these pathways are highly temperature dependent. At low temperatures, DMS oxidation proceeds more via the OH addition pathway, forming abundant DMSO and MSIA, and consequently, a large amount of MSA (Shen et al., 2022). Therefore, MSA may be the dominant oxidation product in high-latitude marine atmospheres. On the other hand, the hydrogen abstraction pathway becomes more important at high temperatures. Approximately 95 % of MSP undergoes isomerisation to HPMTF (Berndt et al., 2019), which subsequently increases H₂SO₄ production through the oxidation of HPMTF in clear conditions (Berndt et al., 2019; Ye et al., 2021). This is because in cloudy conditions, HPMTF is rapidly lost to clouds, which was measured by both Veres et al., 2020 and Novak et al., 2021, hence terminating DMS oxidation to SO₂. However, in warmer conditions, MS⁻/MSA in the aqueous phase can thermally decompose to H₂SO₄ (Hoffmann et al., 2016; Shen et al., 2022), which becomes more important in cloudy conditions. Overall, MSIA and HPMTF are useful intermediates that serve as markers for OH addition and hydrogen abstraction pathways respectively (Shen et al., 2022).

Realistically, other oxidants contribute to the loss of DMS. The nitrate radical (NO₃) is an important nighttime oxidant (Yin et al., 1990) and in the remote marine atmosphere, halogens could be an important additional sink for DMS oxidation. For example, BrO would significantly enhance the contribution of the addition pathway (Toumi, 1994; Barnes et al., 2006), thereby decreasing the yield of SO₂ from DMS (Glasow et al., 2004).

Global and regional models often simplify the DMS oxidation mechanism

for the sake of computational costs. For example, previous versions of the CAM-chem model only include OH and NO₃ as oxidants of DMS, directly forming SO₂ which further oxidises to produce sulfate (Lamarque et al., 2012; Emmons et al., 2020). Therefore, many important reaction intermediates which have varying lifetimes, including HPMTF, are unaccounted for in models. This not only affects the spatial distribution of sulfate aerosols but also the effective sulfate yield from DMS. Veres et al., 2020 developed a model constrained to their HPMTF measurements, using the gas phase oxidants OH and BrO and known kinetic data, to simulate the various DMS oxidation pathway contributions. They showed that more than 30 % of oceanic DMS emitted into the atmosphere forms HPMTF. Therefore, including HPMTF in model simulations is thought to cause a 60 % reduction in the yield of SO₂ from DMS (Veres et al., 2020), which is consistent with a more recent study (Khan et al., 2021). However, this represents an upper limit in reduction since the oxidation of HPMTF to SO₂ was not included in the model (Veres et al., 2020). When accounting for HPMTF chemistry, Khan et al., 2021 found that sulfate aerosol increased in the upper troposphere, in addition to the expected significant decrease in boundary layer levels of SO₂ and H₂SO₄. Furthermore, it has been reported that the global HPMTF and sulfate burdens are relatively insensitive to the assumed isomerisation rate of MSP (Fung et al., 2022), however, as aforementioned, the fate of HPMTF is very sensitive to a potential additional cloud loss. Novak et al., 2021 showed that SO₂ production from DMS is reduced by 35 % globally and near-surface (0 to 3 km) SO₂ concentrations over the ocean are lowered by 24 % when accounting for HPMTF cloud loss. As demonstrated here, improvements in model accuracy to align better with observations have only been possible through the availability of measurements. Therefore, gaining a deeper understanding of the DMS oxidation mechanism will require direct observations of DMS and its oxidation products.

1.2 SO₂ measurement techniques

In the remote marine troposphere, mixing ratios of SO₂ are largely between 0 and 200 pptv. Even at these low concentrations, SO₂ may still be the primary source of CCN in the marine atmosphere, hence impacting global climate. Therefore, it is crucial that we can accurately quantify SO₂ concentrations in these environments. However, current commercial SO₂ detection techniques lack the sensitivity and selectivity to quantify trace levels of SO₂ at a reasonable sampling rate for moving platforms (airborne and ship-based measurements), which are essential for better spatial representation and altitude gradients of SO₂. The techniques currently used to measure SO₂ concentrations in the remote marine troposphere are pulsed fluorescence (PF), differential optical absorption spectroscopy (DOAS), chemical ionisation mass spectrometry (CIMS), and more recently laser-induced fluorescence, which are described herein and summarised in Table 1.1.

1.2.1 Pulsed fluorescence (PF)

PF is a popular in situ spectroscopic technique for measuring SO₂, typically using commercial instruments (Thermo Fisher Scientific, previously Thermo Electron). A broad UV excitation wavelength of 190 - 230 nm, corresponding to a strong absorption band of SO₂, is used to electronically excite SO₂, produced from the output of a pulsed xenon flash lamp (130- μ s pulses at 10 Hz repetition rate) and passed through a series of reflective interference filters (Luke, 1997). Three processes compete for the fate of the excited SO₂ intermediate: fluorescence, quenching by a third body, M (typically O₂, N₂, or H₂O), and photolysis, therefore limiting the measured fluorescence. Excited SO₂ fluoresces in a broadband continuum from 240 – 420 nm, with an emission peak at approximately 320 nm (Okabe, 1971). A bandpass filter is used to isolate the emitted radiation, which is monitored by a gated PMT. The sampling window gate is delayed by 30 μ s from the start of the Xe flash

Technique	LoD (integration time) / pptv	Observation type	SO ₂ mixing ratio (altitude) / pptv	Uncertainty / %	Location	Time of year	References
PF	1000	Ship	< LoD		Arctic Ocean	Sep 2019 - Oct 2020	<i>Boyer et al., n.d.</i>
LIF	2 (1 s)	Aircraft	< LoD - 50 (0 - 1.5 km)	± 9	Worldwide	Apr - May 2018	<i>Bian et al., 2024</i>
CIMS	130 (1 s)	Aircraft	< LoD - 170 (0 - 1.5 km)	± 25	Worldwide	Each season from 2016 to 2018	<i>Bian et al., 2024</i>
PF	50 (5 m)	Aircraft	< LoD - 200 (0 - 1.2 km)	± 1 or 200 pptv	Southern Baltic Sea	Aug 2015	<i>Zanatta et al., 2020</i>
PF	25 (5 m)	Ground	50	± 1 or 200 pptv	North Atlantic Ocean	Jan - Nov 2015	<i>Yang et al., 2016</i>
CIMS		Aircraft	26.9 - 69.8 (0 - 3.5 km)		Equatorial Pacific	Aug - Sep 2007	<i>Faloona et al., 2009</i>
CIMS	22 (1 s)	Aircraft	35 (> 6 km)	± 12 > 100 pptv, ± 25 < 100 pptv	Northern France	Jul 2004	<i>Speidel et al., 2007</i>
CIMS	< 1 (2 σ) (1 s)	Aircraft	50 (0.266 km)		Caribbean Sea	Jul 2000	<i>Thornton et al., 2002</i>
CIMS	0.5 (10 s)	Aircraft	10 - 400 (3.3 - 11.4 km)	± 50	Northern Scandinavia	Feb 1987	<i>Möhler et al., 1992a</i>
DOAS	100 at 5 km light path	Ground	< 600 (9.4 km light path)	A few percent	West Coast of Ireland	Apr 1979	<i>Platt et al., 1980</i>

Table 1.1: Literature measurements of SO₂ in the remote marine troposphere made using either the PF, DOAS, CIMS or LIF technique.

lamp trigger to avoid the electrical noise associated with the flash (Luke, 1997). This minimises baseline drift and dark current noise associated with the PMT.

Due to the broad nature of the excitation wavelength, the PF technique is susceptible to interfering species which absorb UV radiation at 190 – 230 nm and subsequently fluoresce at 240 – 420 nm. Of particular concern are aromatic hydrocarbon compounds, which tend to be highly fluorescent at this excitation wavelength. To reduce/eliminate these interferences, a semipermeable hydrocarbon “kicker” membrane is installed in the commercial instruments. Also, the sample airstream is typically dried before detection to minimise water vapour quenching - a relative humidity of 65 % at 25 °C and 1 atmosphere pressure can decrease the response of the instrument by 25 - 35 % (Okabe, 1971; Stelson et al., 1988). Therefore, this limits the selectivity of the PF technique, and hence its sensitivity to SO₂.

Luke, 1997 modified the commercial Thermo Electron instrument (model 43S), details of which are described in subsection 3.3.2. They were able to detect as little as 30 pptv SO₂ in a 25-minute sampling interval. More recently, modifications to newer models (43i-TLE) of the Thermo Fisher Scientific instrument have reported limit of detections (LoDs) of 400 ppt at 10 s (subsection 3.3.2) and 25 pptv at 5 minutes (Yang et al., 2016). However, even at these values, the PF technique has a lower sensitivity compared to CIMS and LIF and struggles to achieve fast sampling rates required for airborne measurements.

1.2.2 Differential optical absorption spectroscopy (DOAS)

DOAS is a remote sensing spectroscopic technique that allows contact-free measurements of atmospheric species, first described by Platt et al., 1979. It uses either sunlight or artificial light to measure the absorption of specific wavelengths by atmospheric gases along a known path length in the open

atmosphere. Therefore, ‘slant’ column densities (SCD) are derived, making DOAS well-suited for satellite applications, as well as for ground-based and aircraft measurements.

DOAS uses the Beer-Lambert law, which relates the ratio of the light intensity in the absence (I_0) and presence (I) of the absorbing species to a SCD via the absorption cross section of the absorber, σ at wavelength, λ and the light’s path length, l (Equation 1.10).

$$SCD = \frac{\ln(\frac{I_0}{I})}{\sigma_\lambda \cdot l} \quad (1.10)$$

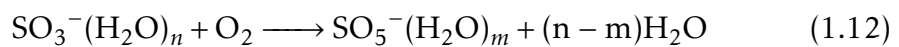
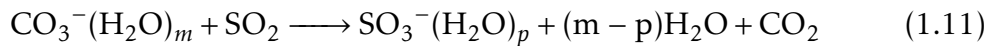
The transmitted light intensity (with the absorber, I) is measured over a relatively broad spectral range compared to the width of the absorption band of the gas species. However, I is also affected by other atmospheric effects, such as Rayleigh scattering by air molecules and Mie scattering by larger particles like aerosols or cloud droplets, which contribute to broad band features of the absorption spectrum. Therefore, high-pass filtering of the spectra is used to isolate the narrow-band absorption features specific to the species, determining the differential absorption signal. This signal is then compared to the reference light intensity (without the absorber, I_0) which can be determined via clear-condition measurements, laboratory calibrations, theoretical models, baseline observations, or signal processing techniques.

For measuring atmospheric SO_2 , Platt et al., 1980 acquired the absorption spectrum by a rapid scanning technique, using a broadband high-pressure Xe lamp (XBO 450) light source. This absorption technique makes DOAS the only measurement method that does not require calibration. It also avoids potential sampling inlet SO_2 losses due to its open path nature. The theoretical accuracy of this technique is thus limited only by the accuracy of the absorption cross-section and the path length. The light is then reflected between mirrors several kilometres apart, giving an average mixing ratio over this distance. While longer path lengths enhance sensitivity, they also

limit spatial resolution, making DOAS difficult to compare with supporting point measurements (although perhaps easier to compare to models and satellite which incur a large degree of averaging). However, recent designs use multi-pass white cells to greater reduce the measurement distance whilst retaining the sensitivity. However, even with this advancement, the DOAS technique typically has a lower sensitivity compared to CIMS and LIF, as shown in Table 1.1.

1.2.3 Chemical ionisation mass spectrometry (CIMS)

CIMS is an indirect in situ technique that relies on the chemical conversion of a species into its ion derivative that is more easily detected. In the case of SO₂, CIMS typically uses the fast ion-molecule reaction of selectively produced CO₃⁻(H₂O)_n ions (mostly with n ≥ 1) to convert SO₂ to SO₅⁻ (via the reactions below), a process first demonstrated in the laboratory by Möhler et al., 1992b. The CO₃⁻(H₂O)_n ion was used by Möhler et al., 1992a, Thornton et al., 2002, Faloona et al., 2009, and Speidel et al., 2007 in Table 1.1, and gives the best reported sensitivity to SO₂ in the literature. As an alternative, Huey et al., 1996 demonstrated in the laboratory that CF₃O⁻ could produce SO₂F⁻ ion for SO₂ determinations in the atmosphere, and has been used in subsequent field studies, including Bian et al., 2024 (Table 1.1). In addition, the use of iodide ions (IO₃⁻) has been reported by Eger et al., and a I⁻CIMS was also employed in this work to measure SO₂ during an aircraft campaign (more details are given in subsection 3.3.3).



A high-frequency gas discharge ion source is used to ionise an oxygen flow to produce the primary reagent ions O⁻, O₂⁻ and O₃⁻, with O₃⁻ ions

being rapidly converted to $\text{CO}_3^-(\text{H}_2\text{O})_m$ by reaction with CO_2 and H_2O . $\text{CO}_3^-(\text{H}_2\text{O})_m$ then further reacts with SO_2 to $\text{SO}_3^-(\text{H}_2\text{O})_p$ which forms the SO_5^- ion by reaction with excess O_2 . SO_5^- ions are then separated by their mass-to-charge ratios, either by time-of-flight via ion velocities (Bian et al., 2024, this work) or quadrupoles mass filter, using oscillating electric fields (Thornton et al., 2002; Faloona et al., 2009; Möhler et al., 1992a) (with Speidel et al., 2007 using two octapoles).

As can be seen in Table 1.1, CIMS can achieve low LoDs, much better than the PF and DOAS techniques. However, CIMS typically exhibits a humidity dependence, with the sensitivity decreasing with increasing water vapour concentration. To maintain a nearly constant low humidity, Faloona et al., 2009 and Thornton et al., 2002 used a dryer, keeping the formation of ion-hydrates in check. Thornton et al., 2002 found that this strategy completely removed the influence of water vapour on the instrument performance even in the highly humid tropical marine boundary layer. Another strategy would be to quantify the humidity dependence via a calibration either in-flight (Speidel et al., 2007) or in the laboratory over the humidity range experienced in situ (Bian et al., 2024, subsection 3.3.3). However, Bian et al., 2024 reported that the ambient water vapour concentrations in remote ocean regions may be sufficiently high that their CIMS SO_2 precision of 130 pptv at 1 second, using the CF_3O^- ion, is insufficient for measuring ambient SO_2 concentration < 100 pptv.

1.2.4 Laser-induced fluorescence (LIF)

The use of laser light to induce fluorescence makes LIF a highly selective and sensitive in situ spectroscopic technique. A laser (Light Amplification by Stimulated Emission of Radiation) generates coherent, monochromatic, and highly collimated electromagnetic radiation through the process of optical amplification based on stimulated emission. It comprises a gain medium

which is capable of amplifying light via stimulated emission, a pump source which excites electrons in the gain medium to a higher energy state, creating the necessary population inversion, and an optical resonator which provides a feedback mechanism to sustain amplification. When an incoming photon with energy matching the transition between an excited and lower energy state interacts with an excited electron in the gain medium, it stimulates the electron to drop to a lower state and release a photon. This emitted photon has identical phase, frequency and direction as the incident photon, resulting in coherent amplification and enabling the highly directional and monochromatic properties characteristic of laser radiation.

The principle of LIF is to use laser light at a wavelength corresponding to a strong peak in the SO₂ absorption cross section spectrum to excite SO₂ molecules, followed by detection of the subsequent fluorescence (more details in Section 2.1). Unlike PF which employs a broad excitation wavelength range, the coherent and monochromatic properties of a laser means it has a narrow linewidth, which allows fine SO₂ spectral details to be resolved. This reduces the susceptibility of LIF to interfering species, including water vapour (subsection 3.3.1), and means a greater signal-to-noise ratio and hence sensitivity can be achieved.

Therefore, from Table 1.1, it is evident that the most popular techniques for measuring SO₂ in the remote marine troposphere are CIMS and more recently LIF, since they can achieve significantly better LoDs compared to PF and DOAS. Since the CIMS is restricted by practical measures such as its large size and heavy weight in addition to high initial and maintenance costs, the LIF may be more desirable for field deployments. Another advantage of the LIF is its lack of interfering species and humidity independence. Having said this, all techniques are useful for improving our understanding of tropospheric SO₂ chemistry, but application dependent.

Chapter 2

Experimental

The University of York laser-induced fluorescence (LIF) instrument is a custom-built system for the highly sensitive detection of sulfur dioxide (SO₂), based on the system originally demonstrated by Rollins et al., 2016. The fifth harmonic (216.9 nm) of an in-house built pulsed tuneable fibre-amplified semiconductor diode laser system (1084.5 nm, 3 ns pulse duration, 200 kHz repetition rate) is used to selectively excite SO₂, and the subsequent fluorescence photons are detected using a photon counting head (Hamamatsu, H10682-210). The laser wavelength is tuned on and off a strong SO₂ transition ($\tilde{C}(^1B_2) \leftarrow \tilde{X}(^1A_1)$) peak, which is tracked using a reference cell at a constant SO₂ concentration. The difference between the number of fluorescence photons at these positions is directly proportional to the SO₂ concentration within the sample cell. The instrument is controlled by a LabVIEW project which is deployed on a National Instruments cRIO computer system.

The instrument is designed for both ground-based and airborne operation on board the UK FAAM (Facility for Airborne Atmospheric Measurements) Bae 146 research aircraft. Its ability to measure low SO₂ mixing ratios allows for quantification of SO₂ in remote marine environments where current measurements are sparse.

The following sections describe the spectroscopy governing the LIF method as well as the individual components of both the laser and LIF system. Characterisation of the York LIF-SO₂ instrument is also given from laboratory experiments.

2.1 Spectroscopy of LIF

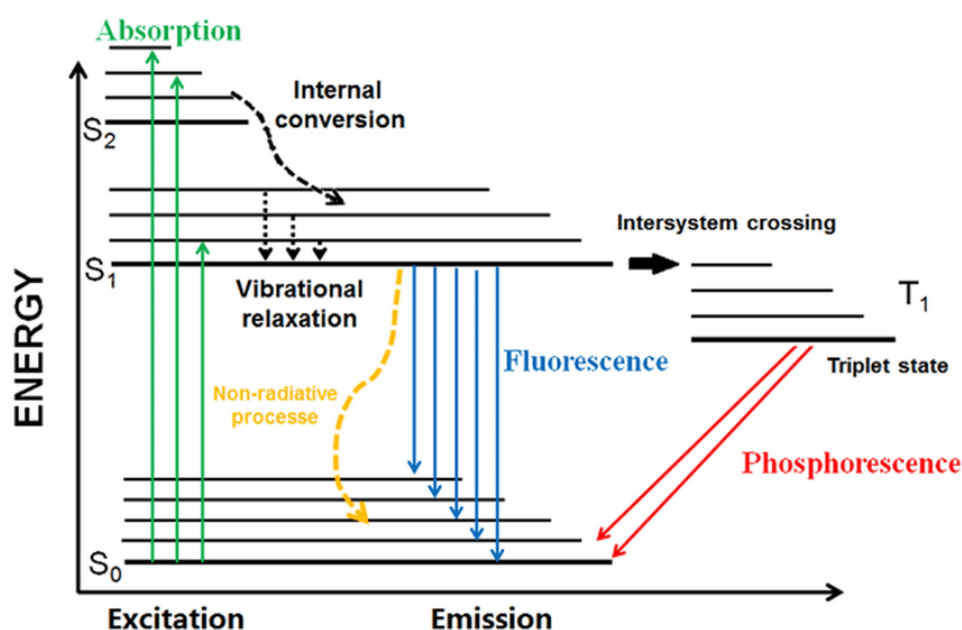


Figure 2.1: Jablonski diagram showing the various radiative and non-radiative emission pathways following excitation.

Laser-induced fluorescence (LIF) is a spectroscopic method which uses laser light to excite a chemical species from its ground electronic state into an excited electronic state. The excited species subsequently undergoes fluorescence via the emission of a photon as it relaxes back to its ground electronic state. Hence, the number of fluorescence photons is proportional to the species concentration. However, various other non-radiative pathways can lead to the de-excitation of the excited state, as shown by the Jablonski diagram in Figure 2.1. Firstly, collisional quenching of the excited state

can occur when excess energy is transferred through collisions with other molecules, causing the molecule to transition from higher to lower vibrational levels within the same electronic state (vibrational relaxation). Excess energy can also be dissipated through transitions to vibrational modes in a lower electronic state (internal conversion). Finally, the excited species can undergo intersystem crossing into an isoenergetic electronic excited state of different electron spin multiplicity, leading to a number of slower routes back to the ground electronic state. In some cases, dissociation of the species can also occur as a result of crossing into an unbound state. The probability of these pathways and hence the relative rates of fluorescence versus the various non-radiative processes depends on the electronic structure of a molecule. External factors such as temperature and pressure can also influence radiative and non-radiative decay rates, most notably that of collisional quenching which increases with increasing pressure and temperature. These factors are summarised by the fluorescence quantum yield, given by Equation 2.1.

$$\phi_f = \frac{k_f}{(k_f + k_{nr} + k_Q[Q])} \quad (2.1)$$

where k_f , k_{nr} , k_Q are the rate constants for fluorescence, non-radiative (excluding collisional quenching), and quenching decay pathways. $[Q]$ is the concentration of the quenching species defined by the ideal gas law (Equation 2.2).

$$[Q] = \frac{P}{k_B T} \quad (2.2)$$

where P and T are the pressure and temperature of the quencher gas respectively, and k_B is the Boltzmann constant ($1.38 \times 10^{-23} \text{ J K}^{-1}$).

The observed fluorescence intensity for a given excitation laser power also depends on how well a molecule absorbs light in the first instance to excite it into a higher electronic state. This is again dependent on its electronic structure since molecules absorb at specific wavelengths corresponding to the energy difference between its electronic states. Hence, a molecule can

be characterised by its absorption cross-section spectrum. Therefore, the absorption cross section of a molecule and its fluorescence quantum yield are both considered when identifying a suitable wavelength of laser light to detect a specific molecule via LIF.

The electronic structure of SO₂ has been the subject of numerous experimental and theoretical studies (Manatt et al., 1993; Stark et al., 1999; Rufus et al., 2003). SO₂ absorbs strongly in the ultraviolet region of the electromagnetic spectrum, characterised by a series of absorption bands at wavelengths from 403 to 106 nm of generally continuous and increasing absorption (Figure 2.2). Three SO₂ absorption bands resulting from transitions from the ground electronic state ($\tilde{X}(^1A_1)$) into different excited electronic states have relevance for detection. These are: $\tilde{a}(^3B_1) \leftarrow \tilde{X}(^1A_1)$ at 340 - 400 nm, $\tilde{B}(^1B_1) \leftarrow \tilde{X}(^1A_1)$ at 240 - 338 nm, and $\tilde{C}(^1B_2) \leftarrow \tilde{X}(^1A_1)$ at 170 - 235 nm. At wavelengths shorter than this (< 150 nm), although SO₂ may have a greater absorption cross-section, it will dissociate and hence not undergo fluorescence. Furthermore, generating laser light in the far UV is challenging, making these wavelengths inaccessible.

Since the transition into the \tilde{a} excited state has the lowest absorption cross section (maximum absorption is below 3.7×10^{22} cm²), the resulting fluorescence is extremely weak and SO₂ detection using this region of the spectrum has not been reported. Transitions into the \tilde{B} and \tilde{C} state have significantly larger absorption cross sections compared to the \tilde{a} state (note the log scale for absorption in Figure 2.2) with maximum absorptions of 10^{18} cm² and 1.5×10^{17} cm² respectively. Due to the Franck-Condon offset between the \tilde{X} and \tilde{C} states, this maximum absorption occurs ~ 35 nm below the 0-0 transition at 235 nm (Rollins et al., 2016). Since the absorption cross sections have been considered, it is necessary to look into the differences in fluorescence quantum yields between the \tilde{B} and \tilde{C} states to identify the optimal transition for targeting SO₂.

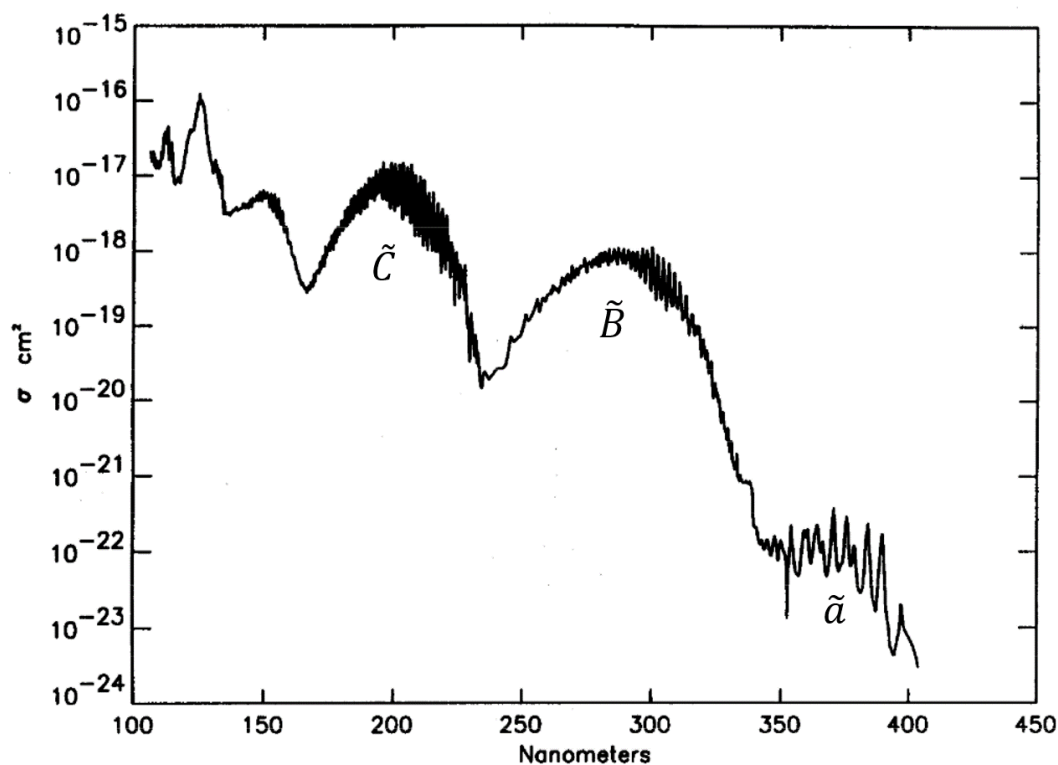


Figure 2.2: SO_2 absorption cross-sections of SO_2 for the gas phase from 106 to 403 nm at 293 ± 10 K. [Reproduced from Manatt et al., 1993]

Here we consider the rates of decay from the respective pathways. The fluorescence decay rate constants for the \tilde{B} and \tilde{C} transitions are $0.5 \pm 0.3 \times 10^4 \text{ s}^{-1}$ (Sidebottom et al., 1972) and $7.4 \times 10^6 \text{ s}^{-1}$ (Hui et al., 1972) respectively. At zero pressure, the non-radiative decay rates for the \tilde{B} transition are minimal, however, at wavelengths shorter than 219.2 nm for the \tilde{C} transition, photochemical predissociation competes with fluorescence (Okabe, 1971), evidenced by the sharp drop in fluorescence intensity in Figure 2.2(b). Based on experimental and theoretical results, Katagiri et al., 1997 proposed that dissociation proceeds primarily through both vibronic mixing between the \tilde{C} state vibronic levels with the quasi-bound dissociation continuum of the electronic ground $\tilde{X}(^1A_1)$ state, and crossing into dissociative singlet and triplet states where they cross the \tilde{C} state. Hui et al., 1972 determined this predissociation rate constant to be $9.643 \times 10^7 \text{ s}^{-1}$ for excitation at 216.9

Chapter 2. Experimental

nm. However, in this work, the range of cell pressures used are 400 - 600 mbar (for reason discussed in subsection 2.5.4), and hence quenching effects are important. Okabe, 1971 reported similar quenching rate constants for the two transitions in argon ($5.2 \times 10^{-11} \text{ cm}^3 \text{ s}^{-1}$ for the \tilde{B} state and $5.0 \times 10^{-11} \text{ cm}^3 \text{ s}^{-1}$ for the \tilde{C} state) and therefore, for pressures around 500 mbar (which give suitable fluorescence lifetimes of around 1.5 ns), the fluorescence quantum yield can be calculated using Equation 2.1. These are 0.0008 % and 1 % for the \tilde{B} and \tilde{C} transitions respectively at 500 mbar and 298.15 K and hence it is apparent that the preferable state to excite SO_2 to is the \tilde{C} state.

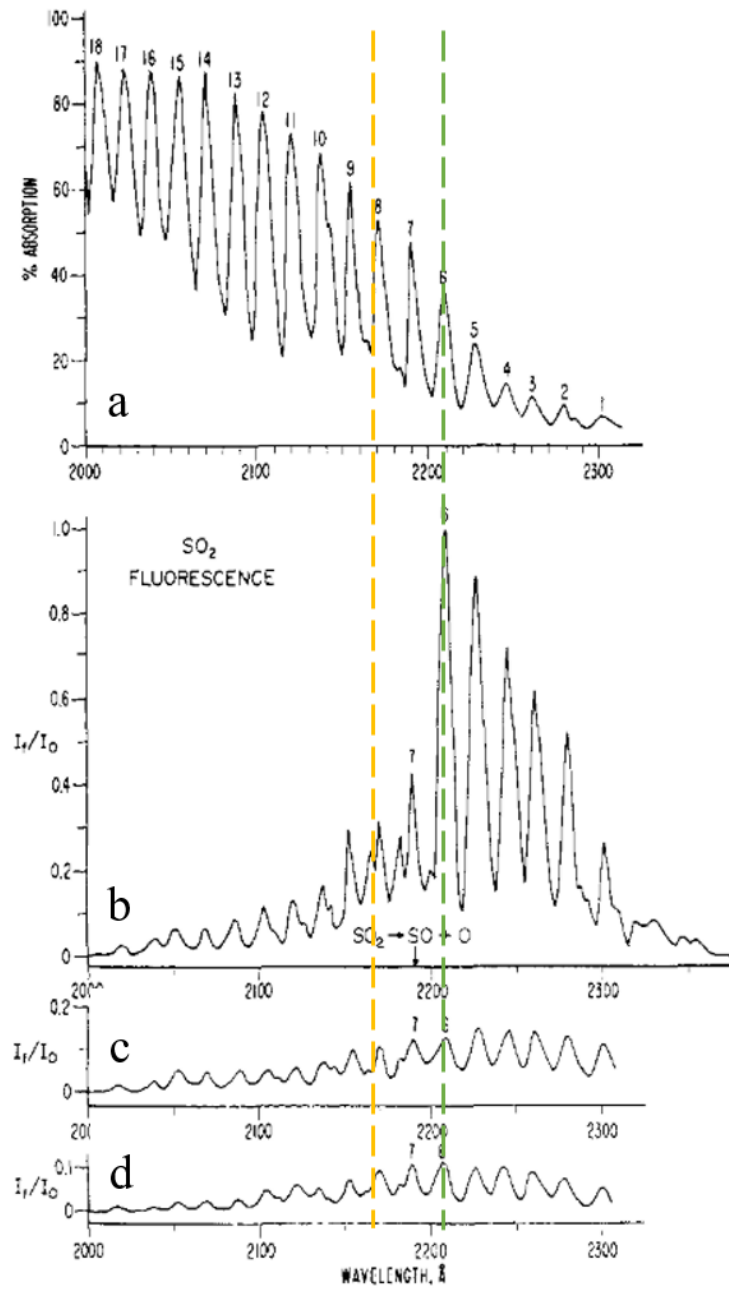


Figure 2.3: (a) Absorption of 0.3 Torr of SO₂, path length 6.95 cm, in the region from 2000 to 2300 Å, resolution 3 Å. (b) Fluorescence intensity (undispersed) of 0.3 Torr of SO₂ as a function of incident wavelength, resolution 3 Å, scanning speed 10 Å/min, time constant 5 sec. An arrow shows the thermochemical threshold of dissociation, corresponding to 2192 Å. (c) Fluorescence intensity as a function of incident wavelength of a mixture of 0.3 Torr of SO₂ and 400 Torr of Ar. (d) Fluorescence intensity as a function of incident wavelength of 0.3 Torr of SO₂ in ambient air. The dashed lines indicate the wavelengths 216.9 nm (yellow) and slightly longer than 220 nm corresponding to greatest fluorescence intensity (green). [Reproduced from Okabe, 1971]

In terms of which wavelength to target SO₂ within the $\widetilde{C}(^1B_2) \leftarrow \widetilde{X}(^1A_1)$ transition, it is apparent from Figure 2.2(b) that wavelengths slightly longer than 220 nm are optimal since it corresponds to the greatest fluorescence intensity, significantly so at zero pressure and minimally so at 400 Torr (~ 533 mbar) of argon (Figure 2.2(c)) and at ambient pressure (Figure 2.2(d)). Although predissociation reduces the fluorescence quantum yield at wavelengths below 220 nm, at pressures of 500 mbar, the quenching rate is 6 times that of the predissociation and hence collisional quenching dominates the non-radiative pathway. Therefore, at low pressures, it would be ideal to excite SO₂ with ~ 220 nm light to maximise the fluorescence quantum yield.

Previous studies demonstrating LIF as a sensitive technique for measuring SO₂ utilised laser light around 220 nm. Bradshaw et al., 1982 first generated 10 mW of tunable light at 222.2 nm by mixing the 1064 nm output of a Nd:YAG laser with the frequency-doubled output of a dye laser at 10 Hz. Experiments were carried out in atmospheric conditions of pressure and composition and a limit of detection (LoD) of 4 ppt at an averaging time of 20 minutes was reported. However, no measurements in the atmosphere

were made. Matsumi et al., 2005 used the third harmonic of a 10 Hz Nd:YAG laser to pump the frequency-doubled output of an optical parametric oscillator to achieve 10 mW of laser light at 220 nm. A cell pressure of 10 Torr (~ 13 mbar) was used and hence a better LoD of 5 ppt at 60 seconds was attained. Matsumi et al., 2005 obtained two hours of atmospheric measurements which showed good agreement with a pulsed fluorescence instrument between SO₂ mixing ratios 3.5 - 12 ppb. Despite their high pulse energies (as a result of high laser power and low laser repetition rates), these studies were limited by the use of noisier analog detectors since the typical rate of photons arriving at the detector was much higher than the laser repetition rate. Also the use of low repetition rates restricted their sampling rate and hence suitability for airborne measurements. Additionally, traditional Nd:YAG and dye-based lasers are limited by their large size, heavy weight and high power requirements in addition to their temperature and vibrational sensitivity and use of often toxic dye materials, making them unsuitable for aircraft deployment. Airborne instruments are important for allowing in situ measurements at a range of altitudes to improve our understanding of tropospheric SO₂ chemistry, for example, exploring the potential uptake of SO₂ to clouds. Therefore, an alternative approach to UV laser light generation for SO₂ detection has been developed by Rollins et al. which makes use of the advantages of fiber-amplified based laser systems. This advancement has led to greatly reduced size, weight and power requirements and significant reductions in the sensitivity of the laser to the vibration and temperature environment of operation. Also, the use of higher repetition rates allows fast sampling rates and single photon counting can be used for measuring fluorescence, therefore overcoming the other limitations of the previous studies. However, compromised by the availability of suitable laser technology, the fifth harmonic of the tunable Yb³⁺-doped fiber-amplified laser at 1084.5 nm is used, determining the excitation wavelength as 216.9 nm. Therefore, at this wavelength, a larger proportion of

excited SO_2 molecules undergo predissociation compared to 220 nm, but for the pressures we work at (500 mbar), quenching competes more with fluorescence, including at wavelengths ≥ 220 nm. The Frank-Condon offset between the ground and electronic excited state means that efficient absorption occurs into a vibrationally excited level of the $\tilde{\text{C}}$ state, and hence the molecules undergo vibrational relaxation followed by red-shifted fluorescence. The fluorescence spans ~ 100 nm between 300 - 400 nm which is collected via a photon counting head (Hamamatsu H10682-210). The schematic in Figure 2.4 summarises the spectroscopy of SO_2 at 216.9 nm.

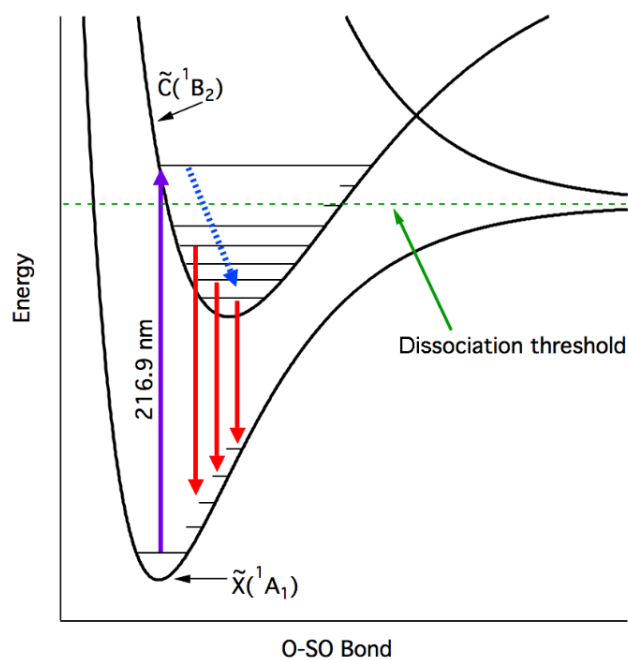


Figure 2.4: Schematic of the relevant SO_2 electronic structure and LIF process. Excitation from the ground state, $\tilde{\text{X}}$, to above the dissociation threshold in the $\tilde{\text{C}}$ state at 216.9 nm (purple line) leads to predissociation in the majority of SO_2 molecules. A small fraction undergo internal vibrational relaxation (dashed blue arrow) followed by red-shifted fluorescence (red arrows). [Reproduced from Rollins et al., 2016]

2.2 The laser

2.2.1 Principle of operation

The requirements of a laser for LIF to target SO₂ are:

- 1 **Pulsed:** To allow for collection of fluorescence light outside of lasing times which would otherwise contribute to the counts and reduce the signal-to-noise ratio (SNR). Also, to allow for high peak pulse powers for nonlinear optics conversion to the fifth harmonic (subsection 2.3.1).
- 2 **High UV power:** To improve the SNR, hence achieving better precision and lower limits of detection (LoD).
- 3 **Narrow linewidth:** To selectively excite SO₂, avoiding interferences from other species which absorb and fluorescence in a similar wavelength region to SO₂ and improving the instrument sensitivity and LoD.
- 4 **Rapid wavelength tunability:** To measure the counts on and off the strong SO₂ transition of interest for targeting SO₂ and minimising background counts.
- 5 **Field deployable:** Small size, relatively light weight, low power requirements, low vibrational sensitivity, no chemical use.

As explained in Section 2.1, traditional YAG-pumped dye lasers that have been used previously to detect SO₂ via LIF do not satisfy the latter requirement. Hence, a fiber optics-based amplification system using semiconductor

laser diodes that satisfies all the above requirements has been developed by Rollins et al., 2016. However, laser diodes that have sufficiently narrow linewidth for resolving the SO_2 spectrum in addition to sufficiently high power for sensitive ppt level detection are not commercially available in the UV wavelength range near 220 nm to target SO_2 . Therefore it is necessary to amplify pulsed infrared light and generate the fifth harmonic of this amplified light using a series of nonlinear crystals to get to the UV.

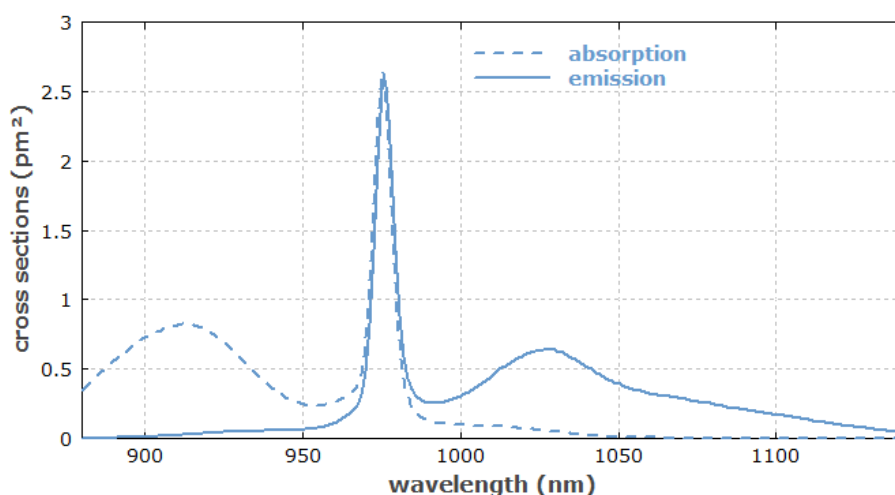


Figure 2.5: Absorption and emission cross-sections of ytterbium(Yb^{3+})-doped germanosilicate glass, as used in the cores of ytterbium-doped fibers (data from spectroscopic measurements by Paschotta et al., 1997). [Reproduced from RP Photonics (*Ytterbium-doped Laser Gain Media* n.d.)]

The amplification process is achieved through the use of Yb^{3+} -doped optical fibers as the lasing medium with a population inversion most efficiently pumped at 976 nm, as shown in Figure 2.5. The spontaneous emission of Yb^{3+} is sharp at the same wavelength (976 nm) and exhibits broader emission at longer wavelengths (Figure 2.5). However, a tunable seed laser diode is used to stimulate the relaxation of the excited Yb^{3+} ions, causing amplified stimulated emission at its set wavelength, which can then stimulate the emission of other Yb^{3+} ions. In terms of the wavelength of stimulated light, the

broader emission between 1000 - 1100 nm is of interest as the fifth harmonic would give wavelengths close to 220 nm, which has been determined as the optimal excitation wavelength for SO₂ (Section 2.1). Since the emission cross section maxima of the excited Yb³⁺ ions lies near 1030 nm (Figure 2.5), amplification via stimulated emission at 1100 nm (to reach a fifth harmonic of 220 nm) would be low as it is far from the emission maxima. Due to inefficiencies of the harmonic generation processes, minimal fifth harmonic power would be available for the excitation of SO₂, despite the benefit of high fluorescence quantum yield at this wavelength. Therefore, a trade off has been struck between fluorescence intensity (max 1100 nm) and laser power (max 1030 nm) and hence amplification occurs at 1084.5 nm, targeting the SO₂ absorption peak at 216.9 nm. Therefore, since the incoming photon (976 nm) to excite Yb³⁺ is of higher energy than the emitted photon (1084.5 nm), some energy is lost via the non-radiative pathway of vibrational relaxation (Figure 2.1).

The York laser system is based on that originally demonstrated by Rollins et al., 2016 but more akin to that described in the subsequent NOAA LIF paper by Rickly et al., 2021. The main differences to our laser system include the methods used to pulse the continuous seed laser diode and tune its wavelength on and off the electronic transition of interest. It is worthy to note that the seed laser wavelength is dependent on both temperature and current supplied via the laser driver board (Wavelength Electronics, f1591 eval). Firstly, Rollins et al., 2016 achieved laser tuning by modulating the temperature of the seed laser, as opposed to the current. However, since thermal equilibrium is reached at a slower rate compared to electronic equilibrium, temperature tuning the seed laser limits the response time of the wavelength shift from on to off the transition peak. Rollins et al., 2016 also pulsed the seed laser directly at 25 kHz via a short-pulse laser driver (Highland Technology). However, changes in driving current for the

pulse production introduces slight temperature variations and hence the wavelength will shift along the pulse (phenomenon of chirping a signal pulse), hence broadening the laser linewidth. The modulation bandwidth also limits the laser repetition rate (*Fiber modulator: how to choose the good technology? Fiber modulator basics* n.d.). Therefore, the second laser iteration by Rickly et al., 2021 used a current tuning method and also pulsed the output of the seed laser via a fiber-coupled electro-optic modulator (EOM). Due to the greater modulation bandwidth of the EOM, higher laser repetition rates of 200 kHz could be achieved, hence allowing faster sampling times. The EOM, however, is limited by its insertion loss and requires good external temperature control (*Fiber modulator: how to choose the good technology? Fiber modulator basics* n.d.), therefore reducing the reproducibility of the laser pulse generation. In our work, a semi-conductor optical amplifier (SOA, Innolume, SOA-1080-20-PM-40dB) is used in place of the EOM to pulse the output of the seed laser. The advantages of an SOA over an EOM are that it is a temperature-independent method of producing consistent pulses since an internal thermoelectric cooler keeps the SOA at 25 °C, in addition to its ability to amplify the pulse and hence improve the maximum output power. Therefore, we pulse the seed laser at 200 kHz and current tune it to alter its wavelength.

The laser consists of two amplification stages: a single mode regenerative preamplifier which maximises gain and suppresses amplified spontaneous emission (ASE), followed by a double-clad power amplifier which is able to withstand much larger laser powers. Two stages are necessitated to achieve the required gain and sufficient pulse energies at 1084.5 nm for generating fifth harmonic power through the inefficient process of harmonic generation (see subsection 2.3.1). The amplification stages also contain components (e.g. 2x2 switch, bandpass filter) and Yb³⁺-doped polarisation maintaining fiber types that are suited to the laser powers at the respective stage.

A regenerative design is adopted for the first stage since single pass designs are limited by broadband ASE competing with stimulated emission, hence depleting the pumped population inversion (Xin et al., 2011). This prevents energy storage within the system via stimulated emission and degrades the SNR, especially for small input signals and for applications that require narrow band optical spectra (Yang, 2006). Therefore, to overcome these limitations, regenerative amplification enables optical pulses to gain energy in many round trips, achieving a higher overall gain and improving the SNR and stability of the system whilst maintaining the beam quality. Single mode gain fibers are used for this stage which consist of a small, high refractive index core ($5\ \mu\text{m}$), where the Yb^{3+} ions reside and the pump and stimulated light propagate, surrounded by a low refractive index cladding. The lower refractive index cladding ensures total internal reflection of the stimulated and pump light and the small diameter core only allows one mode of light to propagate (hence single mode), meaning pulse shape distortions are weak (*Tutorial "Fiber Amplifiers" n.d.*). Therefore, the regenerative loop can achieve a high gain efficiency with low power pump light (*Tutorial "Fiber Amplifiers" n.d.*) and we see an average output power of $\sim 20\ \text{mW}$.

The second amplification stage is referred to as the power amplifier since it achieves even higher gain efficiencies compared to the regenerative stage by using larger pump lasers, increasing the laser power from $\sim 20\ \text{mW}$ to $\sim 1\ \text{W}$. To withstand these greater laser powers, multimode fibers are used which have a larger diameter core ($20\ \mu\text{m}$) to reduce the light intensity, hence minimising the potential of nonlinear effects e.g. Brillouin and/or Raman scattering. However, these higher laser powers are unsuitable for some of the components used in the regenerative amplifier stage: the 2x2 switch and hence the power amplifier is a single-pass design, and the bandpass filter for removing residual pump light from the core. Hence an alternative method of removing pump light is made easier by the use of double-clad multimode

fibers for the power amplifier stage. Here, the stimulated light propagates in a multimode core where the Yb^{3+} ions reside, which is surrounded by an inner cladding in which the pump light mainly propagates. The pump light is restricted to the inner cladding by an outer cladding with lower refractive index, and also partly propagates in the core, where it can be absorbed by the Yb^{3+} ions (*Double-clad Fibers* n.d.). Hence, a cladding power stripper can be used, consisting of a fiber splice with a high refractive index outer cladding so the pump light is preferentially lost through the outer cladding. Since the core of the fiber is still multimode (hence allowing multiple modes to propagate), spectral broadening is introduced as a result of modal dispersion.

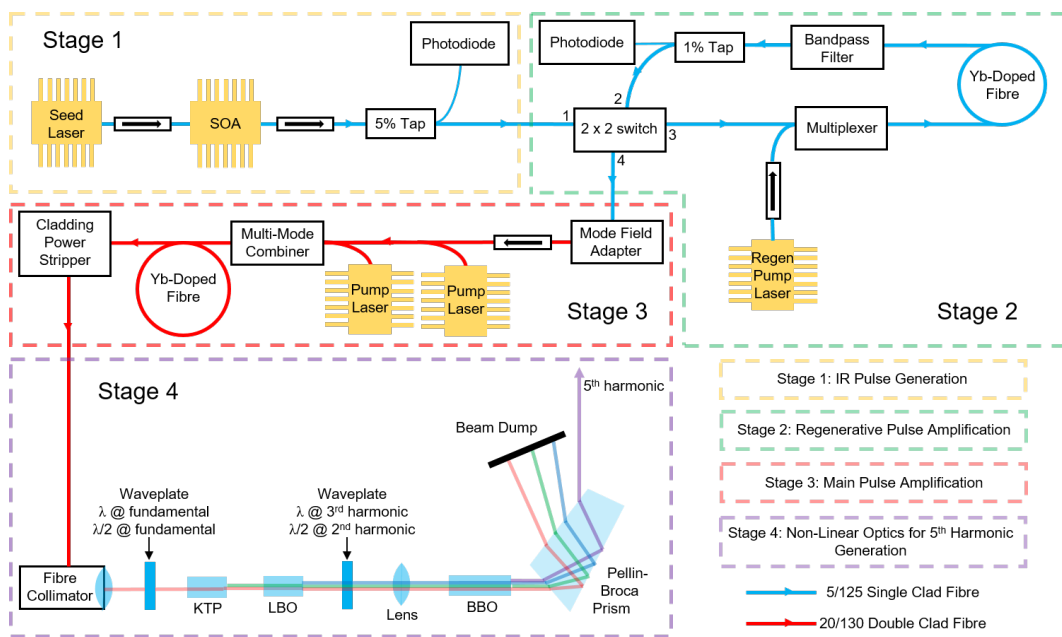


Figure 2.6: Schematic of the fiber-amplified diode laser system at 1084.5 nm, followed by the production of the fifth harmonic at 216.9 nm using nonlinear crystals.



Figure 2.7: Pulses from the 1 % tap within the regenerative loop triggered off the pulse produced by the SOA from the 10 % tap, as displayed by the oscilloscope.

An overview of the laser system, as summarised in the schematic in Figure 2.6, is as follows. All components within the system are connected via an optical fiber splicing technique, more information on which can be found in subsection 2.2.3. Firstly, a distributed feedback (DFB) continuous seed laser diode of linewidth < 5 MHz and wavelength 1084.5 nm is used as the stimulated light to be amplified. The DFB tuning rate is 1.76 pm mA^{-1} and since the current can be controlled to better than $\sim 0.06 \text{ mA}$, the wavelength precision by current tuning is comparable to that reported by Rollins et al., 2016 by temperature tuning of $< 0.07 \text{ pm}$. After passing through a 70 dB optical isolator (Haphit, FPIS-1080-DS-2B10-N), pulses are created from the continuous seed laser via a SOA. Another optical isolator is present after the SOA to protect the DFB seed laser against feedback from the regenerative amplification stage. In our setup, a 5 % optical tap follows which means the

pulse temporal shape after the SOA can be monitored on an oscilloscope (1 GHz) and adjusted via the SOA control board. Then a 2×2 optoceramic-based switch (Boston Applied Technology Inc., FOS2011-4400) is used to allow a seed pulse into the regenerative loop during its initial, de-energised state where port 1 is connected to port 3 and port 2 to port 4. The pulse passes through a wavelength division multiplexer where it combines with 976 nm continuous light from a wavelength-stabilised 300 mW laser diode (3SP Technologies) within the core of a Yb^{3+} -doped single-clad gain fiber (Nufern, PM-YSF-HI-HP). The Yb^{3+} ions reside in the core and hence are excited by the 976 nm light and then stimulated to relax by the 1084.5 nm seed laser pulses. To remove the residual pump light and any broadband ASE which peaks near 1030 nm, a tunable bandpass filter (Agiltron, FOTF-026123331) is used, therefore only allowing the transmission of the amplified stimulated emission at 1084.5 nm. This is followed by a 1 % optical tap which allows the incremental pulse amplification through each pass of the loop to be monitored. On arrival of the 2×2 switch, its current state will enable the passage of the pulse into the next amplification stage. Therefore, the switch must be energised at some point during the first pass of the regenerative loop to enable subsequent passes and hence, de-energised again when the optimal number of passes has been achieved. These timings are controlled by the software and it has been found that ~ 8 passes are optimal for this system, as shown on the oscilloscope display in Figure 2.7. Any additional passes do not yield further improvement in pulse energy, and with even more passes, pulse energy decreases since the component loss becomes larger than the gain. For their regenerative amplifier, Xin et al., 2011 even limit the number of passes to below their pulse energy saturation point as even though increases in the number of passes will further increase the pulse energy, the improvement in pulse energy slows. This is because at high laser repetition rates, there is insufficient time between pulses for the pump light to replenish the Yb^{3+} excited state. We now believe this is what was limiting the regenerative gain

we observed since replacing the 300 mW pump laser diode with a higher power pump improved the overall gain out of the regenerative loop because the Yb^{3+} excited state is repopulated faster.

After the regenerative amplification stage, the single mode fiber is spliced into a multimode fiber (Nufern, PLMA-GDF-20130-VIII) following passage through the de-energised switch. The pulses then pass through a 45 dB optical isolator (Haphit) and into a multimode combiner where the output from two 5 W wavelength-stabilised 976 nm multimode laser diodes (Innovative Photonic Solutions) are coupled into the inner cladding of the Yb^{3+} -doped multimode fiber (Nufern, PLMA-YDF-20130-VIII). A cladding power stripper is used after the gain fiber to remove the residual 976 nm pump light. The final output fiber is encased in an armoured cable to prevent damage to the exposed fiber which is outside of both the laser and LIF box. Also, the end of the fiber is capped with a 600 μm core-free fiber, allowing the beam to expand to $\sim 100 \mu\text{m}$ before exiting the fiber to avoid optical damage.

There are three different modes of the laser: constant, scan and dither. These modes are dictated by the LabVIEW software which determines the current sent to the seed laser diode via its driver board (Highland Technology, t165-2e). Constant mode holds the laser wavelength at a specific value corresponding to the driving current set by the user. Scan mode allows the laser wavelength to be scanned between two driving current values, which is useful for identifying the SO_2 transition peak. Following this, the driving current values corresponding to the online and offline wavelength positions can be set. Hence, dither mode quickly switches the driving current ($\sim 10 \text{ Hz}$) between these two values, and the resultant fluorescence counts are measured. Since the absorption cross section at the online position is significantly greater than the offline, greater noise in the counts at the online position is seen if SO_2 is present, and hence the dither is held at the online position 4 times longer than the offline to improve the statistics. The

transition peak is tracked by a software algorithm, based on the counts at the online and offline positions. The driving current is stepped (0.1 mA) across the top of the transition, whilst maintaining the online-offline current difference, and its direction changes when the counts have fallen for three subsequent steps.

2.2.2 Linewidth versus power

As aforementioned in Section 2.2, a sufficiently narrow laser linewidth is required to resolve the fine SO₂ spectral detail and high UV power is necessary to improve the SO₂ counting statistics, to overall achieve a low LoD. However, for the York LIF system, there exists an inverse relationship between the linewidth and average power of the laser, that is, if the laser linewidth is broader, the average power obtained is greater. To explore this relationship, firstly the factors influencing laser linewidth are determined.

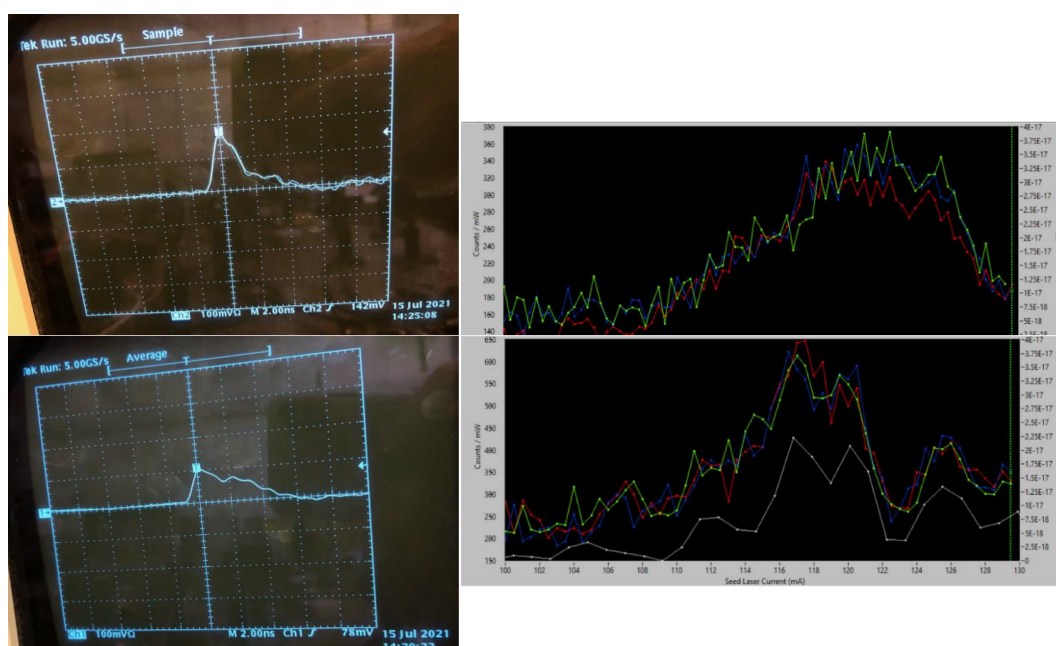


Figure 2.8: The effect of laser pulse duration as displayed on the oscilloscope (left) on the degree of SO_2 spectral detail seen in the resulting fluorescence spectrum. The spectra show three subsequent scans (blue, red, green) and are compared to a literature absorption spectrum (data from Stark et al., 1999). The LIF counts are normalised by laser power.

Firstly, the linewidth of a pulse is limited by its temporal width. This is described by the transform limit of a pulse which refers to the minimum possible spectral bandwidth of an optical pulse for a given duration. For a pulse to be transform-limited, its time-bandwidth product must be at the theoretical minimum dictated by the uncertainty principle (Siegman, 1986). The general form of this relationship can be expressed as:

$$\Delta\nu \cdot \Delta t \geq K \quad (2.3)$$

where $\Delta\nu$ is the spectral bandwidth (full width at half maximum, FWHM), Δt is the pulse duration (FWHM), and K is a constant that depends on the shape of the pulse. Pulses with little chirp or other internal substructure will have a value of K close to 0.5 (Siegman, 1986). This effect can be seen experimentally by varying the pulse duration via the SOA driver board

and measuring the resulting fluorescence spectrum around the transition of interest, as shown in Figure 2.8. The ~ 2 ns FWHM pulse does not capture the fine structures of the SO_2 transition but an overall transition shape is detected since the laser linewidth is too broad. Doubling the pulse width to ~ 4 ns FWHM and hence halving the laser linewidth allows the fine structures to be resolved and the obtained fluorescence spectrum matches the detail of the literature absorption spectrum very closely. For a pulse duration of ~ 4 ns which gives a narrower laser linewidth, using Equation 2.3, a theoretical minimum linewidth of 0.11 GHz is obtained. Since the pulse shape contains internal substructure and has a long tail, this is a very rough approximation but is useful for a first order analysis. Considering the spectral width of the continuous seed laser diode is ≤ 5 MHz, this means that pulsing the laser via an SOA broadens the laser linewidth by at least a factor of 22. The linewidth can be calculated/measured at other points in the amplification stage to assess this broadening and identify the causes.

The laser power aspect comes into effect as a result of this time-bandwidth product and the efficiency of the nonlinear harmonic generation process. As explained in subsection 2.3.1, the efficiency of fifth harmonic generation is higher for pulses that are temporally concentrated. Therefore, for a broader linewidth laser, its temporal width is narrower and hence more fifth harmonic power is generated.

The laser linewidth was measured experimentally after the regenerative amplification stage due to suitable laser power (~ 20 mW) and wavelength for the use of a scanning Fabry-Pérot interferometer (SA210-8B, Thorlabs). Interferometry is typically used for continuous wave laser linewidth measurements, however, due to our high laser repetition rate of 200 kHz, we can essentially treat our pulsed laser as continuous (Xue et al., 2016 even reported interferometry measurements of their 1 Hz pulsed laser). An interferometer consists of a resonant cavity with two partially reflecting mirrors

facing one another, between which the light waves travel a number of times to produce multiple transmitted waves. To scan the spectra of the laser beam entering the interferometer, a small displacement is applied to one of the cavity mirrors mounted on the piezoelectric transducers. The signal generator sends a ramp voltage to the piezoelectric elements, typically a continuous saw-tooth wave voltage. When the mirror spacing becomes equal to an integral number of half the wavelength of the laser, constructive interference occurs. This signal is detected by the interferometer's photodiode and can be visualised with an oscilloscope. A series of periodical peaks due to constructive interference can be seen and the temporal distance between the peaks can be measured corresponding to the free spectral range (FSR) of the interferometer. The interferometer used for these experiments (SA210-8B, Thorlabs) has a FSR of 10 GHz and highly reflective mirrors (high finesse of > 150) to achieve a resolution of 7.5 MHz. Therefore, the FSR allows time-base of an oscilloscope to be calibrated and hence the spectral width of a laser, $\Delta\nu_{FWHM}$ can be calculated via the following relationship:

$$\Delta\nu_{FWHM} = \frac{\Delta\tau_{FWHM}}{\Delta\tau_{diff}} \times FSR \quad (2.4)$$

where $\Delta\tau_{FWHM}$ is the temporal FWHM and $\Delta\tau_{diff}$ is the temporal difference between two consecutive peaks as displayed on the oscilloscope.

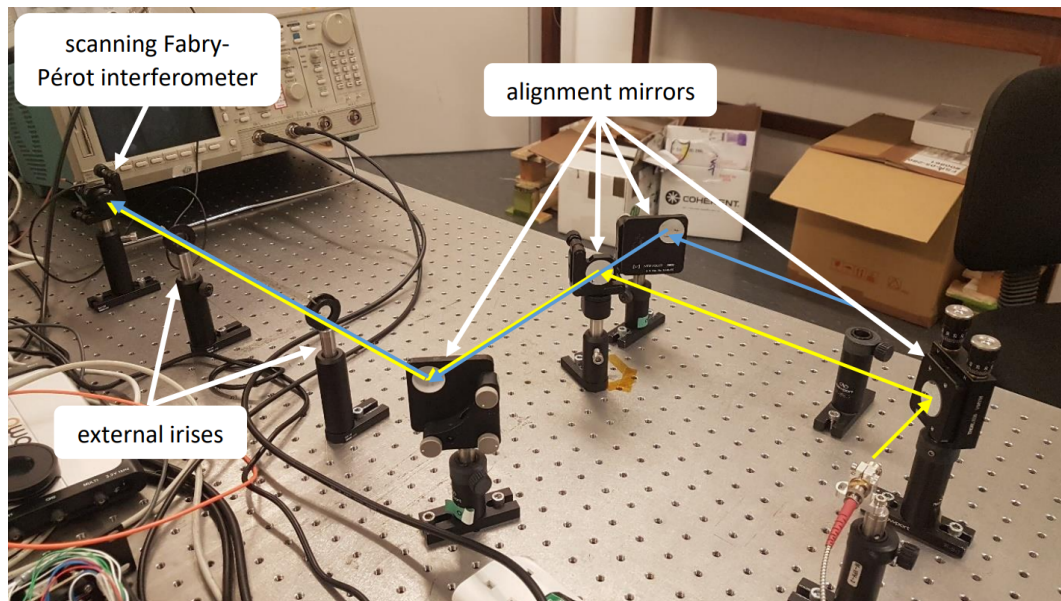


Figure 2.9: Optics alignment setup into the interferometer with the visible alignment beam path (blue) and our invisible laser beam path (yellow) marked.

Since our amplified infrared laser light at 1084.5 nm is invisible without additional equipment (such as an IR viewer or heat sensitive paper), a visible blue continuous laser at 455 nm was first used to achieve good alignment inside the cavity of the interferometer, as shown in Figure 2.9. The use of a flip mount as the second alignment mirror for both laser paths meant that after optimising the alignment for the visible laser light, the mirror could be flipped back up to intercept our invisible laser light and direct it into the interferometer. Figure 2.10 shows the interferometer response for our aligned infrared laser with a 4 ns FWHM pulse to determine the minimum linewidth at this stage of the amplification process. With a $\Delta\tau_{FWHM}$ of ~ 25 ns and a $\Delta\tau_{diff}$ of ~ 220 ns and given the FSR of the interferometer of 10 GHz, the laser linewidth has been calculated as 1.1 GHz using Equation 2.4. Therefore, since the linewidth of a transform limited pulse after the SOA is 0.11 GHz, it is evident that amplifying a pulse is also a source of linewidth broadening, increasing the spectral width by \sim one order of magnitude

for the regenerative stage. The magnitude of the linewidth at this stage is sufficient to resolve the SO_2 spectrum, and a comparable value is achieved by Rollins.

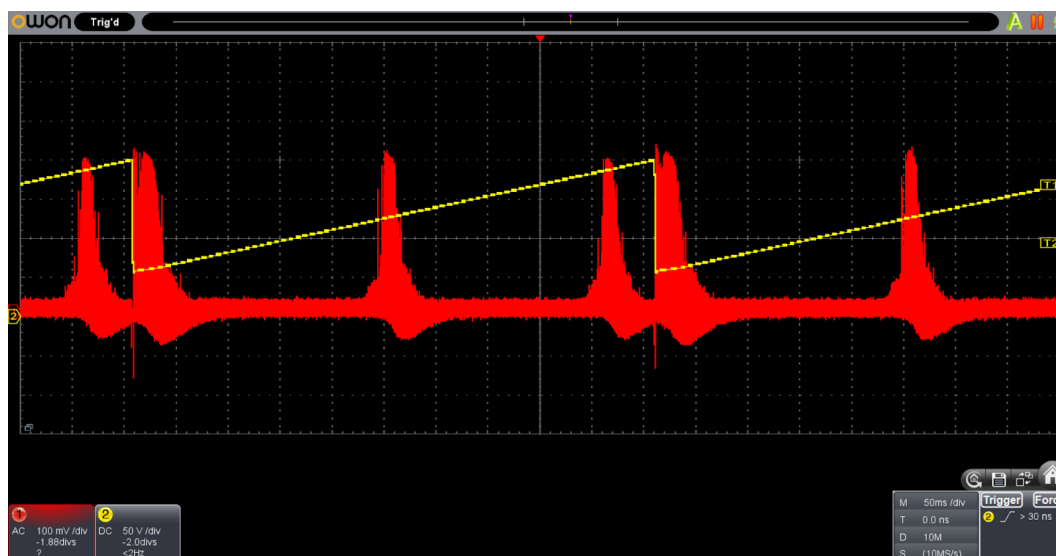


Figure 2.10: Interferometer response of our 1084.5 nm laser after the regenerative amplification stage using a 10 GHz scanning Fabry-Pérot interferometer. Each vertical division corresponds to 50 ms.

Due to the higher powers generated by the power amplification stage (~ 1 W), interferometry measurements were unsuitable. However, optical fibers transmitting high laser powers can lead to linewidth broadening due to nonlinear optical effects. Also, since multimode fibers are used in the power amplification stage, modal dispersion and intermodal interferences can add to linewidth broadening. Therefore, one expects a fairly large broadening effect from the power amplification stage, which provides the input light to the nonlinear optics stage. As a rough estimate, due to the simpler absorption cross section of NO, Rollins et al., 2020 was able to assess his laser linewidth after the power amplification stage. He reports it to be comparable to the Doppler broadened linewidth of NO at 300 K which was determined as 3 GHz.

2.2.3 Mitigation strategies and improvements

During the laser build, a number of laser issues were encountered, including failure of the laser system. Hence, an account of these failure modes and issues, as well as the solutions that were found to overcome them, are given here as a guide for others using or developing a LIF-SO₂ laser. Finally, an overview of improvements that have been made to the laser since this work are outlined.

The main laser failure mode results from insufficient amplified stimulated light from the regenerative amplifier reaching the power amplification stage to cause stimulated emission of the excited Yb³⁺ ions. Therefore, the Yb³⁺ ions in the power amplifier undergo spontaneous emission in all directions and hence, ASE in the fiber core and pump light in the inner cladding builds up and damages the fiber, potentially leading to fiber breakage. This is diagnosed using an optical spectrum analyser (OSA, Ocean Optics) which provides information on the wavelengths of light present in the fiber, but lacks the resolution to determine their linewidths. During normal, working operation of the laser, there is little/no ASE present in the power amplifier (since sufficient amplified stimulated light from the regenerative amplifier is present), as shown in Figure 2.11(a). The intensity of emission around 1030 nm corresponding to the ASE maximum is negligible in comparison to the large peak at 1084.5 nm due to stimulated emission. However, a damaged fiber results in the OSA spectrum in Figure 2.11(b), showing a large ASE and pump light (976 nm) peak, in addition to a stimulated emission peak. The presence of pump light is likely due to leakage from the inner cladding into the core of the damaged fiber since the CPS removes pump light in the inner cladding where it normally resides. Likewise, ASE would not be removed by the CPS since it is produced in the core of the fiber. Fiber breakage/damage typically occurs at the position of a splice where the fiber is weakest. This is fairly easy to identify using an infrared viewer as the splice looks brighter

than usual and the problem is overcome by removing the damaged fiber and splicing the ends back together. Therefore, efforts have been directed towards improving the splicing method since this work to enhance their strength and durability (see details below).

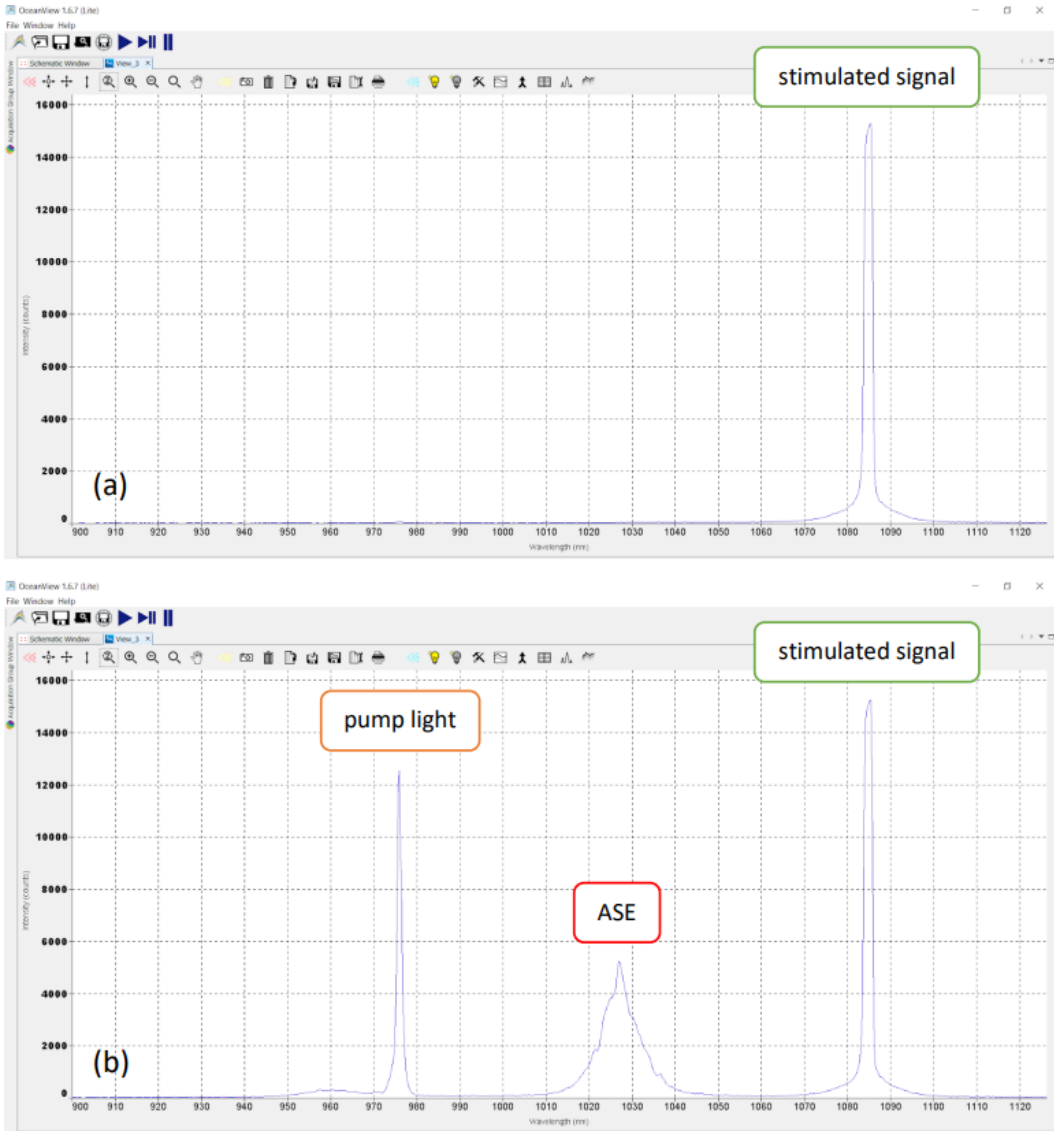


Figure 2.11: Optical spectra of (a) a working laser system and (b) a damaged laser system, displayed on the OSA. To note, the resolution of the OSA is insufficient to provide an accurate representation of the laser linewidth and the peak intensities and relative ratios of intensities is arbitrary as it depends on how you angle the fibre into the OSA.

Insufficient stimulated light from the regenerative amplifier was caused by adjusting the pulse shape via the SOA board so that the temporal width was too large, hence meaning the power of the stimulated light dropped too low (see subsection 2.2.2). This was done with the power amplifier pump laser diodes on, leading to the failure mode described above. Therefore, it is now a general rule that adjustments to the pulse shape are made without the power amplifier pump laser diodes on and they are only turned on when the amplitude of the largest amplified peak within the regenerative amplifier exceeds a certain threshold, as diagnosed in an oscilloscope via the 1 % tap to the photodiode. In addition, since this work, the 300 mW regenerative pump laser diode has been replaced by a 500 mW one to achieve greater output powers of stimulated light from this stage.

Another failure mode was due to reflected light from the nonlinear optics setup, which resulted in breakage of the regenerative pump laser diode. This happened when the lens before the final crystal was being introduced into the optics system and the laser power was at a maximum, resulting in large back reflections of most notably the second harmonic. Slight back reflections from certain angular displacements of the crystals have also been seen. Since there is no isolator or method of removing this mainly 542 nm light, it can make its way back down the fiber, however, the details of how this failure mode occurred are not fully understood. Again, this was overcome by reducing the power of the beam during laser alignment and optic setup changes.

Fiber splicing is an essential part of the laser build as it is used to join two optic fibers together, end-to-end. However, there were issues with our splicing method at the time, which led to large power losses across a splice. A brief introduction to the splicing method and equipment used is now given, followed by the changes that have been made to the method since this work as our knowledge had improved.

There are four steps in our fiber splicing method, governed by four different instruments: a fiber stripper, cleaver, splicer and recoater. Firstly, it is necessary to remove the protective polymer coating surrounding the optical fibre using a fibre stripper (Fujikura, HTS-12). The stripper protects the exposed fibre's glass surface from physical contact when removing the coating to avoid damage. The bare fibre is then cleaned with ethanol and optical cleaning tissues (Thorlabs) to keep the glass free of any contaminants. Secondly, a cleaver (Fujikura, CT106+) is used to cause a clean break near the end of the fibre. For a successful splice, the cleaved end must be mirror-smooth and perpendicular to the fibre axis which is optimised by adjusting the cleaver parameters. For example, the optimum clamp force depends on the optical fibre structure and coating material and should be the minimum force that does not slip while the cleaver applies fibre tension. Once a good quality cleave has been achieved, a splicer (Fujikura, FSM-100P+) is next used to fuse the fibres together which involves alignment of the fibres followed by heating. A number of automated alignment methods are offered by the splicer which are specific to the fibre type, for example, its overall shape and the position and shape of its stress rods. For the instrument splices, the splicer is set to 'PANDA' mode (polarisation-maintaining and absorption-reducing) since this mode matches the instrument fibre's circular cross-section consisting of a central core with two circular stress rods either side. This means that the laser light maintains its linear polarisation across a splice and loss of light transmission to the splice is minimised. Once aligned, the fibres are melted by an electric arc which permanently welds them together. Finally, to protect the bare splice from bending and hence potential breakage, it is necessary to reapply a coating. The recoater (Fujikura, FSR-05) achieves consistent resin application through its programmable injection system which provides an exact volume of resin to the mold cavity and rapid curing time due to the position of LEDs both above and below the cavity. The type of resin used dictates the recoater parameters, for example the

injection volume and curing time. For the instrument splices, either low or high index resin is applied for different effects; low index resin is mainly used for the double-clad fibre to retain the pump light within the cladding whereas high index resin is used for the single-mode fibre and the splice within the cladding power stripper to remove light from the cladding.

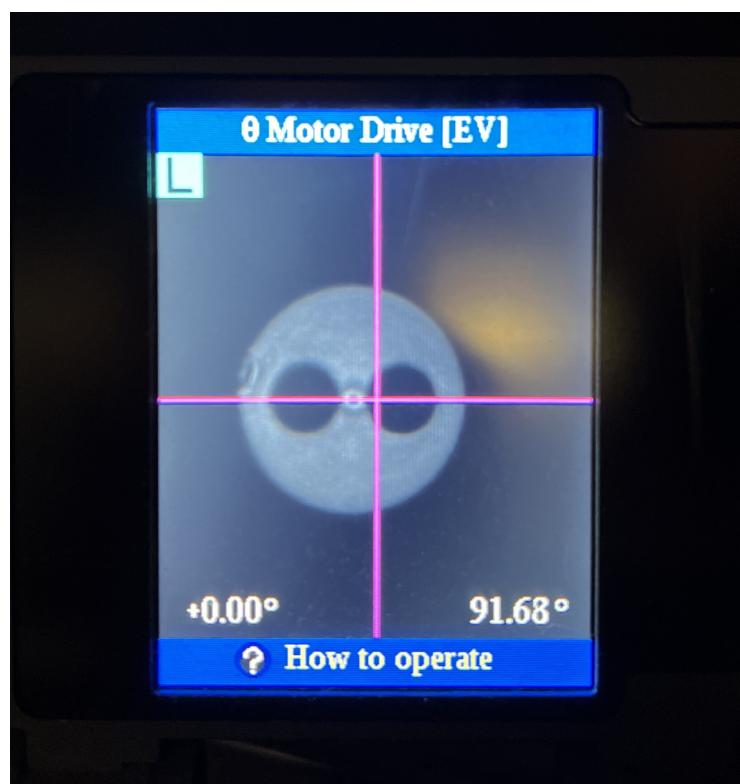


Figure 2.12: Photograph of the splicer display in end view mode of one of the fibers to be spliced, showing a clean, non-damaged cleave. Note the mark on the left edge of the fiber is due to the blade from the cleaving method and is present on all cleaved fibers.

The main issue with this splicing method was the fiber cleaver, which gave inconsistent cleave angles and difficulty was found with optimising the clamp force and fiber tension. This, together with a relatively long minimum cleave length of 5 mm, meant a lot of fiber was wasted during this step. However, even if a good cleave angle of $< 2^\circ$ was achieved, analysis

of the fiber ends for damage was not possible as the end view mode of the splicer was unavailable. Hence, since this work, a new fiber cleaver (Fujikura, CT-101), which has a lower minimum cleave length of 3 mm, and splicer (Fujikura, FSM-100P+) have been purchased. The new cleaver gives more dependable cleaves and, using the end view mode of the splicer to quality assure the cleave (which should typically look like that in Figure 2.12 for a single mode fiber), lower power losses across a splice have been seen (typically 0.01 dB). One final point to note is the splice that causes the biggest power loss, that being the single to multimode splice after the 2×2 switch. This is because the core diameters are very different - $5 \mu\text{m}$ for the single mode compared to $20 \mu\text{m}$ for the multimode fiber. Therefore, the splicer settings were adapted to offset the electric arc meaning the fibers were heated asymmetrically to expand the core of the single mode fiber to better match that of the larger multimode fiber core. This reduced the power loss across the splice and, since this work, further advancements have made use of mode field adapters (Haphit) to achieve negligible losses.

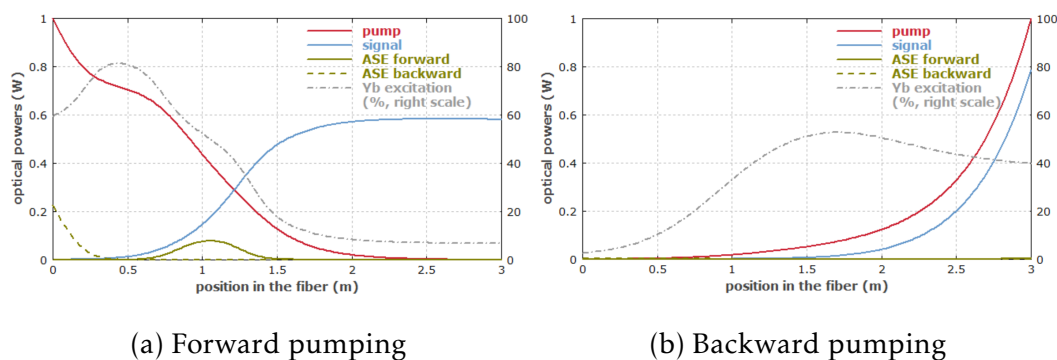


Figure 2.13: Optical powers along the length of a Yb^{3+} -doped fiber amplifier with different types of ion pumping schemes. [Reproduced from RP Photonics (*Tutorial “Fiber Amplifiers”* n.d.)]

A description of a few further improvements to the laser system are described here, which have not been implemented yet. To improve the laser output power at 1084.5 nm, an additional amplification stage could

be added between the regenerative and power amplifier. This has already been done by Rollins and for our NO system and is identical to that of the power amplifier but using only one 5 W pump laser diode and a 15 μm core multimode fiber. Another potential laser power improvement is backward pumping the regenerative amplifier, which means the signal and pump light propagate in opposite directions. Generally, there exists lower ASE losses for backward pumping, and therefore a higher power conversion efficiency in this configuration (*Tutorial "Fiber Amplifiers" n.d.*). This is because amplification occurs nearer to the end of the fibre where the signal is stronger and a greater proportion of the Yb^{3+} ions are in the excited state. Also, amplified short pulses often lead to nonlinear effects which backward pumping is best at suppressing (*Tutorial "Fiber Amplifiers" n.d.*). Figure 2.13 demonstrates how the pump, signal and ASE evolve along the length of a Yb^{3+} -doped fibre for forward and backward pumping. For forward pumping, it can be seen that backward ASE dominates at the beginning of the fibre and forward ASE also has an effect, but only at some region within the fibre. However, ASE is negligible in backward pumping, hence leading to a greater signal output power.

2.3 The LIF system

2.3.1 Harmonic generation

To convert the amplified 1084.5 nm light into the fifth harmonic at 216.9 nm in order to excite SO₂, a series of nonlinear crystals are used. Noncentrosymmetric crystals (those lacking inversion symmetry) can exhibit non-linear responses to the electric field of incident light. This non-linear response can lead to the phenomenon of sum frequency generation whereby two incident beams of frequency ν_1 and ν_2 can combine in a nonlinear crystal to produce a third beam with $\nu_3 = \nu_1 + \nu_2$ (*Frequency Doubling* n.d.).

Harmonic generation requires the input waves to be phase-matched along the length of the nonlinear crystal, leading to constructive interference which maximises the conversion efficiency to the desired sum frequency. The degree of phase matching depends on the refractive index of the crystal through which the light waves propagate, which increases monotonically with increasing frequency - the phenomenon of chromatic dispersion. Therefore, for waves of different frequencies which experience different refractive indices, the result is poor conversion efficiency. However, this limitation can be overcome by careful utilisation of crystal birefringence, meaning the refractive index experienced by a wave traversing the crystal depends on its polarisation. Therefore, the polarisations of the waves can be chosen such that the birefringence of the crystal exactly offsets chromatic dispersion, so that the waves all experience the same refractive index overall and hence good conversion efficiency. There are two possible ways of achieving this: type I and type II phase-matching. In type I phase matching, both incident beams are polarised to maximise their refractive index and the sum frequency with the opposite polarisation can then be phase matched (*Phase Matching* n.d.). In type II phase matching the input beams are given opposite polarisations and once again the sum frequency is produced with the polarisation that

gives it the lower refractive index (*Phase Matching* n.d.).

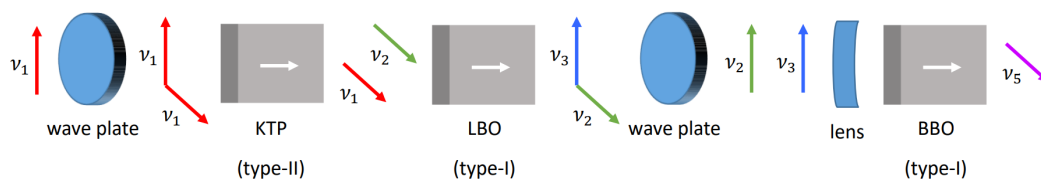


Figure 2.14: Schematic of the nonlinear optics setup showing the polarisation of the fundamental ($\nu_1 = 1084.5$ nm) and various harmonics (second harmonic = $\nu_2 = 542.3$ nm, third harmonic = $\nu_3 = 361.5$ nm, fifth harmonic = $\nu_5 = 216.9$ nm).

The nonlinear optics setup, as shown in Figure 2.14 and identical to that by Kliner et al., 2002, consists of three nonlinear crystals to produce the fifth harmonic. These are potassium titanyl phosphate (KTP, KTiOPO_4) for the second harmonic generation, lithium triborate (LBO, LiB_3O_5) for the third harmonic, and β -barium borate (BBO, $\beta\text{-BaB}_2\text{O}_4$) for the fifth harmonic. These crystals are chosen based on their nonlinear coefficients, birefringence properties and optical transparency. KTP is highly transparent for wavelengths between 350 – 2700 nm and exhibits a large second harmonic generation coefficient. Borate crystals (LBO and BBO) are suitable for the generation of relatively short wavelengths due to their large energy band gap meaning they are relatively resistant to UV light. The crystals are all critically phase matched meaning an angular adjustment of the crystal is used to optimise the phase matching configuration. The use of half-waveplates also allow optimisation of the phase matching by altering the polarisation of the input waves. Firstly, a zero-order half-wave plate is used to rotate half of the linearly polarised fundamental light (1084.5 nm) through 90° before it passes through a type-II phase matched KTP crystal ($3 \times 3 \times 10$ mm) to generate the second harmonic (Figure 2.14). The resultant 542.3 nm light combines with the residual parallel-polarised 1084.5 nm in a type-I phase matched LBO crystal ($3 \times 3 \times 10$ mm) to generate the third harmonic (361.5

nm). A second custom wave-plate ($\lambda/2$ at 542.3 nm, λ at 361.5 nm) rotates the polarisation of the 532 nm beam to be parallel to that of the 355 nm beam before the type-I phase matched BBO crystal ($3\times 3\times 20$ mm). The beam is focused by a lens to achieve higher intensities within the longer BBO crystal to generate the fifth harmonic at 216.9 nm. The various harmonics are then separated using a UV fused silica Pellin-Broca prism (Thorlabs) and all but the 216.9 nm, which exits the prism at 90° , are dumped into a beam block. Typically, the harmonic generation step achieves an average fifth harmonic power of ~ 50 μW but this is sensitive to the alignment and temperature of the nonlinear crystals.

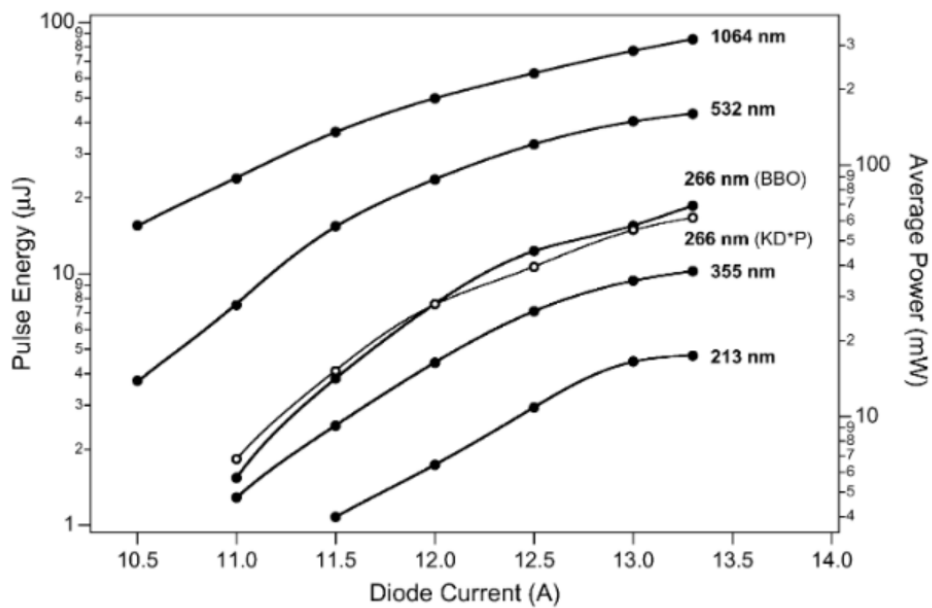


Figure 2.15: Pulse energy and corresponding average power as a function of current supplied to the pump diode by Kliner et al.¹³ for their amplifier output at 1064 nm and for the indicated harmonics. The points are the experimental results and the curves are smoothing splines. [Reproduced from Kliner et al.]

Typically for our laser system, the maximum average 1084.5 nm power exiting the armoured cable is ~ 1 W. This corresponds to a pulse energy of \sim

5 μJ at a laser repetition rate of 200 kHz and a peak pulse power of ~ 2.5 kW for an approximately Gaussian pulse (very rough estimate) with a full-width half maximum (FWHM) of 2 ns. Due to an extremely low overall harmonic conversion efficiency of ~ 0.005 %, a maximum fifth harmonic average power of 50 μW is seen at 216.9 nm, only measurable using a UV specific power meter (Hamamatsu, see subsection 2.5.1). Also, estimates of the second and third harmonic conversion efficiencies are as low as singular figure percentages. Rollins et al., 2016 achieved a significantly higher average fifth harmonic power of 2 - 4 mW with 600 mW of average fundamental power (overall conversion efficiency of 0.3 - 0.7 %) and comparable nonlinear optics setup, however, a laser repetition rate of 25 kHz was used, hence giving a much larger peak pulse power of ~ 12.5 kW (2 ns FWHM pulse width). An even higher fifth harmonic conversion efficiency of 6 % was reported by the original Kliner et al., 2002 study, but again an even lower laser repetition rate of 3.7 kHz and FWHM pulse width of 0.97 ns was used, therefore attaining peak pulse powers of the fundamental light of ~ 89 kW. Conversion efficiencies for the second and third harmonic of 50 % and 24 % respectively were also obtained. Harmonic generation relies on pulses of high peak power to generate large optical electric fields within the nonlinear crystal for the frequency conversion process to occur. Therefore, as evident in the above results, increasing the peak pulse power leads to a better conversion efficiency. This relationship is nonlinear as shown in Figure 2.15 by Kliner et al., 2002 where the difference in average power between the harmonics decreases with greater diode currents meaning the conversion efficiency increases with higher input powers. Theoretically, the conversion efficiency is proportional to the square of the input power for second harmonic generation, and to the cube for third harmonic generation. Experimentally, however, many other variables are also at play which reduce the conversion efficiency, for example, spatial walk off and the distance between the individual optics components affects the spatial overlap of the

light within the crystals. Therefore, to achieve greater fifth harmonic power, it is not only worth improving the conversion efficiency of each nonlinear crystal, but also increasing the fundamental power.

For our setup, the reason for using a high laser repetition rate (200 kHz) at the expense of lower peak pulse powers is due to the better counting statistics achieved at faster sampling rates. Likewise, the rationale behind a longer than 1 ns pulse width are outlined in subsection 2.2.2. Since this work, improvements have been made to the fifth harmonic generation by replacing the KTP crystal with a temperature-controlled periodically poled lithium niobate (PPLN) crystal. This is a quasi-phased matched crystal meaning its conversion efficiency is insensitive to angular displacements, however, temperature adjustments can be made to optimise the phase matching configuration. Therefore, due to the less stringent alignment, phase matching stability, broad angular acceptance and reduced walk-off of the PPLN crystal, the second harmonic conversion efficiency has massively improved to yield a 20-fold increase in laser power. This has substantially improved the instrument's precision, detailed in subsection 2.5.3.

2.3.2 The sample cell

After the harmonic generation stage, the 216.9 nm light is directed by dielectric mirrors into the sample LIF cell where it passes through a series of baffles which collimates the beam and reduces the background counts from scattering. The laser pulse intersects the sample gas flow at right angles in the centre of the signal cell, causing excitation of SO₂ followed by redshifted fluorescence. A fraction of the fluorescence photons are collected by a collimating aspheric lens (Edmund Optics, 49-695) which lies perpendicular to both the laser beam and gas flow. These photons then pass through a 240 - 400 nm bandpass filter (Asahi, XUV0400) to select the photons from SO₂ fluorescence before being imaged onto the photocathode of a photomul-

tiplier tube module (PMT, Hamamatsu H10682). To increase the fraction of photons with a direction of travel incident to the PMT module, a concave mirror (Thorlabs, CM127-025-F01) located opposite the collection optic is used which has been reported by Rollins et al., 2016 to increase the signal by $\sim 50\%$. The PMT works via the photoelectric effect - when a photon hits the PMT photocathode, a photoelectron is emitted. The focusing electrode then accelerates the photoelectron onto the first dynode where it is multiplied by means of secondary electron emission which is repeated at each of the successive dynodes. Due to this amplification, a larger current is generated which is analysed using a high-speed pulse amplifier-discriminator module (PAD) for single-photon counting. Due to this single photon counting nature, it is necessary to apply a correction to linearise the counts, as described in Section 2.4. The PAD outputs a digital 5 V signal of 10 ns length which is read by a fast speed module before the cRIO.

2.3.3 The reference cell

After exiting the sample LIF cell, the laser beam is directed by two more dielectric mirrors into the reference LIF cell. The function of the reference cell is to verify the absolute wavelength tuning of the laser with respect to the position of the $\widetilde{C}(^1B_2) \leftarrow \widetilde{X}(^1A_1)$ transition. It determines the online (corresponding to a maximum signal when the laser is tuned to the absorption peak) and offline (minimum signal) wavelength positions as shown in Figure 2.16. Therefore, a high mixing ratio of SO_2 in the ppb or ppm region constantly flows through this cell. As in the sample cell, the laser beam enters the reference cell on an axis perpendicular to the gas flow, and the fluorescence signal is detected along the third perpendicular axis. In order to find the online position, the laser wavelength is scanned across a 0.01 nm range which encompasses the transition peak wavelength whilst simultaneously recording the PMT signal from the reference cell. From this

scan, a rough input of current values corresponding to the online and offline wavelength positions are entered into the LabVIEW code by the user. A peak is then found via an algorithm which, above a set threshold value, identifies three consecutive increases in fluorescence counts followed by a decrease. This dictates the peak maximum, defining the online position. The offline position is determined at a given wavelength difference from the online peak, specified in the LabVIEW code. From dithering online and offline this peak, the SO_2 concentration is proportional to the difference between the online and offline LIF counts.

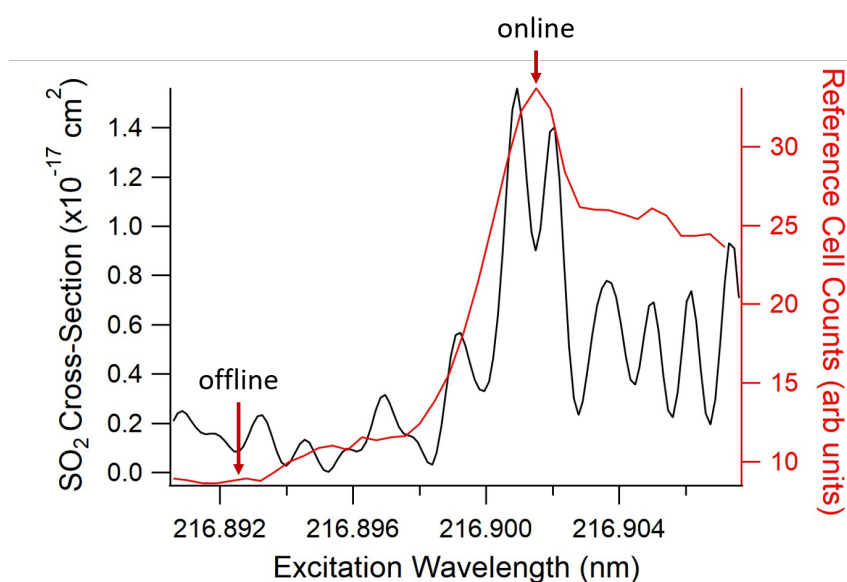


Figure 2.16: Example of the observed reference cell fluorescence counts during a scan of laser excitation wavelength, plotted in red on the right axis. The literature SO_2 absorption cross section is plotted in black on the left axis.

After passing through the reference cell and a diffuser, the laser power is measured by a UV sensitive phototube (PT, Hamamatsu R6800U-01) with an in-house made amplifier board which is used to normalise the SO_2 fluorescence signal for laser power fluctuations. The advantages of a PT over a UV sensitive photodiode used by Rollins et al., 2016 is that a PT is

both less sensitive to ambient light and temperature changes within the LIF box.

2.3.4 Instrument control, timings and data logging

The instrument is controlled by a LabVIEW project which is deployed on a National Instruments cRIO computer system. The fastest loop within this project is run by a field-programmable gate array (FPGA) at 200 MHz, meaning commands initiated by the LabVIEW code can be computed with 5 ns precision, which defines a 'tick' within the code. Therefore, since a pulse rate of 200 kHz corresponds to a laser 'shot' duration of 5 μ s, a 'tick' represents one thousandth of a laser shot. This FPGA loop is responsible for controlling the fast laser timings within the system: the production of a pulse via the SOA and the regenerative amplifier, photon counting, and dark counting gates, as outlined in Figure 2.17.

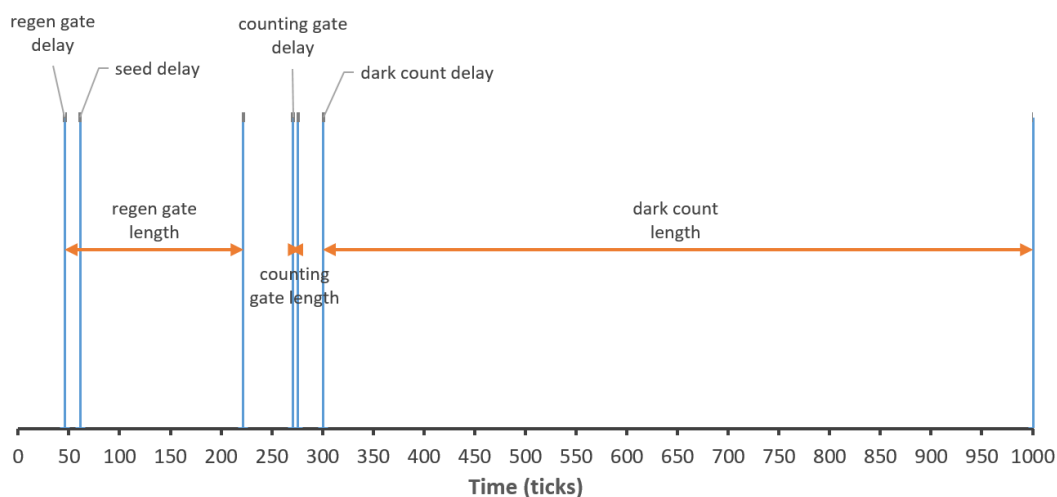


Figure 2.17: Laser timings for a single laser shot, as controlled by the FPGA LabVIEW code at 200 MHz, where 1000 ticks is equal to 5 μ s.

Within a single laser shot, the following timings are important to optimise for increasing laser amplification (regenerative gate timings) and fluorescence intensity (counting gate timings). Firstly, the seed delay at

60 ticks determines when a pulse is made by the SOA. Theoretically, the pulse must occur before the regenerative gate delay when the 2×2 switch becomes energised but experimentally it has been found that the switch takes longer than 15 ticks to change state and hence the regenerative gate delay signal must be sent prior to the generation of a pulse. The regenerative gate length determines the number of round trips of the pulse before the switch is de-energised at 221 ticks. As previously mentioned in Section 2.2, the optimal number of passes of the regenerative loop is approximately 8 times, before gain saturation is achieved. A significant delay of 49 ticks is then required for the pulse to travel through the power amplification stage, harmonic generation setup and LIF cells to initiate the excitation of SO_2 . Therefore, the counting gate delay, which marks the beginning of SO_2 fluorescence detection by the PMT modules, occurs much later at 270 ticks and lasts for only 5 ticks (25 ns). This is due to firstly the short SO_2 fluorescence lifetime of ~ 4 ns at 50 hPa (e-folding, Rollins et al., 2016), and secondly to maximise the SNR since scattering of laser light by the baffles and other small particles can contribute to the fluorescence signal. Following this, the background fluorescence counts are measured, given as the dark counts in Figure 2.17. These counts result from species that have a longer fluorescence lifetime than SO_2 , for example, other species that absorb and emit in a similar wavelength region, or the anodised coating of the LIF cell itself.

In terms of data logging, three different files are created by the LabVIEW code, which are saved on the cRIO: a log file, counts file and 'housekeeping' file. The log file is a text file that contains information on the instrument startup, including most importantly, the date and time that the log file was created. Secondly, the counts file is a binary file which records fluorescence counts data at 100 Hz. This means that each data point consists of 2000 laser shots, the counts from which are summed in the FPGA code and outputted. The data headings within the counts file are: time since instrument turn on,

sample cell counts, reference cell counts, laser power, and laser mode. Therefore, since the counts file records the time since instrument turn on, the log file start time is used to calculate an absolute time. The laser mode variable is used to determine whether the laser is in constant, scanning or dithering mode, the latter of which is necessary for a measurement (subsection 2.2.1). In dither mode, the laser wavelength is held at the online position for 8 consecutive 100 Hz data points, followed by 2 points at the offline, which are averaged separately. This means that the averaged fluorescence count at the online position results from 16,000 laser shots for every 4000 at the offline. Details on how the counts data is used to calculate an SO₂ mixing ratio can be found in Section 2.4. Finally, the housekeeping file is a text file at a data rate of 5 Hz which contains a range of variables, from the mass flow controller set and read values, to the temperature readings of the various thermistors in the system. It is used as diagnostic data and can be viewed remotely using an external computer. Adjustments to the system can be made through the LabVIEW display on the computer, however, the cRIO can run headlessly. Also, files populated with a sequence of commands (for a calibration, scan, ambient sampling etc.) can be deployed on the cRIO and set to run on a ring by the LabVIEW display, therefore allowing fully automated operation of the instrument.

2.3.5 Gas flow system

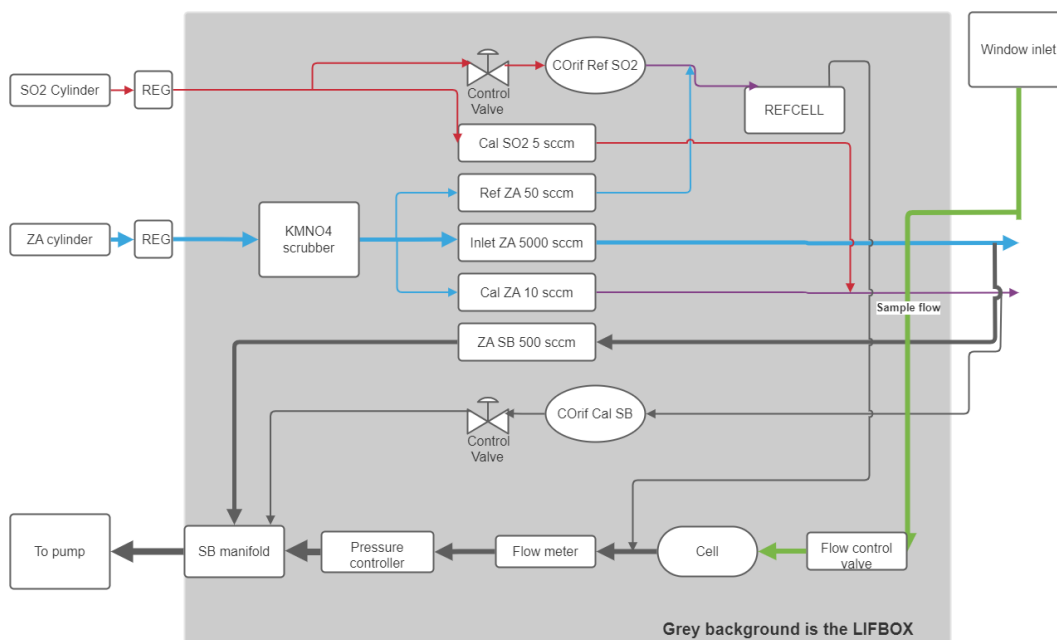


Figure 2.18: Schematic of the gas flow and calibration system. All instrument components within the grey box are housed in the LIF box. The five mass flow controllers (Cal SO₂, Ref ZA, Inlet ZA, Cal ZA and ZA SB (suck back)) are labelled with their maximum flow rate.

Figure 2.18 shows a schematic of the sampling and calibration system used by the LIF-SO₂ instrument. Ambient air is pulled into the sample cell with a 60 L min⁻¹ scroll pump (Agilent IDP-3). A flow rate of 2 slpm is maintained by a proportional valve (Bürkert 2873) servo-controlled to a mass flow meter on the cell exhaust line to ensure a constant flushing rate. Similarly, the sample and reference cell pressures are maintained by an exhaust pressure controller (Alicat, PCH-100TORRA-D-MODTCPIP-A515) with an internal servo-controlled valve to eliminate fluctuations in LIF sensitivity. The operation cell pressure chosen is typically the highest pressure that can be achieved to maximise fluorescence counts (subsection 2.5.4), which is lower for aircraft measurements compared to ground-based due to external pressure variations. Details on the optimal pressures used for the specific

field campaigns can be found in subsection 3.3.1 and Section 4.2. The reference cell receives a constant small flow (~ 10 sccm but not regulated) of calibration gas via a critical orifice and solenoid valve from a compressed gas standard of SO₂ in N₂ (BOC), typically near 5 ppm with ± 5 % uncertainty.

As outlined in subsection 2.5.2, calibrating the system is necessary to convert the fluorescence counts into an SO₂ mixing ratio. Two tees into the inlet are used to add zero air and/or calibration gas. The inlet zero air mass flow controller (MFC) can achieve significantly high flow rates up to 5 slpm in order to overflow the inlet during a calibration or zeroing procedure. A calibration zero air MFC with a small maximum flow of 10 sccm is also used as a 'carrier' gas to improve the time taken for the calibration gas to reach the sample cell. The zero air from the commercial compressed gas standard (BOC) is initially passed through a trap filled with potassium permanganate (KMnO₄) impregnated zeolite to eliminate any remaining SO₂. This is important as commercial zero air still contains a measurable amount of SO₂ which could be detected by our sensitive system. When zero air is not being added to the sample line, it is returned to the vacuum pump through a low-pressure-drop MFC with a small excess return flow so as to eliminate contamination of the zero air line. Similarly, when calibration gas is not being delivered to the inlet line, it is diverted to the vacuum pump using a critical orifice and solenoid valve. This ensures a constant flow of calibration gas throughout the calibration system, enabling quick calibrations by minimising line effects. The cell exhaust then passes through the suck back manifold to the scroll pump. All tubing and fittings are constructed of Teflon PFA (perfluoroalkoxy alkane) or PEEK (polyetheretherketone) material.

During a calibration sequence, the inlet is overflowed with 2.5 - 3 slpm of zero air, which is mixed with small varying flows (0.2 - 5 sccm) of SO₂ calibration gas. Therefore, using a 5 ppm SO₂ standard, the sample cell receives a range of SO₂ concentrations from 0.5 - 12.5 ppb and the LIF response to each

Chapter 2. Experimental

is measured to produce a calibration plot (subsection 2.5.2). Occasionally, only zero air (with the calibration gas diverted) is passed through the sample cell as a background measurement to record the fluorescence counts without SO₂.

2.4 Analysis code

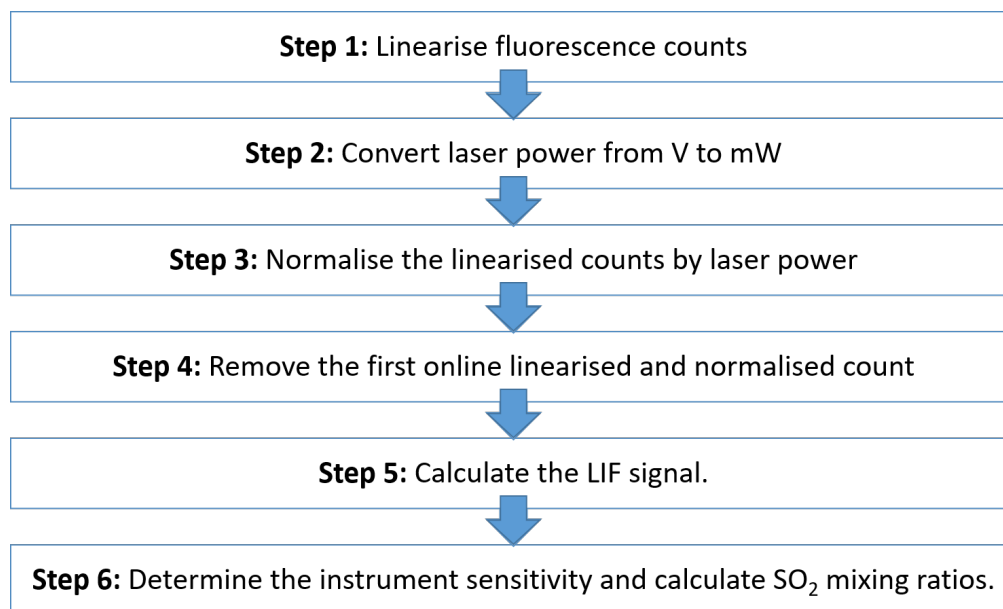


Figure 2.19: Flow diagram showing the steps taken in the Python analysis code to convert the fluorescence sample cell counts within the 100 Hz counts file into an SO₂ mixing ratio.

An analysis code to convert the data from the 100 Hz counts binary file into a 10 Hz mixing ratio has been written in the programming language Python and can be found on GitHub (<https://github.com/wacl-york/LIF-cals>). The main steps taken by the code to achieve this are outlined in the flow diagram in Figure 2.19. A more detailed description for each step is given below. To note, since the dark counts measured in this work are essentially zero, they have not been subtracted from the fluorescence counts.

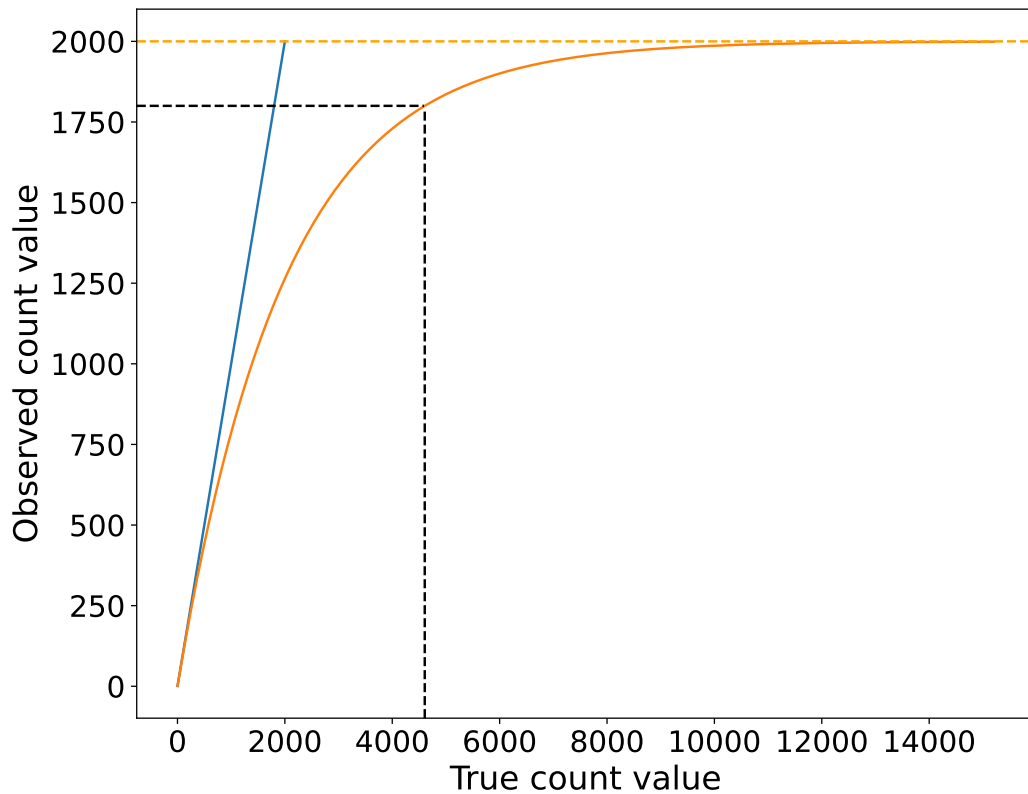


Figure 2.20: Relationship between the observed and true photon count values (orange), calculated via Equation 2.5, assuming 1 count per laser shot (200 kHz) and hence a maximum of 2000 counts for a 100 Hz data point. The blue line indicates a 1:1 ratio for the observed count values and the black dashed lines represent the upper limit of this correction, as described by Rollins et al., 2016.

Step 1: The single photon counting nature of the PMT module means that at most, one count can be registered per laser shot. Since each data point within the 100 Hz file consists of 2000 laser shots, the maximum observed count value that can be recorded in this file is 2000. However, there are instances where more than one photon reaches the detector but only a single count is registered, and hence the relationship between the observed (O) and true (T) count value is nonlinear, which is more prominent at observed count values close to 2000 (Figure 2.20). This nonlinear relationship is described

by Equation 2.5 (Wennberg et al., 1994), which is based on Poisson statistics and forms the count linearity correction in this work.

$$T = -2000 \cdot \ln\left(1 - \frac{O}{2000}\right) \quad (2.5)$$

This correction has been demonstrated by Wennberg et al., 1994 to provide linearity to true count rates that are a factor of four times greater than the laser repetition rate, corresponding to an observed count value of 1960 in this work. However, Rollins et al., 2016 found that at very high observed count values, the precision of the SO₂ measurement is degraded and hence only the data when the observed count rate is less than 90 % of the laser repetition rate is used, as shown in Figure 2.20. This upper limit is redundant in this work, however, since the maximum observed count value recorded was 1600, corresponding to a SO₂ mixing ratio of 140 ppb within a ship plume during the aircraft campaign (subsection 3.4.1). Due to a combined effect of low laser power (maximum of ~ 50 μW), high laser repetition rate (200 kHz), and the typical measurement of low SO₂ mixing ratios in this work, the majority of observed count values were below 300 and hence the count linearity correction made little difference. For an observed count rate of 90 % the laser repetition rate, Rollins et al., 2016 observed a significantly lower SO₂ mixing ratio of 8 ppb, which is a result of their higher pulse energies (due to their greater laser power and lower laser repetition rate) and better fluorescence collection efficiency compared to this work, therefore increasing their observed count rate.

Step 2: The response of the PT to laser power is assessed via a calibration of the phototube (subsection 2.5.1), from which a laser power conversion from V to mW is derived. This conversion is necessary to account for any nonlinearities of the PT response.

Step 3: Since fluorescence intensity is proportional to both laser power

and SO₂ mixing ratio, it is necessary to divide the fluorescence counts by laser power (in mW) to remove this effect, so that fluorescence intensity is solely dependent on SO₂ mixing ratio.

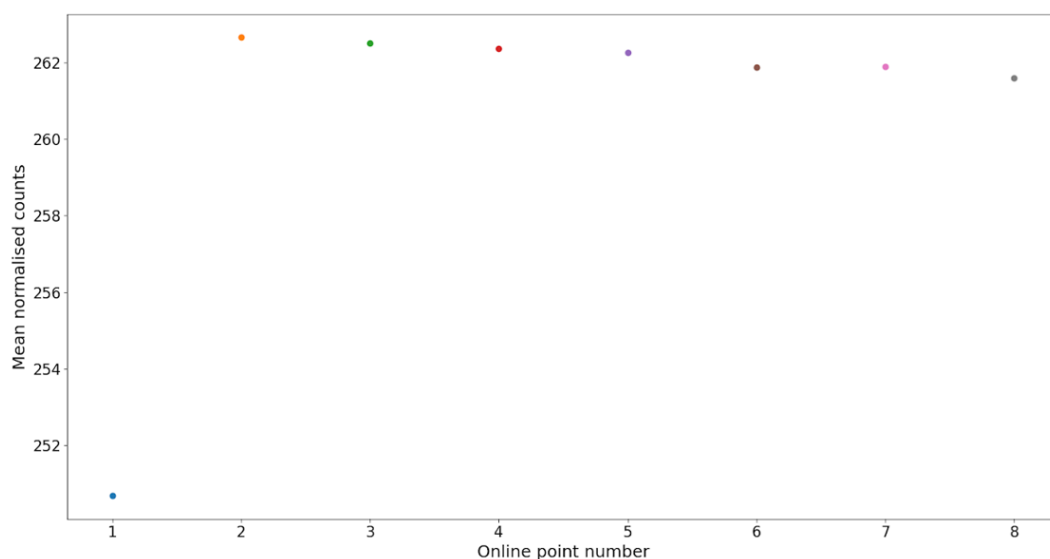


Figure 2.21: Mean online linearised and normalised count values for a minute long calibration point.

Step 4: The laser dithers via current tuning between the online and offline wavelength positions with a typical current difference of 27 mA, resulting in 8 count values at the online position for every 2 offline counts, as explained in subsection 2.3.4. However, the current cannot switch instantaneously between these positions which is apparent when comparing the online linearised and normalised count values. As shown in Figure 2.21, the first online point is lower than the subsequent 7 points, which suggests that the wavelength is still shifting and is perhaps on the increasing edge of the transition peak. However, for the reverse situation i.e. current switching from the online to offline position is not apparent in the data since the two offline points are not statistically different. Therefore, only the first online point is discarded. This effect is exacerbated during the Arctic cruise campaign

since the dither current difference was unintentionally twice that typically used (as explained in subsection 4.2.2), however, removal of the first online point was found to be sufficient. In the 100 Hz file, the online points are deciphered from the offline by the laser mode variable which returns the number 5 for offline and 6 for online.

Step 5: The LIF signal is the difference between the online and offline linearised and normalised counts in cps mW^{-1} , used from hereon, which is directly proportional to the SO_2 mixing ratio, as described in Equation 2.6. It is calculated by first finding the mean of the 7 online and 2 offline linearised and normalised counts and then subtracting the mean offline value from the mean online. To convert this difference in counts mW^{-1} into a per second value (cps), it is multiplied by 100.

Step 6: The instrument sensitivity is determined from a calibration, which is either performed in zero air or ambient air. For a zero air calibration, the mean of the LIF signal is simply taken for each known mixing ratio. For a calibration in ambient air, however, the mean of the ambient LIF signal measurements before and after each calibration point is found and then subtracted from the mean of the calibration LIF signal. The resulting calibration plot (Figure 2.23) is fitted via a York regression analysis to find the slope which is equal to the sensitivity. SO_2 mixing ratios are then calculated by dividing ambient LIF signal measurements by this sensitivity value, again as described by Equation 2.6.

2.5 Characterisation

2.5.1 PT calibration

Laser power is measured after the sample and reference cells by a phototube (PT), which records laser power as a voltage. It is necessary to assess the response of the PT to laser power to account for any nonlinearities in order to correctly normalise the fluorescence counts and make a laser power conversion from V to mW. To do this, the laser power was varied by altering the current supplied to the pump laser diodes in the power amplifier stage, and the resulting power was measured by both the PT and an external UV specific power meter (Hamamatsu). A mirror was used to allow a laser power measurement by the PT and power meter at each current set point by intercepting the laser beam from travelling to the PT and directing it into the power meter. To ensure reproducibility of this mirror position, it was placed between two fixed screws each time, therefore enabling precise power meter measurements, against which the PT response can be determined. The results of this calibration experiment are displayed in subsection 2.5.1. It is apparent that the PT response is nonlinear due to the slight UV power meter saturation at high PT voltages. However, since the maximum PT voltage reached in this work was 1.6 V during the Arctic cruise campaign (Section 4.2), the correction at high PT voltages is not used.

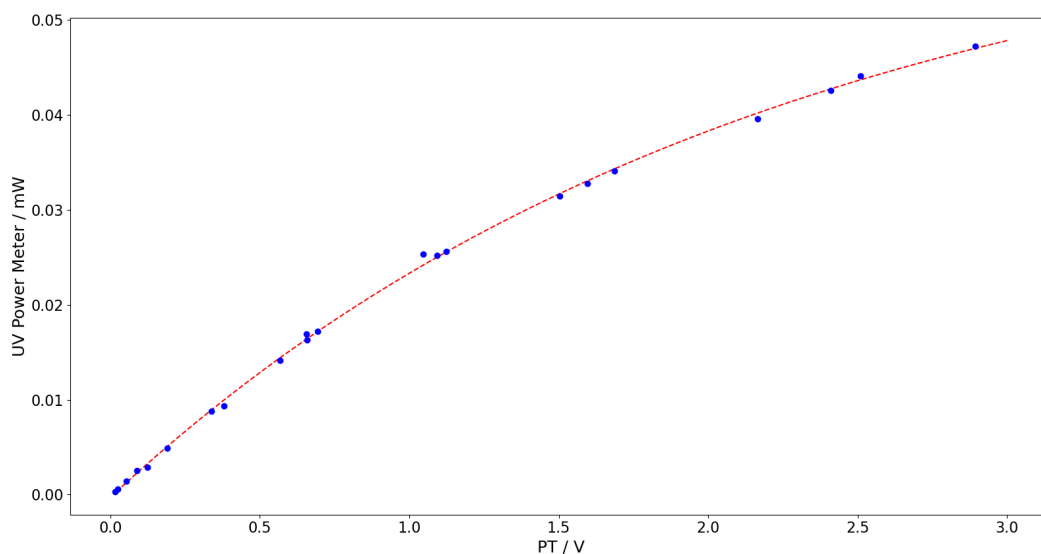


Figure 2.22: Calibration of the PT against a UV power meter. The data is fitted to a curve of the form $y = a \cdot e^{(-b \cdot x)}$ where $a = -0.0647$, $b = 0.454$, and $c = 0.0644$, with a root mean square error of 0.0004.

The PT calibration curve has been fitted using the equation: $y = a \cdot e^{(-b \cdot x)}$ where x and y are the laser power readings on the PT (in V) and power meter (in mW) respectively, and a , b , and c are all constants. The post analysis code (see Section 2.4) has been altered to account for this relationship, and calibrations of the PT will be carried out regularly to check it is still valid.

2.5.2 Sensitivity

The sensitivity of the LIF-SO₂ instrument can be defined as the smallest change in target gas concentration that is detected by the instrument. The units of this quantity are therefore counts per second per mW (cps mW⁻¹, to eliminate changes in counts with laser power) for a given change in SO₂ concentration (altogether cps mW⁻¹ ppt⁻¹). The sensitivity of an instrument can be determined experimentally via a calibration. Since LIF is a relative rather than an absolute technique, the sensitivity of the system is essential for converting the fluorescence counts into an SO₂ concentration, through

the following relationship:

$$[SO_2] = \frac{F_{online} - F_{offline}}{S_{SO_2}} \quad (2.6)$$

where $[SO_2]$ is the SO_2 mixing ratio in ppt, F_{online} and $F_{offline}$ are the online and offline linearised and normalised fluorescence counts in cps mW^{-1} , and S_{SO_2} is the sensitivity of the system to SO_2 in $\text{cps mW}^{-1} \text{ ppt}^{-1}$.

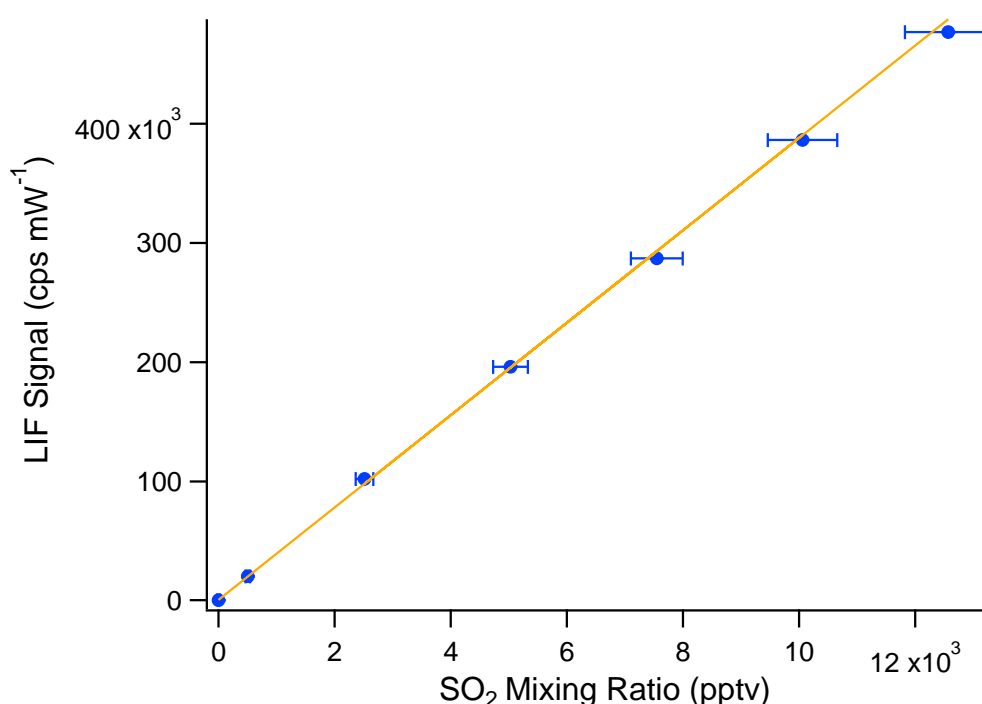


Figure 2.23: Example laboratory SO_2 calibration in zero air where the LIF signal is the difference between linearised and normalised online and offline sample cell counts. The orange line shows a York regression fit to the seven data points, indicating a slope of $38.7 \pm 2.1 \text{ cps mW}^{-1} \text{ ppt}^{-1}$, a y-intercept of $620 \pm 1700 \text{ cps mW}^{-1}$ (both 2σ confidence), and a correlation coefficient of $R^2 = 1.00$.

Therefore, calibrations must be performed to characterise the instrument sensitivity. This is done by sampling known concentrations of SO_2 and measuring the corresponding fluorescence counts. A description of the gas

flow system to achieve this can be found in subsection 2.3.5. An example multi-point calibration from a laboratory experiment is shown in Figure 2.23 over the range 0 - 12 ppb, yielding a slope equal to S_{SO_2} of 38.4 ± 1.3 cps mW^{-1} ppt $^{-1}$. Rollins et al., 2016 achieve a sensitivity of 3.5 cps mW^{-1} ppt $^{-1}$, however, a comparison of sensitivities cannot be made since it is inherent to the system. This is because the sensitivity is dependent on where in the system the PT is calibrated and the type of detector used, for example. If the power meter intersects the laser beam after the sample cell where the laser power is higher (compared to after the reference cell), then the calculated sensitivity will appear smaller, however, the mixing ratios will be unaffected. The positive background of 1180 ± 3050 cps mW^{-1} could be due to residual SO_2 in the sample cell during the zero measurement or potentially laser clipping by the baffles which could be wavelength dependent due to the slightly different laser beam paths.

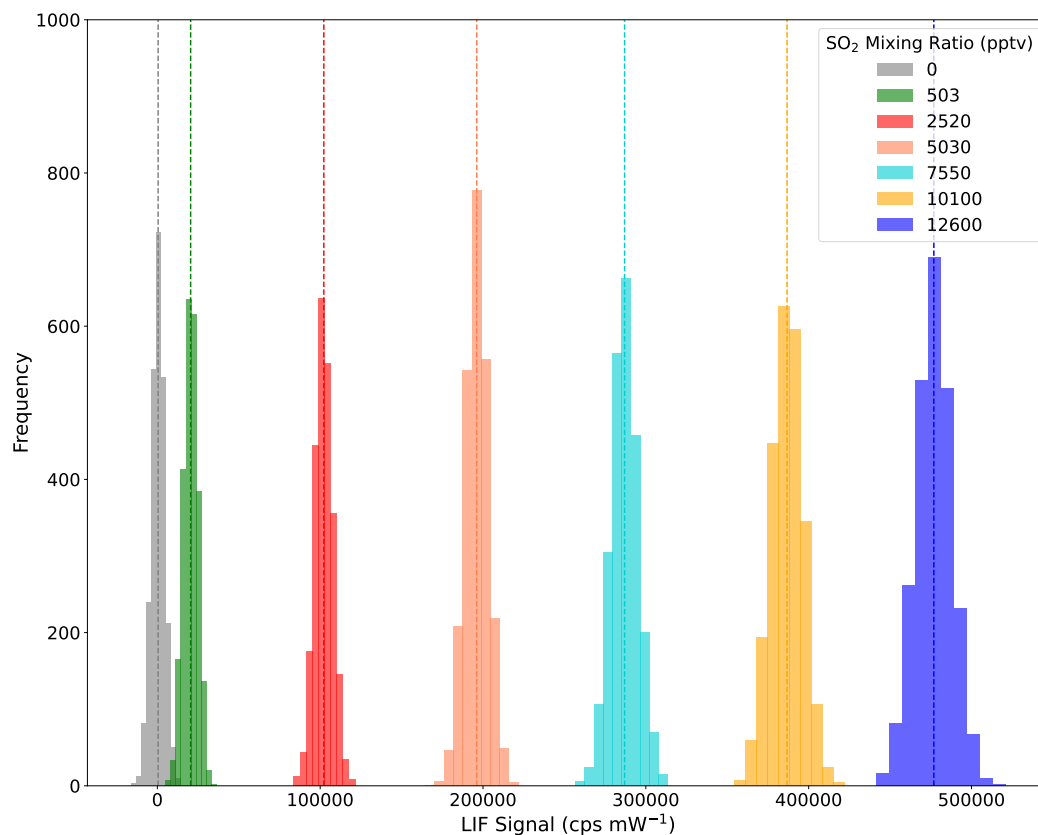


Figure 2.24: Histogram of each calibration point shown in Figure 2.23, coloured by the corresponding SO₂ mixing ratio to 3 significant figures. The mean LIF signal value for each calibration point is marked by the coloured dashed line.

A histogram of each calibration point in Figure 2.23, consisting of 4 minutes of 10 Hz data, is shown in Figure 2.24. As can be seen, every LIF signal distribution is bell-shaped and centered around its mean, indicating Gaussian behaviour at all SO₂ mixing ratios, which has been further confirmed via a Kolmogorov-Smirnov statistical test. To note, the standard deviation or width of the distributions increases with increasing LIF signal since the precision scales with SO₂ mixing ratio (subsection 2.5.7).

The instrument sensitivity is dependent on many instrumental parameters, including laser linewidth, cell pressure (see subsection 2.5.4), and

fluorescence collection efficiency. Since this work, improvements to the instrument sensitivity have been achieved by optimising the focal lengths and distances of the collection mirror and lens to the point of SO₂ fluorescence, in addition to incorporating another lens after the Asahi bandpass filter to focus the fluorescence onto the PMT detection area.

2.5.3 Precision

Precision refers to the consistency and repeatability of measurements taken by the instrument. It can be assessed by the distribution of noise in the measurements; the greater the precision, the greater the ability to consistently reproduce a measurement and therefore the lower the noise, whether it be due to random errors and/or bias or systematic errors. In this work, Allan deviation analyses were carried out to estimate the stability of our system due to noise processes from random errors (and not that of systematic errors), in addition to determining the optimum mixing ratio averaging time. This is done by continuously sampling zero air through the sample cell for a duration dependent on the averaging times of interest, for example, a 10 minute zero can be used to look at the 1 second precision, whereas longer zeros are required to look at longer averaging times. An example Allan deviation analysis of an hour long zero air measurement from a laboratory experiment is shown by the orange trace in Figure 2.25.

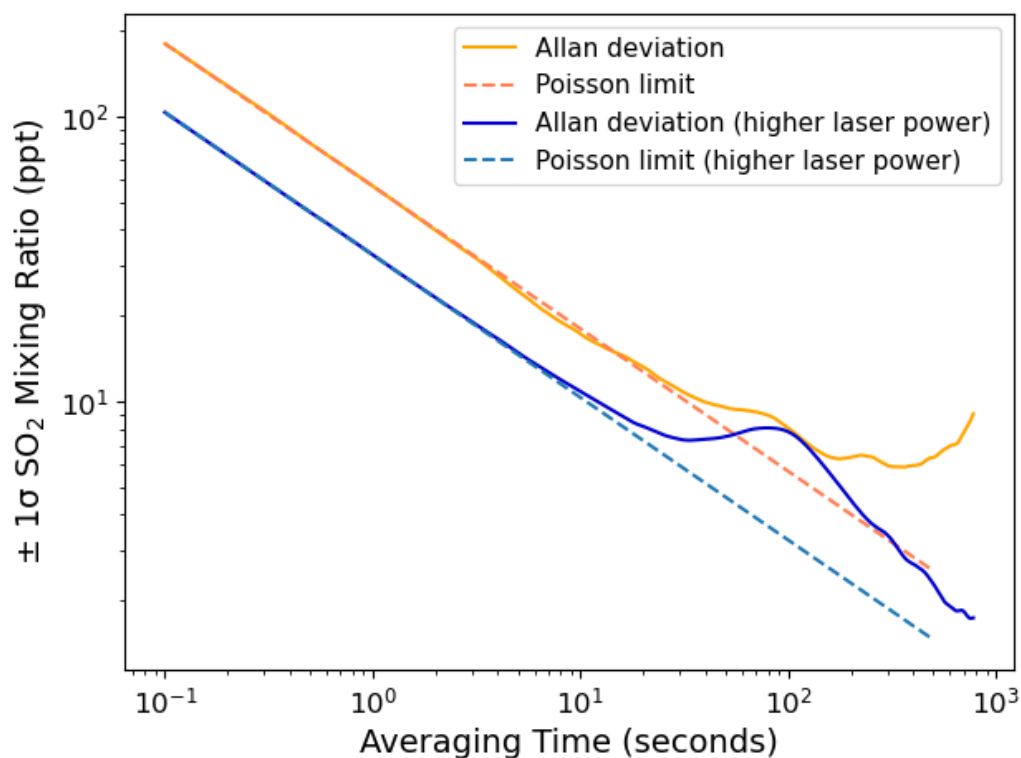


Figure 2.25: Instrument precision (Allan deviation) of a 1 h duration zero air measurement for different laser powers, as performed in the laboratory before the aircraft and ship-based campaigns (orange) and more recently with improved laser power (blue). Both traces are compared to the expected precision (Poisson limit).

The general shape of the Allan deviation traces in Figure 2.25 indicates that the noise in the SO_2 mixing ratio measurements diminishes, and thus the precision improves, with longer averaging times. This occurs because the Allan deviation examines the differences between averages of varying length data groups corresponding to the averaging time, and therefore there will be less variation between the averages of longer time-averaged data. Conversely, a random spike in noise will be more apparent in shorter time-averaged data. The measurement precision is initially consistent with that expected from Poisson statistics, which is the theoretical precision limit from solely random noise. However, at longer averaging times, deviations from this Poisson limit

are seen which suggests that either other sources of noise other than random noise (systematic noise such as temperature variations) are contributing to the data, or that the zero measurement was not long enough for a statistical analysis at these longer averaging times. The minimum point in this Allan deviation plot before it deviates determines the longest averaging time that is possible for the benefits of better precision, which is ~ 200 seconds for the orange trace in Figure 2.25.

The instrument precision is again dependent on many instrumental factors, including laser power, background counts, and sensitivity of the system. At the time of this work, difficulties were being faced with low fifth harmonic power of $\sim 50 \mu\text{W}$, compared to Rollins et al., 2016 of 2 - 4 mW, and hence we achieve an order of magnitude worse precision (1σ) of 20 ppt at an averaging time of 10 seconds. As described in subsection 2.3.1, increases in laser power have been achieved since this work and hence a demonstration of the improvement to precision with higher laser powers is shown by the blue trace in Figure 2.25. Also, attempts have been made to drive down the background counts and enhance the signal counts. For example, the PMT modules have been completely light sealed so no external lights from the LIF box contribute to the background counts. The PT has also been secured at a slight angle rather than perfectly perpendicular to the laser beam to reduce background counts from laser reflections back into the LIF cells. Another potential improvement that is being investigated is the size of the baffle holes since there is evidence of clipping of the laser beam as it enters the cell and laser scattering from the exit baffles, which could be increasing the background counts.

The limit of detection (LoD) of an instrument is defined as three standard deviations (3σ) of the zero signal and hence can be calculated from the 1σ precision at a given averaging time. Therefore, the LoD from the zero measurement in Figure 2.25 is 60 ppt at 10 seconds.

2.5.4 Effect of pressure

To determine the effect of pressure on sensitivity, calibrations were performed at different pressures from 100 to 500 mbar. The experimental results are plotted in Figure 2.26, which shows that sensitivity increases with pressure. This is because at higher pressures, there exists a greater number of SO_2 molecules per unit volume, each with the potential of fluorescing if excited by laser light. Therefore, for a given laser power, we observe more fluorescence counts compared to at lower pressures. However, for aircraft measurements, it is necessary to compromise the instrument sensitivity due to the lower external pressures at high altitudes, as detailed in subsection 3.3.1.

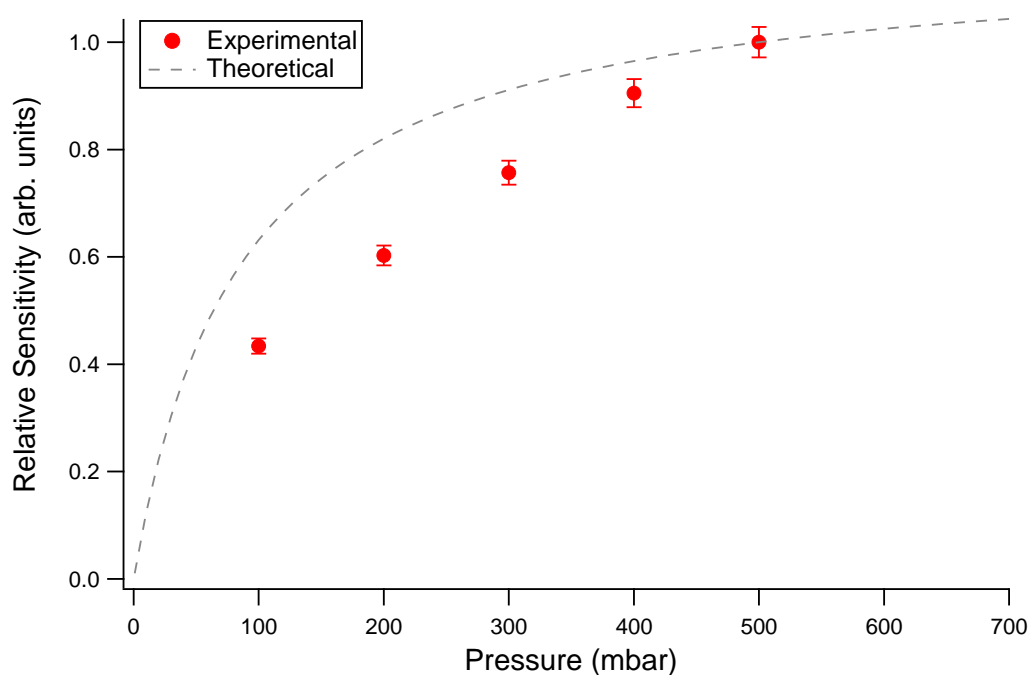


Figure 2.26: Relative instrument sensitivity, determined experimentally and theoretically, over a cell pressure range of 100 to 500 mbar.

As the pressure increases from 100 to 500 mbar, the number of SO_2 molecules per unit volume also increases by a factor of 5. However, the sensitivity only increases by approximately a factor of 2 due to the increasing importance

of quenching at higher pressures, which will eventually lead to a plateau in sensitivity, as shown by the theoretical plot.

2.5.5 Effect of temperature

Two main temperature effects exist for the LIF system. Firstly, the nonlinear optical crystals (NLO), which are housed in a separate container within the LIF box, are temperature sensitive since the phase matching, and thus nonlinear conversion efficiency are significantly impacted by temperature. This temperature effect is most obvious when the instrument is initially turned on and warms up. Therefore the crystal positions are not optimised until an equilibrium temperature is reached inside the NLO box (as determined by a thermistor). More recently a heater has been added to the NLO box, which is controlled via a feedback loop to maintain the temperature, typically at a higher temperature than ambient. This makes it more resistant to external temperature changes in the LIF box, and reduces the warm up time of the instrument.

The second main temperature effect is that of the seed laser diode temperature, which is susceptible to large changes in laser box temperature. Although the seed laser temperature is controlled via a PID loop from a control board (Meerstetter Engineering, TEC-1092) that drives seed laser's internal thermoelectric plate, this internal temperature is not perfectly representative of the lasing medium, which determines the laser wavelength. Therefore, changes in the laser box temperature can lead to an under- or over-correction of the true lasing medium temperature, causing the wavelength to shift. Again, a good example of this effect is seen as the laser box warms up. This increases the internal temperature of the seed laser to a greater degree than the true lasing temperature, which is over-corrected for by the PID loop meaning the SO₂ transition shifts to higher driving current values, as observed during a scan of laser wavelength. Because of this, we do

not typically set the dither algorithm (explained in section subsection 2.2.1) until the laser box temperature has equilibrated as it cannot keep up with this shifting transition and loses the peak. This effect was particularly prominent during the Arctic cruise campaign when the instrument was run for a prolonged period of time and was not continuously monitored (more details in subsection 4.2.2).

2.5.6 Response time

Response time of an instrument is typically defined as the time taken for the concentration of a quantity it is measuring to reach a certain percentage of its final or initial value after a step change in the quantity concentration. It is found by the sudden introduction of a concentration or sudden removal of a stable concentration from the system, and subsequent fitting of the resulting growth or decay of the concentration respectively via an exponential function. Therefore, response time is dependent on the sample flow rate, in addition to the volume of the cell or similar in which the concentration is measured. Additionally, it can be impacted by the system's measurement rate if the response time is similar to or faster than the measurement rate. It is important to make the distinction between response time and inlet or transit time, which is the time it takes for the sample to travel down the sample line and into the cell.

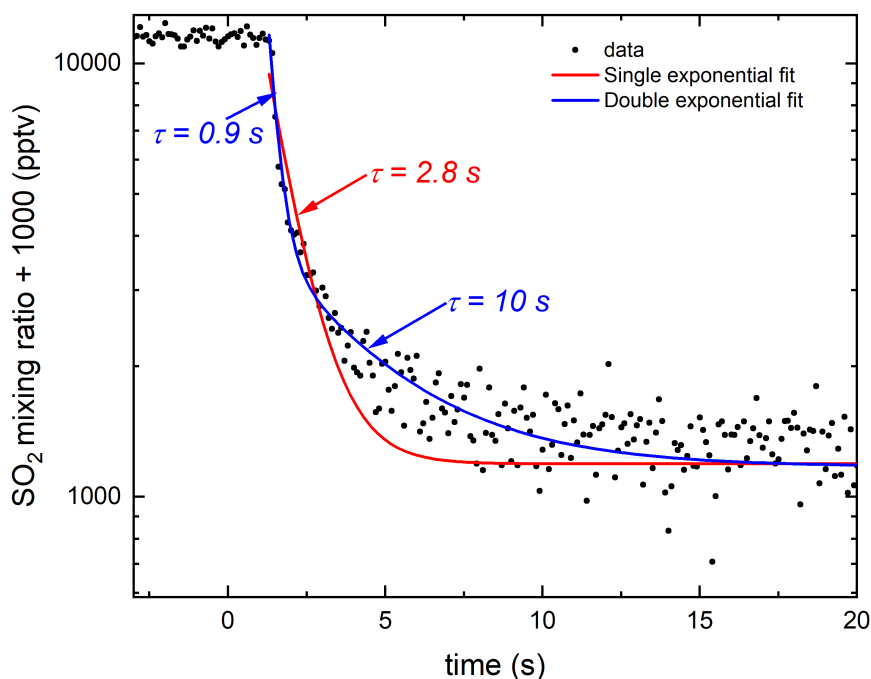


Figure 2.27: A comparison of exponential fitting methods to determine the 3 e-folding response time (τ) from a stable concentration to ambient air during a laboratory calibration. [Figure made by Sam Rogers.]

In this work, the response time is determined from a calibration in ambient air, since the suck back valve allows sudden removal of the calibration gas from the sample cell to achieve an ambient measurement quickly, as shown in Figure 2.27. Therefore, we look at the decay of the concentration and define the response time as the time taken for the initial concentration to reduce by a factor of e^3 (5 % remaining in the sample cell), known as the 3 e-folding time (e^{-3}). However, it was found that the concentration decay is not described well by a single exponential fit. A double exponential, given by an initial fast decay and a later slower decay, provides a better fit to the data (Figure 2.27), and is also independent of initial concentration. This means the majority of gas flushes the sample cell within 0.9 s, however, a

small amount of gas remains up to 10 s, likely due to dead volume within the sample cell. Therefore, the slower decay extends the 3 e-folding response time, however, since it is a small contribution to the overall concentration decay, the response time reported in this work is more akin to the initial fast 3 e-folding response time, averaged across multiple decays within different calibrations in ambient air. This flushing issue is unimportant in this work since SO₂ measurements are not reported at time resolutions shorter than a few seconds. Instead, data is averaged to 10 seconds for the aircraft campaign to match the greatest time resolution instrument whilst achieving fairly high temporal resolution, and 5 minutes for the Arctic cruise campaign to capture the low SO₂ background mixing ratios in the Arctic. However, future work aims to reduce this dead volume to achieve more consistent flushing and, in addition to increasing the flow rate, attain a sufficiently fast response time to enable true 10 Hz flux measurements.

For a calibration in zero air, except for the change from a calibration measurement to zero air, it is less obvious as to how to calculate the response time since changes between different concentrations involves some equilibrium time. Therefore, response time has solely been calculated from calibrations in ambient air in this work.

2.5.7 Uncertainty analysis

The observational uncertainty in SO₂ mixing ratios measured by the LIF is determined by the accuracy and precision of the instrument. Aside from the random errors in a calibration that determine the precision of the experiment, there are considerable uncertainties in the fixed parameters used to calculate the sensitivity which give rise to possible systematic errors (Faloona et al., 2004). The largest of these uncertainties comes from the SO₂ calibration standard, which is reported by the gas cylinder manufacturer (BOC gases) as $\pm 5\%$ (Δb). Other systematic errors are the uncertainties in the cal SO₂ MFC

($\pm(0.8\%$ of reading + 0.2% of full scale), Δa) and the cell flow meter ($\pm 3\%$, Δc). Since the SO_2 mixing ratios, $[\text{SO}_2]$ introduced into the sample cell during a calibration are calculated via Equation 2.7, the propagation of these uncertainties is found using Equation 2.8 to give the overall systematic error, defining the x-axis error of a calibration plot (Figure 2.23).

$$[\text{SO}_2] = \frac{a \times b}{c} \quad (2.7)$$

where a is the cal SO_2 MFC read value (0 - 5 sccm), b is the SO_2 cylinder concentration (usually 5 ppm, including during the two campaigns), and c is the cell flow read value (typically 2000 sccm).

$$\Delta[\text{SO}_2]^2 = \left(\frac{\partial\Delta[\text{SO}_2]}{\partial a} \times \Delta a\right)^2 + \left(\frac{\partial\Delta[\text{SO}_2]}{\partial b} \times \Delta b\right)^2 + \left(\frac{\partial\Delta[\text{SO}_2]}{\partial c} \times \Delta c\right)^2 \quad (2.8)$$

The random, y-axis error of a calibration is taken as the standard error of the LIF signal. However, as can be seen by the magnitude of the error bars in Figure 2.23, the random error is small in comparison to the systematic error. To combine the systematic and random errors, York regression is used, which incorporates errors in both axes (Wu et al., 2018), to fit the calibration plot, yielding an overall uncertainty in the instrument sensitivity, which is calculated as 5 % for the calibration in Figure 2.23 for a confidence interval of 2σ .

For a measurement without SO_2 , however, the uncertainty is not zero as the system has a random error associated with it. To capture this precision at the time of the observation (different to an Allan deviation analysis which looks at instrument stability), the standard error of a zero measurement is determined. This has been calculated as 3 ppt with 2σ confidence for the zero measurement used in the blue Allan deviation trace in Figure 2.25, at 10 seconds since precision varies with averaging time, unlike accuracy. The overall uncertainty in SO_2 mixing ratios is therefore $\pm(5\% + 3\text{ ppt})$ (at 10 seconds).

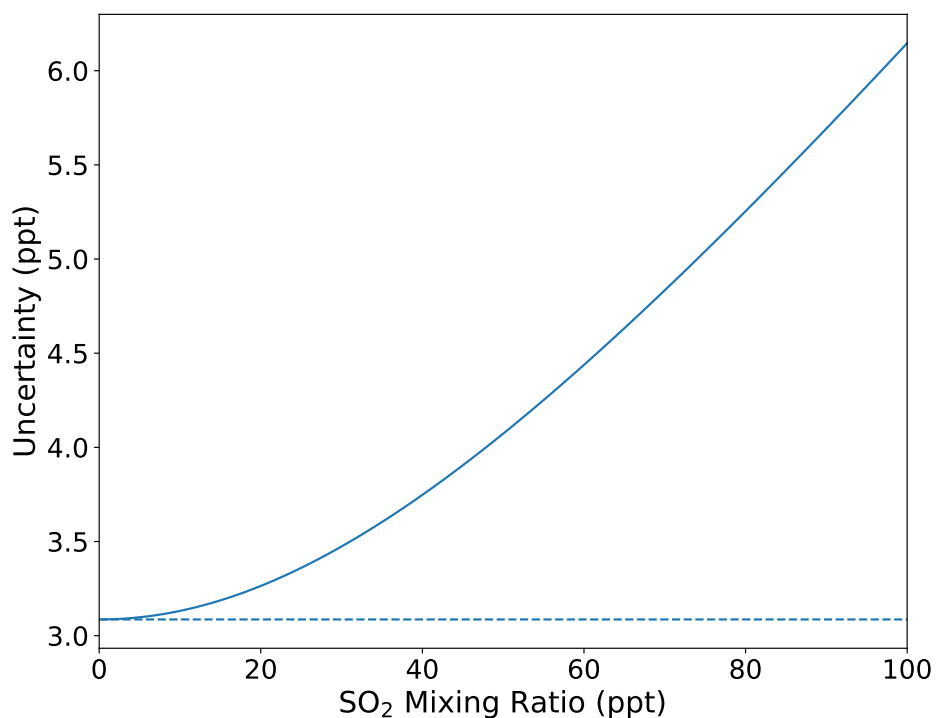


Figure 2.28: Uncertainty in SO₂ mixing ratios for the range 0 to 100 ppt.

The sensitivity- and zero-derived errors are combined in quadrature to give an overall uncertainty in ppt. The variation of this uncertainty with SO₂ mixing ratio is shown in Figure 2.28. Since the sensitivity-derived error is defined as a percent, the uncertainty increases with increasing SO₂ mixing ratio whereas the zero-derived error dominates at lower SO₂ mixing ratios.

2.6 Conclusions and future work

The University of York's LIF-SO₂ instrument for highly sensitive in situ measurements of SO₂ has been developed and tested, based on the system originally described by Rollins et al., 2016. It uses a custom-built fibre-amplified laser system to amplify infrared pulses at 1084.5 nm from a tunable narrow-linewidth laser. These amplified pulses are then passed through a series of nonlinear crystals to generate pulsed UV light at the fifth harmonic (216.9 nm) to excite SO₂. Predissociation and quenching (at non-zero pressures) compete with fluorescence of an SO₂ molecule, which is detected using a photon counting head. The laser wavelength is rapidly tuned online and offline a strong SO₂ transition ($\widetilde{C}(^1B_2) \leftarrow \widetilde{X}(^1A_1)$) peak, which is tracked using a reference cell at a constant SO₂ concentration. The laser power is measured at the end of the system by a phototube and is used to normalise the fluorescence counts. Also, the pulse pair resolution of the photon counting head detector (20 ns) limits the available counts to the repetition rate of the excitation laser, resulting in a need for a linearity correction. Therefore, the difference between the linearised and normalised fluorescence counts (termed LIF signal) at the online and offline wavelength positions is related to the SO₂ concentration within the sample cell via the sensitivity of the system, which is experimentally determined from a calibration.

High sensitivity and precision are required to achieve sufficient limits of detection (LoDs) to be able to accurately and precisely quantify trace levels of SO₂ in remote marine environments. Parameters that contribute to better sensitivity include a narrower laser linewidth, while higher laser power is a parameter that contributes to improved precision. However, a trade off exists for the LIF system between laser linewidth and average power, that is, if the laser linewidth is broader, the average power obtained is greater as a result of the higher efficiency of fifth harmonic generation for pulses that are temporally concentrated. For a sufficient linewidth to resolve the fine

spectral details of the SO₂ absorption spectrum (determined by interferometer measurements), we faced challenges with low fifth harmonic power of maximum $\sim 50 \mu\text{W}$. Therefore, attempts were made to improve the output power of the regenerative amplifier by using a higher power pump laser diode, along with other parameters to enhance precision, such as reducing the background counts. Despite the low laser power, we achieved a 3σ LoD of 60 ppt at 10 seconds, which is better than all commercial techniques for measuring SO₂. The LIF is also small in size, light in weight, vibrationally and temperature resistant and has low power requirements, making it suitable for deployment on a range of platforms and more favourable over a chemical ionisation mass spectrometer.

Since this work, improvements have been made to the fifth harmonic generation by replacing the KTP crystal with a temperature-controlled PPLN crystal, yielding a ~ 30 -fold increase in laser power. Additionally, the efficiency of the collection optics has also been improved by adding a lens (Edmund, 49-695) before the PMT module to focus the fluorescence into the detection head, giving a factor of ~ 4 better sensitivity. Therefore, these advancements have substantially improved the instrument's LoD (3σ) to 16 ppt at 10 seconds. Also, a more robust splicing method has been developed which has improved the stability of the laser system. Additionally, experiments have been undertaken to reduce the laser light scatter from the two baffles after the SO₂ detection in the sample cell, which contribute to the background counts and hence limit the precision. Also, the proposed effect of laser clipping has been investigated, which may be wavelength dependent due to the slightly different beam paths and hence affect the online counts to a different extent to the offline. It is thought that increasing the size of the baffle holes on entry to the sample cell (before SO₂ detection) may help.

I think that further advancements could be aimed at improving the precision and instrument stability. In terms of the precision, an additional

amplification stage between the regenerative and power loop could be added to achieve greater output fundamental power (which has already been done for the NO-LIF system at the University of York). To attain greater fifth harmonic power, it is not only worth increasing the fundamental power, but also the conversion efficiency of each nonlinear crystal, particularly the third and fifth harmonic conversion efficiencies. Therefore, ways to correct for the spatial walk-off of the light exiting a crystal (as a consequence of the anisotropy of the nonlinear crystal material) to achieve better spatial overlap within the next crystal could be investigated. One way this could be achieved is by using two LBO crystals of opposite orientation placed one after the other with a combined length of that currently used in the nonlinear optics system, for example. In terms of stability, it would be worth better controlling the temperature of the laser box to improve sensitivity stability and allow the instrument to be run for prolonged periods without the algorithm walking off the transition peak. This is especially important during campaign work or where the instrument is contained within a non-temperature controlled environment.

An analysis method for the instrument has also been developed in this chapter to convert the fluorescence counts at 100 Hz into a 10 Hz mixing ratio, which is further time averaged. The key steps include: linearising the fluorescence counts; normalising by laser power in mW; removing the first online point due to insufficient switching time; calculating the LIF signal from the 7 averaged online points and 2 averaged offline; and dividing the LIF signal by sensitivity. It was found that due to low laser power at the time of this work, even a sampled mixing ratio of 140 ppb was not near the upper limit for the linearisation correction. Further improvements to the analysis code need to be made to improve its automated applicability to alternative ways the instrument is run. Another notable improvement is to normalise the sample LIF signal to the reference LIF signal, since, provided there is a

well-controlled flow of constant SO₂ concentration into the reference cell, it can account for any variations in laser linewidth.

Chapter 3

Intercomparison of SO₂ Techniques

This chapter will be submitted to the journal Atmospheric Measurement Techniques (AMT), and so is presented here in paper-format. Therefore, the LIF technique description section (subsection 3.3.1) contains some figures that are repeated from the characterisation section (Section 2.5) of the previous chapter.

These aircraft measurements were taken as part of the Atmospheric Composition and Radiative forcing change due to the International Ship Emissions regulations (ACRUISE) project, consisting of three aircraft campaigns. The project was motivated by the International Maritime Organisation (IMO) regulation introduced in January 2020 (IMO2020), which required ships operating in international waters to reduce their sulfur emissions from a maximum of 3.5 % to 0.5 %. While the IMO regulations were primarily designed to improve air quality, particularly in coastal regions, they also have implications for climate. Therefore, this project aimed to investigate whether the IMO2020 regulation substantially reduced the climate cooling effect from ship pollution and to assess the compliance of ships to this regulation. Hence, the flights consisted of sampling individual ship plumes, shipping lanes and more remote marine environments. The ship positions and types were obtained from an automated information system for tracking

Chapter 3. Intercomparison of SO₂ Techniques

marine traffic (MarineTraffic; <https://www.marinetraffic.com/>).

To allow for a pre- and post-IMO2020 comparison, the ACRUISE-1 aircraft campaign was conducted in 2019, whereas ACRUISE-2 and ACRUISE-3 were undertaken in 2021 and 2022 respectively. During the ACRUISE-1 and ACRUISE-2 campaigns, the pulsed fluorescence analyser (described in subsection 3.3.2) was the primary instrument for measuring SO₂, as the LIF was still under development. The LIF instrument was part of the ACRUISE-3 campaign, which was useful for characterising the lower concentrations of SO₂ in ship plumes and over the oceans as a result of the IMO2020 regulation. It also allowed for a rigorous comparison to be made between the various techniques measuring SO₂ (including a chemical ionisation mass spectrometer) since a range of concentrations were measured, the results of which are presented below.

An intercomparison of aircraft sulfur dioxide measurements in remote and polluted marine environments

Loren G. Temple¹, Stuart Young¹, Thomas Bannan², Stephanie Batten³, Stéphane Bauguitte³, Hugh Coe², Stuart Lacy¹, James Lee¹, Emily Matthews², Dominika Pasternak¹, Andrew Rollins⁴, Jake Vallow¹, Mingxi Yang⁵, Pete M. Edwards¹

¹Wolfson Atmospheric Chemistry Laboratories, Department of Chemistry, University of York, York, YO10 5DD, UK

²Department of Earth and Environmental Sciences, University of Manchester, Manchester, M13 9PL, UK

³Facility for Airborne Atmospheric Measurements, Cranfield University, Cranfield, MK43 0AL, UK

⁴Chemical Sciences Laboratory, National Oceanic and Atmospheric Administration, Boulder, CO, USA

⁵Plymouth Marine Laboratory, Prospect Place, Plymouth, PL1 3DH, UK

3.1 Abstract

The University of York's laser-induced fluorescence (LIF) instrument for measuring sulfur dioxide (SO₂) was compared to a commercial pulsed fluorescence (PF) and iodide chemical ionisation mass spectrometer (I⁻CIMS) aboard the UK FAAM research aircraft in both remote and ship-polluted marine environments. Given their limits of detection (LoD, 3 σ) during the campaign of 0.07, 0.4 and 2 ppb at 10 seconds for the LIF, PF and I⁻CIMS respectively, the percentage of data below their LoDs across these three flights were 9, 91 and 98 % respectively. Therefore, a comparison of instruments could only be made in polluted environments. The LIF, PF and I⁻CIMS agreed well, once an interference affecting the sensitivity of the I⁻CIMS was taken into account. A comparison of response time was also made, for which

the I-CIMS and LIF proved much faster than the PF with 3-folding times of 0.6, 2 and 17 seconds respectively. This work demonstrates the importance of sensitive instrumentation like the LIF for quantifying low concentrations of SO₂, such as over remote marine environments, at the time resolutions required for a fast moving platform. This is particularly relevant now as a result of stringent sulfur emission regulations from shipping, and likely more so in the future as SO₂ concentrations continue to decline.

3.2 Introduction

Sulfur dioxide (SO₂) plays a pivotal role in the chemistry of the troposphere, and has been long recognised as an anthropogenic air pollutant (Firket, 1936) and contributor to acid rain (Gorham, 1958), leading to a number of legislations limiting its emission. Since the 1970's, global anthropogenic SO₂ emissions have been decreasing (Smith et al., 2011) and are now below many countries' emission commitment limits (Environment et al., 2024). However, even at present day levels, SO₂ from both anthropogenic and biogenic sources still plays an important role in the Earth's radiative budget (Capaldo et al., 1999; Myhre et al., 2013). In the atmosphere, SO₂ is oxidised by gas- and aqueous-phase chemistry to sulfate aerosols, which contribute to the formation of cloud condensation nuclei (Merikanto et al., 2009; Faloon, 2009). Both the direct radiative forcing from these aerosols, and the indirect forcing from aerosol-cloud interactions result in a net cooling effect on the planet (Penner et al., 2001). Understanding the extent to which aerosol-cloud interactions are masking greenhouse gas-induced warming remains the largest source of uncertainty in quantifying present day anthropogenic radiative forcing (Forster et al., 2021). In situ measurements are necessary to reduce this uncertainty and to validate climate model estimations of radiative forcing. Therefore, it is of interest to accurately and precisely quantify the concentration of SO₂ in the background atmosphere if we are to predict the

effects of changing emission rates on the climate.

SO₂ emissions from the global shipping sector have been reducing over recent years as a result of regulations introduced by the International Maritime Organisation (IMO), limiting the sulfur content of ship's fuel. These measures were implemented in response to air quality concerns in coastal regions, where aerosols from ship emissions are estimated to cause 400,000 premature deaths and ~ 14 million childhood asthma cases annually (Sofiev et al., 2018). The most recent regulation in January 2020, hereafter referred to as IMO2020, enforced a reduction of sulfur fuel content from 3.5 to 0.5 % by mass at the point of exhaust emission for ships in international waters. The global climate consequence of this regulation has been assessed by a recent surge of radiative forcing estimates from 0.02 to 0.2 W m⁻² (Bilsback et al., 2020; Diamond, 2023; Gettelman et al., 2024; Jin et al., 2018; Jordan et al., 2024; Quaglia et al., n.d.; Skeie et al., n.d.; Sofiev et al., 2018; Yoshioka et al., n.d.; Yuan et al., 2022; Yuan et al., 2024), made using a range of modelling methods and assumptions. Yoshioka et al., n.d. predicted a corresponding global mean warming of 0.04 K averaged over 2020 - 2049, making it more difficult to limit warming to 1.5 °C, in line with the Paris Agreement, over the next few decades. Nevertheless, these regulations have resulted in significant reductions in atmospheric SO₂ concentrations over the ocean, and thus increased the relative importance of biogenic precursor emissions such as dimethyl sulfide (Yang et al., 2016).

Current model estimates of SO₂ in remote marine environments range from 0 to 150 pptv (Bian et al., 2024). In order to test our understanding of SO₂ production and loss in these remote marine environments and over the range of altitudes where sulfate aerosol production is important, airborne sampling is required. Unfortunately, typical commercial instruments currently used for the detection of SO₂ lack the sensitivity to perform these measurements at the time resolutions required for a fast moving platform.

Chapter 3. Intercomparison of SO₂ Techniques

Aircraft studies using the pulsed fluorescence (PF) technique to measure SO₂ over the ocean are dominated by measurements of high SO₂ concentrations in ship plumes, mainly for assessing compliance to IMO regulations (Beecken et al., 2014; Lack et al., 2011; Yu et al., 2020). The only recent PF aircraft measurements of remote marine SO₂ were conducted by Zanatta et al., 2020, who struggled to quantify the low SO₂ concentrations seen at high altitudes. Other remote marine SO₂ measurements via PF were performed at a stationary site, hence making use of long-term averaging to achieve a detection limit of 25 pptv at 5 minutes in order to quantify the background levels as low as 50 pptv (Yang et al., 2016). However, these PF studies were both conducted pre-IMO2020 regulation. Alternative aircraft techniques used to measure SO₂ include the remote sensing technique of differential optical absorption spectroscopy (DOAS), which has again been reported for measurements of ship plumes (Berg et al., 2012; Cheng et al., 2019; Seyler et al., 2017). The most recent measurements (post-IMO2020) using this technique were made by Mahajan et al., 2024 during a stationary site campaign to measure ship plumes, however, it was noted that SO₂ concentrations were below their detection limit on a particular day due to sampling of clean air masses. Therefore, more specialised instruments with greater sensitivities are required for measurements of further declining SO₂ concentrations.

Chemical ionisation mass spectrometry (CIMS) measurements of SO₂ have been conducted on airborne platforms using a range of negative ion chemistries (Lee et al., 2018), with the best reported sensitivity coming from the use of a CO₃⁻ ion by Thornton et al., 2002, Speidel et al., 2007 and Fiedler et al., 2009, achieving 3 σ detection limits of \sim 1 pptv, 22 pptv and 30 pptv respectively at 1 s. More recently, an instrument that uses the technique of laser-induced fluorescence (LIF) to measure SO₂ has been developed by Rollins et al., 2016 and its performance on an aircraft has since been demonstrated on multiple field campaigns (Rickly et al., 2021; Rickly et al., 2022; Rollins et al., 2016;

Rollins et al., 2017). This LIF instrument has been reported to attain a detection limit (3σ) of ~ 18 pptv at 1 s and can achieve a true 5 Hz measurement rate (Rollins et al., 2016). With comparably low detection limits to CIMS, LIF may be more favourable, especially for aircraft measurements of SO₂, due to its smaller size and weight, and ease of operation, and lack of known interferences, mainly that of water vapour (Rickly et al., 2021). In this work, we introduce the University of York’s custom-built LIF instrument, based on Rollins et al., 2016, for in situ trace measurements of SO₂, and compare airborne measurements with both an iodide CIMS (I⁻CIMS) and a commercial PF SO₂ analyser.

3.3 SO₂ Instrumentation

The third Atmospheric Composition and Radiative forcing change due to the International Ship Emissions regulations (ACRUISE-3) campaign took place on 29th April to 3rd May 2022 aboard the UK Facility for Airborne Atmospheric Measurements (FAAM) BAe-146 research aircraft (Yu et al., 2020). The campaign consisted of three 5-hour flights, spanning a range of altitudes between 0.07 and 3.2 km. The instrumentation available for measuring SO₂ during this campaign included the York LIF instrument, a PF SO₂ analyser, and an I⁻CIMS which are described herein. Both individual ship plumes on the order of one to tens of ppb of SO₂ (termed ‘polluted’) and more remote marine regions outside of shipping lanes on the order of tens to a few hundred ppt (termed ‘remote’) were sampled in international waters around Milford Haven, UK and the Bay of Biscay. Hence, these flights were ideal for comparing the three techniques as a wide range of concentrations were measured. In this work, the LoDs of the instruments are described to a 3σ confidence interval at 1 and 10 second averaging times and response time is defined as the time taken for 5 % of the initial concentration to remain, referred as the 3 e-folding response time (e^{-3}). A summary comparing these

statistical characterisations of the techniques as run during the ACRUISE-3 flights can be found in Table 3.1.

Technique	Organisation	LoD at 10 seconds σ , ppbv	3 e-folding response time (seconds)	Sampling rate (Hz)	Uncertainty in mixing ratios (2σ)
LIF	University of York	0.07 (0.22)	2	5	10 % + 6.5 pptv
PF	FAAM	0.4 (1.1)	17	1	18 %
I ⁻ CIMS	University of Manchester	2 (5)	0.6	4	212 %

Table 3.1: Comparison of the LIF, PF and I⁻CIMS techniques in terms of limit of detection (LoD), response time, sampling rate, and mixing ratio uncertainty as performed during the ACRUISE-3 campaign. The I⁻CIMS parameters are given for the in-flight calibration method (see subsection 3.4.1 for discussion on different calibration methods for I⁻CIMS).

3.3.1 Laser-induced fluorescence

The University of York’s laser-induced fluorescence (LIF) instrument is a custom-built system for the highly sensitive detection of SO₂, based on the system originally demonstrated by Rollins et al., 2016. The fifth harmonic (216.9 nm) of an in-house built pulsed tuneable fibre-amplified semiconductor diode laser system (1084.5 nm, 3 ns pulse duration, 200 kHz repetition rate) is used to selectively excite SO₂, and the subsequent fluorescence photons are detected using a photon counting head (Hamamatsu H10682-210). The laser wavelength is tuned on and off a strong SO₂ transition ($\tilde{C}(^1B_2) \leftarrow \tilde{X}(^1A_1)$) peak, which is tracked using a reference cell at a con-

Chapter 3. Intercomparison of SO₂ Techniques

stant SO₂ concentration. The difference between the number of fluorescence photons at these positions is directly proportional to the SO₂ concentration within the sample cell.

The York laser system differs from that described in Rickly et al., 2021 in that we use a semiconductor optical amplifier (SOA, Innolume) to pulse the continuous wave output of a distributed feedback seed laser diode (Innolume) at 200 kHz. The SOA is temperature controlled to 25 °C to ensure reproducible laser pulse generation. Other notable differences to Rollins et al., 2016 are that we use a proportional valve (Bürkert 2873) to maintain constant mass flow, and a pressure controller (Alicat PCH-100TORRA-D-MODTCPIP-A515) to maintain cell pressure.

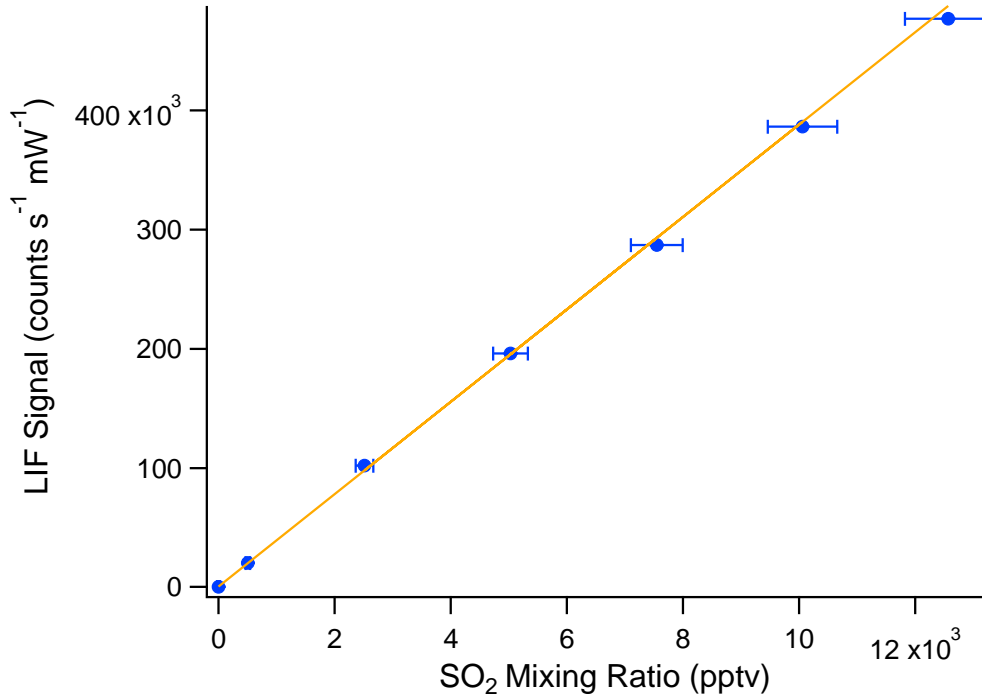


Figure 3.1: Example laboratory SO₂ calibration in zero air where the LIF signal is the difference between linearised and normalised on-line and off-line sample cell counts. The orange line shows a York regression fit to the seven data points, indicating a slope of 38.7 ± 2.1 cps mW⁻¹ ppt⁻¹, a y-intercept of 620 ± 1700 cps mW⁻¹ (both 2σ confidence), and a correlation coefficient of $R^2 = 1.00$.

The pulse pair resolution of the photon counting head detector (20 ns) limits the available counts to the repetition rate of the excitation laser, resulting in a need for a linearity correction (Rollins et al., 2016). Linearised counts are then normalised by laser power, which is measured by a phototube. The difference between the corrected fluorescence counts at the on-line and off-line laser wavelength positions is converted to SO₂ mixing ratio via the sensitivity of the system (Equation 3.1), which is derived from the slope of a calibration plot (Figure 3.1).

$$[\text{SO}_2] = \frac{F_{\text{online}} - F_{\text{offline}}}{S_{\text{SO}_2}} \quad (3.1)$$

Chapter 3. Intercomparison of SO₂ Techniques

where $[SO_2]$ is the SO₂ mixing ratio (pptv), F_{online} and $F_{offline}$ are the on-line and off-line linearised and normalised fluorescence counts (counts s⁻¹ mW⁻¹), and S_{SO_2} is the experimentally determined sensitivity of the system to SO₂ (counts s⁻¹ mW⁻¹ pptv⁻¹).

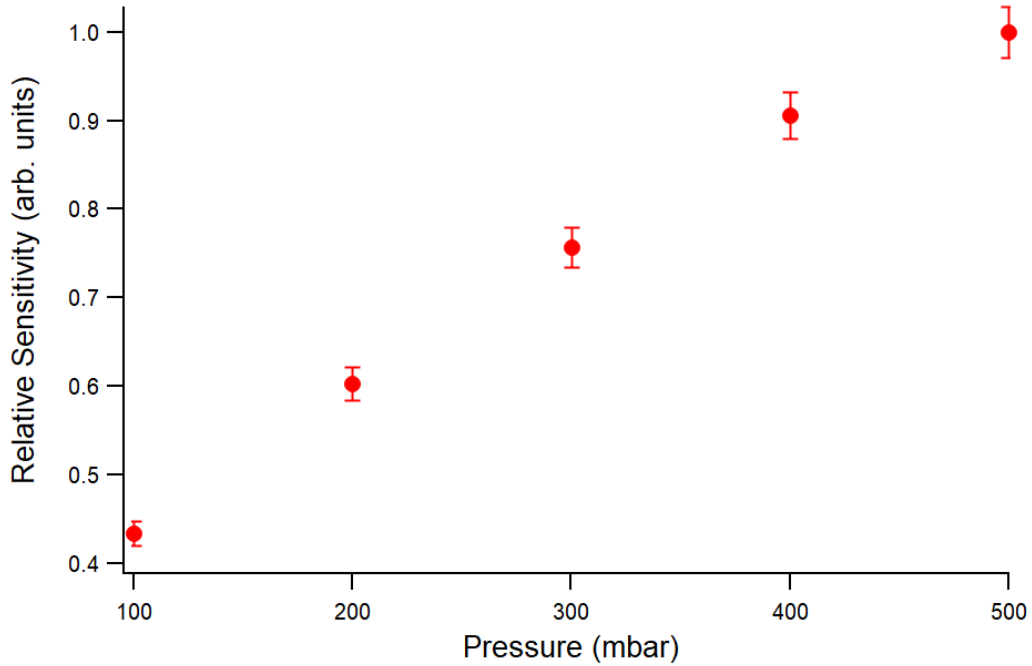


Figure 3.2: Relative instrument sensitivity over a cell pressure range of 100 to 500 mbar.

During the ACRUISE-3 flights, the York LIF instrument was operated at a flow rate of 2 SLPM, giving a 3 e-folding response time of ~ 2 seconds. Also, the use of a pressure-building ram inlet allowed both the sample and reference cells to be operated at 400 ± 2 mbar for the full altitude range (between 0.07 and 3.2 km) of the campaign to maximise instrument sensitivity (Figure 3.2).

Chapter 3. Intercomparison of SO₂ Techniques

Flight	Ambient Air			Zero Air		
	\bar{x} (counts s ⁻¹ mW ⁻¹ pptv ⁻¹)	σ (counts s ⁻¹ mW ⁻¹ pptv ⁻¹)	N	\bar{x} (counts s ⁻¹ mW ⁻¹ pptv ⁻¹)	σ (counts s ⁻¹ mW ⁻¹ pptv ⁻¹)	N
C285	33.8	0.7	9	34.0	1.7	10
C286	32.7	1.5	7	34.8	0.9	7
C287	34.8	0.8	14	35.7	1.3	4

Table 3.2: Summary of the calibrations performed in both ambient air and zero air during each flight, showing the mean sensitivity (\bar{x}), standard deviation of the sensitivities (σ) and the number of calibrations (N).

Multi-point calibrations were carried out using a 5 ppm SO₂ in N₂ standard (BOC, $\pm 5\%$) added to the end of the inlet across the expected concentration range (0.5 –12.5 ppb) approximately every 30 minutes to ensure data accuracy and to capture instrumental drift (see Section 3.6). An example of a multi-point calibration from a laboratory experiment is shown in Figure 3.1. To assess the possible quenching effect of excited SO₂ by water vapour, or increased wall losses when sampling humid air, calibrations in both stable ambient air and dry zero air were carried out, for which these effects proved negligible as shown in Table 3.2. For calibrations in zero air, it was necessary to overflow the inlet, however, subsequent analysis deemed this overflow insufficient for a true zero to be measured, likely a result of pressure build-up in the inlet line from the ram inlet** (see additional information after the paper). Due to the relatively stable ambient mixing ratios during the zero air calibrations and the similarities in sensitivities obtained from these calibrations compared to those in ambient air, we justify including the calibrations in zero air. As a result of inconsistencies in the laser linewidth, the sensitivities were seen to vary slightly during the course of a flight (Section 3.6), and hence a mean sensitivity has been calculated from both calibrations in

ambient and zero air, and applied on a flight-by-flight basis. Finally, the uncertainty in the SO₂ mixing ratios was calculated from the uncertainty in the instrument sensitivity via a York regression fit to a calibration plot (Wu et al., 2018, Figure 3.1). This gives a 2 σ uncertainty of $\sim 10\% + 6.5$ pptv across each flight.

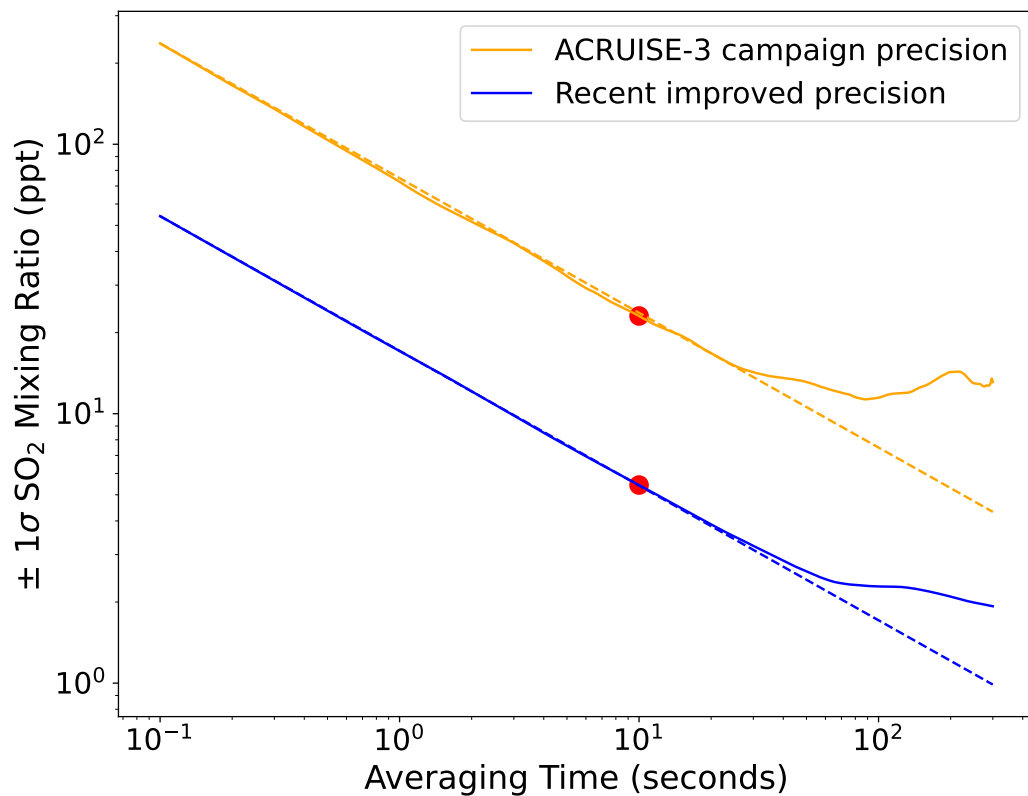


Figure 3.3: Instrument precision (Allan deviation) of a 10 min stable ambient measurement of mean mixing ratio 75 pptv during flight C287 (orange) and a 3.5 h zero air measurement, performed recently in the laboratory with improved laser power and sensitivity (blue). Both traces are compared to the expected precision (Poisson limit). The precision (1σ) at an averaging time of 10 s for each trace is marked by the red dots (23 pptv for the orange trace, 5.4 pptv for the blue).

The ACRUISE-3 aircraft campaign was the first deployment of the York LIF instrument in the field. At the time, we were facing difficulties with lower

fifth harmonic laser power (mean power of $\sim 27 \mu\text{W}$ during the campaign) compared to Rollins et al., 2016 ($\sim 1 \text{ mW}$), using a comparable optical setup. Therefore, during the ACRUISE-3 flights, the 3σ LoD was determined as 70 pptv at 10 seconds from a stable ambient measurement of mixing ratio close to the LoD (due to insufficient zero air overflow), as shown by the orange Allan deviation trace in Figure 3.3.

Since the ACRUISE-3 campaign, improvements have been made to the fifth harmonic generation by replacing the KTP crystal with a temperature-controlled PPLN crystal, yielding a ~ 30 -fold increase in laser power. In addition, the efficiency of the collection optics has also been improved by adding a lens (Edmund, #49-695) before the PMT module to focus the fluorescence into the detection head, giving a factor of ~ 4 better sensitivity. These advancements have substantially improved the instrument's precision, as shown by the blue Allan variance trace in Figure 3.3. The instrument response time has also been improved by increasing the flow rate and reducing the cell volume to achieve a true 10 Hz measurement rate for deriving SO₂ fluxes by the eddy covariance method.

3.3.2 Pulsed fluorescence

As part of the core instrumentation on board the FAAM aircraft, a commercial Thermo Fisher Scientific model TEi-43i TLE SO₂ analyser was used to measure SO₂ during the entire ACRUISE campaign. Based on the UV pulsed fluorescence (PF) method, it uses a broader SO₂ excitation wavelength range compared to LIF and hence is more susceptible to interfering species. To minimise SO₂ fluorescence quenching by water vapour, the PF is equipped with an external Nafion dryer (PermaPure Multi-strand, PD-50T-24MPR). A heated hydrocarbon kicker is used to remove interferences caused by volatile organic compounds which fluoresce at similar UV wavelengths to that of SO₂.

Chapter 3. Intercomparison of SO₂ Techniques

Modifications were made to the PF instrument in 2016 to improve its suitability for airborne measurements. The sample flow rate was increased from approximately 0.5 to 2 SLPM to improve the instrument response time by replacing the original TEi43i glass capillary and flow sensor with a mass flow controller (MFC3, Alicat Scientific, MCS-5SLPM-D-I-VITON). Also, a second hydrocarbon kicker was added to enhance sample flow conductance at this higher sample mass flow rate.

During the flights, the PF was run at a flow rate of 2 SLPM, giving an in-flight response time (3 e-folding) of 17 seconds. A comparable inlet to the LIF instrument was used. In-flight single point calibrations were carried out by overflowing the instrument inlet with a 2.5 SLPM mass flow controlled calibration gas mixture of 374 ppb SO₂ in Air (BOC, $\pm 6\%$). Multi-point calibrations were also performed on the ground post-ACRUISE-3 deployment as a check of the sensitivity. To account for baseline drift, frequent (~ 10 to 15-minute interval) zero measurements were performed by passing the air sample through an external zero air scrubber cartridge filled with activated charcoal. Mean zeros are then linearly interpolated to provide a drift-corrected baseline, which is subtracted from the raw fluorescence counts, before being scaled by the detector sensitivity.

The instrument LoD (3σ) during the ACRUISE-3 deployment has been determined as 400 ppt at 10 seconds. Finally, the overall uncertainty in SO₂ mixing ratios has been calculated as $\pm 18\%$ for a 2σ confidence interval.

3.3.3 Iodide chemical ionisation mass spectrometry

Matthews et al., 2023 have previously described in detail the University of Manchester (UoM) iodide ion-High Resolution-Time of Flight-Chemical Ionisation Mass Spectrometer (I⁻CIMS, Aerodyne Research, Inc) for use on the FAAM Research Aircraft. Briefly, iodide ions cluster with sample gases in the pressure-controlled ion-molecule reaction (IMR) region creating a

stable adduct. The flow is then sampled through a critical orifice into the first of the four differentially pumped chambers in the I⁻-CIMS, the short segmented quadrupole (SSQ), which is also independently pressure controlled. Quadrupole ion guides transmit the ions through these stages. The ions are then subsequently pulsed into the drift region of the I⁻-CIMS where the arrival time is detected with a pair of microchannel plate detectors with an average mass resolution of 4000 ($m/\Delta m$). The UoM I⁻-CIMS operates with an IMR pressure of 72 mbar for aircraft campaigns and instrument backgrounds are taken every minute for 6 seconds by overflowing the inlet with ultra-high purity (UHP) nitrogen. The CIMS instrument analysis software (ARI Tofware version 3.1.0, Stark et al., 2015) was utilized to obtain high resolution, 1 Hz, time series of the compounds presented here. Mass-to-charge calibration was performed for 5 known masses; I⁻, I⁻.H₂O, I⁻.HCOOH, I₂⁻, I₃⁻, covering a mass range of 127 to 381 m/z . The mass-to-charge calibration was fitted using a square-root equation and was accurate to within an average of 1 ppm.

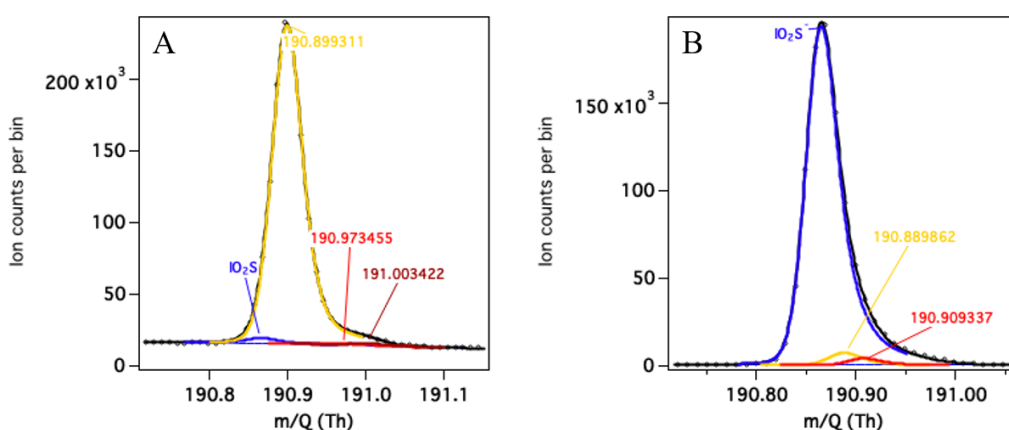


Figure 3.4: High resolution peak fitting at m/z 191 during ambient sampling in ACRUISE-3 (A) and calibration using a commercial standard (B).

I⁻-CIMS detects SO₂ as a cluster with iodide at m/z 190.866372. During the ACRUISE-3 campaign, the SO₂ peak is in close proximity to a signifi-

Chapter 3. Intercomparison of SO₂ Techniques

cantly larger interfering peak (Figure 3.4A). The UoM I⁻CIMS has sufficient resolving power to accurately separate the overlapping peaks (Figure 3.5). However, the peak shape and multipeak fitting presents challenges in accurately quantifying the small shouldering SO₂ peak at m/z 191. Diagnostic tools in the analysis software (ARI Tofware version 3.1.0, Stark et al., 2015) have been used to estimate the uncertainties in the signal intensity fitted for SO₂ due to the mass calibration, peak width and multipeak fitting. However, despite the very accurate mass calibrations there is still an associated uncertainty of approximately 30 % for the signal intensity from an offset of 1 ppm (Figure 3.6A). Similarly, small changes in the peak width at m/z 191 results in large uncertainties in the signal intensity of SO₂ (Figure 3.6B). Additional uncertainties arise from the multipeak fitting at m/z 191 and for SO₂ is 97 %. In comparison, the uncertainty in the signal fitted for SO₂ during the offline calibration (Figure 3.4B) is significantly reduced and is 3 % for the multipeak fitting. The combined uncertainty (i.e. the square root of the sum of the squares of the individual uncertainties) arising from the mass calibration and multipeak fitting is 101 % for the ambient measurements and is dominated by the multipeak fitting.

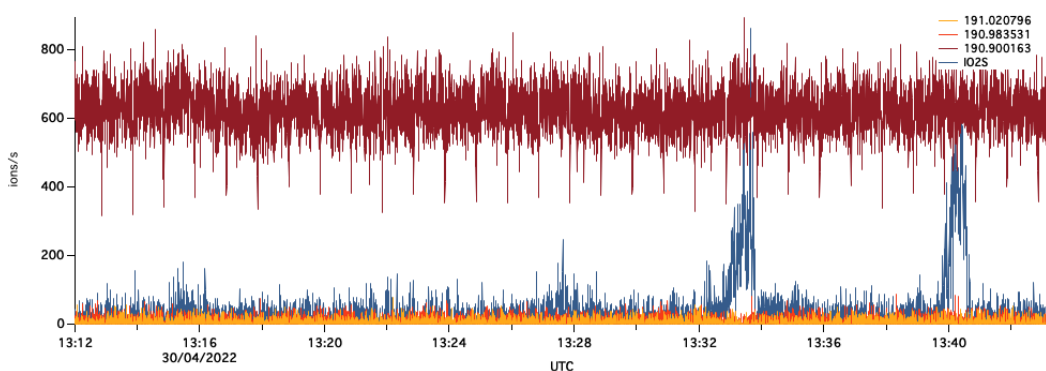


Figure 3.5: Time series of the high-resolution peak fitting at m/z 191 taken at 4 Hz.

Chapter 3. Intercomparison of SO₂ Techniques

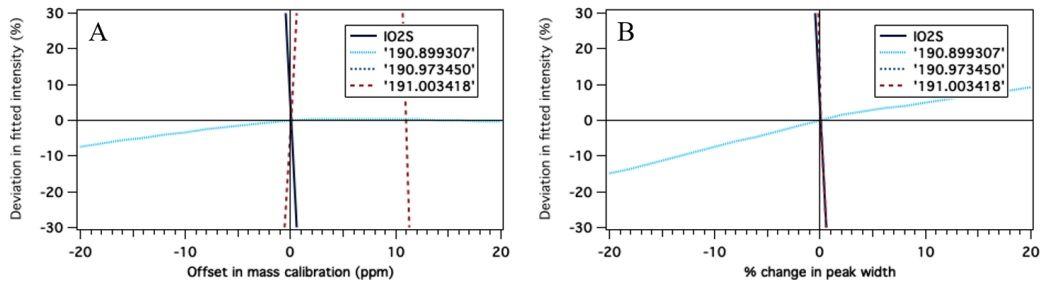


Figure 3.6: Changes in the intensity of the peaks identified at m/z 191 as a result of A) offset in the mass calibration and B) changes in the peak width.

The I⁻CIMS SO₂ measurements were calibrated offline on 26th April 2022, following installation on the aircraft and four days prior to the first ACRUISE-3 flight. Firstly, a stable flow of SO₂ was generated using a commercially sourced known concentration gas mixture (BOC, 1 ppm ± 5 % of SO₂ diluted in air) and a custom-built dynamic dilution system, which allows for a calibration gas to be diluted into a carrier gas, and in this instance, ultra-high purity (UHP) N₂ was used. The concentration of the outflow can be controlled by varying the flows of the calibrant and carrier gas, each of which are individually regulated using two MFCs (Alicat Scientific, MCS-5SLPM-D-I-VITON and MCS-500SCCM-D-I-VITON). In this case 1.2 SLM of the outflow was delivered to the I⁻CIMS by 1/4" PTFE tubing and the overflow exhausted at concentrations of 25, 50, 75, and 100 ppb. Additionally, the instrument's humidity dependence to the detection of SO₂ was calculated by actively adding water vapour into the IMR by passing UHP N₂ through deionised water. The presence of I.H₂O⁻ clusters, which are related to humidity of the air as it enters the instrument, can alter the ionisation efficiency of species detected by I⁻CIMS sensitivity and for SO₂ results in decreased sensitivity with increasing I.H₂O⁻ clusters (i.e. negative humidity dependence, Figure 3.7).

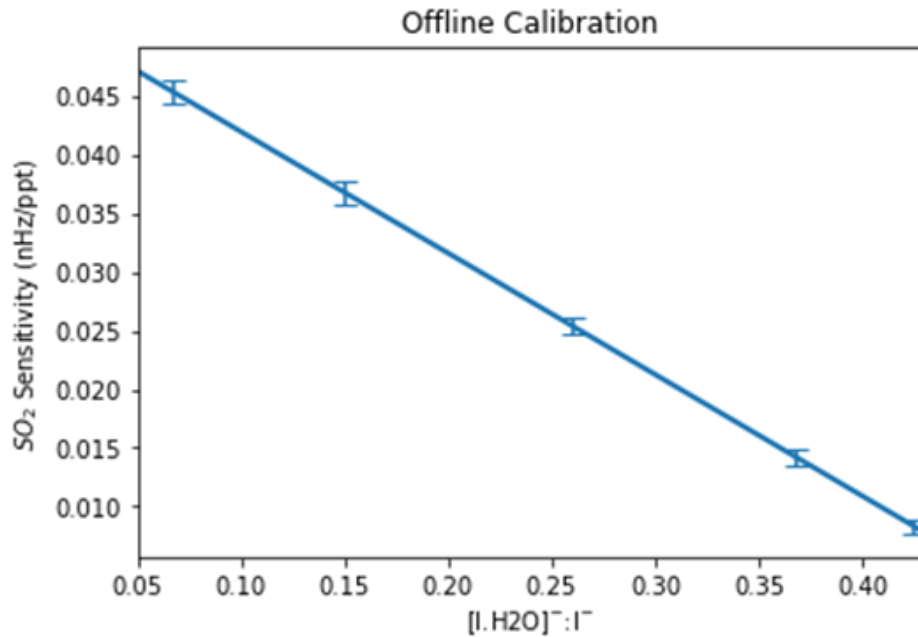


Figure 3.7: UoM I⁻CIMS humidity dependent sensitivity to SO₂ determined from an offline calibration using a commercial standard of SO₂. The error bars represent one standard deviation.

3.4 Results and Discussion

This work compares airborne SO₂ measurements from LIF, PF and I⁻CIMS based on their measured time series, instrument precision and response time during the ACRUISE-3 campaign. To construct a consistent dataset from all three instruments, each time series has been averaged to 10 seconds (by taking the mean of each 10 s block). This averaging time was chosen as a balance between the rapid changes observed due to the direct sampling of ship plumes and the response time of the PF system of 17 seconds. The comparison is split between polluted (high SO₂) and remote (low SO₂) regions due to the different analytical requirements for measurements in these distinct environments. A map showing all three flight tracks, coloured by the LIF SO₂ mixing ratios, is given in the SI (Figure 3.18).

3.4.1 Polluted environments

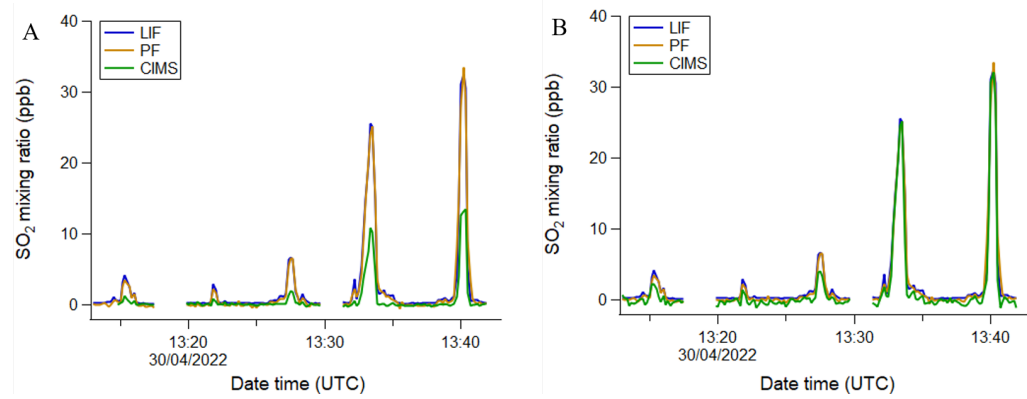


Figure 3.8: Time series of 10 s averaged, time matched data during flight C285, comparing the LIF, PF and I⁻CIMSSO₂ measurements for an offline pre-campaign I⁻CIMS sensitivity (A) and in-flight I⁻CIMS sensitivity (B).

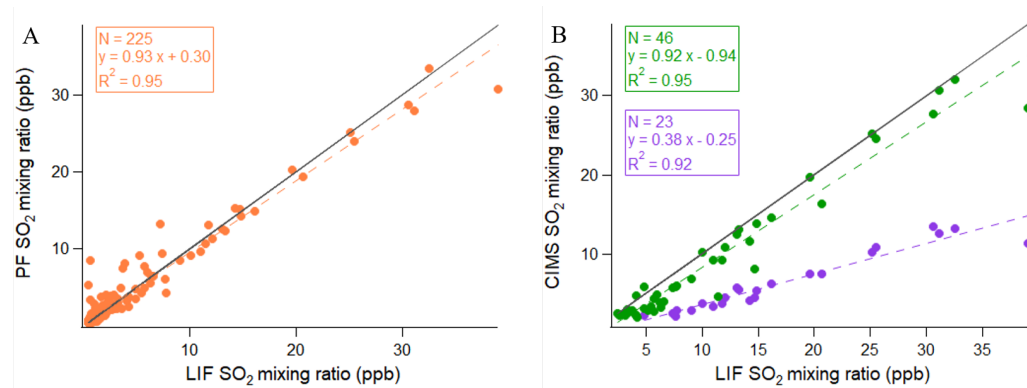


Figure 3.9: Correlation of the 10 s averaged, time matched data for all three ACRUISE-3 flights, excluding points which are below the instrument's LoD. (A) Correlation between the PF and LIF instruments. (B) Correlation between the I⁻CIMS and LIF instruments, for an offline pre-campaign I⁻CIMS sensitivity (purple) and in-flight I⁻CIMS sensitivity (green). The coloured dashed lines represent the linear fit and the solid black line represents the 1:1 ratio.

Measurements made in polluted SO₂ marine environments include those in individual ship plumes and within shipping lanes. An example of a

polluted time series comparison from flight C285 is shown in Figure 3.8A which contains a series of time-matched ship plume events. Comparing the magnitude of these peaks suggests that the LIF and PF agree well whereas the I⁻CIMS measures lower SO₂ mixing ratios for every plume event. These conclusions are consistent with the correlation plots containing data from all three ACRUISE-3 flights. Figure 3.9A shows the correlation between the LIF and PF from 400 pptv (the LoD of the PF at 10 s) to the greatest plume mixing ratio of ~ 40 ppb, and shows near-unity agreement (slope = 0.93) to within the combined uncertainty of the LIF and PF. However, the initial I⁻CIMS-LIF correlation (purple trace in Figure 3.9B, from the I⁻CIMS 10 s LoD of 2 ppb) displays a similar linear relationship between the two instruments but poor agreement as its fit is far from unity (slope = 0.38). For the offline pre-campaign calibration, the shape and multiplex fitting for the peak observed during the calibration compared with ambient measurements at m/z 191 also have considerable differences which may add significant error to this calibration (Figure 3.4). Therefore, an alternative method for calibrating the I⁻CIMS measurements of SO₂ is presented here by calculating an in-flight sensitivity using the concentrations reported by one of the dedicated SO₂ instruments. In this way, the uncertainties as a result of the multiplex fitting are better accounted for in the derived sensitivity. We used the concentrations reported by the LIF during periods where SO₂ exceeded 5 ppb and changes in the instrument's humidity did not exceed 10 %. Individual humidity thresholds were selected for each flight to capture the greatest concentration range. The LIF was chosen over the PF instrument due to its more similar time response to the I⁻CIMS. Figure 3.10A shows the linear response rate of the I⁻CIMS SO₂ signal as a function of SO₂ concentrations for the two flights which met the selection criteria. The difference in sensitivities between the two flights is expected due to the I⁻CIMS negative humidity dependence to the detection of SO₂. Using the sensitivity yielded from flight C285 to calculate, the expected sensitivity for

Chapter 3. Intercomparison of SO₂ Techniques

flight C287 is in agreement with the observed sensitivity to within 2 % and as such validates the humidity dependence. The resulting sensitivity from the in-flight intercomparison calibration method, combined with the offline determined humidity gradient, is shown in Figure 3.10B. The two calibration methods give sensitivities that differ by almost 2-fold. This discrepancy has been attributed to the large interfering peak (Figure 3.4A), and has assumed to be constant during each flight.

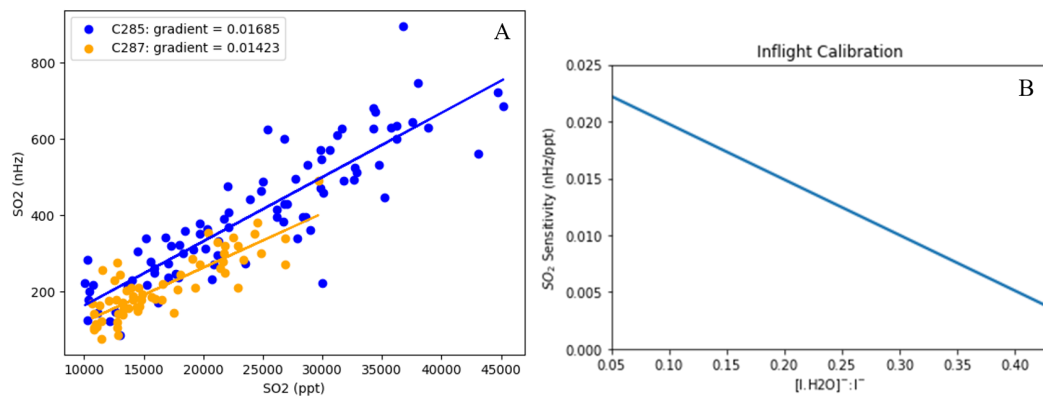


Figure 3.10: Response of I-CIMS SO₂ signal as a function of SO₂ concentration measured by LIF (A) UoM I-CIMS humidity dependent sensitivity to SO₂ determined from an in-flight intercomparison calibration with LIF (B).

Applying this in-flight sensitivity to the I-CIMS data results in improved agreement with the LIF, as demonstrated by the time series plot in Figure 3.8B and the green correlation trace in Figure 3.9B, which has a slope of 0.92. The I-CIMS concentrations presented hereafter are determined using the in-flight intercomparison method, though the results may not be transferable due to potential changes in instrument performance.

A comparison of response time can be made from the time series of a single ship plume peak in Figure 3.11, recorded at 5 Hz, 1 Hz and 4 Hz for the LIF, PF and I-CIMS respectively. To remove the lag time as a result of different inlet lengths, the peaks have been time-matched by the

increase in SO₂ mixing ratios upon intersecting a ship plume. Figure 3.11 shows the SO₂ mixing ratios recorded by the I⁻CIMS fall to out-of-plume levels the quickest and its time series displays the greatest structure. This is evident in the faster I⁻CIMS response time of 0.6 s (3 e-folding) compared to the LIF of 2 seconds and the PF of 17 seconds. The LIF signal shows similar structure to the I⁻CIMS data, but the slower gas flush rate means the features are smoothed and the LIF takes longer than the I⁻CIMS to return to background levels. Further improvements to the LIF system, detailed in subsection 3.3.1, have increased the LIF true measurement rate to 10 Hz. The comparatively slow response time of the PF instrument results in it being unable to resolve the plume structure, and shows a significant delay in returning to background levels.

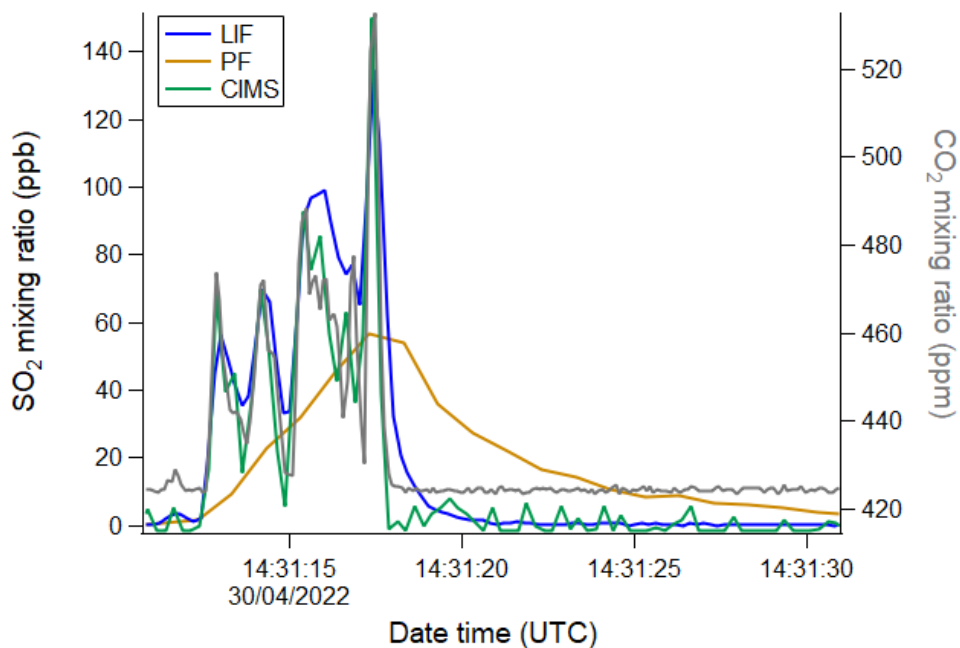


Figure 3.11: Time series comparing instrument response time, matched by the increasing SO₂ mixing ratio due to measurement of a ship plume during flight C285. The LIF data is presented at 5 Hz, the PF at 1 Hz, the I⁻CIMS at 4 Hz and the CO₂ data at 10 Hz.

Plume sampling can be used to quantify emissions ratios, and the ratio of

Chapter 3. Intercomparison of SO₂ Techniques

SO₂:CO₂ can be used to calculate ship sulfur fuel content for applications in compliance monitoring (Beecken et al., 2014; Berg et al., 2012; Kattner et al., 2015; Lack et al., 2011; Yu et al., 2020). Average emissions ratios can be derived via two methods for a ship plume event: a) the integration method where the area under the peak and above the baseline is calculated (Beecken et al., 2014; Kattner et al., 2015; Lack et al., 2011; Yang et al., 2016), and b) the regression method where the slope of a correlation plot is taken (Aliabadi et al., 2016). The regression method is a less popular approach, especially for in situ airborne sampling, since it relies on sufficient data points for a statistically valid regression analysis and a similar plume structure between the two species, as shown by the SO₂ I⁻CIMS and CO₂ trace in Figure 3.11. Hence, this requires fast response time instrumentation for aircraft measurements of plume transects as the plume duration can be extremely short. On the other hand, the integration method provides a response time-independent way of reliably analysing these short duration plume events.

This work makes use of the fast response time of the I⁻CIMS and the accuracy of the LIF to compare the integration and regression methods, which has not been done before for aircraft measurements. The interfering species for the I⁻CIMS measurements has assumed to be constant during each flight, however, variations in agreement to the LIF suggest this may not be the case. Therefore, the peak area of the I⁻CIMS has been matched to that of the LIF to retain the accuracy of the SO₂ measurements in addition to the plume structure. For the integration method, a trapezoidal approximation has been used to calculate the peak area from the baseline. For the plume in Figure 3.11, the SO₂:CO₂ emission ratio has been calculated as 2.07 ± 0.21 and 1.82 ± 0.52 ppb ppm⁻¹ for the integration and regression method respectively, which agree within errors. The same result has also been obtained through analysis of other ship plume events, as shown in Table 3.3.

Chapter 3. Intercomparison of SO₂ Techniques

Therefore, we conclude that both methods are a valid and reliable way of calculating emission ratios and the choice of method depends on the instrumentation available and ship plume durations.

Flight	Plume duration (seconds)	Number of data points	Integration (SO ₂ :CO ₂ , ppb ppm ⁻¹)	Regression (SO ₂ :CO ₂ , ppb ppm ⁻¹)	SFC (%)
C285	6	28	2.08 ± 0.05	1.80 ± 1.66	0.45 ± 0.42
C286	5	24	1.24 ± 0.06	1.07 ± 0.99	0.27 ± 0.25
C287	51	208	1.95 ± 0.03	1.98 ± 0.76	0.46 ± 0.18
C288	112	452	1.78 ± 0.03	1.70 ± 0.58	0.40 ± 0.14

Table 3.3: Comparison of integration and regression methods for calculating SO₂:CO₂ emission ratios of four ship plumes during different flights. The SO₂ data has been obtained from the fast I⁻CIMS, and its peak area has been scaled to match the accuracy of the LIF. Therefore, the uncertainties associated with the emission ratios calculated via the integration method are based on the LIF data. All emission ratio uncertainties have been given to a 2 σ confidence interval. The corresponding sulfur fuel content (SFC) has been calculated via Equation 3.2 using the mean of the emission ratios obtained from the two methods.

A check of the compliance of the sampled ships to the IMO2020 regulation (0.5 % sulfur fuel content in international waters) can be made through calculation of the sulfur fuel content (SFC) from the emission ratios. Assuming that 87 % of ship fuel by mass is carbon, the SFC mass percent is related to the emission ratio via the following equation (Kattner et al., 2015).

$$SFC(\%) = \frac{SO_2(ppb)}{CO_2(ppm)} \times 0.232(\%) \quad (3.2)$$

where the SO₂:CO₂ ratio is the emission ratio, calculated above, and 0.232 is the mass conversion factor for fuel content. Equation 3.2 also assumes

that all sulfur is emitted as SO₂ and all carbon as CO₂. The latter of these assumptions is a better estimate since little to no CO was measured during the ACRUISE-3 campaign, suggesting a complete combustion pathway. However, it is known that not all sulfur is released as SO₂ – some is directly emitted as sulfate, SO₄²⁻. The amount of SO₄²⁻ released has been shown to correlate with the SFC (Yu et al., 2020) and it also increases with plume aging. Since the calculation of plume age is beyond the scope of this paper, the SFC is not corrected for sulfate (which is estimated as 6 % for a maximum plume age of 15 minutes (Yu et al., 2020), and this 6 % discrepancy has been included in the uncertainty. Therefore, using the mean of the emission ratios calculated via the two methods, the corresponding SFCs of the sampled ships are given in Table 3.3, which shows they are all compliant to the IMO2020 regulation.

3.4.2 Remote environments

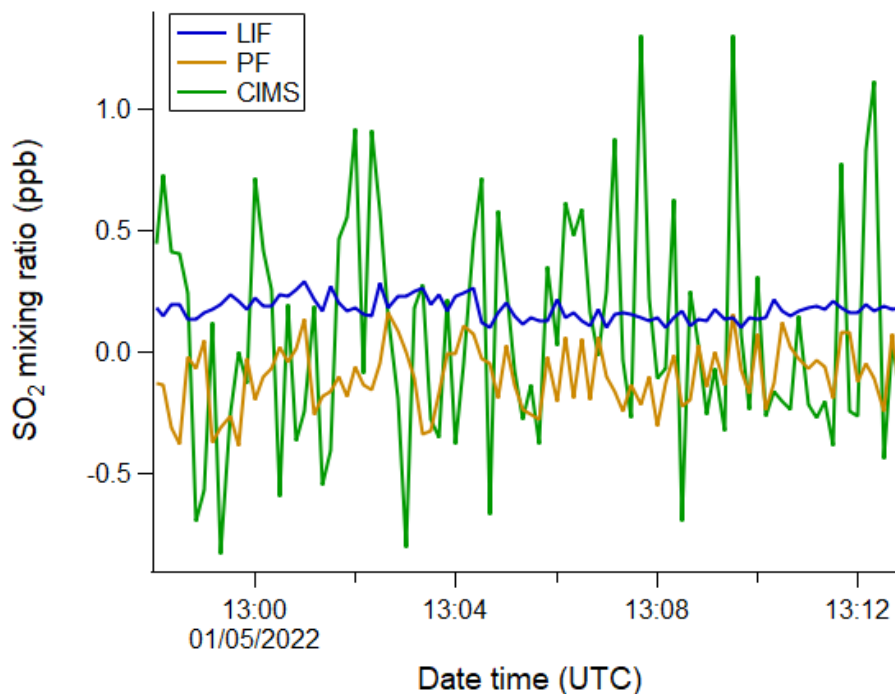


Figure 3.12: Time series of 10 s averaged, time matched data during flight C286, comparing the LIF, PF and I-CIMS SO₂ measurements.

Chapter 3. Intercomparison of SO₂ Techniques

A comparison of precision and noise distribution can be made from low SO₂ mixing ratios measured in remote marine environments, outside of shipping lanes. Figure 3.12 shows an example time series comparison of remote SO₂ measurements from flight C286. Two observations can be made from this time series comparison which are more evident in the corresponding histogram plot in Figure 3.13: (1) the LIF is reading non-zero, unlike the PF and I⁻CIMS and (2) the distribution of the LIF is much narrower than the PF and I⁻CIMS. For exploring statement (1), it is necessary to consider the 3σ LoDs of the three instruments during the flight at the same averaging time as the time series and each other (10 s). These are 70, 400, and 2000 pptv for the LIF, PF and I⁻CIMS respectively at 10 s. Since the mean ambient mixing ratio recorded by the LIF of 176 pptv is greater than its LoD, the LIF is sensitive enough to capture these low mixing ratios. This is not the case for the PF and I⁻CIMS and therefore their observed distributions are indistinguishable from a measurement of zero.

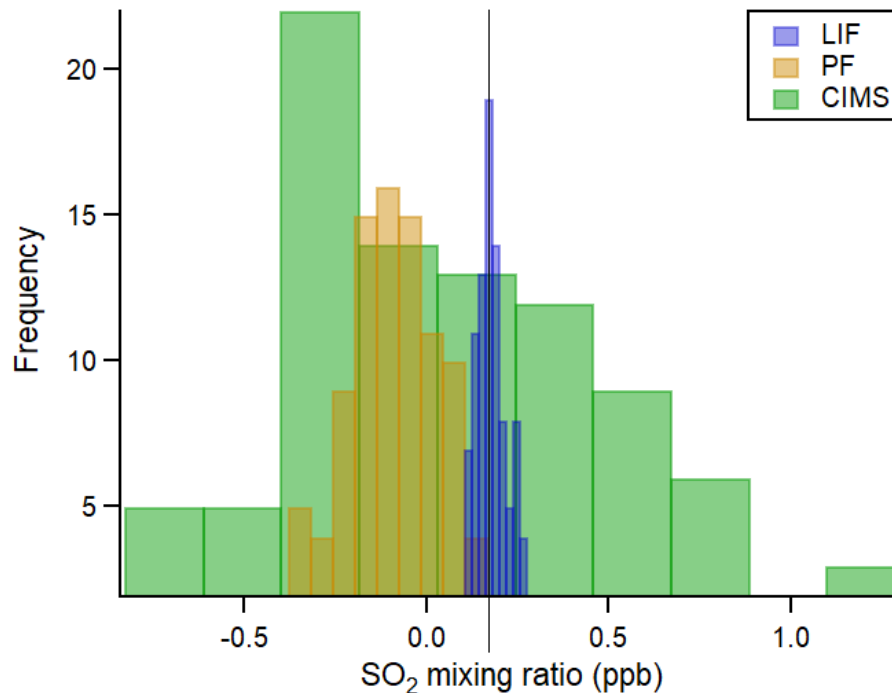


Figure 3.13: Histogram of data presented in Figure 3.12, comparing the noise distributions of the LIF, PF and I⁻CIMS SO₂ measurements for a mixing ratio of 176 ppt, as marked by the black solid line.

The 15-minute time period in Figure 3.12 has been chosen as the ambient measurements are relatively stable and hence useful for comparing instrumental noise in flight via the width of the distributions in Figure 3.13. We have assumed a well-mixed atmosphere and that the LIF distribution is determined predominantly by instrumental noise (evidenced by the autocorrelation plot in Section 3.6). Therefore, as ambient variability is present but minimal, the LIF distribution is an upper limit assessment of its precision. We conclude that the noise distribution for the LIF is significantly narrower than the PF and I⁻CIMS, making it a powerful tool for capturing SO₂ mixing ratios in remote marine environments at a range of altitudes. Figure 3.19 in the SI shows an altitude plot of LIF SO₂ mixing ratios averaged across each 100 m bin width for all three ACRUISE-3 flights. This data is compared to SO₂ mixing ratios measured by the LIF during the seventh aircraft campaign

of The North Atlantic Climate System Integrated Study (ACSIS-7), which sampled clean remote marine air over the North Atlantic during 5th – 9th May 2022.

The distribution of LIF mixing ratios in Figure 3.13 appears to exhibit non-Gaussian behaviours due to its asymmetric shape around the mean (176 pptv). This has been confirmed via a Kolmogorov-Smirnov statistical test, which suggests the data is likely not normally distributed. The observed non-normality may result from the characteristics of Poisson distribution inherent to the single photon counting nature of the PMT module (which only takes positive values, see Section 2.4). However, since the absorption cross section of SO₂ and hence fluorescence is non-zero at the offline position, the distribution of fluorescence counts is likely to be more Gaussian-like even at low mixing ratios, as shown in Figure 2.24. Since a lower cell pressure was used during the flights, this Poisson distribution may explain the apparent cutoff observed at lower mixing ratios in Figure 3.13. However, a more likely explanation is the presence of non-Gaussian variability in the ambient SO₂ mixing ratios being sampled, especially since the PF and CIMS distributions also exhibit non-Gaussian behaviours. Over 15 minutes, the aircraft will have travelled approximately 100 km (for a speed of 110 m s⁻¹) and hence the SO₂ concentration may not be uniformly mixed over that space/time.

3.5 Conclusions

Three SO₂ instruments were involved in an intercomparison experiment on board the UK FAAM research aircraft: LIF, PF and I⁻CIMS. A range of SO₂ concentrations were measured, from < 70 ppt in remote marine environments up to 40 ppb in ship-polluted environments (at 10 seconds averaging), west of the English Channel over international waters. In polluted environments, SO₂ measurements made by the LIF and PF agreed within the

Chapter 3. Intercomparison of SO₂ Techniques

errors of the instruments. However, the LIF and I⁻CIMS measurements were found to disagree by a constant factor, which has been attributed to challenges in accurately quantifying the I⁻CIMS SO₂ peak due to a large neighbouring interference peak. A 50 % reduction in the sensitivity of the I⁻CIMS instrument has been estimated to better account for this interference, which is unique to the measurements made during ACRUISE-3. However, similar challenges may arise for other I⁻CIMS measurements of SO₂. This work has also allowed a comparison of SO₂:CO₂ emission ratio calculation methods (integration versus regression), and both methods have proven to be a valid approach. In remote environments, the ambient mixing ratios are below the LoDs of the PF and I⁻CIMS instruments, and therefore the LIF is the only instrument able to detect SO₂ mixing ratios between 70 and 400 ppt. From this intercomparison, we conclude that for measurements of low SO₂ concentrations requiring high sensitivity and low noise, such as those in remote marine environments, LIF is a powerful technique. While I⁻CIMS has demonstrated a response time approximately three times faster than LIF, making it more suitable for aircraft measurements, its sensitivity to SO₂ is limited by an interference. Ongoing improvements to the LIF are increasing its flush rate towards flux-scale response times, therefore allowing both fast and accurate measurements of SO₂. All three techniques are valuable for improving our understanding of atmospheric SO₂, but application dependent. The LIF technique is becoming more crucial both today and in the future, as more stringent emission reductions, such as the IMO2020 regulation, lead to cleaner SO₂ environments.

3.6 Supplementary Information

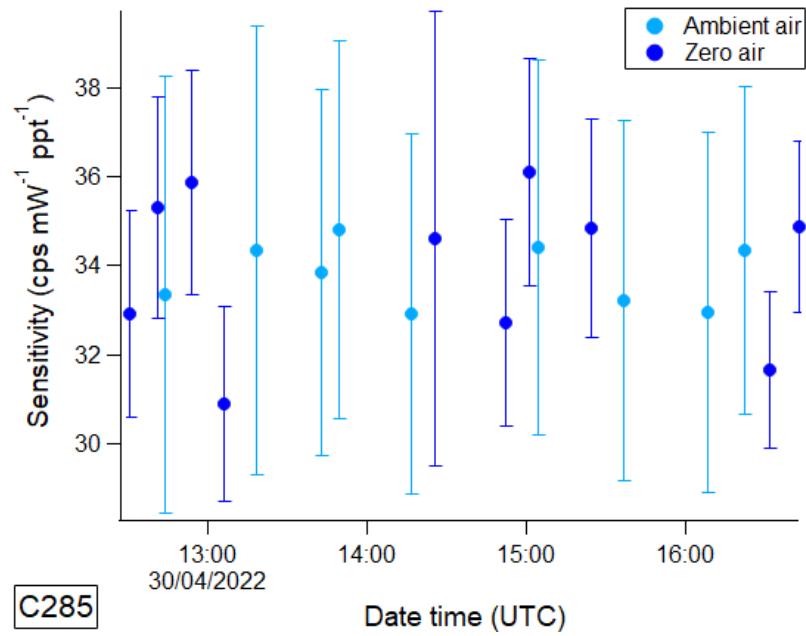


Figure 3.14: LIF sensitivity variation over time during flight C285 for calibrations in ambient air and zero air. Error bars are given to a 2 σ confidence interval.

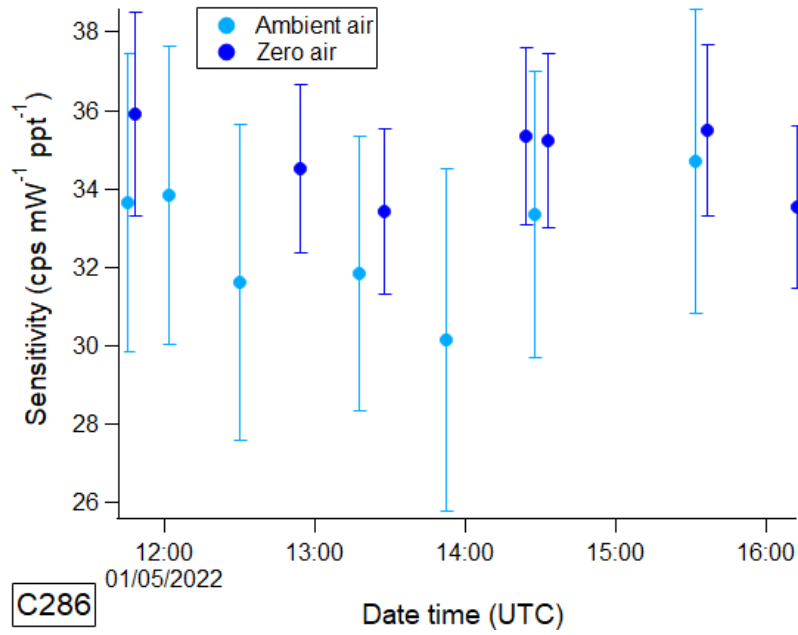


Figure 3.15: LIF sensitivity variation over time during flight C286 for calibrations in ambient air and zero air. Error bars are given to a 2σ confidence interval.

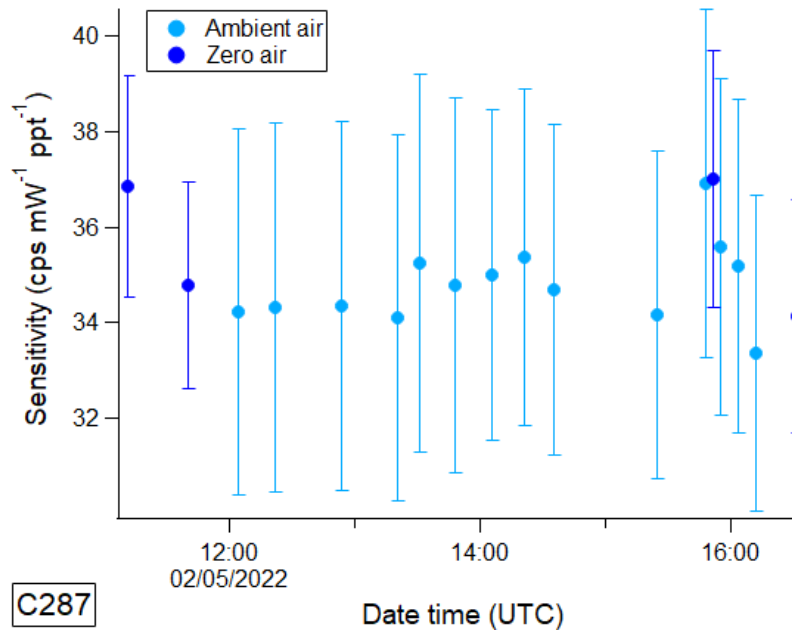


Figure 3.16: LIF sensitivity variation over time during flight C287 for calibrations in ambient air and zero air. Error bars are given to a 2σ confidence interval.

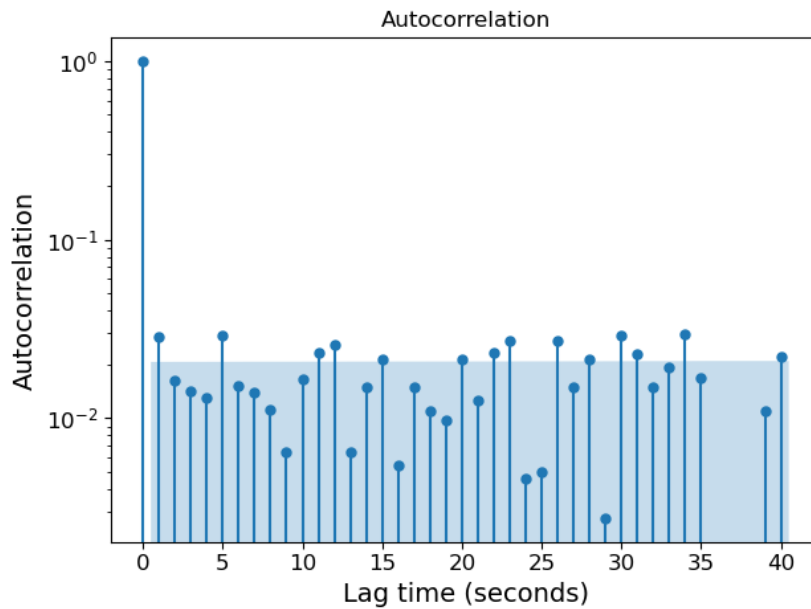


Figure 3.17: Autocorrelation plot of the LIF data presented in Figure 3.12 and Figure 3.13 at 10 Hz.



Figure 3.18: Colour map of 10 s LIF SO₂ mixing ratios along all three ACRUISE-3 flight tracks.

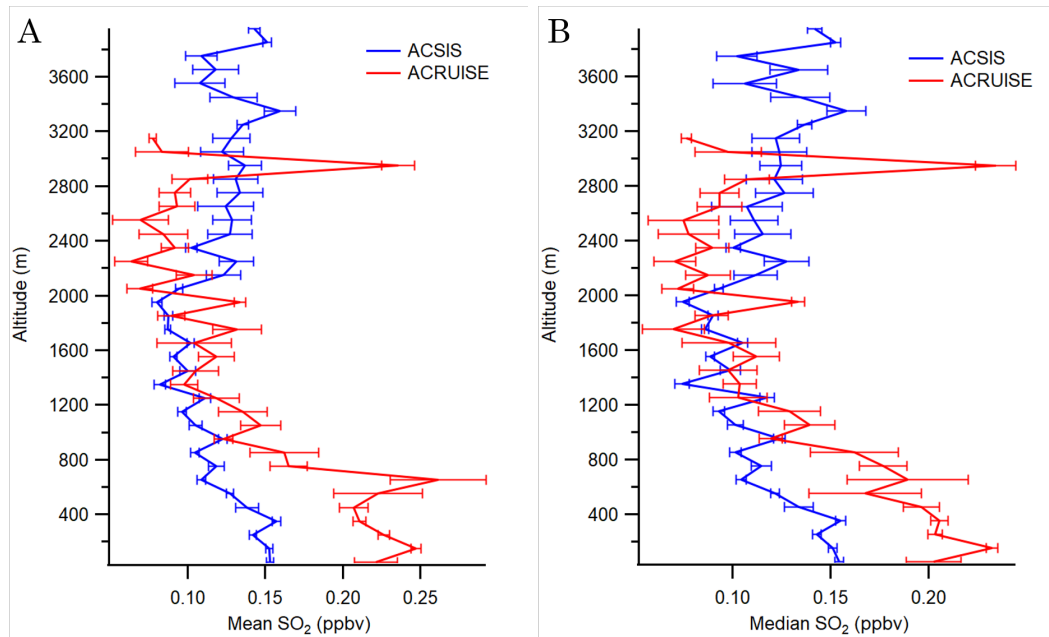


Figure 3.19: Profiles of mean (A) and median (B) 10 s LIF SO₂ mixing ratios for each 100 m altitude bin, comparing the ACRUISE-3 and ACSIS-7 data. The error bars indicate 2 standard errors.

**More details on the zeroing issue are given here, which are not included in the paper. Due to the use of the ram inlet, it is thought that the pressure build up in the inlet line was preventing the zero air from fully overflowing the inlet line (the Inlet ZA MFC was typically set to 2.5 SLPM to overflow 2 SLPM). This is evidenced by Figure 3.20, which shows the mean zero measurements, performed as part of a calibration in zero air, following ambient mixing ratios measured by the LIF-SO₂ instrument. Altitude is also plotted since it is likely governing the proportion of zero air that makes its way into the inlet line. This is because at higher altitudes and hence lower external pressures, even with the ram inlet pressure, more zero air will be able to overflow the inlet compared to at lower altitudes. However, the altitude effect is less apparent in the data.

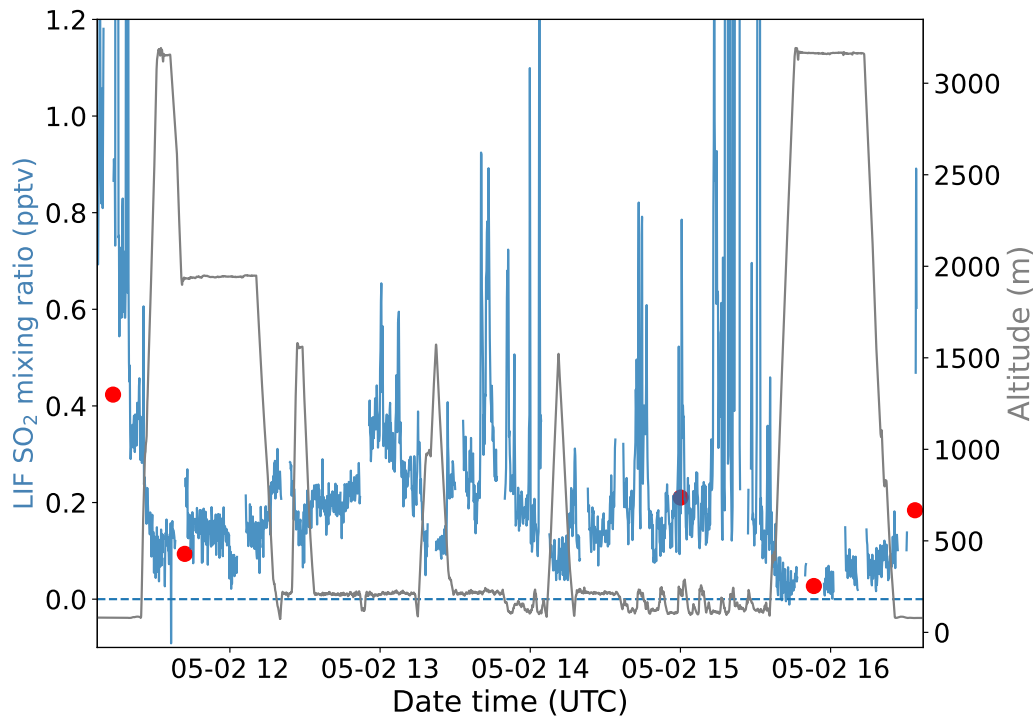


Figure 3.20: Variation of LIF zero measurements (red dots) over time, plotted against the LIF-SO₂ ambient time series averaged to 10 seconds (blue) and the altitude (grey) during flight C287.

Due to the nature of LIF where the difference between the online and offline fluorescence counts is proportional to an SO₂ mixing ratio, a zero measurement is not required for subtraction from the LIF signal as the difference between the online and offline counts should be zero. However, for experiments where the inlet has been fully overflowed with zero air, this has not always been the case and non-zero zero measurements, both positive and negative average values (such as that measured during the Arctic cruise campaign, as explained in subsection 4.2.1), have been recorded. This could be due to a number of factors: laser clipping which is wavelength dependent, temperature effects, or possibly interferences from other atmospheric species that fluoresce at a similar wavelength. Since the importance of zero measurements had not been realised at the time of the campaigns, regular true

Chapter 3. Intercomparison of SO₂ Techniques

zero measurements (overflowing fully with zero air) were not performed. Therefore, the time scales over which these zero measurements vary and hence the appropriate frequency at which to perform these measurements could not be determined. This will be the focus of future work but it is advised to perform a zero measurement as often as a calibration to keep track of the baseline.

Chapter 4

Arctic SO₂ Measurements

It is important to study the Arctic region since it is particularly sensitive to climate change and plays a crucial role in regulating the Earth's climate. Over recent decades, the Arctic has experienced rapid warming which is occurring nearly four times faster than the global average since 1979 (Rantanen et al., 2022; Chylek et al., 2022). This phenomenon, known as Arctic amplification, is due to strong climate feedback mechanisms at high latitudes (Shindell et al., 2009; Pithan et al., 2014). For example, as the Arctic warms and ice melts, this reflective surface area decreases, leading to more solar absorption and further global warming - a process known as the ice-albedo feedback. Therefore, among other climate effects, Arctic amplification is causing accelerated sea ice melt and since global and thus Arctic temperatures will further increase in the near future, the Arctic is expected to become ice-free in late summer within the next several decades (Wang et al., 2009).

Reductions in both Arctic sea ice extent and thickness increase the flux of ocean-atmosphere interactions, thereby affecting the composition and number of aerosols, which in turn influence cloud properties and climate. Model studies suggest that increased open waters and melt ponds lead to greater emissions of dimethyl sulfide (DMS) from marine phytoplankton (Abbatt et al., 2019; Galí et al., 2019; Mahmood et al., 2019). This trend has

also been determined experimentally by Kurosaki et al., 2022 who presented a 55-year high-resolution ice record of methane sulfonic acid (MSA) flux from the southeast Greenland Ice Sheet. As an oxidation product of DMS, MSA fluxes in summertime (July - September) were found to be 3 to 6 times higher between 2002–2014 than 1972–2001 (Kurosaki et al., 2022), which was attributed to a combination of earlier sea ice retreat and an increase in chlorophyll-a concentration (an indicator of phytoplankton biomass and productivity in the ocean) in the adjacent open coastal waters. However, it is unknown what effect increasing DMS concentrations will have on aerosols and climate. The simulations run by Mahmood et al., 2019 using an atmospheric global climate model suggest that despite large increases in DMS emission between 2000 and 2050 due to sea ice retreat, similar amounts of sulfate are produced via the oxidation of DMS. This is because sulfate removal through precipitation is enhanced in 2050, however, simulated aerosol nucleation rates are higher at this time which results in an overall increase in cloud droplet number concentration and hence an overall negative radiative forcing.

A decline in Arctic sea ice is also leading to an increase in Arctic ship traffic as shipping routes are opening up more frequently, for longer (Smith et al., 2013; Stephenson et al., 2013) and become faster to traverse (Melia et al., 2016), such as the Northwest Passage allowing a faster route from Europe to Asia. In addition to the expanding community re-supply, fishing, tourism, fossil fuel exploitation and cargo trading (Corbett et al., 2010), shipping emissions are projected to increase rapidly by 2050 (Melia et al., 2016; Sofiev et al., 2018) when many models predict that the Arctic Ocean will largely be free of ice toward the end of summer (Eguíluz et al., 2016). For example, Eckhardt et al., 2013 showed that tourist cruise ships at Ny Ålesund and Zeppelin Mountain on Svalbard in the Norwegian Arctic increase the total summer mean concentration of SO₂ by 15 %. Similarly, Marelle et

al., 2016 reported ship pollution to be significant along the Norwegian coast, enhancing 15-day-averaged surface concentrations of SO₂ (~+80 %) in the summer of 2012. However, since then, the IMO 2020 regulation enforced a reduction of sulfur fuel content from 3.5 to 0.5 % by mass for ships in international waters. Therefore, when including a regulation of sulfur fuel content in model simulations (using a North American Emission Control Area), Gong et al., 2018 estimate SO₂ would be brought down to below current levels over the Canadian Arctic compared to an increase to up to 20 % for sulfur under the 2030 business as usual scenario, without regulations. Likewise, increases in concentrations of pollutants both globally and in the Arctic were seen in model simulations by Dalsøren et al., 2013 between 2004 and 2030, except for sulfur species in the maximum feasible reduction scenario due to regulations reducing fuel sulfur content. Again, these changing emissions will alter Arctic aerosol in a way that is hard to predict, hence changing climate patterns.

The Shipping Emissions in the Arctic and North Atlantic Atmosphere (SEANA) project was designed to investigate some of these emerging trends and so it involved the measurement of a wide range of species including SO₂ within the Arctic boundary layer. In this chapter, the SEANA project is described in more detail and the SO₂ observations made as part of this campaign are presented. Additionally, the major sources of Arctic SO₂ mentioned above (anthropogenic versus biogenic) are explored.

4.1 The SEANA campaign

4.1.1 Project details

The main objectives of the SEANA campaign are to better understand the impact of i) increasing future ship traffic and ii) the IMO emission regulation on gas-phase chemistry, aerosol composition and radiative forcing at high latitudes by quantifying the present-day atmospheric 'baseline'. This baseline dataset will be used to advance our understanding of the sources and processes of aerosol particles and improve global aerosol models so that we are better able to predict the impact of future changes in ship pollution on aerosol systems and climate. Therefore, to obtain a representative Arctic baseline dataset, the SEANA campaign occurred in the late spring/summer months of May and June when the Arctic region is largely separated from air masses associated with strong sources of pollution during Arctic haze events (Leck et al., 1996), which are more frequent in the winter and spring (more on this in subsection 4.3.2. Additionally, the spring/summer sea ice melt allows measurements to be taken farther north within the Arctic circle (66 ° N).

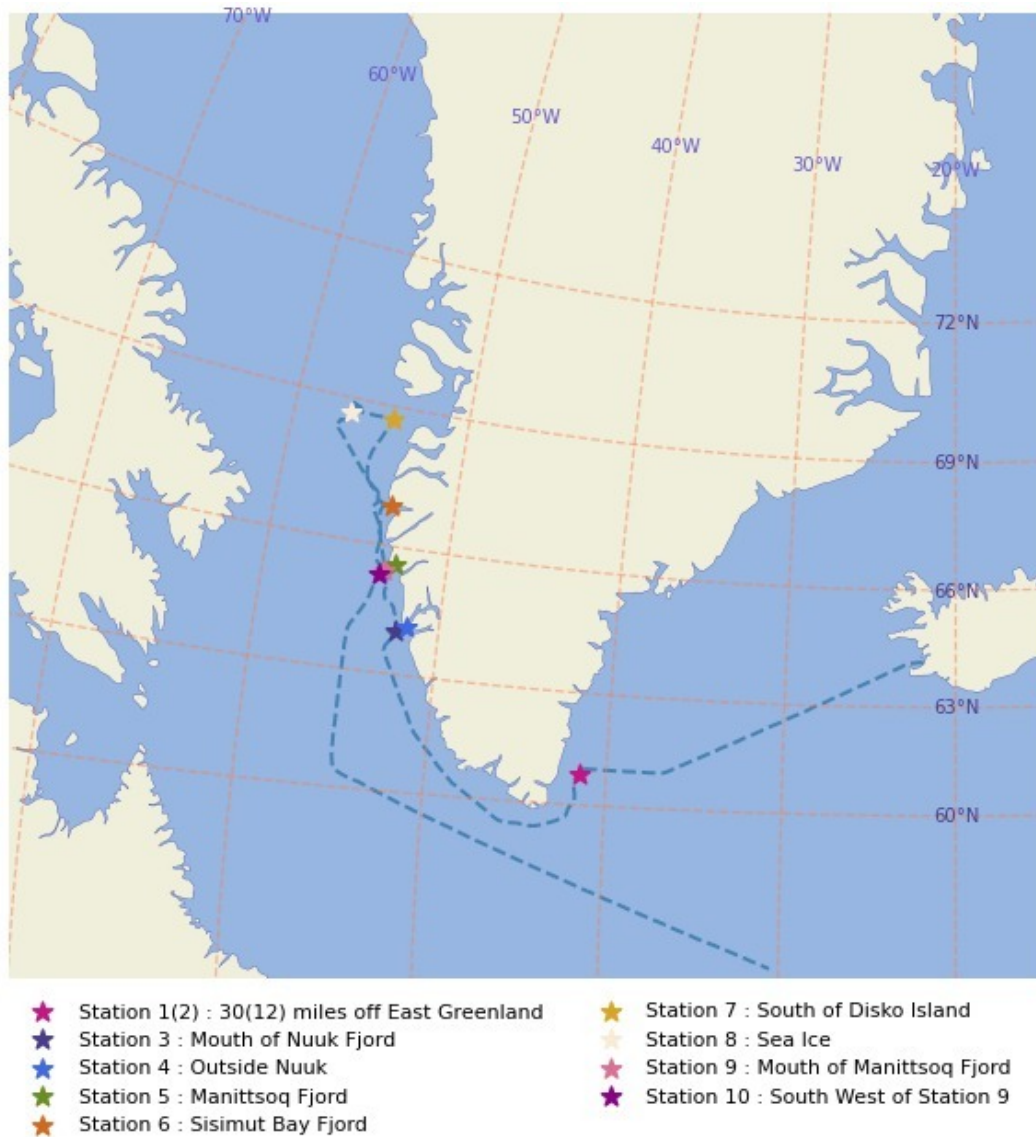


Figure 4.1: Map showing the sailing route of the RRS Discovery with the stations that were stopped at marked by a star.

The SEANA ship-based campaign, funded by the Natural Environment Research Council (NERC), took place on 16th May - 27th June 2022 on board the RRS Discovery, which is owned by NERC but operated by the National Oceanography Centre. It consisted of teams from the universities of Birmingham, Exeter, Zhejiang and York and from the organisations of the British Antarctic Survey (BAS), and Plymouth Marine Laboratory (PML). An

overview of the sailing route and the various stations that were stopped at is given in figure Figure 4.1. The RRS Discovery departed Reykjavik, Iceland on 20th May 2022 and sailed round the southern tip of Greenland through the Labrador Sea and as far north along Davis Strait as the sea ice allowed (given by the white star in Figure 4.1) before returning to Southampton, UK.

The York LIF-SO₂ only made its first ambient measurements in April 2022, and hence the SEANA deployment was a crucial learning experience for the operation of the instrument in the field for prolonged periods of time. Therefore, the aims of the instrument were to demonstrate its capabilities of measuring low ppt mixing ratios of SO₂, gain a baseline pre-shipping dataset, compare our measurements to models, and investigate the sources of Arctic SO₂. Despite instrument issues in the first few weeks of the campaign, 2 weeks of intermittent data were obtained, which is viewed as a major success given the new nature of the instrument and the limited testing of such a complex custom-built system prior to the deployment. The instrument issues and the aims for the instrument are discussed over the next few sections.

4.1.2 Instrumentation

A range of measurements were taken during the SEANA campaign, including SO₂, DMS, NO_x (NO + NO₂), CO₂, CO and O₃, which are used in this work and hence described herein. Firstly, an online proton transfer reaction time-of-flight mass spectrometer (PTR-ToF-MS) was used to measure DMS. A Teledyne T200UP instrument was used to measure NO_x and a Picarro G2508, that employed precise cavity ring-down spectroscopy technology, was used to measure CO₂. Finally, CO was measured by an AL5005 Aerolaser and O₃ by a Thermo 49iq ozone analyser. In addition to SO₂ measurements made by our LIF instrument, SO₂ was also measured by a Teledyne T101 analyser. Since the majority of SO₂ mixing ratios measured by the LIF during the campaign were below the LoD of the Teledyne T101 SO₂ analyser of 500 ppt

Chapter 4. Arctic SO₂ Measurements

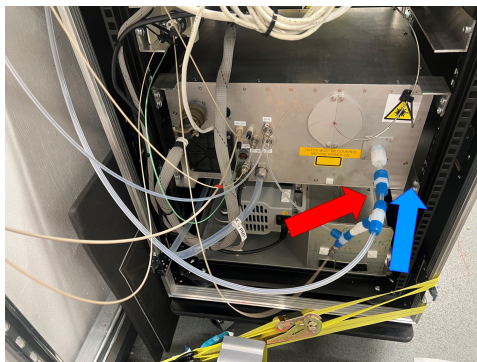
at 5 minutes, the Teledyne data has not been used in this work. In terms of meteorology measurements, wind speed and direction were characterised by an anemometer. These measurements form the basis of the first filtering method used in this work to remove instances when we were measuring our own ship stack (see subsection 4.3.1).

4.2 LIF performance

4.2.1 Characterisation during campaign



Figure 4.2: The container laboratories on deck of the RRS Discovery. The LIF-SO₂ instrument was housed inside the red container.



(a) The back of LIF box



(b) The inlet

Figure 4.3: The plumbing setup for the two different calibration methods, showing the sample line (blue arrow) and the calibration line (red arrow).

The LIF-SO₂ instrument was located in the red container (belonging to BAS) on the foredeck and the inlet was located on the roof of the container

(Figure 4.3b). It was necessary for the sample inlet to be 10 m in length, and hence, in order to quantify any SO₂ wall loss effects, the plumbing was adapted to allow calibrations to be performed both at the back of the LIF box and at the end of the inlet (Figure 4.3). To minimise these potential wall effects, a critical orifice was used at the end of the inlet to drop the pressure in the 10 m inlet line. Both the sample and reference cells were operated at a pressure of 600 mbar to maximise instrument sensitivity.

Multi-point calibrations were performed approximately every 1.5 hours to ensure the instrument sensitivity was well characterised. Similar to during the aircraft campaign (subsection 3.3.1), calibrations were performed in both ambient and zero air, and the calculated sensitivities agreed within error. In addition, since the SEANA campaign followed closely after the aircraft campaign, the same setup was employed, including the 5 ppm SO₂ in balance N₂ standard (BOC, $\pm 5\%$). To accommodate the lower mixing ratios observed in the Arctic (on the order of tens of ppt), smaller Cal SO₂ MFC setpoints were used compared to the aircraft campaign to achieve a lower mixing ratio range of calibration points, spanning 0.5 to 3.8 ppb. However, it was still necessary to extrapolate the calibration fit, assuming linearity at these low mixing ratios, which has been verified in post-campaign laboratory experiments using a 100 ppb SO₂ in balance N₂ standard (BOC, $\pm 5\%$). For reasons described later in this section, only the calibrations at the back of the box are used to determine the instrument sensitivity. Therefore, a plot of instrument sensitivity from back of the box calibrations with time during the SEANA campaign is shown in Figure 4.4. The reference cell was used as a diagnostic aid for assessing laser linewidth since, for a constant SO₂ mixing ratio, any variations in the difference between the online and offline linearised and normalised counts (reference LIF signal) are attributable to changes in laser linewidth. Periods of significant reduction in laser linewidth are discarded from the dataset, which were identified by a significant decrease in the ref-

erence LIF signal value. This was primarily due to the LabVIEW algorithm losing track of the transition peak, which we believe resulted from large changes in the laser box temperature, as explained in subsection 4.2.2 (point 9) and shown in Figure 4.5 where the seed laser online voltage is indicative of tracking the transition peak. Although deviations from the transition maximum occurred during the aircraft campaign, it was not as prevalent in the data since the instrument performance was continually being monitored and so was quickly corrected for. Finally, the sensitivities have been grouped into 'data blocks' between instrument turn on and off, as shown by the shading in figure Figure 4.4, since the laser system and hence sensitivities are largely consistent within each data block. Following the same method as for the aircraft data, a mean sensitivity has been applied to each data block and a mixing ratios uncertainty has been calculated, based on this mean sensitivity, as summarised in table Table 4.1.

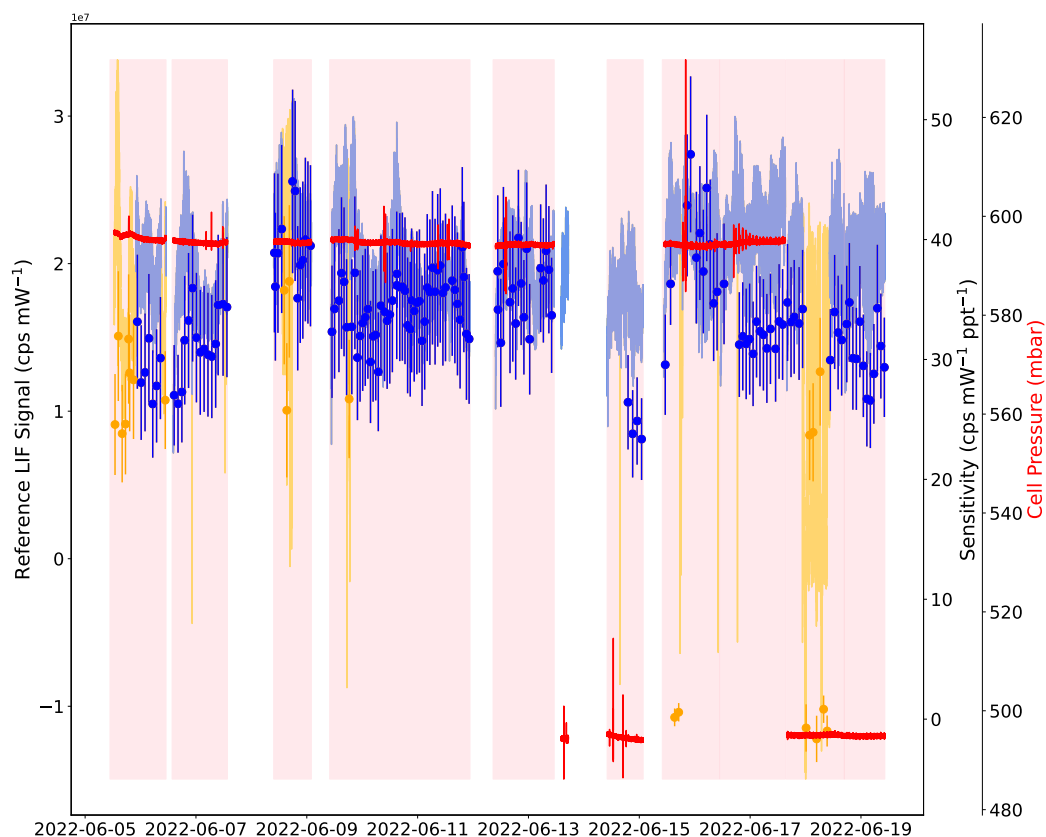


Figure 4.4: Instrument sensitivities over time for back-of-the-box calibrations performed in both ambient and zero air during the SEANA campaign are plotted as scatter points (blue), with error bars representing 2σ standard error of the York regression fit. These scatter points are overlaid onto the reference LIF signal data (10 Hz, blue). Significant decreases in the reference LIF signal due to poor laser linewidth are highlighted in orange, along with the corresponding sensitivities during these times, for which the data has been discarded. The length of each data block is indicated by pink shading, showing the sensitivities used to calculate the mean sensitivity for each block. The cell pressure (5 Hz, red) was mainly maintained at 600 mbar, with some unintended periods at 500 mbar due to an unchanged default value at instrument startup.

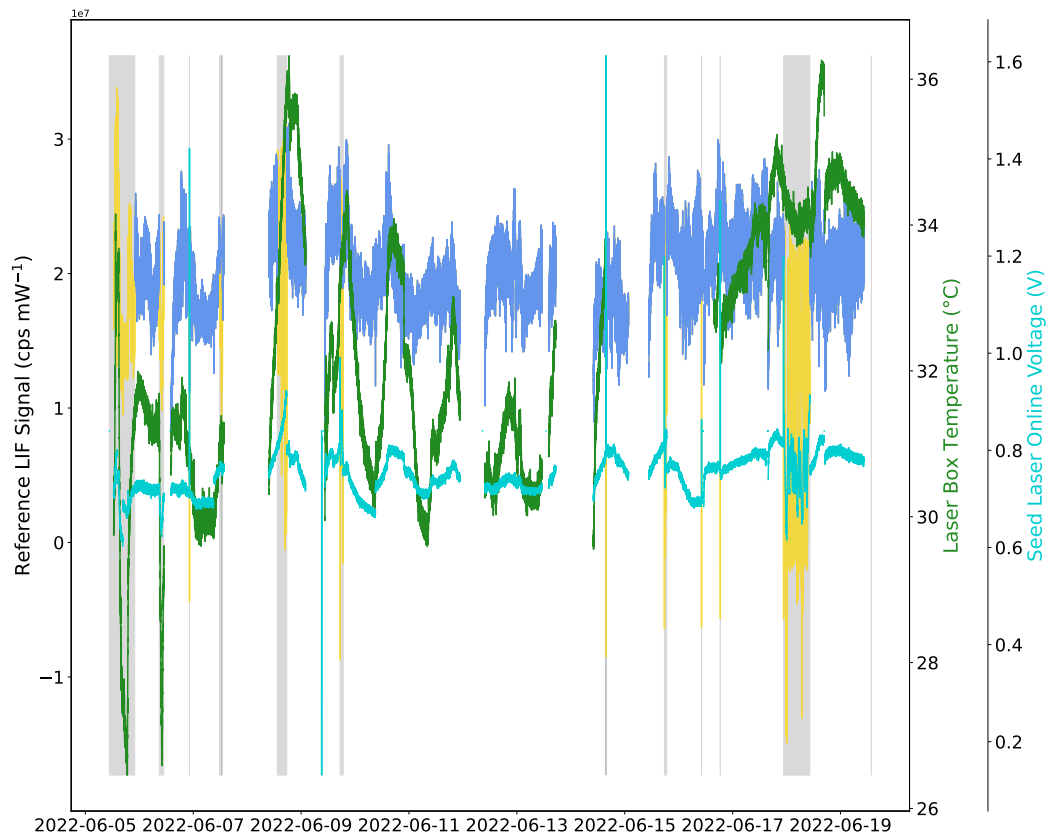


Figure 4.5: Reference LIF signal variation over time (10 Hz, blue) with yellow coloured periods, corresponding to the grey shaded regions, indicating data discarded due to laser linewidth issues. Large variations in the laser box temperature (green) are thought to causes these linewidth deviations, which can also be seen in the online seed laser voltage (cyan), representing tracking of the transition peak.

Chapter 4. Arctic SO₂ Measurements

Data block number	Start time	End time	\bar{x} (cps mW ⁻¹ ppt ⁻¹)	σ (cps mW ⁻¹ ppt ⁻¹)	N	Uncertainty (%) + 1.6 ppt
1	05 10:45:10	06 11:02:40	29.4	2.4	13	17
2	06 13:39:41	07 13:38:08	31.3	2.9	15	17
3	08 09:40:05	09 01:59:15	39.5	2.8	12	17
4	09 09:54:31	11 22:41:02	34.4	2.2	51	17
5	12 08:40:00	13 11:08:15	35.9	2.7	17	15
6	14 10:04:03	15 01:40:30	24.6	1.4	4	15
7	15 09:57:49	16 10:45:25	38.8	4.9	11	13
8	16 10:54:59	17 15:14:32	32.2	1.5	14	14
9	17 15:38:06	18 16:45:13	32.9	1.5	9	14
10	18 16:46:44	19 15:45:14	30.6	2.7	12	14

Table 4.1: Summary of the back-of-the-box calibrations performed in both ambient and zero air during the SEANA campaign. The mean (\bar{x}), standard deviation (σ), number of calibrations (N) and mean uncertainty for the sensitivities within each data block are given.

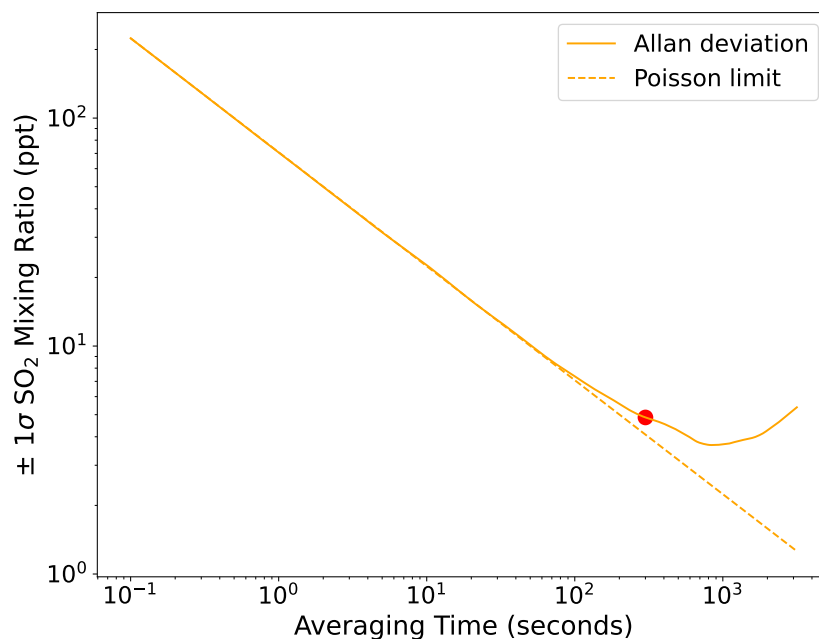


Figure 4.6: Instrument precision (Allan deviation) of a 9 h long ambient measurement on 11th June (mean mixing ratio of -10 ppt due to laser clipping). The trace is compared to the Poisson limit (dashed line) and the precision at an averaging time of 5 minutes is marked by the red dot.

During the SEANA deployment, the instrument had a 3σ LoD of 15 pptv at a 5-minute averaging time (70 pptv at 10 seconds), as shown in Figure 4.6 for a stable 9 hour measurement period on 11th June. This is comparable to the LoD seen during the aircraft campaign (70 pptv at 10 seconds, subsection 3.3.1) and in the laboratory (60 pptv at 10 seconds, subsection 2.5.3) due to comparable laser power. However, this snapshot of precision may not be representative of the instrument performance throughout the entire campaign, especially since the laser power reduced from $\sim 33 \mu\text{W}$ at the start to $\sim 15 \mu\text{W}$ by the end. Therefore the precision became worse over time, as evidenced by the increase in noise in the reference LIF signal data in Figure 4.4 and Figure 4.5. The Allan deviation can also tell us the maximum averaging time for the benefit of better precision, this being around 12 minutes, however, an averaging time of 5 minutes was used for this work, as

marked by the red dot in Figure 4.6.

Finally, a flow rate of 2 slpm was used throughout the campaign, giving a 3 e-folding response time similar to that during the aircraft campaign of ~ 2 s.

4.2.2 Instrument issues

As the LIF-SO₂ instrument had previously not been operated for a prolonged period of time, or in such challenging conditions, there were many issues impacting data coverage. The main issues resulted from laser failure early in the campaign, and complications optimising the spare laser that was brought in case of this eventuality. Hence, data was only obtained from 5th June onwards, for approximately 2 weeks intermittently. The instrument issues are listed below, including the solutions that were found to overcome them.

1 **Laser 1 failure:** The first of the two lasers brought on the campaign failed on 24th May, following three days of system optimisation and initial ambient measurements, due to failure of the pump laser diode within the regenerative amplifier. This appeared to happen gradually since the number of instances where the photodiode output from the 1 % tap within the regenerative loop dropped below the safety power threshold, hence causing the entire laser system to shut down, increased significantly until complete failure occurred. However, the cause of this gradual failure is unknown. Therefore, laser 2 was used for the remainder of the campaign, although issues with the setup of this spare laser were encountered and are detailed in points 2 to 5.

2 **Inconsistent pulse generation:** During the setup of laser 2, it was observed that the signal pulse after the SOA, monitored via the 5 % tap to the oscilloscope, was not being produced consistently as it kept intermittently disappearing in the oscilloscope. Therefore, the pump laser diode within the

regenerative loop was not turned on as with little/no pulsed seed light produced from the SOA to cause the relaxation of the Yb³⁺ ions in the gain fiber, stimulated emission would not occur regularly and hence a single large ASE event could break the optical fiber. This was seen in laboratory experiments and described as one of the laser failure modes in subsection 2.2.3. The cause of the inconsistent pulse generation was found to be a poor connection between the SOA and its control board. Therefore, since the failure of laser 1 did not involve its SOA control board, this was used in place of the board in laser 2, forming a more secure connection to the SOA and producing reliable pulses.

3 Insufficient laser power obtained from laser 2: Despite optimising laser 2 in the laboratory prior to the campaign, which involved determining the seed laser temperature, scanning current, laser timings, and bandpass filter position, the laser power initially obtained was extremely low and adjustments to the nonlinear crystal positions made little difference. The cause of the low laser power was diagnosed as an incorrectly positioned bandpass filter and since it allows a 1 nm wavelength range of light through the regenerative loop, most of the stimulated light at 1084.5 nm was being blocked. Divergence of the bandpass filter position from the laboratory-determined optimum suggests it could be sensitive to vibrations during the shipment of the instrument or temperature since the laser box during the campaign equilibrated at a different temperature compared to in the laboratory. Therefore, the bandpass filter position was corrected for 1084.5 nm which significantly increased the overall laser power.

4 Difficulty identifying the SO₂ transition peak: During a scan of the laser wavelength around 216.9 nm, the SO₂ transition was apparent but indistinct, and the LIF signal in the reference cell, typically 6000 cps mW⁻¹ for 5 ppm of SO₂, did not reach this value. It was necessary to further finely

adjust the bandpass filter to reveal greater structure in the SO₂ spectrum, including the SO₂ transition of interest, and to gain a greater sensitivity. The reason for this is speculated to be the result of the wide gain bandwidth of the SOA (~ 20 nm), producing a pulse that is primarily amplified at the stimulated wavelength of 1084.5 nm, but with some amplification extending approximately 10 nm either side of this wavelength. Therefore, when the bandpass filter, with a bandwidth of 1 nm, is positioned to perfectly center the amplified stimulated wavelength, it also permits the maximum intensity of adjacent amplified wavelengths to pass through, which degrades the SO₂ spectrum but gives the highest overall laser power. Hence, it is optimal to place the bandpass filter slightly offset to this maximum laser power so that the greater amplified wavelengths on one side of the stimulated signal are blocked. This means that a higher percentage of the pulse consists of stimulated light at 1084.5 nm and hence the spectral detail can be resolved due to the better linewidth, which also improves the instrument sensitivity. It is important to emphasise that this is a theory to explain that observed experimentally.

5 Reference cell counts too high: Following the resolution of issue 4, another problem became apparent when scanning the laser wavelength over the SO₂ transition peak. The reference cell linearised and normalised counts at the online position exceeded the limits of the software variable data type, leaving an apparent data gap in the scan, as observed on the LabVIEW display. This is because the LabVIEW code can only record count values within the range of a signed 16-bit integer (32768 to 32767 inclusively) and hence, when the value exceeds 32767, it becomes negative and is not viewed in the counts range. Consequently, dithering of the laser wavelength became problematic as, after setting an approximate current value for the online position, the LabVIEW algorithm was unable to find the online peak and hence no measurements of SO₂ could be performed. However, since it was easier to

adapt the hardware rather than the software during the campaign, a critical orifice was added before the reference cell to mix the 5 ppm SO₂ standard with ambient air from the container, hence reducing the reference cell counts to a measurable level.

6 Losing control of the seed laser temperature: To achieve a wavelength of 1084.5 nm, it was necessary to control the seed laser temperature for laser 2 at 13 ° C compared to 21.3 ° C for laser 1 at a similar driving current. This was due to slight manufacturing differences between the seed lasers and because the current output from the seed laser driver board (Wavelength Electronics, fl591 eval) for laser 2 was set up incorrectly, which was only realised after the campaign (more details on this below). However, the control board that drives the seed laser's internal thermoelectric plate (Meerstetter Engineering, TEC-1092) was unable to maintain a seed laser temperature of 13 ° C since the laser box typically equilibrated around 30 ° C due to the temperature inside the container. As a result, the board was drawing too much current and hence deviations from this target temperature were seen. To overcome this, the air conditioning unit in the container was used to cool the laser box directly by constructing a tube to direct cold air from the air conditioner to the intake fans at the base of the laser box, enabling the seed laser temperature to be controlled at 13 ° C.

7 Quantifying SO₂ wall loss effects: As mentioned in subsection 4.2.1, a 10 m long sample inlet was used and hence calibrations were performed both at the back of the LIF box and at the inlet to capture potential wall loss effects. There did exist a disparity between the sensitivities calculated from identical calibrations at the inlet compared to the back of the box of ~ 38 %, with the back of the box calibrations giving higher sensitivities due to greater concentrations of calibration gas measured in the sample cell. This difference seemed too large to attribute solely to SO₂ sticking to the walls of

the inlet tubing, however, other potential causes such as a leak in the line or fittings, were ruled out. This issue was overcome during post-campaign testing, as described below.

8 Laser power reduction over time: The maximum average laser power achievable with an optimised setup at the start of the data collection period was $\sim 33 \mu\text{W}$. However, by the end of the campaign, this was $\sim 15 \mu\text{W}$. Post-campaign testing suggested that the laser power drop is largely attributable to humidity affecting the alignment mirrors, which damages their coating and thus reduces their reflectivity. The relative humidity in the container was monitored during the campaign and ranged from 22 % to 75 % with a mean of 33 % and hence, periods at these higher humidities could have affected the mirrors. High humidity could also have affected the performance of the nonlinear conversion efficiency, since the BBO crystal is particularly hygroscopic. Another factor that could potentially contribute to the reduction in laser power with time is the high intensity laser beam burning off the anti-reflective coating of the crystals, especially the KTP since it receives the greatest power, hence reducing its conversion efficiency. If this was the issue, it could have been overcome by adjusting the crystal position slightly so the light penetrates a different, undamaged part of the crystal. This was not done during the campaign due to the risk of potential misalignment of the system.

9 Dither losing the SO₂ transition: The dither mode of the laser, which tracks the transition peak based on SO₂ in the reference cell, occasionally failed to maintain the online and offline wavelength positions. It was found that the seed laser diode temperature is influenced by external temperature variations in the laser box, as mentioned above and in subsection 2.5.5, which, for large temperature changes, means the dither algorithm cannot keep up with the shifting SO₂ transition peak. This issue was particularly

prevalent during the campaign due to the requirement of controlling the seed laser at 13 ° C (point 6). Therefore the laser was routinely checked (except overnight) and any data that resulted from the transition peak not being tracked, as diagnosed by a significant decrease in the reference cell LIF signal value, was discarded.

10 Losing connection to the LabVIEW software: The LabVIEW code deployed on the cRIO occasionally stopped communicating with the control laptop, resulting in the LabVIEW interface used for controlling the laser to become unresponsive. This meant the entire system was frozen in its most recent state and the only way to turn it off was at the switch, which shuts the laser down all at once rather than in a controlled way i.e. turning the pump laser diodes in the power amplifier off first, followed by the regenerative pump laser diode and lastly, the seed laser diode. This issue was avoided by manually power cycling the instrument in a controlled way once a day. The cause of this issue has been identified in post-campaign testing as a memory leak on the cRIO due to the LabVIEW code and attempts to overcome it have enabled the system to run continuously for 48 hours.

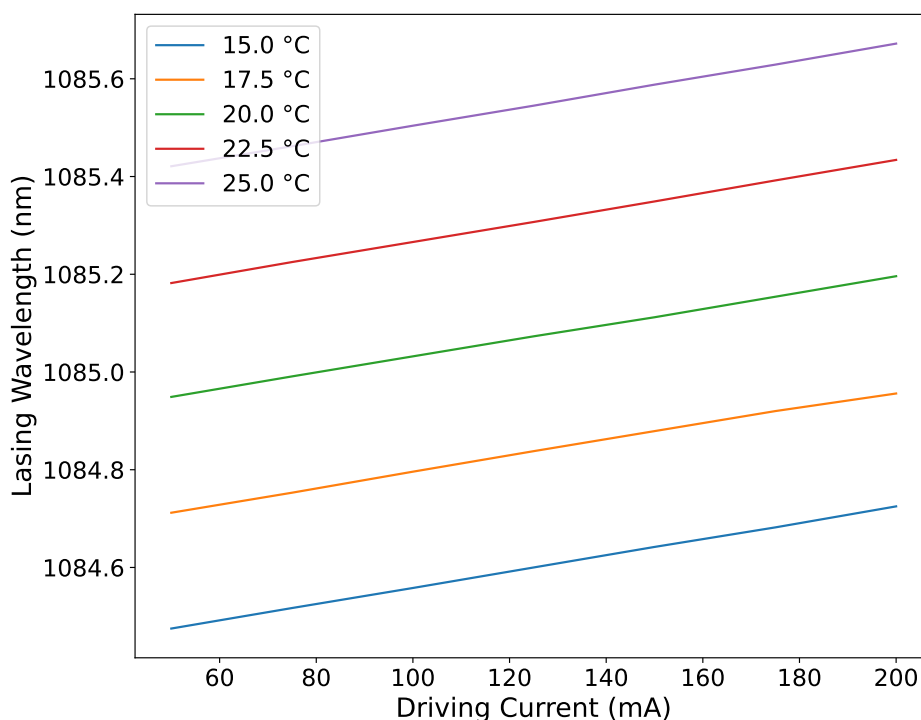


Figure 4.7: Experimentally determined wavelength tuning of the seed laser diode via driving current supplied from the seed laser driver board and temperature. The laser wavelength was measured using a wavemeter (moglabs MWM wavemeter).

A few other solutions to some of the issues were realised during post-campaign testing and development, which are described here. Firstly, the seed laser driver board (Wavelength Electronics, fl591 eval) was incorrectly configured during the campaign as its 500 mA output (maximum driving current) was connected to the seed laser, instead of the 250 mA output. Therefore, the seed laser driver was outputting double the intended driving current. As a result, the seed laser had to be operated at a lower temperature than would be required for the 250 mA output to achieve the desired wavelength of 1084.5 nm, as shown by the wavemeter measurements in Figure 4.7. For a set seed laser driving current of 90 mA as used during the campaign, the seed laser temperature required, with the normal 250 mA output, would

approximately lie just below the blue line in Figure 4.7 corresponding to 15 ° C. However, since the seed laser was actually driven at 180 mA using the unintended 500 mA output, a seed laser temperature below 15 ° C was necessary for a wavelength of 1084.5 nm, which was determined as 13 ° C. This led to control issues of the seed laser temperature, as described above in point 6. The error in current control during the campaign also meant that the difference between the online and offline currents was unintentionally double that set by the dither parameters. The laser cannot switch instantaneously between the online and offline current values and the bigger the difference, the longer the switch over will take, which is apparent in the data by a lower count value for the first online point compared to the subsequent 7 points (explained in section Section 2.4). To avoid this biasing the measurement, the first online point is discarded in the data processing procedure. A large dithering distance may also introduce greater temperature fluctuations, and hence increase the noise in the data. Finally, the algorithm used for tracking the online peak will be stepping twice as far, and since it looks for 3 decreasing counts values before reversing its current direction, we may see a greater pronunciation of this peak curvature in the data.

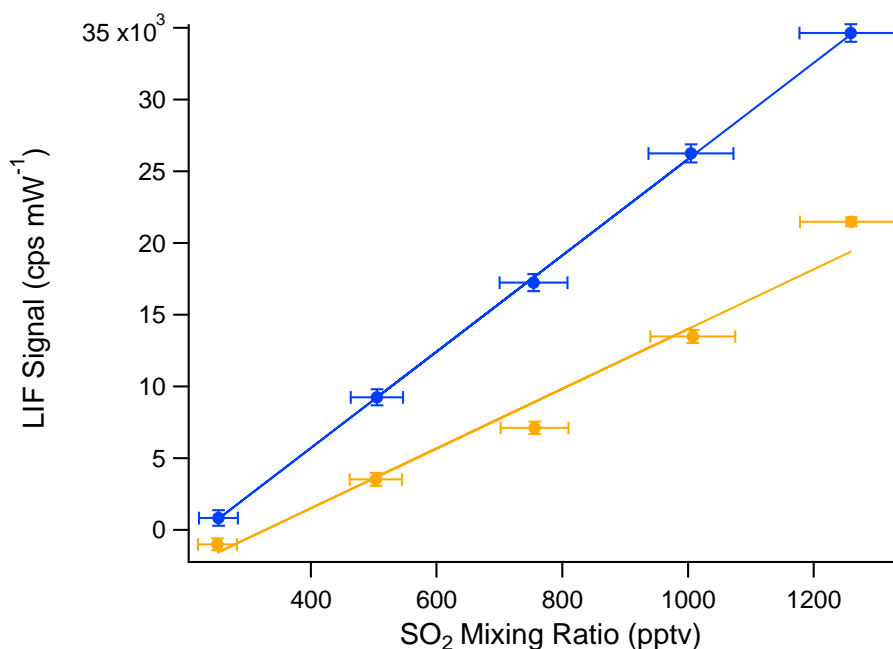


Figure 4.8: Calibrations performed in ambient air at the back of the LIF box (blue, starting at 19:05) and the inlet (orange, starting at 19:33) on 17th June 2022 during the SEANA campaign, yielding sensitivities of $33.6 \pm 4.7 \text{ cps mW}^{-1} \text{ ppt}^{-1}$ and $20.8 \pm 3.0 \text{ cps mW}^{-1} \text{ ppt}^{-1}$ (both 2σ confidence) respectively.

The disparity between the sensitivities determined when introducing calibration gas at the inlet and the back of the box during the campaign, as shown in Figure 4.8, were replicated in the laboratory post-campaign. Since a lower concentration of calibration gas was reaching the sample cell during a calibration at the inlet, the 10 m 1/16th inch peek tubing supplying calibration gas to the inlet was changed out for an equal length of the same peek tubing to that supplying calibration gas to the back of the box. The laboratory experiment showed an increase from 6.6 ppb to 13 ppb with a shorter length of tubing for a Cal SO₂ MFC setpoint of 5 sccm and a fixed sensitivity, compared to 16.4 ppb when the calibration gas was introduced at the back of the box. It was also found that the critical orifice, placed after the tee at the inlet where the calibration gas was introduced, was also

Chapter 4. Arctic SO₂ Measurements

preventing some of the calibration gas entering the sample inlet. When the calibration gas was introduced into the reduced pressure side, after the critical orifice, the mixing ratio increased to 15.3 ppb. The 1 ppb difference between the inlet and back of the box (15.3 vs. 16.4 ppb) was unaccounted for, but is likely due to an insufficient conditioning time of this new length of shorter tubing to the inlet. Further laboratory testing using the same length calibration line, but introducing calibration gas at the inlet versus at the back of the box has shown minimal SO₂ wall loss effects (Figure 4.9). Hence, we conclude that the discrepancy between the calibrations during the campaign were due to both the calibration gas line being too restrictive and the critical orifice restricting the flow of the calibration gas into the sample line. For the analysis of sensitivity during the campaign, the calibrations at the inlet have been disregarded and only those performed at the back of the box are used.

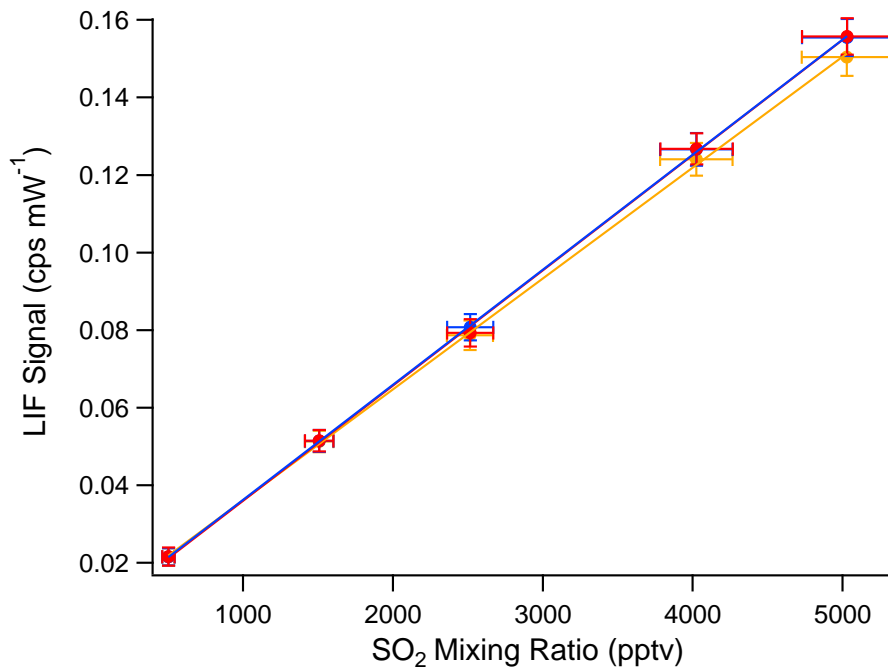


Figure 4.9: Calibrations performed in the laboratory post-campaign using the same length calibration line but introducing the calibration gas at the end of the 10 m long inlet (orange) versus at the back of the box (blue). The calibration at the inlet was repeated (red) to capture any drift in instrument sensitivity. [Data collected by Eve Grant.]

4.3 Observations of SO₂ mixing ratios

4.3.1 Time series

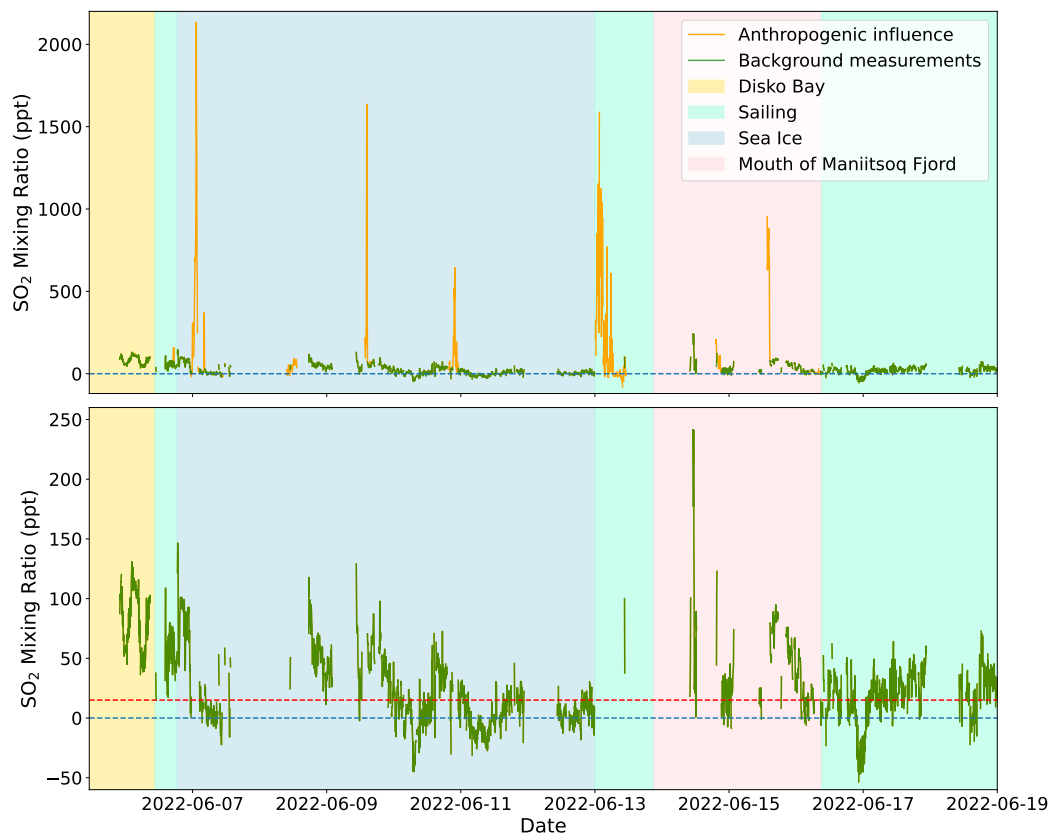


Figure 4.10: 5-minute averaged SO₂ time series for the campaign, shaded by the ship position. The time series is coloured by background SO₂ measurements (green) and anthropogenic influenced measurements (orange). The 3 σ limit of detection of the LIF-SO₂ during the campaign is marked by the red dashed line (15 ppt).

Figure 4.10 shows the time series of 5-minute averaged SO₂ mixing ratios. Two filtering methods are used in this work, the first of which removes instances when we were measuring our own ship stack and has been applied to both plots in Figure 4.10. Data corresponding to a relative wind direction between 157.5 ° and 202.5 ° (a 45 ° range around 180 °) and/or a relative

wind speed of below 3 m s⁻¹ have been filtered out. However, following application of this filtering method, enhancements in SO₂ mixing ratios still remained, and hence a second filtering method, based on the anthropogenic markers of NO_x, CO₂ and CO was developed, as explained later in subsection 4.4.1. This second filtering method has only been applied to the bottom plot in Figure 4.10 and the resulting SO₂ data are described as background measurements in this work. Therefore, the background measurements possess a significantly lower scale with the majority of measurements (78 %) lying between 0 and 100 ppt. Comparing the background SO₂ measurements during stationary observations (when we were not sailing), SO₂ mixing ratios are lowest during the beginning and end of the period at the sea ice and many measurements are below the instrument's LoD (3 σ) of 15 ppt. A histogram of the background SO₂ measurements can be found in Figure 4.11. The campaign median SO₂ mixing ratio of 20.9 ppt means that mixing ratios were close to the LoD, with 42 % of measurements falling below 15 ppt, including negative SO₂ mixing ratios below the noise of the instrument (-15 ppt) where issues with the alignment of the laser were experienced. The campaign mean SO₂ mixing ratio of 26.9 ppt is slightly skewed by the seemingly errant background SO₂ measurements which extend the range to 241.4 ppt, however, no justification for removing these measurements from the data were found.

4.3.2 Comparison to literature values

The first systematic measurements of SO₂ in the Arctic were made in the late 1970s when the anthropogenic origin of the Arctic haze was realised (Quinn et al., 2007). The Arctic haze is caused by the long range transport of air pollution from midlatitude industrial regions and primarily forms during the late winter and spring months because of a combination of factors: strong surface-based temperature inversions (Quinn et al., 2007),

Chapter 4. Arctic SO₂ Measurements

stable atmospheric conditions, increased meridional transport of pollutants (Iversen et al., 1985), low precipitation rates (Barrie et al., 1981; Shaw, 1995; Heintzenberg et al., 1983), and longer lifetimes of pollutants. These pollutant haze events can last for up to 15 to 30 days (Shaw, 1995). Rahn et al., 1980 reported daily SO₂ measurements at Bear Island, a stationary Arctic measurement site located at 74° N and 19° E, and found that from May to October 1978, there were only 10 days when SO₂ mixing ratios exceeded 140 pptv, however, during the winter (November 1977 to April 1978) when the Arctic haze is most pronounced, there were 65 days when the SO₂ mixing ratios exceeded this value. Arctic haze events were also captured by Heidam et al., 1999 who reported weekly SO₂ measurements from 1991 to 1996 at the stationary measurement site of Nord in the Northeastern part of Greenland.

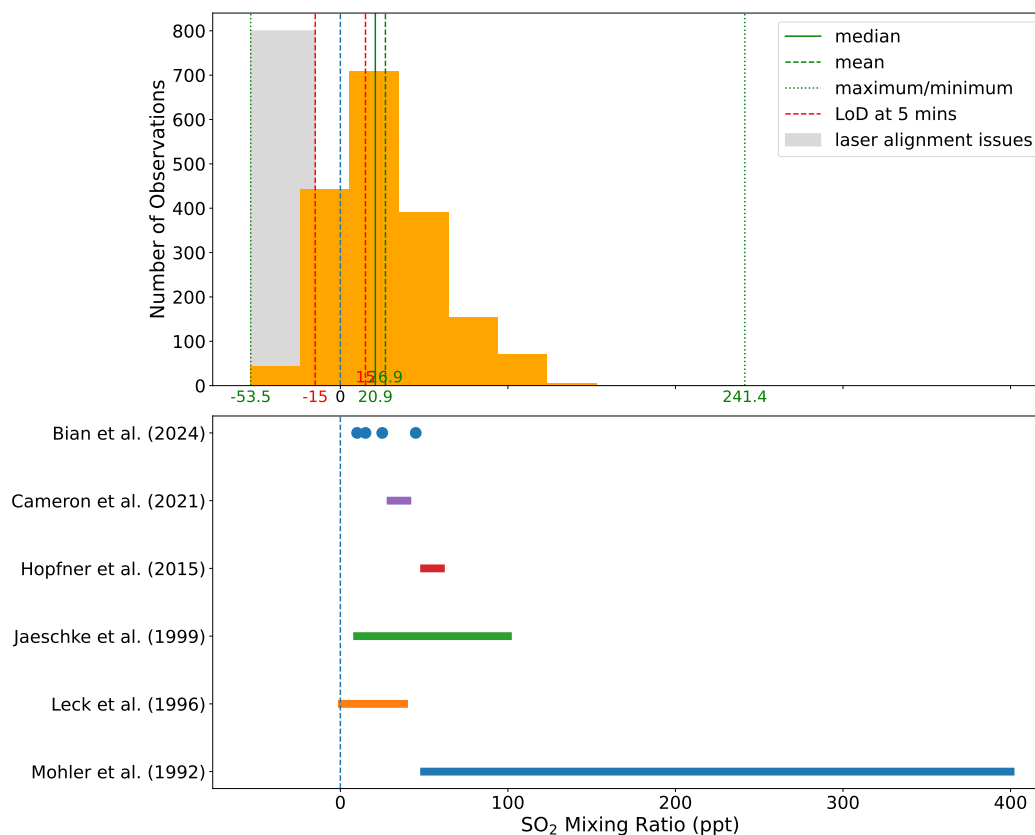


Figure 4.11: Histogram of the background SO₂ measurements made on the SEANA campaign, annotated with statistical parameters, compared to literature concentration values or ranges of SO₂ in the Arctic. For literature values that were reported in units other than ppt (mainly either nmol m^{-3} or $\mu\text{g m}^{-3}$), a conversion has been made into ppt using a standard temperature of 273 K and pressure of 1 atm.

Of greater relevance to this work are background measurements of Arctic SO₂, outside of these Arctic haze events as well as at alternative time of the year. As shown in Figure 4.11, literature measurements of background Arctic SO₂ mixing ratios are in good agreement with those measured during the SEANA campaign in this work. Most of these literature reports use aircraft and ship-based platforms to survey the Arctic, enabling greater data coverage and in situ measurements at a range of altitudes. Möhler et al., 1992a flew over Northern Scandinavia in February 1987, covering altitudes between 3.5

Chapter 4. Arctic SO₂ Measurements

and 11.4 km. They measured SO₂ mixing ratios between 50 - 400 pptv using an aircraft-borne mass spectrometer. However, the wind directions during the flights suggest that the air masses were likely to have been exposed to lower latitude regions and therefore may not be best representative of background Arctic SO₂ mixing ratios. On a ship-based campaign in August to mid October 1991, Leck et al., 1996 set out to quantify relationships within the natural sulfur cycle in the marine boundary layer under conditions of limited anthropogenic influence. They collected filter samples between the latitudes of 75 ° N to 90 ° N, including in the open waters and along the ice edge zone in the Greenland Sea-Fram Strait, with subsequent analysis via ion chromatography (following conversion of all the SO₂ to sulfate). A significantly lower SO₂ mixing ratio range of 0.9 - 38 pptv was observed, and mixing ratios were generally higher in the open ocean and ice edge compared to the pack ice area. This suggests that SO₂ originated from biogenic emissions of DMS and are representative of background Arctic SO₂ mixing ratios. Background measurements were also made by Jaeschke et al., 1999 during two aircraft-based campaigns in early spring 1994 and 1995 (March/April) and one campaign in summer 1994. Using a filter method followed by chemiluminescence analysis, SO₂ mixing ratios ranged from the LoD of 11 ppt to 112 ppt during both spring and summer at various sites in the Eastern and Western Arctic.

Since the 1990s, relatively few campaigns measuring SO₂ in the Arctic have been reported, likely due to the lack of instrumentation available to detect pptv levels of SO₂ in a continuous sense (Boyer et al., n.d.; Willis et al., 2018). Again, Rempillo et al., 2011 used the filter sample technique followed by ion chromatography analysis during a ship-based campaign to measure SO₂ in the Northwest Passage (fall of 2007) and Baffin Bay (fall of 2008). Like many of the aforementioned campaigns that used filter sampling, only daily samples were taken due to the nature of the technique. They reported

Chapter 4. Arctic SO₂ Measurements

SO₂ mixing ratios ranging from 2 - 3000 ppt in 2007 and 7 - 600 ppt in 2008 and, through stable isotope apportionment, attributed a significant fraction of the higher mixing ratios to long range transport of biogenic SO₂. Therefore, these observations have been omitted from Figure 4.11. Continuous measurements of SO₂ (at a sampling rate of 1 s) were made on the NASA-funded ATom campaigns, which were executed over each of the four seasons from 2016 to 2018 and included measurements over Western Greenland and the Canadian Arctic for each season. A chemical ionisation mass spectrometer (CIMS) measured SO₂ throughout all four campaigns, and the NOAA LIF instrument was available for the final campaign (ATom-4) in April-May 2018. At a latitude of 54 - 90 ° N and an altitude of 0 - 1.5 km, the median SO₂ mixing ratios were approximately 45, 25, 15 and 10 pptv during ATom-1, -2, -3, and -4. The NOAA LIF also reported 10 pptv for ATom-4, which is above its LoD. Besides these in situ measurements, mixing ratios of SO₂ in the Arctic have been measured by satellites. Data from the NASA Atmospheric Chemistry Experiment - Fourier Transform Spectroscopy (ACE-FTS) on the satellite SCISAT measured an SO₂ volume mixing ratio of 30 - 40 ppt at 10 km, during June and August 2004 to 2019 (Cameron et al., 2021). Likewise, the Michelson Interferometer for Passive Atmospheric Sounding (MIPAS) on the satellite Envisat gave a similar range of 50 - 60 ppt at 10 km during July 2002 and April 2012 (Höpfner et al., 2015), which is again within the range of Arctic SO₂ concentrations seen in this work. Finally, although LIF aircraft measurements of SO₂ have been made previously in the Arctic region, this work presents the first ship-based measurements of Arctic SO₂ using the LIF technique. The poor time resolution of most previous measurements has made quantifying variability and identifying sources of Arctic SO₂ more difficult. This is investigated in the following sections using the continuous, in situ, sensitive LIF measurements of SO₂ made during the SEANA campaign.

4.4 Potential sources of Arctic SO₂

4.4.1 Anthropogenic

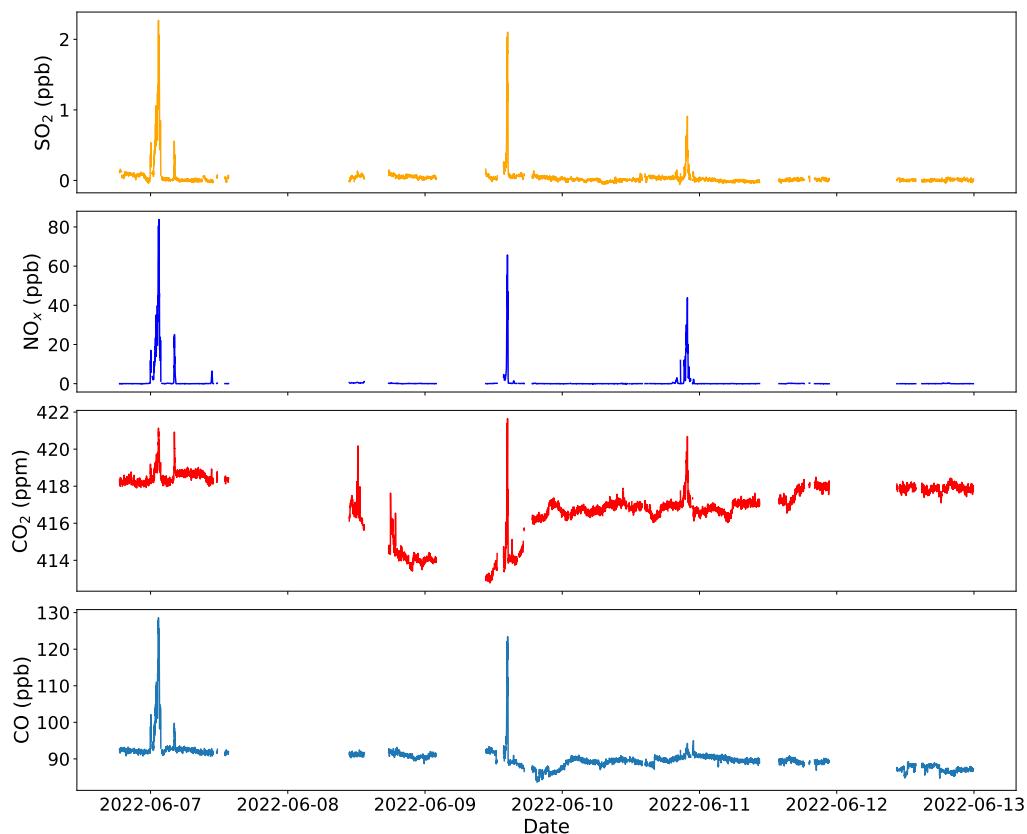


Figure 4.12: 1-minute averaged SO₂, NO_x, CO₂ and CO time series at the sea ice station. All datasets have been filtered for relative wind speed and direction to remove instances when we are measuring our own ship stack.

To assess the anthropogenic influence on the LIF-SO₂ measurements other than our own ship stack, the data have been filtered via the first method (to remove ship stack instances) and the resulting measurements have been compared to the anthropogenic markers of NO_x, CO₂ and CO (Rempillo et al., 2011), as shown in Figure 4.12. It is evident that the large spikes in SO₂ mixing ratios correlate with spikes in NO_x, CO₂ and CO, which suggests that these enhancements could be due to combustion. Also, the relatively

sharp nature of these spikes, typically lasting between tens of minutes to a few hours, are indicative of a local source. Given the absence of evidence for local fires and the unexpectedly large number of other ships observed at the sea ice edge, particularly fishing vessels, these spikes in SO₂ have been attributed to nearby ships. Although the marine traffic AIS software was not used at the time to track individual ships, the density of ships around this region in the Arctic, as shown in Figure 4.13, demonstrates this as an already popular fishing area. Finally, to provide further evidence for local ship pollution, emission ratios for SO₂ and NO_x to CO₂ were calculated for the 4 spikes shown in Figure 4.12. Both the integration and regression methods were used (subsection 3.4.1), which agreed well within error and hence the average emission ratios are reported here. NO_x:CO₂ emission ratios ranged from 9 - 27, which are on the order of those reported by Schlager et al., 2007 of 32 - 34 for younger ship plumes and 18 for older plumes. Additionally, SO₂:CO₂ emission ratios spanned 0.21 - 0.81 ppb ppm⁻¹, which although are slightly lower than the range seen during the aircraft campaign of 1.17 - 1.9 ppb ppm⁻¹ (Figure 4.12), shows that the ships are even more compliant to the 0.5 % sulfur fuel content IMO2020 regulations. This also demonstrates that both the integration and regression methods are suitable for ground-based measurements of longer ship plumes, in addition to second duration plumes for the aircraft campaign.

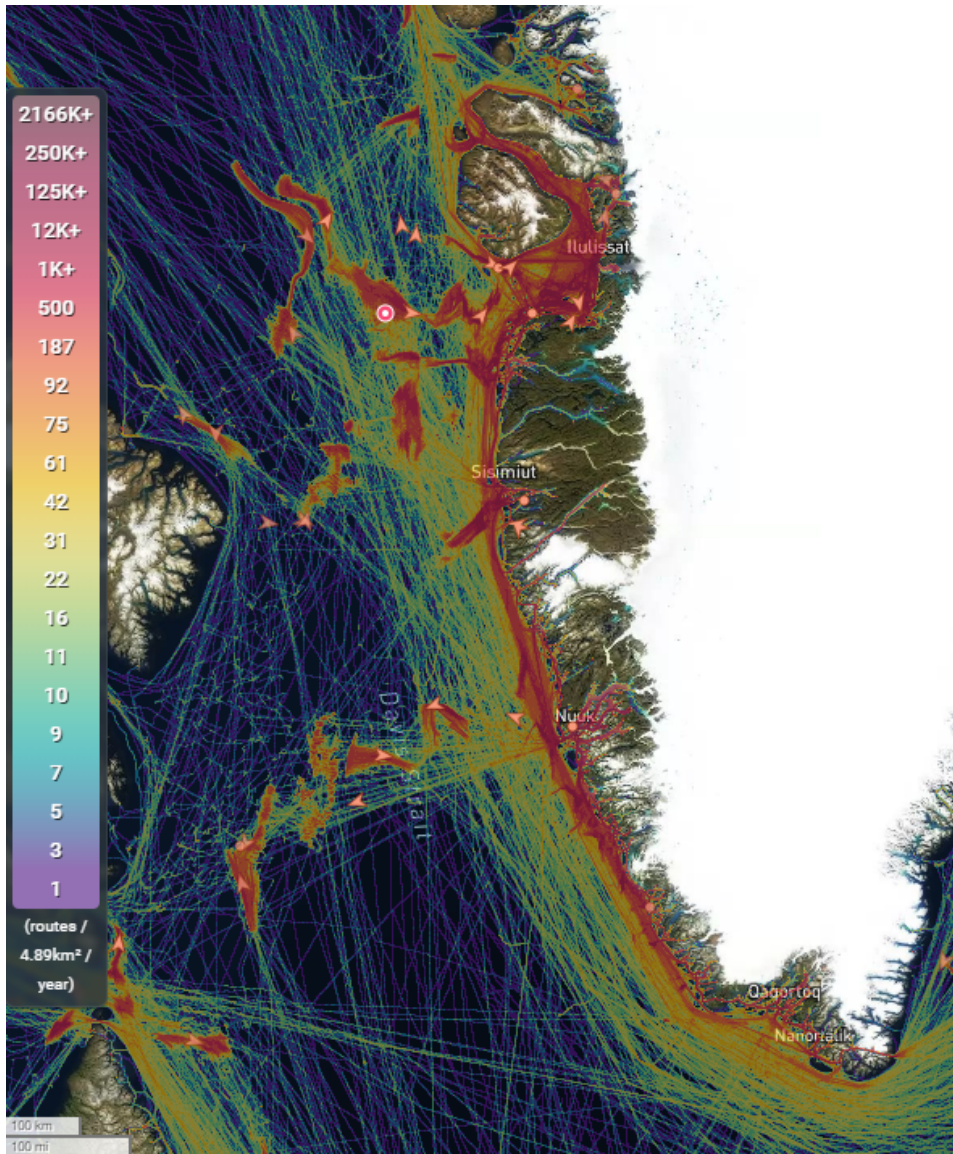


Figure 4.13: Satellite density map of west Greenland showing the total number of shipping routes (for all ship types) per 4.89 km² per year during 2022. A snapshot of the positions of fishing vessels only is captured by the orange triangles on 31.07.24 at 11 am (similar time of year to when the measurements were taken in 2022) to demonstrate that this region of the Arctic is already being exploited for fishing purposes. The map is also marked (red circle with central white dot) with our ship position at the sea ice edge, during which time the measurements in Figure 4.12 were taken.

It is also possible that more distant ship pollution contributes to the background SO₂ measurements in this work. Without model simulations or source apportionment techniques, we are unable to discern the mixing ratio contribution of anthropogenic SO₂ to the observed background, and is beyond the scope of this work. Boyer et al., n.d. used the ECLIPSE v6b emission inventory coupled with the FLEXPART simulations to determine the contribution of shipping to anthropogenic SO₂ concentrations that they observed in the Arctic. Since the conversion of SO₂ to sulfate aerosol usually occurs on the order of hours in the atmosphere (Lee et al., 2011), FLEXPART treated anthropogenic SO₂ emissions as SO₄-S, which yields the SO₄-S weighted influence from anthropogenic sources. They found that in June, anthropogenic emissions from ships formed a significant fraction (nearly 50 %) of the anthropogenic concentration of SO₂. However, since the background SO₂ concentrations observed in June were below their instrument's LoD of 1 ppb, a percentage contribution to the total SO₂ could not be made.

4.4.2 Biogenic

The main source of biogenic SO₂ to the remote marine atmosphere is via the oxidation of DMS, largely in the presence of sunlight (subsection 1.1.6). DMS was also measured during the SEANA campaign (subsection 4.1.2) and hence this section investigates DMS observed at the ship position as a source of SO₂. Due to the SO₂ data availability in the latter half of the campaign, this analysis has been performed for the following stations where the ship stopped at: Disko Bay, sea ice, and the mouth of Maniitsoq Fjord (Figure 4.1). Therefore, to aid with interpretation of observed SO₂ and DMS mixing ratios, satellite sea ice and chlorophyll concentrations have been mapped between longitudes 75 to 40 °W and latitudes 64 to 78 °N (Figure 4.14) to account for these stations. Modelled hourly back trajectories coloured by hourly-averaged observed SO₂ and DMS mixing ratios respectively have then

been overlaid onto Figure 4.14, as shown in Figure 4.16. Back trajectories at the sea ice station (68.7 °N and 56.9 °W), where the ship remained for 6 days, are highly variable but predominantly traverse either along the ice edge, where sea ice concentrations are < 80 %, or over the pack ice, with sea ice concentrations of ≥ 80 %. Therefore, these back trajectories have been grouped as 'ice edge' and 'pack ice' respectively. In contrast, the back trajectories at Disko Bay (68.7 °N and 54.4 °W), where the ship was stationed for 1 day, consistently originate from a northerly direction, traversing partly over the west coast of Greenland but also over open ocean. Finally, back trajectories at Maniitsoq (65.4 °N and 53.5 °W), where the ship spent 2.5 days, also come from the north and pass over the sea ice (pack ice and ice edge) as well as the open ocean. A detailed interpretation of the SO₂ and DMS mixing ratios for these groups is given in the following sections, presented in a manner deemed most appropriate. However, there are caveats to this analysis method which have been recognised, including the effects of DMS and SO₂ atmospheric lifetimes as well as air mass mixing and dispersion on their observed mixing ratios, which are explored below and in subsection 4.4.2.3 respectively.

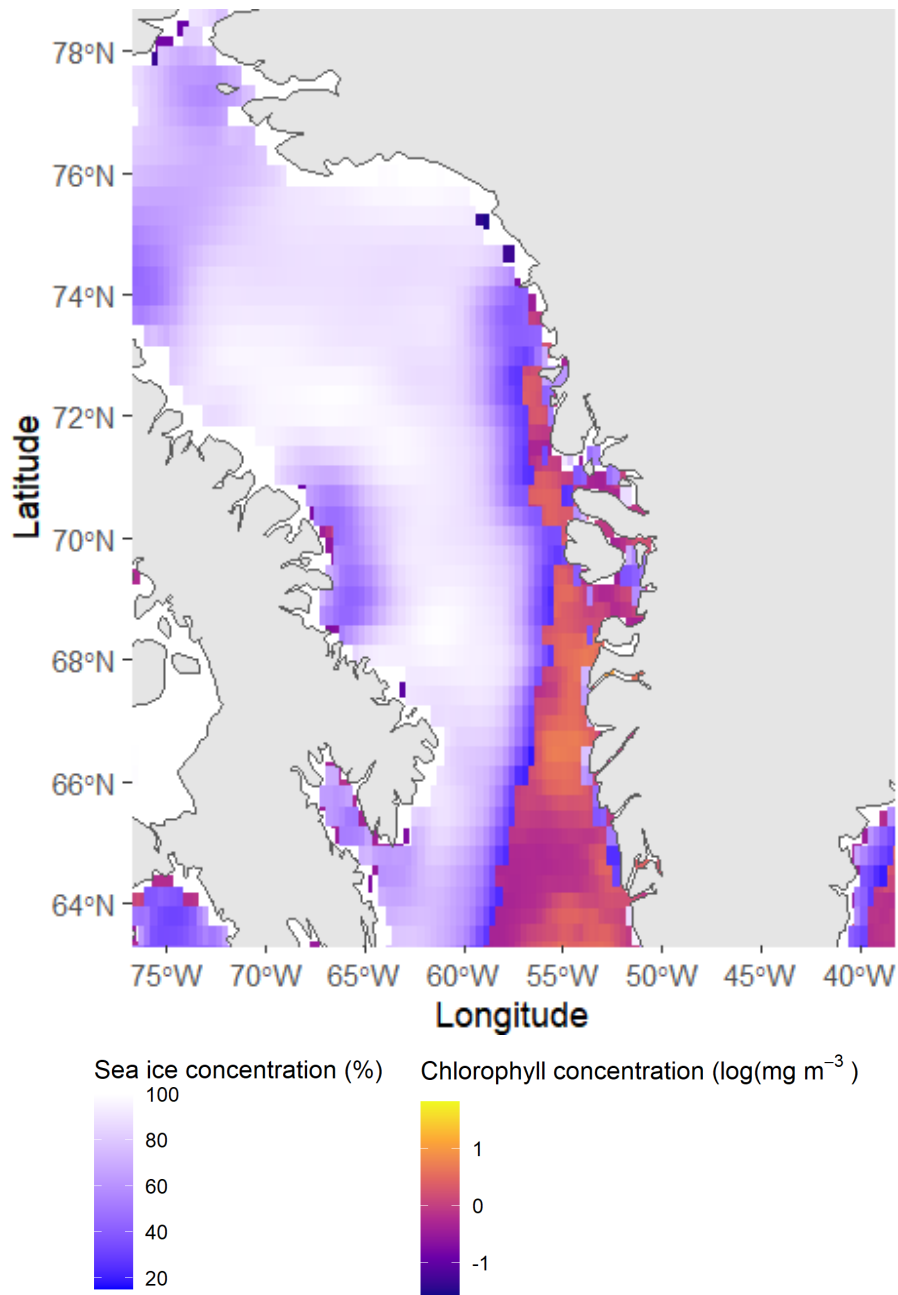


Figure 4.14: Mapped satellite sea ice and chlorophyll concentrations. Sea ice concentrations are obtained from the National Snow and Ice Data Center (<https://nsidc.org/data/g02135/versions/3>) and have a temporal resolution of 1 day (on 6th June 2022) and a spatial resolution of 25 km. Chlorophyll-a concentrations from the AQUA MODIS satellite can be found here (https://modis.gsfc.nasa.gov/data/dataproduct/chlor_a.php), and have a temporal resolution of 8 days (from 2nd June to 9th June 2022) and a spatial resolution of 4 km.

It is necessary to consider the atmospheric lifetimes of DMS and SO₂ to enable interpretation of the mixing ratios seen at the ship position. It has been assumed that their loss rates are solely determined by OH oxidation, which is largely considered the dominant oxidant for DMS and SO₂ in the remote marine boundary layer (Faloona, 2009). Therefore, an estimate of OH concentration has been made from a 0-D box model constrained to the measured DMS mixing ratios (amongst other species), which was performed by collaborators at the University of Cambridge (more details in subsection 4.4.2.3). DMS and SO₂ lifetimes have then been calculated from the International Union of Pure and Applied Chemistry (IUPAC) recommended rate constants for the reactions of DMS and SO₂ with OH respectively and the modelled OH concentration. Realistically, other oxidants in the atmosphere such as peroxides and halogens, as well as alternative loss pathways other than oxidation like deposition, also contribute to the loss rates of DMS and SO₂. However, due to large uncertainties in the modelled concentrations and deposition rates, in addition to the absence of measurements of these other oxidants during the campaign, only oxidation via OH has been considered in this work. Hence, the calculated atmospheric lifetimes are an upper estimate.

Firstly, the oxidation of DMS by OH can occur via two major reactions: that of abstraction and addition, as explained in subsection 1.1.6. The modelled campaign mean OH concentration, $[OH]$ has been determined as 5.0×10^5 molecules cm⁻³ at atmospheric pressure (1 bar) and a temperature of 0 °C (273 K). Although this value is uncertain due to missing constraints in the box model, it aligns with literature reports of OH concentrations in the Arctic spring (Mao et al., 2010). Therefore, the DMS lifetime has been calculated via Equation 4.1.

$$\tau_{DMS} = \frac{1}{k_{abstraction}[OH] + k_{addition}[OH]} \quad (4.1)$$

where $k_{abstraction}$ and $k_{addition}$ are the rate constants for the two OH oxidation pathways, which have been calculated as 4.5×10^{-12} cm³ molecules⁻¹ s⁻¹

and $9.6 \times 10^{-12} \text{ cm}^3 \text{ molecules}^{-1} \text{ s}^{-1}$ respectively at 1 bar and 273 K, based on the IUPAC preferred values. Therefore, the campaign mean DMS lifetime has been estimated as 1.7 days. It is important to note that the lifetime will vary throughout the day as the OH concentration follows a diel pattern with shortwave irradiance, with peak OH concentrations giving a lifetime as short as 8 hours. The mean DMS lifetime is in agreement with literature DMS lifetimes in the Arctic, with Lundén et al., 2007 reporting a value of 1.8 days over the central Arctic Ocean in August from a box model calculation of DMS oxidation by OH. Furthermore, Ghahremaninezhad et al., 2019 included the nighttime nitrate radical (NO₃) oxidant of DMS via the NO₃ abstraction pathway, as well as the OH abstraction and addition pathways, in their 1-D photochemical box model. They estimated a DMS lifetime range from < 1 to 5 days at latitudes < 70 °N in July. Similarly, Sharma et al., 1999, who also modelled the DMS lifetime due to OH and NO₃ oxidation, estimated a DMS lifetime of 6 to 8 days in the central Arctic during August. However, their modelled DMS loss rates accounted for only 33 % of the measured loss rate, suggesting that inclusion of halogen chemistry, such as reactions with Br/BrO and other halogenated radicals, may be an important sink for DMS in the Arctic atmosphere. The importance of halogens has also been highlighted by a number of other modelling studies (Ghahremaninezhad et al., 2019; Glasow et al., 2004; Hoffmann et al., 2016; Fung et al., 2022). An estimation of the contribution of these other oxidants to the DMS lifetime calculated in this work is given later.

The SO₂ atmospheric lifetime has been calculated in a similar manner, although the oxidation of SO₂ by OH predominantly proceeds via a single reaction involving a third species to dissipate the excess energy. The rate constant for this reaction in 1 bar of dry N₂ has been determined as $1.2 \times 10^{-12} \text{ cm}^3 \text{ molecules}^{-1} \text{ s}^{-1}$ at 273 K. Hence, for the same modelled campaign mean OH concentration, the mean SO₂ lifetime has been estimated as 19

Chapter 4. Arctic SO₂ Measurements

days, but again will vary throughout the day with OH concentration. The mean SO₂ lifetime (although an upper estimate) is consistent with literature Arctic SO₂ lifetimes of several weeks, reported by Thornton et al., 1989 over the North American Arctic during the winter, and 10 to 19 days, calculated by Barrie et al., 1984 within a similar region but in April.

Therefore, the analysis of back trajectories in Figure 4.16 has been limited to 48 hours prior to the arrival of air masses at the ship position since the mean lifetime of DMS has been estimated as 1.7 days.

Chapter 4. Arctic SO₂ Measurements

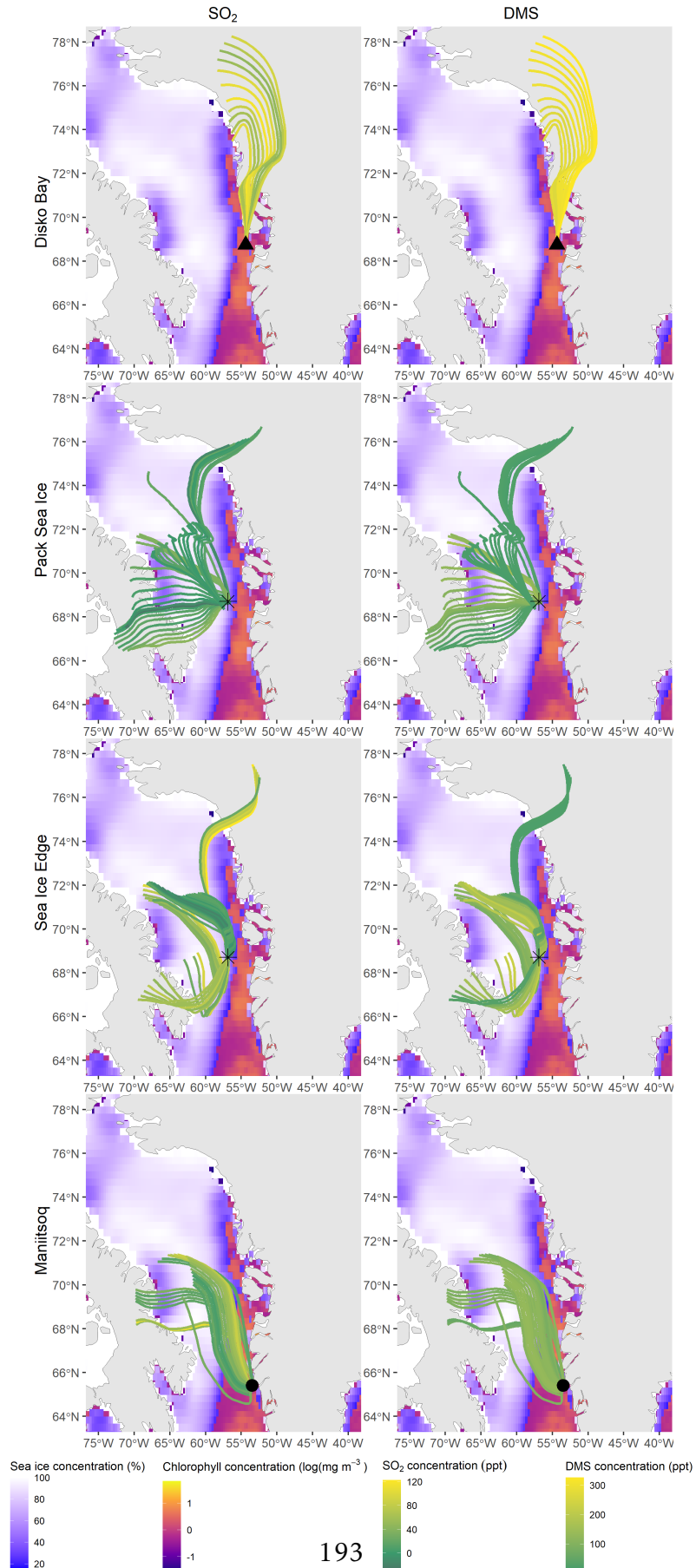


Figure 4.16: 48-hour air mass back trajectories at 1-hour intervals, simulated by the HYSPLIT model which was run by collaborators at the University of Birmingham for Disko Bay, the pack ice, ice edge, and Maniitsoq. The back trajectories are coloured by hourly averaged SO₂ and DMS mixing ratios respectively (provided that at least 20 % of data is available within that hour) and overlaid onto satellite sea ice and chlorophyll concentrations. Sea ice concentrations are obtained from the National Snow and Ice Data Center (<https://nsidc.org/data/g02135/versions/3>) and have a temporal resolution of 1 day (on 6th June 2022) and a spatial resolution of 25 km. Chlorophyll-a concentrations from the AQUA MODIS satellite can be found here (https://modis.gsfc.nasa.gov/data/dataproduct/chlor_a.php), and have a temporal resolution of 8 days (from 2nd June to 9th June 2022) and a spatial resolution of 4 km.

4.4.2.1 Disko Bay

Firstly, Disko Bay experiences the highest mixing ratios of both DMS and SO₂ on average compared to the other stations. This is likely due to the continuous emission of DMS from the open ocean to the north of the ship along the coast where chlorophyll-a concentrations, which are frequently used as a proxy for biological activity (including DMS-producing phytoplankton)(Park et al., 2013), are on the order of 1 to 10 mg m⁻³. However, the back trajectories suggest that the time taken for DMS to arrive at the ship position from the open ocean is shorter than its lifetime of 1.7 days. Therefore, SO₂ could originate from DMS emitted further up the west coast of Greenland (≥ 48 hours prior to arriving at the ship), hence allowing sufficient time for oxidation to occur. Elevated SO₂ mixing ratios could also result from anthropogenic emissions, for example, from other ships contributing to the observed background (Figure 4.12) or from small settlements along the coast of Greenland, especially since the air masses spend a significant amount of

time over land. Longer range transport of SO₂ could also contribute due to its lifetime of 19 days. These different sources of SO₂, as well as the time of day, which affects both the DMS lifetime and anthropogenic activity, could provide an explanation for the greater observed variability in SO₂ mixing ratios, which span 40 to 120 ppt.

4.4.2.2 Pack ice

The lowest SO₂ and DMS mixing ratios were seen for back trajectories that have travelled over the pack ice. This is likely because the pack ice inhibits air-sea exchange, as evidenced by literature DMS flux measurements (Leck et al., 1996). However, some back trajectories show slightly non-zero mixing ratios of SO₂ and DMS, despite the lack of known SO₂ and DMS sources over the pack ice. For the air masses enhanced in SO₂, this again suggests a DMS source perhaps from the exposed parts of the ocean close to the coasts of Greenland and Canada or long range transport of anthropogenic SO₂ emissions. Elevated DMS mixing ratios within other air masses could also be a result of distant emissions from the exposed ocean, which is consistent with the absence of a DMS diel pattern. These elevated DMS mixing ratios for air masses that have travelled over the pack ice can be more clearly seen by the time series in Figure 4.20 (in between the blue highlighted regions), particularly on 10th June. This is a good example of a limitation of this analysis method for explaining the observed mixing ratios and highlights the need to consider atmospheric lifetimes and air mass mixing/dispersion effects.

4.4.2.3 Sea ice edge: a case study



Figure 4.17: Photograph of the sea ice edge, taken from the ship on 7th June.

In contrast to the pack ice, the back trajectories traversing close to the sea ice edge before arriving at the ship position contain higher SO₂ and DMS mixing ratios on average. This could be explained by the thin coverage and broken up nature of the sea ice, as evidenced by the photograph of the sea ice edge in Figure 4.17, hence allowing DMS emissions from exposed parts of the ocean or from melt ponds that form from snowmelt on top of the sea ice in spring and summer (Mungall et al., 2016). Some back trajectories provide evidence for local DMS emissions at the ice edge. For example, the group of back trajectories from the north that first travel over the pack ice and then along the ice edge contain high DMS mixing ratios of ~ 200 ppt and near zero SO₂ mixing ratios. This suggests DMS was emitted close to the ship, within the ice edge, and hence has not had time to oxidise before the air masses reach the ship. Other air masses seem to be influenced by more

distant DMS emissions close to the coast or anthropogenic SO₂ emissions, as explained previously.

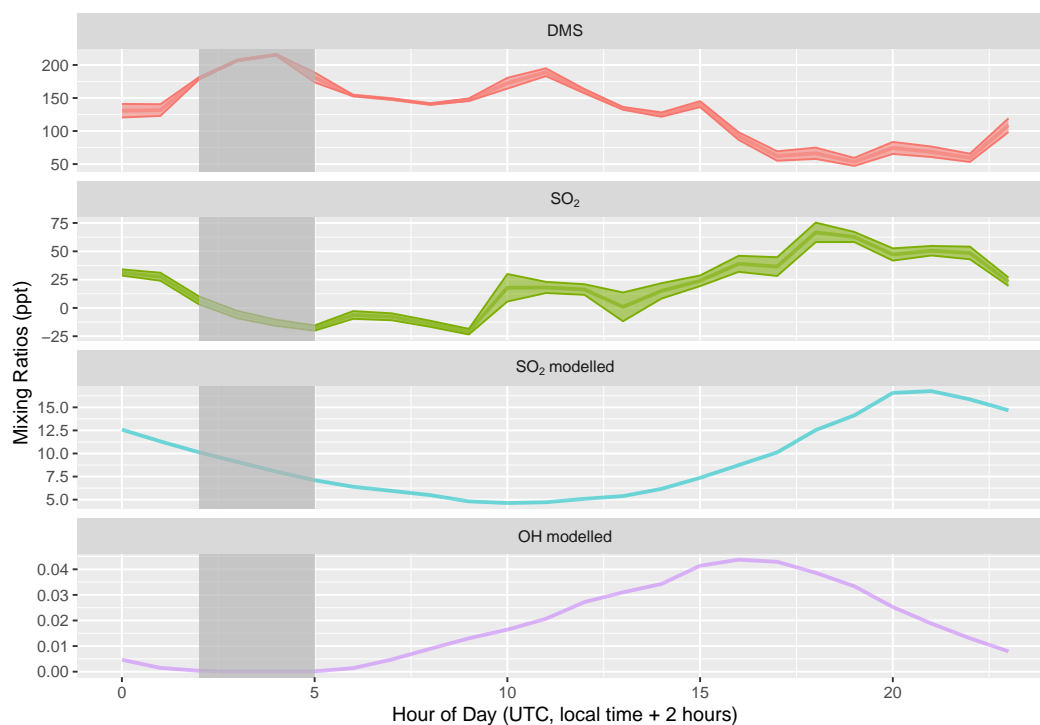


Figure 4.18: Hourly averaged diel profiles of observed DMS and SO₂ mixing ratios, and modelled SO₂ and OH mixing ratios, obtained from a 0-D box model run by collaborators at the University of Cambridge (more details below). The coloured shading around the observed mixing ratios represents two standard errors since some hours contain more measurements than others. Note the hour of day is UTC, which is 2 hours ahead of local time. The grey shading between hours 2 and 5 corresponds to a modelled UVA and UVB irradiance from the Tropospheric Ultraviolet and Visible (TUV) Radiation Model of zero, which defines nighttime at the sea ice.

A clear diel pattern is seen for SO₂ and DMS mixing ratios at the ice edge, as shown in Figure 4.18, which is consistent with and likely driven by the more local DMS emissions within the ice edge. Also, sufficient SO₂ and DMS data were obtained at the sea ice to enable a representative and sta-

tistically valid analysis of these mean diel profiles, which are compared to modelled parameters (more details below). The DMS diel profile has an overall decreasing trend throughout the day, while the modelled OH mixing ratios increase and peak around 16:00 (UTC). DMS is also anticorrelated with SO₂, which peaks at 19:00 (UTC) when the DMS mixing ratios are at a minimum. Therefore, these trends provide evidence for the loss of DMS via photooxidation to SO₂. This anticorrelation relationship between DMS and SO₂ is also shown by the negative trend of the correlation plot in figure Figure 4.19, with the ratio of DMS:SO₂ mixing ratios reaching a maximum when the modelled UVA irradiance is lowest, therefore limiting oxidation. However, the relationship is very poor, as shown by the R² value of 0.21, which is unsurprising considering the factors of lifetimes and transport times meaning there are added effects of air mass mixing and dispersion contributing to the observed mixing ratios.

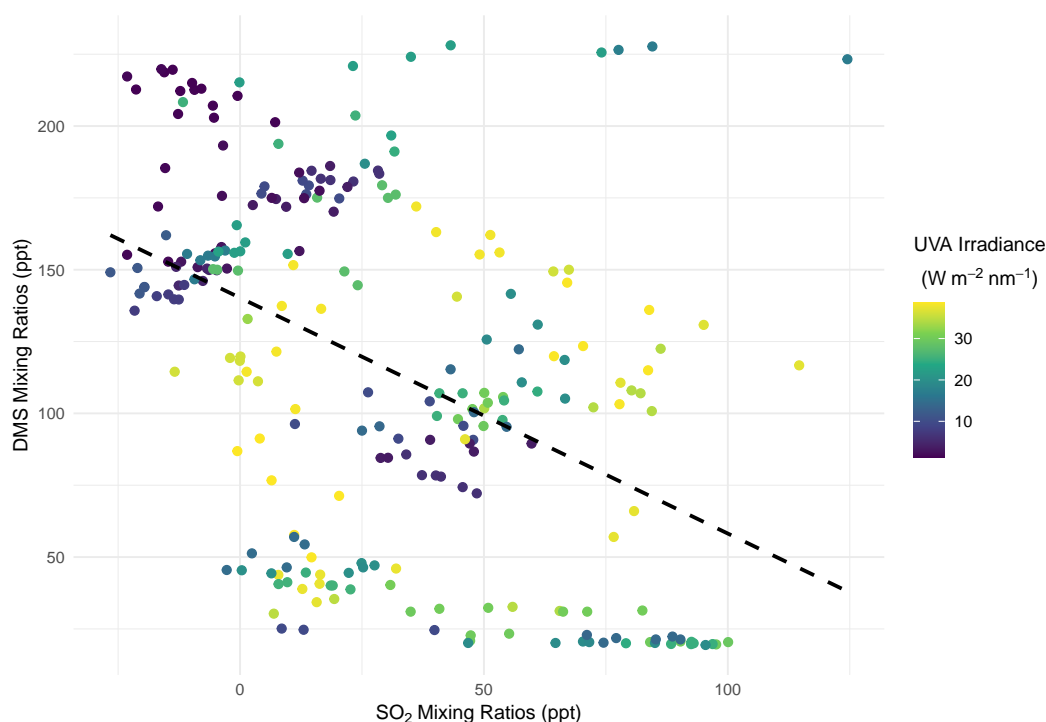


Figure 4.19: Correlation of SO₂ and DMS mixing ratios at a 5 minute averaging time coloured by modelled UVA irradiance from the Tropospheric Ultraviolet and Visible (TUV) Radiation Model. The linear least squares best fit is plotted as the dashed black line. The slope of the best fit line is -0.83, and $R^2 = 0.21$.

Since no air mass is ever transported and photochemically aged in isolation, it is necessary to also consider the dispersion and mixing effects of an air mass (Parrish et al., 2007), which contribute to the observed mixing ratios and hence diurnal pattern seen in Figure 4.18. To assess the influence of mixing of different air masses (some potentially more polluted), the SO₂ and DMS time series at the sea ice station have been compared those of CO and O₃ (Figure 4.20), which can be used as tracers of aged anthropogenically influenced air. A more detailed modelled analysis of air mixing effects, such as using a transport treatment of the Lagrangian particle dispersion model FLEXPART (Parrish et al., 2007), are beyond the scope of this work. Figure 4.20 provides evidence of a potential air mass change around the start of

Chapter 4. Arctic SO₂ Measurements

10th June 2022 from greater anthropogenically influenced and hence long range transported air masses to cleaner air masses that are more impacted by local sources. This is because the relatively high initial concentrations of SO₂ align with higher concentrations of both CO and O₃, whereas the latter half of the time series shows lower concentrations of these anthropogenic markers and SO₂. Although DMS loses its diurnal cycle within the cleaner air mass and is present at consistently high concentrations (which could be attributable to its local source), the SO₂ time series still displays a diurnal structure that aligns with UVA irradiance, supporting the idea of DMS photooxidation to SO₂. Therefore, this qualitative analysis suggests that photooxidation of DMS released from the exposed ocean at the sea ice edge or from melt ponds on the ice surface contributes a greater amount to the observed SO₂ mixing ratios during the cleaner air mass time period (from 10th June onward) compared to the relatively more polluted period (up to 10th June). However, a quantitative analysis of the contribution of anthropogenic versus natural sources to the observed SO₂ mixing ratios cannot be made without a comprehensive modelling study, although the importance of considering complex meteorology effects, namely mixing and dispersion of air masses, when interpreting this data has been demonstrated.

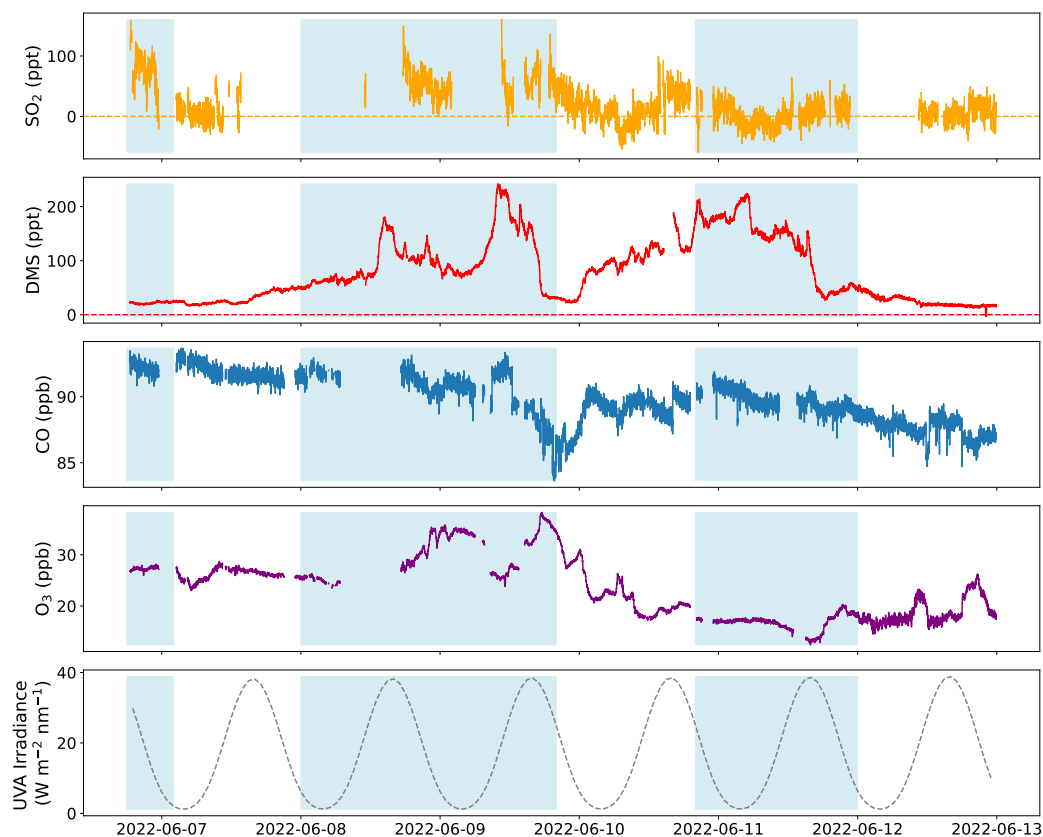


Figure 4.20: 1-minute averaged SO₂, DMS, CO and O₃ time series at the sea ice station, with the sea ice edge data highlighted in blue. All datasets have been filtered for relative wind speed and direction (to remove ship stack measurements) as well as spike enhancements due to anthropogenic influences. Hourly modelled UVA irradiance from the TUV Radiation Model is also plotted.

Evidence of DMS photooxidation to SO₂ is supported by box-modelling work performed by collaborators at the University of Cambridge. They developed an updated Master Chemical Mechanism (MCM, v3.3.1) scheme for DMS oxidation by adding 62 reactions, including those for the HPMTF pathway, and adjusting 21 reactions, as described in Jacob et al., 2024. Using this updated mechanism, they then ran a 0-D box model (BOXMOX) constrained to the DMS mixing ratios measured during the campaign, in addition to O₃, CO, CH₄, and HCHO mixing ratios and meteorological measurements of

relative humidity, temperature and pressure. Photolysis and dilution/mixing rates, condensation sinks (loss of H₂SO₄ and MSA to aqueous phase) and initial/background concentrations were also considered and included as inputs into the model. It is also worthy to point out that the mechanism only includes gas-phase reactions and excludes halogen chemistry. A comparison of observed and modelled diel profiles can be seen in Figure 4.18. The shape of the modelled diel cycle is in excellent agreement with the observed, which is consistent with DMS photooxidation to SO₂. However, comparing the SO₂ mixing ratio ranges for the observed and modelled diel profiles shows that the range of modelled mixing ratios are a factor of approximately four times lower than the observed. This underestimation of SO₂ by the model could be explained by DMS being emitted at a distance from the ice edge. Therefore, less DMS would be measured at the ship position due to oxidation and since the model uses the DMS mixing ratios as its input to model SO₂, lower SO₂ mixing ratios would be predicted. Furthermore, as suggested earlier, other sources of SO₂ could be contributing to the observed background SO₂ mixing ratios at the ice edge, such as those from anthropogenic emissions.

4.4.2.4 Maniitsoq

Finally the SO₂ and DMS mixing ratios seen at Maniitsoq are consistent with the interpretations made thus far. The high DMS mixing ratios (~ 150 ppt) are likely to result from DMS emissions from the sea ice edge and open ocean where chlorophyll-a concentrations are relatively high at approximately 10 mg m⁻³. Depending on the time of day and therefore the lifetime of DMS, the source of SO₂ could also be from this region but again, could also originate from more distant DMS emissions as well as potential transported anthropogenic sources.

Reaction	Reaction rate ($\times 10^{-12}$ cm ³ molec ⁻¹ s ⁻¹)	Mixing ratio of oxidant (ppt)	Lifetime of DMS due to oxidant (days)
DMS + OH abstraction	4.5	0.018	1.7
DMS + OH addition	9.6		
DMS + NO ₃	1.3	0.13	2.6
DMS + BrO	0.58	1*	0.74

Table 4.2: Estimated atmospheric lifetimes of DMS due to the oxidants OH, NO₃ and BrO, calculated from the IUPAC recommended reaction rates of DMS + oxidant and the approximated campaign mean oxidant concentrations. *The mixing ratio of BrO is taken from observations made by Jeong et al., 2022.

The observations and subsequent interpretation of the data from the SEANA campaign is also consistent with literature studies. Firstly, for the diel profiles in Figure 4.18, a similar anticorrelation relationship between DMS and SO₂ has been observed by Bandy et al., 1996, Chen et al., 2000, and Faloon et al., 2009 in the equatorial Pacific, by De Bruyn et al., 1998, De Bruyn et al., 2002 and Shon et al., 2001 in the Southern Ocean and by Yang et al., 2016 in the North Atlantic, which has been attributed to DMS photooxidation to SO₂. Also, the conversion efficiency from DMS to SO₂ can be calculated from the difference between the maxima and minima mixing ratios of their diel cycles, which has been reported as 70 - 90 % due to OH oxidation (Davis et al., 1999; Chen et al., 2000; Shon et al., 2001) and 75 % due to OH and NO₃ (Chen et al., 2018). The diel profiles in Figure 4.18 yield a conversion efficiency of 56 %, which is somewhat inconsistent with

Chapter 4. Arctic SO₂ Measurements

DMS oxidation solely by OH. Therefore, an estimation of the lifetime of DMS due to NO₃ and BrO has been made. Firstly, the concentration of NO₃ has been calculated from the measured reactant concentrations of NO₂ + O₃, assuming NO₃ only reacts with NO₂ and DMS and only during hours 2 to 5 when the UVA irradiance is zero ('nighttime'). However, since the mean NO₂ concentration measured during the campaign of 46 ppt is below the instrument's LoD of 50 ppt, the LoD value has been used for the calculation of NO₃ concentration. The campaign mean O₃ concentration was 27 ppb. Therefore, using the IUPAC recommended reaction rate constant for NO₂ + O₃ of $1.6 \times 10^{-17} \text{ cm}^3 \text{ molecules}^{-1} \text{ s}^{-1}$ at 1 bar and 273 K, the NO₃ concentration has been estimated as 0.13 ppt. Therefore, the DMS lifetime due to NO₃ has been calculated via Equation 4.1 as 2.6 days, which is longer than that due to OH. Considering NO₃ primarily exists during the 3 hours of nighttime, its overall contribution to DMS oxidation is likely to be fairly negligible compared to OH. For the BrO-determined DMS lifetime, the absence of BrO measurements during the SEANA campaign and the large uncertainties in modelled BrO in this work means that a BrO concentration of 1 ppt (maximum estimate) has been used, based on observations reported by Jeong et al., 2022 during late May in the Alaskan Arctic. Their observations prior to this are influenced by the bromine explosion event that occurs in the polar spring (March to May in the Arctic) due to the return of sunlight after polar night through snowmelt, when halogens dominate oxidation processes (Simpson et al., 2015). Therefore, despite the DMS + BrO reaction rate being slower than with OH, the potentially higher concentration of BrO means that the DMS lifetime due to BrO is shorter compared to OH, however, this result is highly uncertain. It does show that BrO could be responsible for a significant rate of oxidation, in line with other studies (Glasow et al., 2004; Toumi, 1994; Chen et al., 2018; Fung et al., 2022). Since BrO increases the importance of the addition branch in the oxidation of DMS, this gives smaller DMS to SO₂ conversion efficiencies (Glasow et al., 2004), which

could contribute to the lower conversion efficiency than that of solely OH oxidation seen in this work.

Literature studies also support the conclusions made from Figure 4.16. Leck et al., 1996 measured atmospheric SO₂ and DMS and seawater DMS in the open waters and along the ice edge zone in the Greenland Sea-Fram Strait area as well as in the permanent pack ice of the Nansen and Amundsen basins. They reported generally higher atmospheric SO₂ and DMS concentrations over the open ocean at the ice edge compared to the pack ice, with the lowest concentrations observed in air masses that spent significant time over the pack ice. Also during their pack ice measurements, the ratio of atmospheric DMS to seawater DMS was for most of the time < 10 %, hence providing evidence for the assumption that the pack ice inhibits sea-air exchange. Finally, Rempillo et al., 2011 measured atmospheric SO₂ and DMS in the Canadian Arctic and Baffin Bay and, using stable isotope apportionment techniques, approximated the contribution of biogenic SO₂. They found instances where biogenic SO₂ concentrations exceeded DMS concentrations, which they attributed to biogenic SO₂ being transported from a wider source region. Similar instances were seen in the SEANA SO₂ and DMS data and we suggested that SO₂ could originate from DMS emitted at distances longer than its atmospheric lifetime. However, in absence of source apportionment techniques or regional model studies, anthropogenic sources of SO₂ cannot be ruled out.

4.5 Conclusions

The LIF-SO₂ instrument was deployed and demonstrated on a research cruise to the Arctic. Despite a number of instrument issues which delayed the start of data acquisition, approximately 2 weeks of intermittent data was obtained to form a unique dataset of Arctic SO₂ measurements and the first LIF measurements of SO₂ on board a ship. Background SO₂ mixing ratios in the Arctic were on the order of 0 to 100 pptv (78 % of measurements), and hence the data was averaged to 5 minutes, for which our LoD (3σ) was 15 pptv, in order to capture these low concentrations.

Regarding the instrument performance, issues with temperature consistency was found to be the main cause of sensitivity variations across the campaign. However, for each data block (from instrument turn on to turn off), sensitivities largely agreed within error and hence a mean sensitivity has been applied to each data block. The reference LIF signal has also been used to identify periods of poor laser linewidth due to more extreme temperature changes within the laser box, causing the dither algorithm to lose track of the transition peak. Therefore, these periods have been discarded from the dataset. Another issue impacting data coverage was loss of connection to the LabVIEW software due to an apparent memory leak on the cRIO. This meant that the instrument was unable to run for longer than ~ 48 hours without having to be power cycled in a controlled way. Finally, due to the necessity for a long inlet line during this campaign (~ 10 m), post-campaign testing demonstrated that inlet losses of SO₂ to the walls of the tubing were negligible.

The potential sources of SO₂ were investigated during this Arctic campaign. The spikes of SO₂ mixing ratio enhancements were found to correspond to spikes in anthropogenic markers of NO_x, CO₂ and CO. Since these enhancements were relatively short in duration and their NO_x:CO₂ and SO₂:CO₂ emission ratios were on the order of those expected for shipping

emissions, these SO₂ spikes were attributed to shipping activity in the local area. Observations during the cruise of fishing vessels in the vicinity of the ship position, particularly at the sea ice, are also consistent with this conclusion.

Biogenic sources of SO₂ from photooxidation of DMS were found to be consistent with back trajectory analyses and lifetimes of DMS and SO₂ in the Arctic, determined as 1.7 and 19 days respectively from solely OH oxidation. It was seen that both SO₂ and DMS concentrations were highest for air masses that had travelled over the open ocean and along the sea ice edge where DMS air-sea exchange is greatest. However, a clear diurnal pattern of decreasing DMS throughout the day, anticorrelated with SO₂, was only seen at the sea ice edge, where sufficient data was collected for a statistically valid analysis and where DMS emissions are thought to be relatively close to the ship (minimising the effect of transport times, lifetimes etc.). This observed diurnal pattern was consistent with box model estimates, using an updated MCM DMS oxidation mechanism, which includes the HPMTF pathway.

The observed conversion efficiency of SO₂ from DMS (56 %) was found to be lower than model estimates due to DMS oxidation solely by OH (70 - 90 %). Hence, it is suggested that other oxidants, mainly that of BrO could be significant at these latitudes, making the DMS addition pathway that leads to MSA formation more important. Due to the lack of measurements of other species involved in the DMS oxidation mechanism, such as BrO, NO₃ (nighttime oxidant), HPMTF, MSA, MSIA etc., the measurements during this campaign are unable to provide more insights into the DMS oxidation mechanism, which should be the focus of future campaigns.

Bibliography

- [1] Abbatt, J. P., Richard Leitch, W., Aliabadi, A. A., Bertram, A. K., Blanchet, J. P., Boivin-Rioux, A., Bozem, H., Burkart, J., Chang, R. Y., Charette, J., Chaubey, J. P., Christensen, R. J., Cirisan, A., Collins, D. B., Croft, B., Dionne, J., Evans, G. J., Fletcher, C. G., Gali, M., Ghahremaninezhad, R., Girard, E., Gong, W., Gosselin, M., Gourdal, M., Hanna, S. J., Hayashida, H., Herber, A. B., Hesarakı, S., Hoor, P., Huang, L., Hussherr, R., Irish, V. E., Keita, S. A., Kodros, J. K., Köllner, F., Kolonjari, F., Kunkel, D., Ladino, L. A., Law, K., Levasseur, M., Libois, Q., Liggio, J., Lizotte, M., MacDonald, K. M., Mahmood, R., Martin, R. V., Mason, R. H., Miller, L. A., Moravek, A., Mortenson, E., Mungall, E. L., Murphy, J. G., Namazi, M., Norman, A. L., O'Neill, N. T., Pierce, J. R., Russell, L. M., Schneider, J., Schulz, H., Sharma, S., Si, M., Staebler, R. M., Steiner, N. S., Thomas, J. L., Von Salzen, K., Wentzell, J. J., Willis, M. D., Wentworth, G. R., Xu, J. W., and Yakobi-Hancock, J. D. (2019). Overview paper: New insights into aerosol and climate in the Arctic. *Atmospheric Chemistry and Physics* 19.4, pp. 2527–2560. DOI: 10.5194/acp-19-2527-2019 (cit. on p. 153).
- [2] Aliabadi, A. A., Thomas, J. L., Herber, A. B., Staebler, R. M., Leitch, W. R., Schulz, H., Law, K. S., Marelle, L., Burkart, J., Willis, M. D., Bozem, H., Hoor, P. M., Köllner, F., Schneider, J., Levasseur, M., and Abbatt, J. P. (2016). Ship emissions measurement in the Arctic by plume intercepts of the Canadian Coast Guard icebreaker Amundsen from the Polar 6 aircraft platform. *Atmospheric Chemistry and Physics* 16.12, pp. 7899–7916. DOI: 10.5194/acp-16-7899-2016 (cit. on p. 139).

Chapter 4. Arctic SO₂ Measurements

- [3] Almeida, J., Schobesberger, S., Kürten, A., Ortega, I. K., Kupiainen-Määttä, O., Praplan, A. P., Adamov, A., Amorim, A., Bianchi, F., Breitenlechner, M., David, A., Dommen, J., Donahue, N. M., Downard, A., Dunne, E., Duplissy, J., Ehrhart, S., Flagan, R. C., Franchin, A., Guida, R., Hakala, J., Hansel, A., Heinritzi, M., Henschel, H., Jokinen, T., Junninen, H., Kajos, M., Kangasluoma, J., Keskinen, H., Kupc, A., Kurtén, T., Kvashin, A. N., Laaksonen, A., Lehtipalo, K., Leiminger, M., Leppä, J., Loukonen, V., Makhmutov, V., Mathot, S., McGrath, M. J., Nieminen, T., Olenius, T., Onnela, A., Petäjä, T., Riccobono, F., Riipinen, I., Rissanen, M., Rondo, L., Ruuskanen, T., Santos, F. D., Sarnela, N., Schallhart, S., Schnitzhofer, R., Seinfeld, J. H., Simon, M., Sipilä, M., Stozhkov, Y., Stratmann, F., Tomé, A., Tröstl, J., Tsagkogeorgas, G., Vaattovaara, P., Viisanen, Y., Virtanen, A., Vrtala, A., Wagner, P. E., Weingartner, E., Wex, H., Williamson, C., Wimmer, D., Ye, P., Yli-Juuti, T., Carslaw, K. S., Kulmala, M., Curtius, J., Baltensperger, U., Worsnop, D. R., Vehkamäki, H., and Kirkby, J. (2013). Molecular understanding of sulphuric acid–amine particle nucleation in the atmosphere. *Nature* 502.7471, pp. 359–363. DOI: 10.1038/nature12663 (cit. on p. 28).
- [4] Andreae, M. O., Ferek, R. J., Bermond, F., Byrd, K. P., Engstrom, R. T., Hardin, S., Houmère, P. D., LeMarrec, F., Raemdonck, H., and Chatfield, R. B. (1985). Dimethyl sulfide in the marine atmosphere. *Journal of Geophysical Research: Atmospheres* 90.D7, pp. 12891–12900. DOI: 10.1029/JD090iD07p12891 (cit. on p. 35).
- [5] Andreae, M. O. (1990). Ocean-atmosphere interactions in the global biogeochemical sulfur cycle. *Marine Chemistry* 30, pp. 1–29. DOI: 10.1016/0304-4203(90)90059-L (cit. on p. 35).
- [6] Atkinson, R, Baulch, D. L., Cox, R. A., Crowley, J. N., Hampson, R. F., Hynes, R. G., Jenkin, M. E., Rossi, M. J., and Troe, J (2004). Atmospheric Chemistry and Physics Evaluated kinetic and photochemical data for atmospheric chemistry: Volume I-gas phase reactions of O_x, HO_x, NO_x and SO_x species The IUPAC Subcommittee on Gas Kinetic Data Evaluation for Atmospheric Chemistry. *Atmos. Chem. Phys* 4.6, pp. 1461–1738. DOI: 10.5194/acp-4-1461-2004 (cit. on p. 27).

Chapter 4. Arctic SO₂ Measurements

- [7] Ayers, G. P. and Cainey, J. M. (2007). The CLAW hypothesis: a review of the major developments. *Environmental Chemistry* 4.6, pp. 366–374. DOI: 10.1071/EN07080 (cit. on p. 35).
- [8] Bandy, A. R., Thornton, D. C., Blomquist, B. W., Chen, S., Wade, T. P., Ianni, J. C., Mitchell, G. M., and Nadler, W. (1996). Chemistry of dimethyl sulfide in the equatorial Pacific atmosphere. *Geophysical Research Letters* 23.7, pp. 741–744. DOI: 10.1029/96GL00779 (cit. on p. 203).
- [9] Barnes, I., Hjorth, J., and Mihalopoulos, N. (2006). Dimethyl Sulfide and Dimethyl Sulfoxide and Their Oxidation in the Atmosphere. *Chem. Rev.* 106.3, pp. 940–975. DOI: 10.1021/cr020529+ (cit. on p. 38).
- [10] Barrie, L. A. and Hoff, R. M. (1984). The oxidation rate and residence time of sulphur dioxide in the arctic atmosphere. *Atmospheric Environment (1967)* 18.12, pp. 2711–2722. DOI: 10.1016/0004-6981(84)90337-8 (cit. on p. 192).
- [11] Barrie, L. A., Hoff, R. M., and Daggupati, S. M. (1981). The influence of mid-latitude pollution sources on haze in the Canadian arctic. *Atmospheric Environment (1967)* 15.8, pp. 1407–1419. DOI: 10.1016/0004-6981(81)90347-4 (cit. on p. 180).
- [12] Bates, T. S., Lamb, B. K., Guenther, A., Dignon, J., and Stoiber, R. E. (1992). Sulfur emissions to the atmosphere from natural sources. *Journal of Atmospheric Chemistry* 14.1, pp. 315–337. DOI: 10.1007/BF00115242 (cit. on p. 35).
- [13] Beecken, J., Mellqvist, J., Salo, K., Ekholm, J., and Jalkanen, J. P. (2014). Airborne emission measurements of SO₂, NO_x and particles from individual ships using a sniffer technique. *Atmospheric Measurement Techniques* 7.7, pp. 1957–1968. DOI: 10.5194/amt-7-1957-2014 (cit. on pp. 121, 139).
- [14] Berg, N., Mellqvist, J., Jalkanen, J. P., and Balzani, J. (2012). Ship emissions of SO₂ and NO₂: DOAS measurements from airborne platforms. *Atmospheric Measurement Techniques* 5.5, pp. 1085–1098. DOI: 10.5194/amt-5-1085-2012 (cit. on pp. 121, 139).

Chapter 4. Arctic SO₂ Measurements

- [15] Berndt, T., Scholz, W., Mentler, B., Fischer, L., Hoffmann, E. H., Tilgner, A., Hyttinen, N., Prisle, N. L., Hansel, A., and Herrmann, H. (2019). Fast Peroxy Radical Isomerization and OH Recycling in the Reaction of OH Radicals with Dimethyl Sulfide. *Journal of Physical Chemistry Letters* 10.21, pp. 6478–6483. doi: 10.1021/acs.jpcllett.9b02567 (cit. on pp. 36, 38).
- [16] Bian, H., Chin, M., Colarco, P. R., Apel, E. C., Blake, D. R., Froyd, K., Hornbrook, R. S., Jimenez, J., Jost, P. C., Lawler, M., Liu, M., Lund, M. T., Matsui, H., Nault, B. A., Penner, J. E., Rollins, A. W., Schill, G., Skeie, R. B., Wang, H., Xu, L., Zhang, K., and Zhu, J. (2024). Observationally constrained analysis of sulfur cycle in the marine atmosphere with NASA ATom measurements and AeroCom model simulations. *Atmospheric Chemistry and Physics* 24.3, pp. 1717–1741. doi: 10.5194/ACP-24-1717-2024 (cit. on pp. 41, 44, 45, 120).
- [17] Bilsback, K. R., Kerry, D., Croft, B., Ford, B., Jathar, S. H., Carter, E., Martin, R. V., and Pierce, J. R. (2020). Beyond SO_x reductions from shipping: assessing the impact of NO_x and carbonaceous-particle controls on human health and climate. *Environmental Research Letters* 15.12, p. 124046. doi: 10.1088/1748-9326/abc718 (cit. on p. 120).
- [18] Blitz, M. A., Hughes, K. J., and Pilling, M. J. (2003). Determination of the high-pressure limiting rate coefficient and the enthalpy of reaction for OH + SO₂. *Journal of Physical Chemistry A* 107.12, pp. 1971–1978. doi: 10.1021/jp026524y (cit. on pp. 26, 27).
- [19] Boy, M., Kulmala, M., Ruuskanen, T. M., Pihlatie, M., Reissell, A., Aalto, P. P., Keronen, P., Dal Maso, M., Hellen, H., Hakola, H., Jansson, R., Hanke, M., and Arnold, F. (2005). Sulphuric acid closure and contribution to nucleation mode particle growth. *Atmos. Chem. Phys* 5.4, pp. 863–878. doi: 10.5194/acp-5-863-2005 (cit. on p. 28).

Chapter 4. Arctic SO₂ Measurements

- [20] Boyer, M., Aliaga, D., Quéléver, L. L. J., Bucci, S., Angot, H., Dada, L., Heutte, B., Beck, L., Duetsch, M., Stohl, A., Beck, I., Laurila, T., Sarnela, N., Thakur, R. C., Miljevic, B., Kulmala, M., Petäjä, T., Sipilä, M., Schmale, J., and Jokinen, T. (n.d.). The annual cycle and sources of relevant aerosol precursor vapors in the central Arctic (). doi: 10.5194/egusphere-2023-2953 (cit. on pp. 41, 182, 187).
- [21] Bradshaw, J. D., Rodgers, M. O., and Davis, D. D. (1982). Single-photon laser-induced fluorescence detection of NO and SO₂ for atmospheric conditions of composition and pressure: errata. *Applied optics* 21.21, p. 3810. doi: 10.1364/AO.21.003810 (cit. on p. 54).
- [22] Butkovskaya, N. I., Poulet, G, and Lebras, G (1995). Discharge Flow Study of the Reactions of Chlorine and Fluorine Atoms with Dimethyl Sulfide. *J. Phys. Chem* 99.13, pp. 4536–4543 (cit. on p. 38).
- [23] Cameron, W. D., Bernath, P, and Boone, C (2021). Sulfur dioxide from the atmospheric chemistry experiment (ACE) satellite. *Journal of Quantitative Spectroscopy & Radiative Transfer* 258.107341. doi: 10.1016/j.jqsrt.2020.107341 (cit. on p. 183).
- [24] Capaldo, K., Corbett, J. J., Kasibhatla, P., Fischbeck, P., and Pandis, S. N. (1999). Effects of ship emissions on sulphur cycling and radiative climate forcing over the ocean. *Nature* 400.6746, pp. 743–746. doi: 10.1038/23438 (cit. on p. 119).
- [25] Carslaw, K. S., Boucher, O., Spracklen, D. V., Mann, G. W., L. Rae, J. G., Woodward, S., and Kulmala, M. (2010). A review of natural aerosol interactions and feedbacks within the Earth system. *Atmospheric Chemistry and Physics* 10.4, pp. 1701–1737. doi: 10.5194/acp-10-1701-2010 (cit. on p. 35).
- [26] Carslaw, K. S., Lee, L. A., Reddington, C. L., Pringle, K. J., Rap, A., Forster, P. M., Mann, G. W., Spracklen, D. V., Woodhouse, M. T., Regayre, L. A., and Pierce, J. R. (2013). Large contribution of natural aerosols to uncertainty in indirect forcing. *Nature* 503.7474, pp. 67–71. doi: 10.1038/nature12674 (cit. on pp. 34, 36).

Chapter 4. Arctic SO₂ Measurements

- [27] Charlson, R. J., Schwartz, S. E., Hales, J. M., Cess, R. D., Coakley, J. A., Hansen, J. E., and Hofmann, D. J. (1992). Climate Forcing by Anthropogenic Aerosols. *Science* 255.5043, pp. 423–430. doi: 10.1126/science.255.5043.423 (cit. on p. 32).
- [28] Charlson, R. J., Lovelock, J. E., Andreae, M. O., and Warren, S. G. (1987). Oceanic phytoplankton, atmospheric sulphur, cloud albedo and climate. *Nature* 326, pp. 655–661. doi: 10.1038/326655a0 (cit. on p. 35).
- [29] Chen, G., Davis, D. D., Kasibhatla, P., Bandy, A. R., Thornton, D. C., Huebert, B. J., Clarke, A. D., and Blomquist, B. W. (2000). A study of DMS oxidation in the tropics: Comparison of christmas island field observation of DMS, SO₂, and DMSO with model simulations. *Journal of Atmospheric Chemistry* 37.2, pp. 137–160. doi: 10.1023/A:1006429932403 (cit. on p. 203).
- [30] Chen, Q., Geng, L., Schmidt, J., Xie, Z., Kang, H., Dachs, J., Cole-Dai, J., Schauer, A., Camp, M., and Alexander, B. (2016). Isotopic constraints on the role of hypohalous acids in sulfate aerosol formation in the remote marine boundary layer. *Atmospheric Chemistry and Physics* 16.17, pp. 11433–11450. doi: 10.5194/acp-16-11433-2016 (cit. on p. 30).
- [31] Chen, Q., Sherwen, T., Evans, M., and Alexander, B. (2018). DMS oxidation and sulfur aerosol formation in the marine troposphere: A focus on reactive halogen and multiphase chemistry. *Atmospheric Chemistry and Physics* 18.18, pp. 13617–13637. doi: 10.5194/acp-18-13617-2018 (cit. on pp. 36, 38, 203, 204).
- [32] Cheng, Y., Wang, S., Zhu, J., Guo, Y., Zhang, R., Liu, Y., Zhang, Y., Yu, Q., Ma, W., and Zhou, B. (2019). Surveillance of SO₂ and NO₂ from ship emissions by MAX-DOAS measurements and the implications regarding fuel sulfur content compliance. *Atmospheric Chemistry and Physics* 19.21, pp. 13611–13626. doi: 10.5194/acp-19-13611-2019 (cit. on p. 121).
- [33] Chylek, P., Folland, C., Klett, J. D., Wang, M., Hengartner, N., Lesins, G., and Dubey, M. K. (2022). Annual Mean Arctic Amplification 1970–2020: Observed and Simulated by CMIP6 Climate Models. *Geophysical Research Letters* 49.13, e2022GL099371. doi: 10.1029/2022GL099371 (cit. on p. 153).

Chapter 4. Arctic SO₂ Measurements

- [34] Corbett, J. J., Lack, D. A., Winebrake, J. J., Harder, S., Silberman, J. A., and Gold, M. (2010). Arctic shipping emissions inventories and future scenarios. *Atmospheric Chemistry and Physics* 10.19, pp. 9689–9704. DOI: 10.5194/acp-10-9689-2010 (cit. on p. 154).
- [35] Dalsøren, S. B., Samset, B. H., Myhre, G., Corbett, J. J., Minjares, R., Lack, D., and Fuglestvedt, J. S. (2013). Environmental impacts of shipping in 2030 with a particular focus on the Arctic region. *Atmospheric Chemistry and Physics* 13.4, pp. 1941–1955. DOI: 10.5194/acp-13-1941-2013 (cit. on p. 155).
- [36] Davis, D., Chen, G., Bandy, A., Thornton, D., Eisele, F., Mauldin, L., Tanner, D., Lenschow, D., Fuelberg, H., Huebert, B., Heath, J., Clarke, A., and Blake, D. (1999). Dimethyl sulfide oxidation in the equatorial Pacific: Comparison of model simulations with field observations for DMS, SO₂, H₂SO₄(g), MSA(g), MS and NSS. *Journal of Geophysical Research: Atmospheres* 104.D5, pp. 5765–5784. DOI: 10.1029/1998JD100002 (cit. on p. 203).
- [37] De Bruyn, W. J., Bates, T. S., Cainey, J. M., and Saltzman, E. S. (1998). Shipboard measurements of dimethyl sulfide and SO₂ southwest of Tasmania during the First Aerosol Characterization Experiment (ACE 1). *Journal of Geophysical Research: Atmospheres* 103.D13, pp. 16703–16711. DOI: 10.1029/98JD00971 (cit. on p. 203).
- [38] De Bruyn, W. J., Harvey, M., Cainey, J. M., and Saltzman, E. S. (2002). DMS and SO₂ at Baring Head, New Zealand: Implications for the yield of SO₂ from DMS. *Journal of Atmospheric Chemistry* 41.2, pp. 189–209. DOI: 10.1023/A:1014252106572 (cit. on p. 203).

Chapter 4. Arctic SO₂ Measurements

- [39] Denman, K. L., Brasseur, G., Chidthaisong, A., Ciais, P., Cox, P. M., Dickinson, R. E., Hauglustaine, D., Heinze, C., Holland, E., Jacob, D., Lohmann, U., Ramachandran, S., Silva Dias, P. L. da, Wofsy, S. C., and Zhang, X. (2007). Couplings Between Changes in the Climate System and Biogeochemistry. In: *Climate Change 2007: The Physical Science Basis. Contribution of Working Group I to the Fourth Assessment Report of the Intergovernmental Panel on Climate Change*. Ed. by S. Solomon, D. Qin, M. Manning, Z. Chen, M. Marquis, K. B. Averyt, M. Tignor, and H. L. Miller. Cambridge, United Kingdom and New York, NY, USA: Cambridge University Press (cit. on p. 32).
- [40] Diamond, M. S. (2023). Detection of large-scale cloud microphysical changes within a major shipping corridor after implementation of the International Maritime Organization 2020 fuel sulfur regulations. *Atmospheric Chemistry and Physics* 23.14, pp. 8259–8269. doi: 10.5194/acp-23-8259-2023 (cit. on p. 120).
- [41] *Double-clad Fibers* (n.d.). doi: 10.61835/TL9 (cit. on p. 62).
- [42] Eckhardt, S, Hermansen, O, Grythe, H, Fiebig, M, Stebel, K, Cassiani, M, Baecklund, A, and Stohl, A (2013). Sciences ess Atmospheric Chemistry and Physics Climate of the Past Geoscientific Instrumentation Methods and Data Systems The influence of cruise ship emissions on air pollution in Svalbard-a harbinger of a more polluted Arctic? *Atmos. Chem. Phys* 13, pp. 8401–8409. doi: 10.5194/acp-13-8401-2013 (cit. on p. 154).
- [43] Eguíluz, V. M., Fernández-Gracia, J., Irigoien, X., and Duarte, C. M. (2016). A quantitative assessment of Arctic shipping in 2010–2014. *Scientific Reports* 6.1. doi: 10.1038/srep30682 (cit. on p. 154).
- [44] Emmons, L. K., Schwantes, R. H., Orlando, J. J., Tyndall, G., Kinnison, D., Lamarque, J. F., Marsh, D., Mills, M. J., Tilmes, S., Bardeen, C., Buchholz, R. R., Conley, A., Gettelman, A., Garcia, R., Simpson, I., Blake, D. R., Meinardi, S., and Pétron, G. (2020). The Chemistry Mechanism in the Community Earth System Model Version 2 (CESM2). *Journal of Advances in Modeling Earth Systems* 12.4, e2019MS001882. doi: 10.1029/2019MS001882 (cit. on p. 39).

Chapter 4. Arctic SO₂ Measurements

- [45] Environment, F. Department for and webmaster@defra.gsi.gov.uk, R. A. D. (2024). *Emissions of air pollutants in the UK – Sulphur dioxide (SO₂) - GOV.UK* (cit. on p. 119).
- [46] Faloon, I. (2009). Sulfur processing in the marine atmospheric boundary layer: A review and critical assessment of modeling uncertainties. *Atmospheric Environment* 43.18, pp. 2841–2854. doi: 10.1016/j.atmosenv.2009.02.043 (cit. on pp. 26, 29, 36, 38, 119, 190).
- [47] Faloon, I., Conley, S. A., Blomquist, B., Clarke, A. D., Kapustin, V., Howell, S., Lenschow, D. H., and Bandy, A. R. (2009). Sulfur dioxide in the tropical marine boundary layer: Dry deposition and heterogeneous oxidation observed during the pacific atmospheric sulfur experiment. *Journal of Atmospheric Chemistry* 63.1, pp. 13–32. doi: 10.1007/s10874-010-9155-0 (cit. on pp. 41, 44, 45, 203).
- [48] Faloon, I. C., Tan, D., Leshner, R. L., Hazen, N. L., Frame, C. L., Simpas, J. B., Harder, H., Martinez, M., Di Carlo, P., Ren, X., and Brune, W. H. (2004). A laser-induced fluorescence instrument for detecting tropospheric OH and HO₂: Characteristics and calibration. *Journal of Atmospheric Chemistry* 47.2, pp. 139–167. doi: 10.1023/B:JOCH.0000021036.53185.0e (cit. on p. 109).
- [49] *Fiber modulator: how to choose the good technology? Fiber modulator basics* (n.d.) (cit. on p. 60).
- [50] Fiedler, V., Nau, R., Ludmann, S., Arnold, F., Schlager, H., and Stohl, A. (2009). East Asian SO₂ pollution plume over Europe – Part 1: Airborne trace gas measurements and source identification by particle dispersion model simulations. *Atmospheric Chemistry and Physics* 9.14, pp. 4717–4728. doi: 10.5194/acp-9-4717-2009 (cit. on p. 121).
- [51] Firket, J. (1936). Fog along the Meuse valley. *Transactions of the Faraday Society* 32.0, pp. 1192–1196. doi: 10.1039/TF9363201192 (cit. on p. 119).

Chapter 4. Arctic SO₂ Measurements

- [52] Forster, P., Storelvmo, T., Armour, K., Collins, W., Dufresne, J.-L., Frame, D., Lunt, D. J., Mauritsen, T., Palmer, M. D., Watanabe, M., Wild, M., and Zhang, H. (2021). Climate Change 2021: The Physical Science Basis. Contribution of Working Group I to the Sixth Assessment Report of the Intergovernmental Panel on Climate Change. *The Earth's Energy Budget, Climate Feedbacks, and Climate Sensitivity*. In *Climate Change 2021: The Physical Science Basis. Contribution of Working Group I to the Sixth Assessment Report of the Intergovernmental Panel on Climate Change*. Ed. by V. Masson-Delmotte, V. P. Zhai, A. Pirani, S. L. Connors, C. Péan, S. Berger, N. Caud, Y. Chen, L. Goldfarb, M. I. Gomis, M. Huang, K. Leitzell, E. Lonnoy, J. B. R. Matthews, T. K. Maycock, T. Waterfield, O. Yelekçi, R. Yu, and B. Zhou. Cambridge, United Kingdom and New York, NY, USA: Cambridge University Press, pp. 923–1054. doi: 10.1017/9781009157896.009 (cit. on pp. 33, 34, 119).
- [53] *Frequency Doubling* (n.d.). doi: 10.61835/7JB (cit. on p. 79).
- [54] Fung, K. M., Heald, C. L., Kroll, J. H., Wang, S., Jo, D. S., Gettelman, A., Lu, Z., Liu, X., Zaveri, R. A., Apel, E. C., Blake, D. R., Jimenez, J.-L., Campuzano-Jost, P., Veres, P. R., Bates, T. S., Shilling, J. E., and Zawadowicz, M. (2022). Exploring dimethyl sulfide (DMS) oxidation and implications for global aerosol radiative forcing. *Atmos. Chem. Phys* 22.2, pp. 1549–1573. doi: 10.5194/acp-22-1549-2022 (cit. on pp. 35, 37, 39, 191, 204).
- [55] Galí, M., Devred, E., Babin, M., and Levasseur, M. (2019). Decadal increase in Arctic dimethylsulfide emission. *Proceedings of the National Academy of Sciences of the United States of America* 116.39, pp. 19311–19317. doi: 10.1073/pnas.190437811 (cit. on p. 153).
- [56] Gao, J., Wang, H., Liu, W., Xu, H., Wei, Y., Tian, X., Feng, Y., Song, S., and Shi, G. (2024). Hydrogen peroxide serves as pivotal fountainhead for aerosol aqueous sulfate formation from a global perspective. *Nature Communications* 15.1, p. 4625. doi: 10.1038/s41467-024-48793-1 (cit. on pp. 29, 30).

Chapter 4. Arctic SO₂ Measurements

- [57] Gettelman, A., Christensen, M. W., Diamond, M. S., Gryspeerdt, E., Man-
shausen, P., Stier, P., Watson-Parris, D., Yang, M., Yoshioka, M., and Yuan,
T. (2024). Has Reducing Ship Emissions Brought Forward Global Warm-
ing? *Geophysical Research Letters* 51.15, e2024GL109077. doi: 10.1029/
2024GL109077 (cit. on p. 120).
- [58] Ghahremaninezhad, R., Gong, W., Galí, M., Norman, A. L., Beagley, S. R.,
Akingunola, A., Zheng, Q., Lupu, A., Lizotte, M., Levasseur, M., and Richard
Leaitch, W. (2019). Dimethyl sulfide and its role in aerosol formation and
growth in the Arctic summer - A modelling study. *Atmospheric Chemistry
and Physics* 19.23, pp. 14455–14476. doi: 10.5194/acp-19-14455-2019
(cit. on p. 191).
- [59] Ghan, S., Wang, M., Zhang, S., Ferrachat, S., Gettelman, A., Griesfeller, J.,
Kipling, Z., Lohmann, U., Morrison, H., Neubauer, D., Partridge, D. G., Stier,
P., Takemura, T., Wang, H., and Zhang, K. (2016). Challenges in constraining
anthropogenic aerosol effects on cloud radiative forcing using present-day
spatiotemporal variability. *Proceedings of the National Academy of Sciences
of the United States of America* 113.21, pp. 5804–5811. doi: 10.1073/pnas.
1514036113 (cit. on p. 35).
- [60] Glasow, R. von and Crutzen, P. J. (2004). Model study of multiphase DMS
oxidation with a focus on halogens. *Atmospheric Chemistry and Physics* 4.3,
pp. 589–608. doi: 10.5194/acp-4-589-2004 (cit. on pp. 38, 191, 204).
- [61] Gong, W., Beagley, S. R., Cousineau, S., Sassi, M., Munoz-Alpizar, R., Ménard,
S., Racine, J., Zhang, J., Chen, J., Morrison, H., Sharma, S., Huang, L.,
Bellavance, P., Ly, J., Izdebski, P., Lyons, L., and Holt, R. (2018). Assessing
the impact of shipping emissions on air pollution in the Canadian Arctic and
northern regions: current and future modelled scenarios. *Atmos. Chem. Phys*
18, pp. 16653–16687. doi: 10.5194/acp-18-16653-2018 (cit. on p. 155).
- [62] Gorham, E. (1958). The influence and importance of daily weather con-
ditions in the supply of chloride, sulphate and other ions to fresh waters
from atmospheric precipitation. *Philosophical Transactions of the Royal So-
ciety of London. Series B, Biological Sciences* 241.679, pp. 147–178. doi:
10.1098/RSTB.1958.0001 (cit. on p. 119).

Chapter 4. Arctic SO₂ Measurements

- [63] Gryspeerdt, E., Povey, A. C., Grainger, R. G., Hasekamp, O., Hsu, N. C., Mulcahy, J. P., Sayer, A. M., and Sorooshian, A. (2023). Uncertainty in aerosol-cloud radiative forcing is driven by clean conditions. *Atmos. Chem. Phys.* 23.7, pp. 4115–4122. doi: 10.5194/acp-23-4115-2023 (cit. on p. 35).
- [64] He, X. C. et al. (2021). Role of iodine oxoacids in atmospheric aerosol nucleation. *Science* 371.6529, pp. 589–595. doi: 10.1126/science.abe0298 (cit. on p. 28).
- [65] Heidam, N. Z., Wählin, P., and Christensen, J. (1999). Tropospheric Gases and Aerosols in Northeast Greenland. *Journal of the Atmospheric Sciences* 56.2, pp. 261–278. doi: 10.1175/1520-0469(1999)056<0261:TGAAIN>2.0.CO;2 (cit. on p. 180).
- [66] Heintzenberg, J. and Larssen, S. (1983). SO₂ and SO₄ in the arctic: interpretation of observations at three Norwegian arctic-subarctic stations. *Tellus B* 35B.4, pp. 255–265. doi: 10.1111/j.1600-0889.1983.tb00028.x (cit. on p. 180).
- [67] Hobbs, P. V. (2000). *Introduction to Atmospheric Chemistry*. Cambridge: Cambridge University Press (cit. on pp. 29, 30).
- [68] Hoffmann, E. H., Schrödner, R., Tilgner, A., Wolke, R., and Herrmann, H. (2020). CAPRAM reduction towards an operational multiphase halogen and dimethyl sulfide chemistry treatment in the chemistry transport model COSMO-Muscat(5.04e). *Geoscientific Model Development* 13.6, pp. 2587–2609. doi: 10.5194/gmd-13-2587-2020 (cit. on p. 38).
- [69] Hoffmann, E. H., Tilgner, A., Schrödner, R., Bräuer, P., Wolke, R., and Herrmann, H. (2016). An advanced modeling study on the impacts and atmospheric implications of multiphase dimethyl sulfide chemistry. *Proceedings of the National Academy of Sciences of the United States of America* 113.42, pp. 11776–11781. doi: 10.1073/pnas.1606320113 (cit. on pp. 38, 191).
- [70] Hoffmann, M. R. (1986). On the kinetics and mechanism of oxidation of aqueated sulfur dioxide by ozone. *Atmospheric Environment (1967)* 20.6, pp. 1145–1154. doi: 10.1016/0004-6981(86)90147-2 (cit. on p. 29).

Chapter 4. Arctic SO₂ Measurements

- [71] Höpfner, M., Boone, C. D., Funke, B., Glatthor, N., Grabowski, U., Günther, A., Kellmann, S., Kiefer, M., Linden, A., Lossow, S., Pumphrey, H. C., Read, W. G., Roiger, A., Stiller, G., Schlager, H., Von Clarmann, T., and Wissmüller, K. (2015). Sulfur dioxide (SO₂) from MIPAS in the upper troposphere and lower stratosphere 2002-2012. *Atmospheric Chemistry and Physics* 15.12, pp. 7017–7037. doi: 10.5194/acp-15-7017-2015 (cit. on p. 183).
- [72] Huey, L. G., Villalta, P. W., Dunlea, E. J., Hanson, D. R., and Howard, C. J. (1996). Reactions of CF₃O⁻ with atmospheric trace gases. *Journal of Physical Chemistry* 100.1, pp. 190–194. doi: 10.1021/jp951928u (cit. on p. 44).
- [73] Hui, M. H. and Rice, S. A. (1972). Decay of fluorescence from single vibronic states of SO₂. *Chemical Physics Letters* 17.4, pp. 474–478. doi: 10.1016/0009-2614(72)85083-8 (cit. on p. 51).
- [74] Iversen, T. and Joranger, E. (1985). Arctic air pollution and large scale atmospheric flows. *Atmospheric Environment (1967)* 19.12, pp. 2099–2108. doi: 10.1016/0004-6981(85)90117-9 (cit. on p. 180).
- [75] Jacob, D. S. L., Giorio, C., and Archibald, A. T. (2024). Extension, development, and evaluation of the representation of the OH-initiated dimethyl sulfide (DMS) oxidation mechanism in the Master Chemical Mechanism (MCM) v3.3.1 framework. *Atmos. Chem. Phys* 24.5, pp. 3329–3347. doi: 10.5194/acp-24-3329-2024 (cit. on p. 201).
- [76] Jaeschke, W., Salkowski, T., Dierssen, J. P., Trümbach, J. V., Krischke, U., and Günther, A. (1999). Measurements of trace substances in the Arctic troposphere as potential precursors and constituents of Arctic haze. *Journal of Atmospheric Chemistry* 34.3, pp. 291–319. doi: 10.1023/A:1006277230042 (cit. on p. 182).
- [77] Jeong, D., McNamara, S. M., Barget, A. J., Raso, A. R., Upchurch, L. M., Thanekar, S., Quinn, P. K., Simpson, W. R., Fuentes, J. D., Shepson, P. B., and Pratt, K. A. (2022). Multiphase Reactive Bromine Chemistry during Late Spring in the Arctic: Measurements of Gases, Particles, and Snow. *ACS Earth and Space Chemistry* 6.12, pp. 2877–2887. doi: 10.1021/acsearthspacechem.2c00189 (cit. on pp. 203, 204).

Chapter 4. Arctic SO₂ Measurements

- [78] Jin, Q., Grandey, B. S., Rothenberg, D., Avramov, A., and Wang, C. (2018). Impacts on cloud radiative effects induced by coexisting aerosols converted from international shipping and maritime DMS emissions. *Atmospheric Chemistry and Physics* 18.22, pp. 16793–16808. doi: 10.5194/acp-18-16793-2018 (cit. on p. 120).
- [79] Jones, A., Roberts, D. L., Woodage, M. J., and Johnson, C. E. (2001). Indirect sulphate aerosol forcing in a climate model with an interactive sulphur cycle. *Journal of Geophysical Research: Atmospheres* 106.D17, pp. 20293–20310. doi: 10.1029/2000JD000089 (cit. on p. 32).
- [80] Jordan, G. and Henry, M. (2024). IMO2020 Regulations Accelerate Global Warming by up to 3 Years in UKESM1. *Earth's Future* 12.8, e2024EF005011. doi: 10.1029/2024EF005011 (cit. on p. 120).
- [81] Katagiri, H., Sako, T., Hishikawa, A., Yazaki, T., Onda, K., Yamanouchi, K., and Yoshino, K. (1997). Experimental and theoretical exploration of photodissociation of SO₂ via the C1B2 state: identification of the dissociation pathway. *Journal of Molecular Structure* 413-414, pp. 589–614. doi: 10.1016/S0022-2860(97)00199-3 (cit. on p. 51).
- [82] Kattner, L., Mathieu-Üffing, B., Burrows, J. P., Richter, A., Schmolke, S., Seyler, A., and Wittrock, F. (2015). Monitoring compliance with sulfur content regulations of shipping fuel by in situ measurements of ship emissions. *Atmospheric Chemistry and Physics* 15.17, pp. 10087–10092. doi: 10.5194/acp-15-10087-2015 (cit. on pp. 139, 140).

Chapter 4. Arctic SO₂ Measurements

- [83] Kerminen, V. M., Petäjä, T., Manninen, H. E., Paasonen, P., Nieminen, T., Sipilä, M., Junninen, H., Ehn, M., Gagné, S., Laakso, L., Riipinen, I., Vehkamäki, H., Kurten, T., Ortega, I. K., Dal Maso, M., Brus, D., Hyvarinen, A., Lihavainen, H., Leppä, J., Lehtinen, K. E., Mirme, A., Mirme, S., Hörrak, U., Berndt, T., Stratmann, F., Birmili, W., Wiedensohler, A., Metzger, A., Dommen, J., Baltensperger, U., Kiendler-Scharr, A., Mentel, T. F., Wildt, J., Winkler, P. M., Wagner, P. E., Petzold, A., Minikin, A., Plass-Dülmer, C., Pöschl, U., Laaksonen, A., and Kulmala, M. (2010). Atmospheric nucleation: Highlights of the EUCAARI project and future directions. *Atmospheric Chemistry and Physics* 10.22, pp. 10829–10848. doi: 10.5194/acp-10-10829-2010 (cit. on p. 28).
- [84] Kerr, J. A., Hoffmann, M. R., and Calvert, J. G. (1985). *Chemical Transformation Modules for Eulerian Acid Deposition Models: Volume II, the Aqueous-phase Chemistry*. North Carolina: U.S. Environmental Protection Agency (cit. on p. 31).
- [85] Khan, M. A. H., Bannan, T. J., Holland, R., Shallcross, D. E., Archibald, A. T., Matthews, E., Back, A., Allan, J., Coe, H., Artaxo, P., and Percival, C. J. (2021). Impacts of Hydroperoxymethyl Thioformate on the Global Marine Sulfur Budget. *ACS Earth and Space Chemistry* 5.10, pp. 2577–2586. doi: 10.1021/acsearthspacechem.1c00218 (cit. on p. 39).
- [86] Kirkby, J., Amorim, A., Baltensperger, U., Carslaw, K. S., Christoudias, T., Curtius, J., Donahue, N. M., Haddad, I. E., Flagan, R. C., Gordon, H., Hansel, A., Harder, H., Junninen, H., Kulmala, M., Kürten, A., Laaksonen, A., Lehtipalo, K., Lelieveld, J., Möhler, O., Riipinen, I., Stratmann, F., Tomé, A., Virtanen, A., Volkamer, R., Winkler, P. M., and Worsnop, D. R. (2023). Atmospheric new particle formation from the CERN CLOUD experiment. *Nature Geoscience* 16.11, pp. 948–957. doi: 10.1038/s41561-023-01305-0 (cit. on p. 28).

Chapter 4. Arctic SO₂ Measurements

- [87] Kirkby, J., Curtius, J., Almeida, J., Dunne, E., Duplissy, J., Ehrhart, S., Franchin, A., Gagné, S., Ickes, L., Kürten, A., Kupc, A., Metzger, A., Riccobono, F., Rondo, L., Schobesberger, S., Tsagkogeorgas, G., Wimmer, D., Amorim, A., Bianchi, F., Breitenlechner, M., David, A., Dommen, J., downward, A., Ehn, M., Flagan, R. C., Haider, S., Hansel, A., Hauser, D., Jud, W., Junninen, H., Kreissl, F., Kvashin, A., Laaksonen, A., Lehtipalo, K., Lima, J., Lovejoy, E. R., Makhmutov, V., Mathot, S., Mikkilä, J., Minginette, P., Mogo, S., Nieminen, T., Onnela, A., Pereira, P., Petäjä, T., Schnitzhofer, R., Seinfeld, J. H., Sipilä, M., Stozhkov, Y., Stratmann, F., Tomé, A., Vanhanen, J., Viisanen, Y., Vrtala, A., Wagner, P. E., Walther, H., Weingartner, E., Wex, H., Winkler, P. M., Carslaw, K. S., Worsnop, D. R., Baltensperger, U., and Kulmala, M. (2011). Role of sulphuric acid, ammonia and galactic cosmic rays in atmospheric aerosol nucleation. *Nature* 476.7361, pp. 429–433. doi: 10.1038/nature10343 (cit. on p. 28).
- [88] Kliner, D. A., Di Teodoro, F., Koplrow, J. P., Moore, S. W., and Smith, A. V. (2002). Efficient second, third, fourth, and fifth harmonic generation of a Yb-doped fiber amplifier. *Optics Communications* 210.3-6, pp. 393–398. doi: 10.1016/S0030-4018(02)01825-4 (cit. on pp. 80, 82).
- [89] Kulmala, M., Toivonen, A., Mäkelä, J. M., Mäkelä, M., and Laaksonen, A. (1998). Analysis of the growth of nucleation mode particles observed in Boreal forest. *Tellus B* 50.5, pp. 449–462. doi: 10.1034/j.1600-0889.1998.t01-4-00004.x (cit. on p. 28).
- [90] Kurosaki, Y., Matoba, S., Iizuka, Y., Fujita, K., and Shimada, R. (2022). Increased oceanic dimethyl sulfide emissions in areas of sea ice retreat inferred from a Greenland ice core. *Communications Earth & Environment* 3.1, p. 327. doi: 10.1038/s43247-022-00661-w (cit. on p. 154).

Chapter 4. Arctic SO₂ Measurements

- [91] Lack, D. A., Cappa, C. D., Langridge, J., Bahreini, R., Buffaloe, G., Brock, C., Cerully, K., Coffman, D., Hayden, K., Holloway, J., Lerner, B., Massoli, P., Li, S. M., McLaren, R., Middlebrook, A. M., Moore, R., Nenes, A., Nuaaman, I., Onasch, T. B., Peischl, J., Perring, A., Quinn, P. K., Ryerson, T., Schwartz, J. P., Spackman, R., Wofsy, S. C., Worsnop, D., Xiang, B., and Williams, E. (2011). Impact of fuel quality regulation and speed reductions on shipping emissions: Implications for climate and air quality. *Environmental Science and Technology* 45.20, pp. 9052–9060. doi: 10.1021/es2013424 (cit. on pp. 121, 139).
- [92] Lamarque, J. F., Emmons, L. K., Hess, P. G., Kinnison, D. E., Tilmes, S., Vitt, F., Heald, C. L., Holland, E. A., Lauritzen, P. H., Neu, J., Orlando, J. J., Rasch, P. J., and Tyndall, G. K. (2012). CAM-chem: Description and evaluation of interactive atmospheric chemistry in the Community Earth System Model. *Geoscientific Model Development* 5.2, pp. 369–411. doi: 10.5194/gmd-5-369-2012 (cit. on p. 39).
- [93] Leck, C. and Persson, C. (1996). Seasonal and short-term variability in dimethyl sulfide, sulfur dioxide and biogenic sulfur and sea salt aerosol particles in the arctic marine boundary layer during summer and autumn. *Tellus B: Chemical and Physical Meteorology* 48.2, pp. 272–299. doi: 10.3402/tellusb.v48i2.15891 (cit. on pp. 156, 182, 195, 205).
- [94] Lee, B. H., Lopez-Hilfiker, F. D., Schroder, J. C., Campuzano-Jost, P., Jimenez, J. L., McDuffie, E. E., Fibiger, D. L., Veres, P. R., Brown, S. S., Campos, T. L., Weinheimer, A. J., Flocke, F. F., Norris, G., O'Mara, K., Green, J. R., Fiddler, M. N., Bililign, S., Shah, V., Jaeglé, L., and Thornton, J. A. (2018). Airborne Observations of Reactive Inorganic Chlorine and Bromine Species in the Exhaust of Coal-Fired Power Plants. *Journal of Geophysical Research: Atmospheres* 123.19, pp. 225–11. doi: 10.1029/2018JD029284 (cit. on p. 121).

Chapter 4. Arctic SO₂ Measurements

- [95] Lee, C., Martin, R. V., Van Donkelaar, A., Lee, H., Dickerson, R. R., Hains, J. C., Krotkov, N., Richter, A., Vinnikov, K., and Schwab, J. J. (2011). SO₂ emissions and lifetimes: Estimates from inverse modeling using in situ and global, space-based (SCIAMACHY and OMI) observations. *Journal of Geophysical Research Atmospheres* 116.D6. doi: 10.1029/2010JD014758 (cit. on p. 187).
- [96] Lee, L. A., Reddington, C. L., and Carslaw, K. S. (2016). On the relationship between aerosol model uncertainty and radiative forcing uncertainty. *Proceedings of the National Academy of Sciences of the United States of America* 113.21, pp. 5820–5827. doi: 10.1073/pnas.1507050113 (cit. on p. 35).
- [97] Likens, G. E., Wright, R. F., Galloway, J. N., and Butler, T. J. (1979). Acid Rain. *Scientific American* 241.4, pp. 43–51 (cit. on p. 25).
- [98] Liu, T., Clegg, S. L., and Abbatt, J. P. (2020). Fast oxidation of sulfur dioxide by hydrogen peroxide in deliquesced aerosol particles. *Proceedings of the National Academy of Sciences of the United States of America* 117.3, pp. 1354–1359. doi: 10.1073/pnas.1916401117 (cit. on p. 29).
- [99] Lucas, D. D. and Prinn, R. G. (2002). Mechanistic studies of dimethylsulfide oxidation products using an observationally constrained model. *Journal of Geophysical Research: Atmospheres* 107.D14, pp. 12–26. doi: 10.1029/2001JD000843 (cit. on p. 36).
- [100] Luke, W. T. (1997). Evaluation of a commercial pulsed fluorescence detector for the measurement of low-level SO₂ concentrations during the gas-phase sulfur intercomparison experiment. *Journal of Geophysical Research Atmospheres* 102.13, pp. 16255–16265. doi: 10.1029/96JD03347 (cit. on pp. 40, 42).
- [101] Lundén, J., Svensson, G., and Leck, C. (2007). Influence of meteorological processes on the spatial and temporal variability of atmospheric dimethyl sulfide in the high Arctic summer. *Journal of Geophysical Research: Atmospheres* 112.D13. doi: 10.1029/2006JD008183 (cit. on p. 191).

Chapter 4. Arctic SO₂ Measurements

- [102] Mahajan, A. S., Tinel, L., Riffault, V., Guilbaud, S., D’Anna, B., Cuevas, C., and Saiz-Lopez, A. (2024). MAX-DOAS observations of ship emissions in the North Sea. *Marine pollution bulletin* 206, p. 116761. doi: 10.1016/j.marpolbul.2024.116761 (cit. on p. 121).
- [103] Mahmood, R., Von Salzen, K., Norman, A. L., Galí, M., and Levasseur, M. (2019). Sensitivity of Arctic sulfate aerosol and clouds to changes in future surface seawater dimethylsulfide concentrations. *Atmospheric Chemistry and Physics* 19.9, pp. 6419–6435. doi: 10.5194/acp-19-6419-2019 (cit. on pp. 153, 154).
- [104] Manatt, S. L. and Lane, A. L. (1993). A compilation of the absorption cross-sections of SO₂ from 106 to 403 nm. *Journal of Quantitative Spectroscopy and Radiative Transfer* 50.3, pp. 267–276. doi: 10.1016/0022-4073(93)90077-U (cit. on pp. 50, 51).
- [105] Mao, J., Jacob, D. J., Evans, M. J., Olson, J. R., Ren, X., Brune, W. H., St. Clair, J. M., Crouse, J. D., Spencer, K. M., Beaver, M. R., Wennberg, P. O., Cubison, M. J., Jimenez, J. L., Fried, A., Weibring, P., Walega, J. G., Hall, S. R., Weinheimer, A. J., Cohen, R. C., Chen, G., Crawford, J. H., McNaughton, C., Clarke, A. D., Jaeglé, L., Fisher, J. A., Yantosca, R. M., Le Sager, P., and Carouge, C. (2010). Chemistry of hydrogen oxide radicals (HOx) in the Arctic troposphere in spring. *Atmospheric Chemistry and Physics* 10.13, pp. 5823–5838. doi: 10.5194/acp-10-5823-2010 (cit. on p. 190).
- [106] Marelle, L., Thomas, J. L., Raut, J. C., Law, K. S., Jalkanen, J. P., Johansson, L., Roiger, A., Schlager, H., Kim, J., Reiter, A., and Weinzierl, B. (2016). Air quality and radiative impacts of Arctic shipping emissions in the summertime in northern Norway: From the local to the regional scale. *Atmospheric Chemistry and Physics* 16.4, pp. 2359–2379. doi: 10.5194/acp-16-2359-2016 (cit. on p. 154).
- [107] Matsumi, Y., Shigemori, H., and Takahashi, K. (2005). Laser-induced fluorescence instrument for measuring atmospheric SO₂. *Atmospheric Environment* 39.17, pp. 3177–3185. doi: 10.1016/j.atmosenv.2005.02.023 (cit. on p. 55).

Chapter 4. Arctic SO₂ Measurements

- [108] Matthews, E., Bannan, T. J., Khan, M. A. H., Shallcross, D. E., Stark, H., Browne, E. C., Archibald, A. T., Mehra, A., Bauguitte, S. J., Reed, C., Thamman, N. M., Wu, H., Barker, P., Lee, J., Carpenter, L. J., Yang, M., Bell, T. G., Allen, G., Jayne, J. T., Percival, C. J., McFiggans, G., Gallagher, M., and Coe, H. (2023). Airborne observations over the North Atlantic Ocean reveal the importance of gas-phase urea in the atmosphere. *Proceedings of the National Academy of Sciences of the United States of America* 120.25, e2218127120. doi: 10.1073/pnas.2218127120 (cit. on p. 130).
- [109] Mauldin, R. L., Berndt, T., Sipilä, M., Paasonen, P., Petäjä, T., Kim, S., Kurtén, T., Stratmann, F., Kerminen, V. M., and Kulmala, M. (2012). A new atmospherically relevant oxidant of sulphur dioxide. *Nature* 488.7410, pp. 193–196. doi: 10.1038/nature11278 (cit. on p. 27).
- [110] McMurry, P. H. and Wilson, J. C. (1982). Growth laws for the formation of secondary ambient aerosols: Implications for chemical conversion mechanisms. *Atmospheric Environment (1967)* 16.1, pp. 121–134. doi: 10.1016/0004-6981(82)90319-5 (cit. on p. 29).
- [111] Melia, N., Haines, K., and Hawkins, E. (2016). Sea ice decline and 21st century trans-Arctic shipping routes. *Geophysical Research Letters* 43.18, pp. 9720–9728. doi: 10.1002/2016GL069315 (cit. on p. 154).
- [112] Merikanto, J., Spracklen, D. V., Mann, G. W., Pickering, S. J., and Carslaw, K. S. (2009). Impact of nucleation on global CCN. *Atmospheric Chemistry and Physics* 9.21, pp. 8601–8616. doi: 10.5194/acp-9-8601-2009 (cit. on pp. 28, 119).
- [113] Middleton, P., Kiang, C. S., and Mohnen, V. A. (1980). Theoretical estimates of the relative importance of various urban sulfate aerosol production mechanisms. *Atmospheric Environment (1967)* 14.4, pp. 463–472. doi: 10.1016/0004-6981(80)90211-5 (cit. on p. 29).
- [114] Möhler, O. and Arnold, F. (1992a). Gaseous Sulfuric Acid and Sulfur Dioxide Measurements in the Arctic Troposphere and Lower Stratosphere: Implications for Hydroxyl Radical Abundances. *Berichte der Bunsengesellschaft für physikalische Chemie* 96.3, pp. 280–283. doi: 10.1002/bbpc.19920960310 (cit. on pp. 41, 44, 45, 181).

Chapter 4. Arctic SO₂ Measurements

- [115] Möhler, O., Reiner, T., and Arnold, F. (1992b). The formation of SO₅ by gas phase ion–molecule reactions. *The Journal of Chemical Physics* 97.11, pp. 8233–8239. doi: 10.1063/1.463394 (cit. on p. 44).
- [116] Mungall, E. L., Croft, B., Lizotte, M., Thomas, J. L., Murphy, J. G., Levasseur, M., Martin, R. V., Wentzell, J. J. B., Liggio, J., and Abbatt, J. P. D. (2016). Dimethyl sulfide in the summertime Arctic atmosphere: measurements and source sensitivity simulations. *Atmos. Chem. Phys* 16.11, pp. 6665–6680. doi: 10.5194/acp-16-6665-2016 (cit. on p. 196).
- [117] Myhre, G., Shindell, D., Bréon, F.-M., Collins, W., Fuglestvedt, J., Huang, J., Koch, D., Lamarque, J.-F., Lee, D., Mendoza, B., Nakajima, T., Robock, A., Stephens, G., Takemura, T., and Zhang, H. (2013). Anthropogenic and Natural Radiative Forcing. In: *Climate Change 2013: The Physical Science Basis. Contribution of Working Group I to the Fifth Assessment Report of the Intergovernmental Panel on Climate Change*. Ed. by T. Stocker, D. Qin, G.-K. Plattner, M. Tignor, S. K. Allen, J. Boschung, A. Nauels, Y. Xia, V. Bex, and P. M. Midgley. Cambridge, United Kingdom and New York, NY, USA: Cambridge University Press (cit. on pp. 33, 119).
- [118] Novak, G. A., Fite, C. H., Holmes, C. D., Veres, P. R., Neuman, J. A., Faloona, I., Thornton, J. A., Wolfe, G. M., Vermeuel, M. P., Jernigan, C. M., Peischl, J., Ryerson, T. B., Thompson, C. R., Bourgeois, I., Warneke, C., Gkatzelis, G. I., Coggon, M. M., Sekimoto, K., Bui, T. P., Dean-Day, J., Diskin, G. S., DiGangi, J. P., Nowak, J. B., Moore, R. H., Wiggins, E. B., Winstead, E. L., Robinson, C., Thornhill, K. L., Sanchez, K. J., Hall, S. R., Ullmann, K., Dollner, M., Weinzierl, B., Blake, D. R., and Bertram, T. H. (2021). Rapid cloud removal of dimethyl sulfide oxidation products limits SO₂ and cloud condensation nuclei production in the marine atmosphere. *Proceedings of the National Academy of Sciences of the United States of America* 118.42. doi: 10.1073/pnas.2110472118 (cit. on pp. 38, 39).
- [119] Okabe, H. (1971). Fluorescence and Predissociation of Sulfur Dioxide. *Journal of the American Chemical Society* 93.25, pp. 7095–7096. doi: 10.1021/ja00754a072 (cit. on pp. 40, 42, 51, 52, 54).

Chapter 4. Arctic SO₂ Measurements

- [120] Park, K.-T., Lee, K., Yoon, Y.-J., Lee, H.-W., Kim, H.-C., Lee, B.-Y., Hermansen, O., Kim, T.-W., Holmén, K., Lee, K., Yoon, Y.-J., Lee, H.-W., Kim, H.-C., Lee, B.-Y., Hermansen, O., Kim, T.-W., and Holmén, K (2013). Linking atmospheric dimethyl sulfide and the Arctic Ocean spring bloom. *Geophysical Research Letters* 40.1, pp. 155–160. doi: 10.1029/2012GL054560 (cit. on p. 194).
- [121] Parrish, D. D., Stohl, A., Forster, C., Atlas, E. L., Blake, D. R., Goldan, P. D., Kuster, W. C., and Gouw, J. A. de (2007). Effects of mixing on evolution of hydrocarbon ratios in the troposphere. *Journal of Geophysical Research: Atmospheres* 112.D10, pp. 10–34. doi: 10.1029/2006JD007583 (cit. on p. 199).
- [122] Paschotta, R., Nilsson, J., Tropper, A. C., and Hanna, D. C. (1997). Ytterbium-doped fiber amplifiers. *IEEE Journal of Quantum Electronics* 33.7, pp. 1049–1056. doi: 10.1109/3.594865 (cit. on p. 58).
- [123] Patroescu, I. V., Barnes, I., Becker, K. H., and Mihalopoulos, N. (1998). FT-IR product study of the OH-initiated oxidation of DMS in the presence of NO_x. *Atmospheric Environment* 33.1, pp. 25–35. doi: 10.1016/S1352-2310(98)00120-4 (cit. on p. 38).
- [124] Penner, J. E., Andreae, M., Annegarn, H., Barrie, L., Feichter, J., Hegg, D., Jayaraman, A., Leaitch, R., Murphy, D., Nganga, J., and Pitari, G. (2001). Aerosols, their direct and indirect effects. *Climate Change 2001: The Scientific Basis. Contribution of Working Group I to the Third Assessment Report of the Intergovernmental Panel on Climate Change*. Ed. by B. Nyenzi and J. Prospero. Cambridge, United Kingdom and New York, NY, USA: Cambridge University Press (cit. on pp. 26, 32, 119).
- [125] Persad, G. G., Samset, B. H., and Wilcox, L. J. (2022). Aerosols must be included in climate risk assessments. *Nature* 611.7937, pp. 662–664. doi: 10.1038/d41586-022-03763-9 (cit. on p. 33).
- [126] Pham, M., Muller, J. F., Brasseur, G. P., Granier, C., and Megie, G. (1995). A three-dimensional study of the tropospheric sulfur cycle. *Journal of Geophysical Research: Atmospheres* 100.D12, pp. 26061–26092. doi: 10.1029/95JD02095 (cit. on pp. 27, 31).
- [127] *Phase Matching* (n.d.). doi: 10.61835/BPM (cit. on pp. 79, 80).

Chapter 4. Arctic SO₂ Measurements

- [128] Pithan, F. and Mauritsen, T. (2014). Arctic amplification dominated by temperature feedbacks in contemporary climate models. *Nature Geoscience* 2014 7:3 7.3, pp. 181–184. doi: 10.1038/ngeo2071 (cit. on p. 153).
- [129] Platt, U. and Perner, D. (1980). Direct measurements of atmospheric CH₂O, HNO₂, O₃, NO₂, and SO₂ by differential optical absorption in the near UV. *Journal of Geophysical Research: Oceans* 85.C12, pp. 7453–7458. doi: 10.1029/JC085iC12p07453 (cit. on pp. 41, 43).
- [130] Platt, U., Perner, D., and Paetz, H. W. (1979). Simultaneous measurement of atmospheric CH₂O, O₃, and NO₂ by differential optical absorption. *Journal of Geophysical Research* 84.C10, pp. 6329–6335. doi: 10.1029/JC084iC10p06329 (cit. on p. 42).
- [131] Pye, H. O., Nenes, A., Alexander, B., Ault, A. P., Barth, M. C., Clegg, S. L., Collett, J. L., Fahey, K. M., Hennigan, C. J., Herrmann, H., Kanakidou, M., Kelly, J. T., Ku, I. T., Faye McNeill, V., Riemer, N., Schaefer, T., Shi, G., Tilgner, A., Walker, J. T., Wang, T., Weber, R., Xing, J., Zaveri, R. A., and Zuend, A. (2020). The acidity of atmospheric particles and clouds. *Atmospheric Chemistry and Physics* 20.8, pp. 4809–4888. doi: 10.5194/acp-20-4809-2020 (cit. on pp. 27, 29).
- [132] Quaglia, I. and Visioni, D. (n.d.). Modeling 2020 regulatory changes in international shipping emissions helps explain 2023 anomalous warming (). doi: 10.5194/egusphere-2024-1417 (cit. on p. 120).
- [133] Quinn, P. K. and Bates, T. S. (2011). The case against climate regulation via oceanic phytoplankton sulphur emissions. *Nature* 480.7375, pp. 51–56. doi: 10.1038/nature10580 (cit. on p. 36).
- [134] Quinn, P. K., Shaw, G., Andrews, E., Dutton, E. G., Ruoho-Airola, T., and Gong, S. L. (2007). Arctic haze: current trends and knowledge gaps. *Tellus B: Chemical and Physical Meteorology* 59.1, pp. 99–114. doi: 10.1111/j.1600-0889.2006.00236.x (cit. on p. 179).
- [135] Rahn, K. A., Joranger, E., Semb, A., and Conway, T. J. (1980). High winter concentrations of SO₂ in the Norwegian Arctic and transport from Eurasia. *Nature* 287.5785, pp. 824–826. doi: 10.1038/287824a0 (cit. on p. 180).

Chapter 4. Arctic SO₂ Measurements

- [136] Rantanen, M., Karpechko, A. Y., Lipponen, A., Nordling, K., Hyvärinen, O., Ruosteenoja, K., Vihma, T., and Laaksonen, A. (2022). The Arctic has warmed nearly four times faster than the globe since 1979. *Communications Earth & Environment* 2022 3:1 3.1, pp. 1–10. doi: 10.1038/s43247-022-00498-3 (cit. on p. 153).
- [137] Rempillo, O., Seguin, A. M., Norman, A.-L., Scarratt, M., Michaud, S., Chang, R., Sjostedt, S., Abbatt, J., Else, B., Papakyriakou, T., Sharma, S., Grasby, S., and Levasseur, M. (2011). Dimethyl sulfide air-sea fluxes and biogenic sulfur as a source of new aerosols in the Arctic fall. *J. Geophys. Res* 116.D17, pp. 0–4. doi: 10.1029/2011JD016336 (cit. on pp. 182, 184, 205).
- [138] Rickly, P. S., Guo, H., Campuzano-Jost, P., Jimenez, J. L., Wolfe, G. M., Bennett, R., Bourgeois, I., Crouse, J. D., Dibb, J. E., Digangi, J. P., Diskin, G. S., Dollner, M., Gargulinski, E. M., Hall, S. R., Halliday, H. S., Hanisco, T. F., Hannun, R. A., Liao, J., Moore, R., Nault, B. A., Nowak, J. B., Peischl, J., Robinson, C. E., Ryerson, T., Sanchez, K. J., Schöberl, M., Soja, A. J., St. Clair, J. M., Thornhill, K. L., Ullmann, K., Wennberg, P. O., Weinzierl, B., Wiggins, E. B., Winstead, E. L., and Rollins, A. W. (2022). Emission factors and evolution of SO₂ measured from biomass burning in wildfires and agricultural fires. *Atmospheric Chemistry and Physics* 22.23, pp. 15603–15620. doi: 10.5194/acp-22-15603-2022 (cit. on p. 121).
- [139] Rickly, P. S., Xu, L., Crouse, J. D., Wennberg, P. O., and Rollins, A. W. (2021). Improvements to a laser-induced fluorescence instrument for measuring SO₂ - Impact on accuracy and precision. *Atmospheric Measurement Techniques* 14.3, pp. 2429–2439. doi: 10.5194/amt-14-2429-2021 (cit. on pp. 59, 60, 121, 122, 124).
- [140] Rollins, A. W., Thornberry, T. D., Watts, L. A., Yu, P., Rosenlof, K. H., Mills, M., Baumann, E., Giorgetta, F. R., Bui, T. V., Höpfner, M., Walker, K. A., Boone, C., Bernath, P. F., Colarco, P. R., Newman, P. A., Fahey, D. W., and Gao, R. S. (2017). The role of sulfur dioxide in stratospheric aerosol formation evaluated by using in situ measurements in the tropical lower stratosphere. *Geophysical Research Letters* 44.9, pp. 4280–4286. doi: 10.1002/2017GL072754 (cit. on p. 122).

Chapter 4. Arctic SO₂ Measurements

- [141] Rollins, A. W., Rickly, P. S., Gao, R. S., Ryerson, T. B., Brown, S. S., Peischl, J., and Bourgeois, I. (2020). Single-photon laser-induced fluorescence detection of nitric oxide at sub-parts-per-trillion mixing ratios. *Atmospheric Measurement Techniques* 13.5, pp. 2425–2439. doi: 10.5194/amt-13-2425-2020 (cit. on p. 71).
- [142] Rollins, A. W., Thornberry, T. D., Ciciora, S. J., McLaughlin, R. J., Watts, L. A., Hanisco, T. F., Baumann, E., Giorgetta, F. R., Bui, T. V., and Fahey, D. W. (2016). A laser-induced fluorescence instrument for aircraft measurements of sulfur dioxide in the upper troposphere and lower stratosphere. *Atmospheric Measurement Techniques* 9.9, pp. 4601–4613. doi: 10.5194/amt-9-4601-2016 (cit. on pp. 47, 50, 56, 58, 59, 63, 82, 84, 85, 87, 93, 94, 100, 104, 112, 121–125, 129).
- [143] Rufus, J., Stark, G., Smith, P. L., Pickering, J. C., and Thorne, A. P. (2003). High-resolution photoabsorption cross section measurements of SO₂, 2: 220 to 325 nm at 295 K. *Journal of Geophysical Research: Planets* 108.E2, p. 5011. doi: 10.1029/2002JE001931 (cit. on p. 50).
- [144] Sarnela, N., Jokinen, T., Duplissy, J., Yan, C., Nieminen, T., Ehn, M., Schobesberger, S., Heinritzi, M., Ehrhart, S., Lehtipalo, K., Tröstl, J., Simon, M., Kürten, A., Leiminger, M., Lawler, M. J., Rissanen, M. P., Bianchi, F., Praplan, A. P., Hakala, J., Amorim, A., Gonin, M., Hansel, A., Kirkby, J., Dommen, J., Curtius, J., Smith, J. N., Petäjä, T., Worsnop, D. R., Kulmala, M., Donahue, N. M., and Sipilä, M. (2018). Measurement-model comparison of stabilized Criegee intermediate and highly oxygenated molecule production in the CLOUD chamber. *Atmospheric Chemistry and Physics* 18.4, pp. 2363–2380. doi: 10.5194/acp-18-2363-2018 (cit. on p. 28).
- [145] Schlager, H, Baumann, R, Lichtenstern, M, Petzold, A, Arnold, F, Speidel, M, Gurk, C, and Fischer, H (2007). Aircraft-based Trace Gas Measurements in a Primary European Ship Corridor. *Proceedings of an International Conference on Transport, Atmosphere and Climate (TAC)*. vol. 29. Office for Official Publications of the European Communities, Luxembourg, pp. 83–88 (cit. on p. 185).

Chapter 4. Arctic SO₂ Measurements

- [146] Seinfeld, J. H. and Pandis, S. N. (1998). *Atmospheric Chemistry and Physics - From Air Pollution to Climate Change*. New York: John Wiley & Sons Inc. (cit. on pp. 27, 29–31).
- [147] Seyler, A., Wittrock, F., Kattner, L., Mathieu-Üffing, B., Peters, E., Richter, A., Schmolke, S., and Burrows, J. P. (2017). Monitoring shipping emissions in the German Bight using MAX-DOAS measurements. *Atmospheric Chemistry and Physics* 17.18, pp. 10997–11023. doi: 10.5194/acp-17-10997-2017 (cit. on p. 121).
- [148] Sharma, S., Barrie, L. A., Plummer, D., McConnell, J. C., Brickell, P. C., Levasseur, M., Gosselin, M., and Bates, T. S. (1999). Flux estimation of oceanic dimethyl sulfide around North America. *Journal of Geophysical Research: Atmospheres* 104.D17, pp. 21327–21342. doi: 10.1029/1999JD900207 (cit. on p. 191).
- [149] Shaw, G. E. (1995). The Arctic Haze Phenomenon. *Bulletin of the American Meteorological Society* 76.12, pp. 2403–2414. doi: 10.1175/1520-0477(1995)076<2403:TAHP>2.0.CO;2 (cit. on p. 180).
- [150] Shen, J., Scholz, W., He, X. C., Zhou, P., Marie, G., Wang, M., Marten, R., Surdu, M., Rörup, B., Baalbaki, R., Amorim, A., Ataei, F., Bell, D. M., Bertozzi, B., Brasseur, Z., Caudillo, L., Chen, D., Chu, B., Dada, L., Duplissy, J., Finkenzeller, H., Granzin, M., Guida, R., Heinritzi, M., Hofbauer, V., Iyer, S., Kemppainen, D., Kong, W., Krechmer, J. E., Kürten, A., Lamkaddam, H., Lee, C. P., Lopez, B., Mahfouz, N. G., Manninen, H. E., Massabò, D., Mauldin, R. L., Mentler, B., Müller, T., Pfeifer, J., Philippov, M., Piedehierro, A. A., Roldin, P., Schobesberger, S., Simon, M., Stolzenburg, D., Tham, Y. J., Tomé, A., Umo, N. S., Wang, D., Wang, Y., Weber, S. K., Welti, A., Wollesen De Jonge, R., Wu, Y., Zauner-Wieczorek, M., Züst, F., Baltensperger, U., Curtius, J., Flagan, R. C., Hansel, A., Möhler, O., Petäjä, T., Volkamer, R., Kulmala, M., Lehtipalo, K., Rissanen, M., Kirkby, J., El-Haddad, I., Bianchi, F., Sipilä, M., Donahue, N. M., and Worsnop, D. R. (2022). High Gas-Phase Methanesulfonic Acid Production in the OH-Initiated Oxidation of Dimethyl Sulfide at Low Temperatures. *Environmental Science and Technology* 56.19, pp. 13931–13944. doi: 10.1021/acs.est.2c05154 (cit. on p. 38).

Chapter 4. Arctic SO₂ Measurements

- [151] Sherwen, T., Schmidt, J. A., Evans, M. J., Carpenter, L. J., Großmann, K., Eastham, S. D., Jacob, D. J., Dix, B., Koenig, T. K., Sinreich, R., Ortega, I., Volkamer, R., Saiz-Lopez, A., Prados-Roman, C., Mahajan, A. S., and Ordóñez, C. (2016). Global impacts of tropospheric halogens (Cl, Br, I) on oxidants and composition in GEOS-Chem. *Atmospheric Chemistry and Physics* 16.18, pp. 12239–12271. DOI: 10.5194/acp-16-12239-2016 (cit. on p. 30).
- [152] Shindell, D. and Faluvegi, G. (2009). Climate response to regional radiative forcing during the twentieth century. *Nature Geoscience* 2:4 2.4, pp. 294–300. DOI: 10.1038/ngeo473 (cit. on p. 153).
- [153] Shon, Z. H., Davis, D., Chen, G., Grodzinsky, G., Bandy, A., Thornton, D., Sandholm, S., Bradshaw, J., Stickel, R., Chameides, W., Kok, G., Russell, L., Mauldin, L., Tanner, D., and Eisele, F. (2001). Evaluation of the DMS flux and its conversion to SO₂ over the southern ocean. *Atmospheric Environment* 35.1, pp. 159–172. DOI: 10.1016/S1352-2310(00)00166-7 (cit. on p. 203).
- [154] Sidebottom, H. W., Otsuka, K., Horowitz, A., Calvert, J. G., Rabe, B. R., and Damon, E. K. (1972). Vibronic effects in the decay of the fluorescence excited in SO₂ and NO₂. *Chemical Physics Letters* 13.4, pp. 337–343. DOI: 10.1016/0009-2614(72)80096-4 (cit. on p. 51).
- [155] Siegman, A. E. (1986). *Lasers*. United States: University Science Books (cit. on p. 67).
- [156] Simpson, W. R., Brown, S. S., Saiz-Lopez, A., Thornton, J. A., and Von Glasow, R. (2015). Tropospheric Halogen Chemistry: Sources, Cycling, and Impacts. *Chemical Reviews* 115.10, pp. 4035–4062. DOI: 10.1021/cr5006638 (cit. on p. 204).
- [157] Skeie, R. B., Byrom, R., Hodnebrog, Jouan, C., and Myhre, G. (n.d.). Multi-model effective radiative forcing of the 2020 sulphur cap for shipping (). DOI: 10.5194/egusphere-2024-1394 (cit. on p. 120).
- [158] Smith, L. C. and Stephenson, S. R. (2013). New Trans-Arctic shipping routes navigable by midcentury. *Proceedings of the National Academy of Sciences of the United States of America* 110.13, E1191–E1195. DOI: 10.1073/pnas.1214212110 (cit. on p. 154).

Chapter 4. Arctic SO₂ Measurements

- [159] Smith, S. J., Aardenne, J. van, Klimont, Z., Andres, R. J., Volke, A., and Delgado Arias, S. (2011). Anthropogenic sulfur dioxide emissions: 1850–2005. *Atmospheric Chemistry and Physics* 11.3, pp. 1101–1116. DOI: 10.5194/acp-11-1101-2011 (cit. on pp. 25, 119).
- [160] Sofiev, M., Winebrake, J. J., Johansson, L., Carr, E. W., Prank, M., Soares, J., Vira, J., Kouznetsov, R., Jalkanen, J. P., and Corbett, J. J. (2018). Cleaner fuels for ships provide public health benefits with climate tradeoffs. *Nature Communications* 2018 9:1 9.1, pp. 1–12. DOI: 10.1038/s41467-017-02774-9 (cit. on pp. 120, 154).
- [161] Speidel, M., Nau, R., Arnold, F., Schlager, H., and Stohl, A. (2007). Sulfur dioxide measurements in the lower, middle and upper troposphere: Deployment of an aircraft-based chemical ionization mass spectrometer with permanent in-flight calibration. *Atmospheric Environment* 41.11, pp. 2427–2437. DOI: 10.1016/j.atmosenv.2006.07.047 (cit. on pp. 41, 44, 45, 121).
- [162] Stark, G., Smith, P. L., Rufus, J., Thorne, A. P., Pickering, J. C., and Cox, G. (1999). High-resolution photoabsorption cross-section measurements of SO₂ at 295 K between 198 and 220 nm. *Journal of Geophysical Research: Planets* 104.E7, pp. 16585–16590. DOI: 10.1029/1999JE001022 (cit. on pp. 50, 67).
- [163] Stark, H., Yatavelli, R. L., Thompson, S. L., Kimmel, J. R., Cubison, M. J., Chhabra, P. S., Canagaratna, M. R., Jayne, J. T., Worsnop, D. R., and Jimenez, J. L. (2015). Methods to extract molecular and bulk chemical information from series of complex mass spectra with limited mass resolution. *International Journal of Mass Spectrometry* 389, pp. 26–38. DOI: 10.1016/j.ijms.2015.08.011 (cit. on pp. 131, 132).
- [164] Stelson, A. W. and Bao, X. (1988). Water Interference of Pulsed Fluorescence SO₂ Monitor. *JAPCA* 38.4, p. 420. DOI: 10.1080/08940630.1988.10466393 (cit. on p. 42).
- [165] Stephenson, S. R., Smith, L. C., Brigham, L. W., and Agnew, J. A. (2013). Projected 21st-century changes to Arctic marine access. *Climatic Change* 118.3-4, pp. 885–899. DOI: 10.1007/s10584-012-0685-0 (cit. on p. 154).

Chapter 4. Arctic SO₂ Measurements

- [166] Thornton, D. C., Bandy, A. R., and Driedger, A. R. (1989). Sulfur dioxide in the North American Arctic. *Journal of Atmospheric Chemistry* 9.1, pp. 331–346. doi: 10.1007/BF00052841 (cit. on p. 192).
- [167] Thornton, D. C., Bandy, A. R., Tu, F. H., Blomquist, B. W., Mitchell, G. M., Nadler, W., Lenschow, D. H., Thornton, D. C., Bandy, A. R., Tu, F. H., Blomquist, B. W., Mitchell, G. M., Nadler, W, and Lenschow, D. H. (2002). Fast airborne sulfur dioxide measurements by Atmospheric Pressure Ionization Mass Spectrometry (APIMS). *Journal of Geophysical Research: Atmospheres* 107.D22, p. 4632. doi: 10.1029/2002JD002289 (cit. on pp. 41, 44, 45, 121).
- [168] Toumi, R. (1994). BrO as a sink for dimethylsulphide in the marine atmosphere. *Geophysical Research Letters* 21.2, pp. 117–120. doi: 10.1029/93GL03536 (cit. on pp. 38, 204).
- [169] Turnock, S. T., Mann, G. W., Woodhouse, M. T., Dalvi, M., O’Connor, F. M., Carslaw, K. S., and Spracklen, D. V. (2019). The Impact of Changes in Cloud Water pH on Aerosol Radiative Forcing. *Geophysical Research Letters* 46.7, pp. 4039–4048. doi: 10.1029/2019GL082067 (cit. on p. 30).
- [170] *Tutorial “Fiber Amplifiers”* (n.d.) (cit. on pp. 61, 77, 78).
- [171] Twomey, S. (1977). The Influence of Pollution on the Shortwave Albedo of Clouds. *Journal of the Atmospheric Sciences* 34.7, pp. 1149–1152. doi: 10.1175/1520-0469(1977)034 (cit. on p. 32).

Chapter 4. Arctic SO₂ Measurements

- [172] Veres, P. R., Andrew Neuman, J., Bertram, T. H., Assaf, E., Wolfe, G. M., Williamson, C. J., Weinzierl, B., Tilmes, S., Thompson, C. R., Thames, A. B., Schroder, J. C., Saiz-Lopez, A., Rollins, A. W., Roberts, J. M., Price, D., Peischl, J., Nault, B. A., Møller, K. H., Miller, D. O., Meinardi, S., Li, Q., Lamarque, J. F., Kupc, A., Kjaergaard, H. G., Kinnison, D., Jimenez, J. L., Jernigan, C. M., Hornbrook, R. S., Hills, A., Dollner, M., Day, D. A., Cuevas, C. A., Campuzano-Jost, P., Burkholder, J., Paul Bui, T., Brune, W. H., Brown, S. S., Brock, C. A., Bourgeois, I., Blake, D. R., Apel, E. C., and Ryerson, T. B. (2020). Global airborne sampling reveals a previously unobserved dimethyl sulfide oxidation mechanism in the marine atmosphere. *Proceedings of the National Academy of Sciences of the United States of America* 117.9, pp. 4505–4510. doi: 10.1073/pnas.1919344117 (cit. on pp. 36, 38, 39).
- [173] Wang, L., Khalizov, A. F., Zheng, J., Xu, W., Ma, Y., Lal, V., and Zhang, R. (2010). Atmospheric nanoparticles formed from heterogeneous reactions of organics. *Nature Geoscience* 3.4, pp. 238–242. doi: 10.1038/ngeo778 (cit. on p. 28).
- [174] Wang, M. and Overland, J. E. (2009). A sea ice free summer Arctic within 30 years? *Geophysical Research Letters* 36.7. doi: 10.1029/2009GL037820 (cit. on p. 153).
- [175] Watson-Parris, D., Christensen, M. W., Laurenson, A., Clewley, D., Gryspeerd, E., and Stier, P. (2022). Shipping regulations lead to large reduction in cloud perturbations. *Proceedings of the National Academy of Sciences of the United States of America* 119.41, e2206885119. doi: 10.1073/pnas.2206885119 (cit. on p. 26).
- [176] Wennberg, P. O., Cohen, R. C., Hazen, N. L., Lapson, L. B., Allen, N. T., Hanisco, T. F., Oliver, J. F., Lanham, N. W., Demusz, J. N., and Anderson, J. G. (1994). Aircraft-borne, laser-induced fluorescence instrument for the in situ detection of hydroxyl and hydroperoxyl radicals. *Review of Scientific Instruments* 65.6, pp. 1858–1876. doi: 10.1063/1.1144835 (cit. on p. 94).

Chapter 4. Arctic SO₂ Measurements

- [177] Williamson, C. J., Kupc, A., Axisa, D., Bilsback, K. R., Bui, T. P., Campuzano-Jost, P., Dollner, M., Froyd, K. D., Hodshire, A. L., Jimenez, J. L., Kodros, J. K., Luo, G., Murphy, D. M., Nault, B. A., Ray, E. A., Weinzierl, B., Wilson, J. C., Yu, F., Yu, P., Pierce, J. R., and Brock, C. A. (2019). A large source of cloud condensation nuclei from new particle formation in the tropics. *Nature* 574.7778, pp. 399–403. doi: 10.1038/s41586-019-1638-9 (cit. on p. 25).
- [178] Willis, M. D., Leaitch, W. R., and Abbatt, J. P. (2018). Processes Controlling the Composition and Abundance of Arctic Aerosol. *Reviews of Geophysics* 56.4, pp. 621–671. doi: 10.1029/2018RG000602 (cit. on p. 182).
- [179] Wu, C. and Zhen Yu, J. (2018). Evaluation of linear regression techniques for atmospheric applications: The importance of appropriate weighting. *Atmospheric Measurement Techniques* 11.2, pp. 1233–1250. doi: 10.5194/amt-11-1233-2018 (cit. on pp. 110, 128).
- [180] Wu, R., Wang, S., and Wang, L. (2015). New mechanism for the atmospheric oxidation of dimethyl sulfide. The importance of intramolecular hydrogen shift in a CH₃SCH₂OO radical. *Journal of Physical Chemistry A* 119.1, pp. 112–117. doi: 10.1021/jp511616j (cit. on p. 36).
- [181] Xin, R. and Zuegel, J. D. (2011). Amplifying nanosecond optical pulses at 1053 nm with an all-fiber regenerative amplifier. *Optics Letters* 36.14, pp. 2605–2607. doi: 10.1364/OL.36.002605 (cit. on pp. 61, 64).
- [182] Xue, J., Chen, W., Pan, Y., Shi, J., Fang, Y., Xie, H., Xie, M., Sun, L., and Su, B. (2016). Pulsed laser linewidth measurement using Fabry–Pérot scanning interferometer. *Results in Physics* 6.2211-3797, pp. 698–703. doi: 10.1016/j.rinp.2016.10.004 (cit. on p. 68).
- [183] Yang, A. (2006). Experimental demonstration of a ring-cavity Q-switched fiber regenerative amplifier. *Japanese Journal of Applied Physics, Part 2: Letters* 45.7L, p. L673. doi: 10.1143/JJAP.45.L673 (cit. on p. 61).
- [184] Yang, M., Bell, T. G., Hopkins, F. E., and Smyth, T. J. (2016). Attribution of atmospheric sulfur dioxide over the English Channel to dimethyl sulfide and changing ship emissions. *Atmospheric Chemistry and Physics* 16.8, pp. 4771–4783. doi: 10.5194/acp-16-4771-2016 (cit. on pp. 41, 42, 120, 121, 139, 203).

Chapter 4. Arctic SO₂ Measurements

- [185] Ye, Q., Goss, M. B., Isaacman-Vanwertz, G., Zaytsev, A., Massoli, P., Lim, C., Croteau, P., Canagaratna, M., Knopf, D. A., Keutsch, F. N., Heald, C. L., and Kroll, J. H. (2021). Organic Sulfur Products and Peroxy Radical Isomerization in the OH Oxidation of Dimethyl Sulfide. *ACS Earth and Space Chemistry* 5.8, pp. 2013–2020. doi: 10.1021/acsearthspacechem.1c00108 (cit. on p. 38).
- [186] Yin, F., Grosjean, D., Flagan, R. C., and Seinfeld, J. H. (1990). Photooxidation of dimethyl sulfide and dimethyl disulfide. II: Mechanism evaluation. *Journal of Atmospheric Chemistry* 11.4, pp. 365–399. doi: 10.1007/BF00053781 (cit. on p. 38).
- [187] Yoshioka, M., Grosvenor, D. P., Booth, B. B. B., Morice, C. P., and Carslaw, K. S. (n.d.). Warming effects of reduced sulfur emissions from shipping (). doi: 10.5194/egusphere-2024-1428 (cit. on p. 120).
- [188] *Ytterbium-doped Laser Gain Media* (n.d.). doi: 10.61835/zdc (cit. on p. 58).
- [189] Yu, C., Pasternak, D., Lee, J., Yang, M., Bell, T., Bower, K., Wu, H., Liu, D., Reed, C., Bauguitte, S., Cliff, S., Trembath, J., Coe, H., and Allan, J. D. (2020). Characterizing the Particle Composition and Cloud Condensation Nuclei from Shipping Emission in Western Europe. *Environmental Science and Technology* 54.24, pp. 15604–15612. doi: 10.1021/acs.est.0c04039 (cit. on pp. 121, 122, 139, 141).
- [190] Yuan, T., Song, H., Oreopoulos, L., Wood, R., Bian, H., Breen, K., Chin, M., Yu, H., Barahona, D., Meyer, K., and Platnick, S. (2024). Abrupt reduction in shipping emission as an inadvertent geoengineering termination shock produces substantial radiative warming. *Communications Earth & Environment* 5.1, p. 281. doi: 10.1038/s43247-024-01442-3 (cit. on p. 120).
- [191] Yuan, T., Song, H., Wood, R., Wang, C., Oreopoulos, L., Platnick, S. E., Von Hippel, S., Meyer, K., Light, S., and Wilcox, E. (2022). Global reduction in ship-tracks from sulfur regulations for shipping fuel. *Science Advances* 8.29, p. 7988. doi: 10.1126/sciadv.abn7988 (cit. on p. 120).

Chapter 4. Arctic SO₂ Measurements

- [192] Zanatta, M., Bozem, H., Köllner, F., Schneider, J., Kunkel, D., Hoor, P., Faria, J. de, Petzold, A., Bundke, U., Hayden, K., Staebler, R. M., Schulz, H., and Herber, A. B. (2020). Airborne survey of trace gases and aerosols over the Southern Baltic Sea: from clean marine boundary layer to shipping corridor effect. *Tellus B: Chemical and Physical Meteorology* 72.1, pp. 1–24. doi: 10.1080/16000889.2019.1695349 (cit. on pp. 41, 121).